Age and origin of proterozoic kimberlites and lamproites from the Dharwar Craton, southern India

Thesis

Age and origin of Proterozoic kimberlites and lamproites from the Dharwar Craton, southern India

A thesis presented for the degree of Doctor of Philosophy

Ian Osborne

MGeol (University of Leicester); MSc (Loughborough University)

July 2011

Centre for Earth, Planetary, Space and Astronomical Research (CEPSAR)
Department of Earth and Environmental Sciences
The Open University, Walton Hall
Milton Keynes, MK7 6AA
U.K.

DATE OF SUBMISSION: 27 JULY 2011
DATE OF AWARD: 30 JANUARY 2012

APPENDIX A3 P.355-360 AND APPENDIX A4 P.361-END NOT DIGITISED AT REQUEST OF UNIVERSITY

Acknowledgements

I would like to thank my supervisors, Mahesh Anand, Tom Argles and Sarah Sherlock for all their guidance and support throughout my PhD. I would also like to acknowledge my NERC PhD studentship NE/F008805/1 with NHM CASE support.

I would like to thank all the people at the Open University who have assisted with instrumentation and data collection: Sam Hammond (LA-ICP-MS), James Schwanethal (Ar dating), Michelle Higgins (thin-sections), Andrew G. Tindle (Microprobe), Diane Johnson (SEM), John Watson (XRF) and Ian Parkinson (various discussions and Nd bulk-rock analysis).

I am particularly grateful to Chalapathi Rao for his help with the field work and sample collection in India, Catherine Unsworth and Terry Williams at the Natural History Museum for ICP-MS, ICP-AES and microprobe work and Ian Millar at NERC Isotope Geosciences Laboratory (NIGL) for Nd and Hf isotopic analysis of perovskites.

I would also like to thank my fellow PhD students at the OU who provided support throughout my PhD. In particular I would like to thank my office mates Pierre Bonnand and Alison Hunt, for all the fun times in the office, help with my PhD and intellectual discussions.

Abstract

This is a study of kimberlite and lamproite intrusions located in southern India within the Eastern Dharwar craton (EDC). Bulk-rock major-element, trace-element, REE- and Nd-isotopic data support previous studies that have classified the ultramafic magmatism located in the EDC as either Group I kimberlite or lamproite. This study reports new high-precision Ar–Ar age data for southern Indian ultrapotassic rocks (kimberlites and lamproites). Previously, the Chelima lamproite (ca. 1400 Ma) was considered to be one of the oldest lamproites in the world. However, our age data suggest that at least one lamproite (Pochampalle from Krishna lamproite field) was generated in the same region 100 Ma before the Chelima event. The Pochampalle lamproite was emplaced around ~1500 Ma as shown by the Ar–Ar data in this study, roughly 250 Ma before the other Krishna lamproites. It would seem that the Pochampalle lamproite was also derived from an isotopically distinct source region with a lower $^{143}Nd/^{144}Nd$ ratio than other Krishna lamproites. These findings not only have implications for regional ultramafic/ultrapotassic magmatism, but also demonstrate that the mantle processes for producing lamproitic melts existed earlier than previously thought. This study also presents the first Hf isotopic analyses of perovskites from Indian kimberlites. Perovskites fall into two distinct groups in Hf isotope space, suggesting a degree of heterogeneity in the source of the kimberlites in the EDC. The kimberlites are all found in such close proximity that lateral variations in the source are unlikely, but this does not preclude vertical heterogeneity in the source region(s). I propose a model of kimberlite generation with a vertically heterogeneous source that has undergone separate periods of enrichment and depletion before kimberlite melt generation and emplacement at ~1100 Ma.

Contents

Appendices

A.2.7. Bulk-rock XRF Data (p.325-332)

A.2.8. Perovskite Nd and Hf Isotopic Data (p.333)

A.2.9. Perovskite LA-ICP-MS Data (p.334-353)

A.3. 9th International Kimberlite Conference Abstract (p.355-360)

Anand, M., Terada K, **Osborne, I.**, Chalapathi Rao, N. V., Dongre, A. (2008) SHRIMP U-Pb dating of Perovskites from southern Indian kimberlites. 9th International Kimberlite Conference Extended Abstract No. 9IKC-A-00222.

A.4. Co-Authored paper (p.361-376)

Chalapathi Rao, N.V., Anand, M., Dongre, A., **Osborne, I.** (2009) Carbonate xenoliths hosted by the Mesoproterozoic Siddanpalli Kimberlite Cluster (Eastern Dharwar craton): implications for the geodynamic evolution of southern India and its diamond and uranium metallogenesis. International Journal of Earth Sciences, DOI 10.1007/s00531-009-0484-7.

List of Figures and Tables

Figures

Tables

Chapter 3: Bulk-Rock Geochemistry

Chapter 4: Geochronology

Chapter 5: Nd and Hf isotopic composition of perovskites

Appendices

Chapter 1: Introduction

1.1. Introduction

Kimberlites and lamproites are potassic-ultrapotassic, volatile-rich, ultramafic rocks that are the result of partial melting of a mantle rock known as peridotite, which is mineralogically composed of olivine, pyroxene, and minor garnet. Kimberlites are rare in the geological record and are generated at greater depths than those for any other known rock types. When kimberlitic magmas ascend from their places of origin to Earth's surface, they often entrain mantle and crustal xenoliths and are therefore one of our primary windows into Earth's interior (Dawson 1980).

In effect, kimberlites and lamproites provide snapshots of the geochemical and isotopic nature of the deep lithospheric or asthenospheric mantle at the time of their emplacement and although geophysical studies can reveal gross sub-surface features, a direct insight into the lower parts of the continental plates can only be gained through studies of kimberlites, lamproites and their xenoliths.

1.2. The aims of the project

The aims of the project are:

- To perform geochemical and isotopic investigations of southern Indian kimberlites and lamproites to assess the melt generation processes that led to their formation, and investigate the nature of their mantle sources.

- To better constrain the emplacement ages of both kimberlites and lamproites from southern India to enhance our understanding of the palaeo-tectonic evolution of the southern Indian craton in particular and the evolution of Proterozoic supercontinents in general.

1.3. The structure of the thesis

This thesis contains 7 chapters and the appendices. Chapter 1 is the thesis introduction and describes the aims of this project and introduces typical kimberlite and lamproite occurrences in terms of their formation, classification, xenoliths, diamonds, mineralogy and age. Chapter 2 introduces the geology of the field area, and each sample location, providing a field, hand specimen and petrographical description. Chapter 3 presents the bulk-rock geochemistry of the kimberlite and lamproite samples. This chapter provides an assessment of the level of contamination of each of the samples and presents the major element, trace element, rare earth element and bulk rock Nd isotopic data. Chapter 4 discusses new Ar-Ar age data for the Indian kimberlites and lamproites. The bulk of this chapter is comprised of a manuscript which has been published in the journal 'Precambrian Research'. Chapter 5 presents the results of the Nd and Hf isotopic investigations of kimberlitic perovskites. A manuscript is currently under review in the journal 'Earth and Planetary Science Letters' and this chapter is a copy of the submitted manuscript. Chapter 6 presents the conclusions of the thesis in three sections. The first section discusses the contamination of the southern Indian kimberlites and lamproites. The other two sections discuss the classification, age, petrogenesis, and melt generation of the southern Indian kimberlites and then the southern Indian lamproites. Chapter 7 provides a reference list for all the literature sources used in this thesis.

The appendices are comprised of four sections. The first section details the methodology of all analyses used in the thesis to obtain data on the southern Indian kimberlites and lamproites. The second section contains tables of data from the analyses of the southern Indian kimberlites and lamproites. The third section provides an abstract submitted to the 9th International Kimberlite Conference, which discusses a pilot investigation involving U-Pb dating of perovskites in the southern Indian samples. The geochronology work in the thesis

developed from this pilot study, which was presented as a poster at the conference in Frankfurt, Germany, 2008. The third section is a co-authored paper by N.V. Chalapathi Rao in 2009 on carbonate xenoliths in the Siddanpalle Kimberlite Cluster. This paper was the result of the same fieldwork in this study and various contributions were made by all co-authors.

1.4. Kimberlite and Lamproite formation

1.4.1. Potential kimberlite sources

The kimberlites from worldwide collections have been categorized under two main groups (Group I and Group II) based on the South African kimberlites (Smith et al., 1983). The southern India kimberlites are classified as Group I kimberlites (for more details, see section 1.4.1). The origin of Group I kimberlites remains controversial. There are differing opinions on the depth and nature of the source region and the cause(s) of melting.

Currently there are four likely source regions proposed for Group I kimberlites.

- Sub-continental lithospheric mantle (SCLM) (e.g. Tainton and McKenzie, 1994; Le Roex et al., 2003; Chalapathi Rao et al., 2004; Becker and Le Roex, 2006).

- Convecting (asthenospheric) mantle (e.g. Smith et al., 1985; Price et al., 2000; Griffin et al., 2000; Mitchell, 2008).

- Deeper mantle derivatives of ancient subducted oceanic crust (transition zone or deeper) (e.g. Ringwood et al., 1992; Nowell et al., 2004; Sumino et al., 2006; Gaffney et al., 2007; Paton et al., 2007).

- The core-mantle boundary, associated with mantle plumes (e.g. Haggerty, 1994, 1999).

It has been proposed that for partial melting of a primitive peridotite to produce a rock with the geochemistry of a Group I kimberlite, the degree of partial melting has to be extremely low (<0.1%; Arndt, 2003). However, it is also widely accepted that a highly enriched mantle source must be involved in the genesis of kimberlites, to explain their extreme trace element enrichment levels (e.g. Foley et al., 1992). In addition, many authors believe that the mantle source of kimberlites has undergone a depletion (melt extraction) event prior to enrichment, to produce the HREE depletion shown by kimberlites (e.g. Tainton and McKenzie, 1994; Chalapathi Rao et al., 2004).

The enrichment of the kimberlite source has been attributed to melts associated with different processes:

- Subduction derived melts (e.g. Gaffney et al., 2007).

- Volatile and K-rich low viscosity melts derived from convecting mantle that freeze in the sub-continental lithospheric mantle as veins and dykes (e.g. McKenzie, 1989; Foley et al., 1992).

The initial depletion and subsequent enrichment of the kimberlite source is interpreted to be analogous to that experienced by many continental lithospheric peridotite xenoliths entrained in kimberlites (e.g. Carlson and Irving, 1998; Beard et al., 2007).

Currently, there is a general consensus that kimberlitic melts represent very low degrees (<1 %) of partial melting of carbonated lherzolitic mantle sources in the deep part of the upper

mantle located between the base of the cratonic lithosphere and the top of the lower mantle (Ringwood et al., 1992; Dalton and Presnall, 1998; Gregoire et al., 2006).

1.4.2. Potential lamproite sources

It is currently debated whether lamproites are derived from lithospheric (e.g. Foley et al., 1992; Luttinen et al., 2002; Davies et al., 2006) or sub-lithospheric (i.e. asthenospheric) melts (e.g. Murphy et al., 2002). In a similar way to the kimberlites, lamproite geochemistry suggests a mantle source region that has undergone both depletion and enrichment processes (e.g. Tainton and McKenzie, 1994; Chalapathi Rao et al., 2004; Mirnejad and Bell, 2006; Mitchell, 2006). There are three current models proposed for lamproite generation:

- Melting of enriched lithospheric veins derived from asthenospheric mantle (Foley et al., 1987).
- Melting of a subduction-related metasomatised lithosphere (Nelson, 1992).
- Melts derived from sediments subducted to the lower mantle where the sedimentary component remained isolated (Murphy et al., 2002)

The origin of the metasomatism that enriched the lamproite mantle source is currently debated, as lamproites have a very 'ancient' isotopic signature that cannot always be related to known tectonic events. This signature is therefore thought to reflect either an ancient event with a metasomatic component derived from the convecting mantle, or to result from a more recent introduction of an already aged metasomatic component (Prelevic et al., 2008).

The extreme enrichment of lamproites in incompatible elements can be explained either by small degrees of partial melting of a normal or depleted mantle source, or by large degrees of melting of a metasomatised source (Paul et al., 2007). A normal four-phase peridotitic mantle

cannot represent the lamproite source, as a K-rich hydrous mineral (such as phlogopite) is required in the source to generate a lamproitic geochemistry (Prelevic et al., 2008). Therefore, a small degree of melting of peridotite, enriched in K, and other incompatible elements, such as phlogopite-bearing harzburgite, is the preferred model of lamproite generation (Mitchell and Bergman, 1991).

1.4.3. Emplacement of kimberlite and lamproite

A number of models have been proposed for kimberlite and lamproite emplacement:

- The explosive release of highly compressed magmatic gases at shallow depths to produce a volcanic vent (diatreme) (Wagner, 1914).

- The migration upwards of a small-volume subsurface melt, with explosive boring (Kastrovitsky, 1976).

- The breakout to the surface of gas-charged kimberlite magma, resulting in adiabatic expansion that causes the magmatic gases to expand and enlarge the explosion vent, which is then filled with fluidized fragmented kimberlite (McGetchin et al., 1973; Wyllie, 1980; Skinner and Marsh, 2004).

- Hydrovolcanic activity, with the interaction of magma and near-surface water, has been proposed to cause hydrovolcanic explosions that fragment and chill magma while simultaneously brecciating country rock (Wolfe, 1980; Lorenz et al., 1999).

- High-speed, forceful intrusion of magma to the surface, propelled by pressurized volatiles such as H_2O and CO_2 (Sparks et al., 2006; Wilson and Head, 2007).

High-speed, forceful intrusion of magma to the surface propelled by pressurized volatiles such as H_2O and $CO_2$is currently the most favoured model. Wilson and Head (2007) propose that a wedge of liquid CO_2 forms above a source of CO_2-rich magma at a depth of around 250 km. The wedge moves upwards, fracturing the surrounding rock, allowing pieces of rock to sink into the magma below, either being assimilated or entrained as xenoliths. The CO_2 wedge is thought to travel upwards at speeds of about 108-180 km/hr with the underlying magma resupplying CO_2 to the tip of the chamber. Wilson and Head (2007) suggested that the balance between the overlying CO_2 and the excess dissolved in the magma would maintain an equilibrium pressure at the tip of the CO_2 wedge of about 70 MPa during ascent, driving the kimberlite upwards (Fig. 1.1).

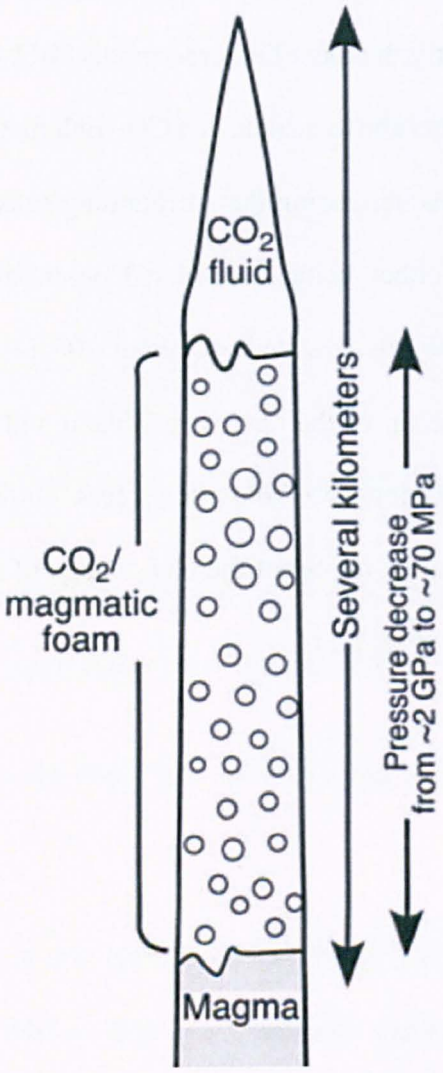

Figure 1.1. A model diagram to show the mechanism for kimberlite emplacement (Wilson and Head, 2007).

Wilson and Head (2007) add that when the tip of the CO_2 chamber breaks the surface the fluid rapidly expands to become a gas. This leads to an explosion of CO_2, magma foam, and rock fragments moving upwards at speeds of up to 5000 km/hr. This explosive event leaves a large cavity and it is thought that a cavity 3 km deep might empty in only about 10 seconds. The rapid expansion flash-freezes the magma near the surface and shock waves implode

cavity walls, filling the chamber with rubble. Pressure builds again in the mostly sealed chamber and waves of expansion and compression move through the chamber, cooling and shattering the magma and brecciating the surrounding rock. The rapid chilling quickly seals off the magma supply from below completely. The whole progression is likely to take only about one hour.

The model presented by Wilson and Head (2007) has features in common with the model of kimberlite ascent and eruption proposed by Sparks et al. (2006). However, kimberlite ascent and eruption is still a controversial topic and aspects of the Wilson and Head (2007) model are still being debated in current literature (e.g. Sparks et al., 2007).

1.4.4. Mode of Occurrence

A typical kimberlite pipe includes both intrusive and extrusive components (Fig. 1.2). The deeper part consists of hypabyssal features such as sills, dykes and a root zone. Pyroclastic rocks are common at the surface as the eruption of a kimberlite is an explosive event, and often a crater is formed that becomes filled with epiclastic materials. A typical kimberlite has a pipe-shaped igneous body known as a diatreme linking the deeper hypabyssal rocks with the pyroclastics at the surface.

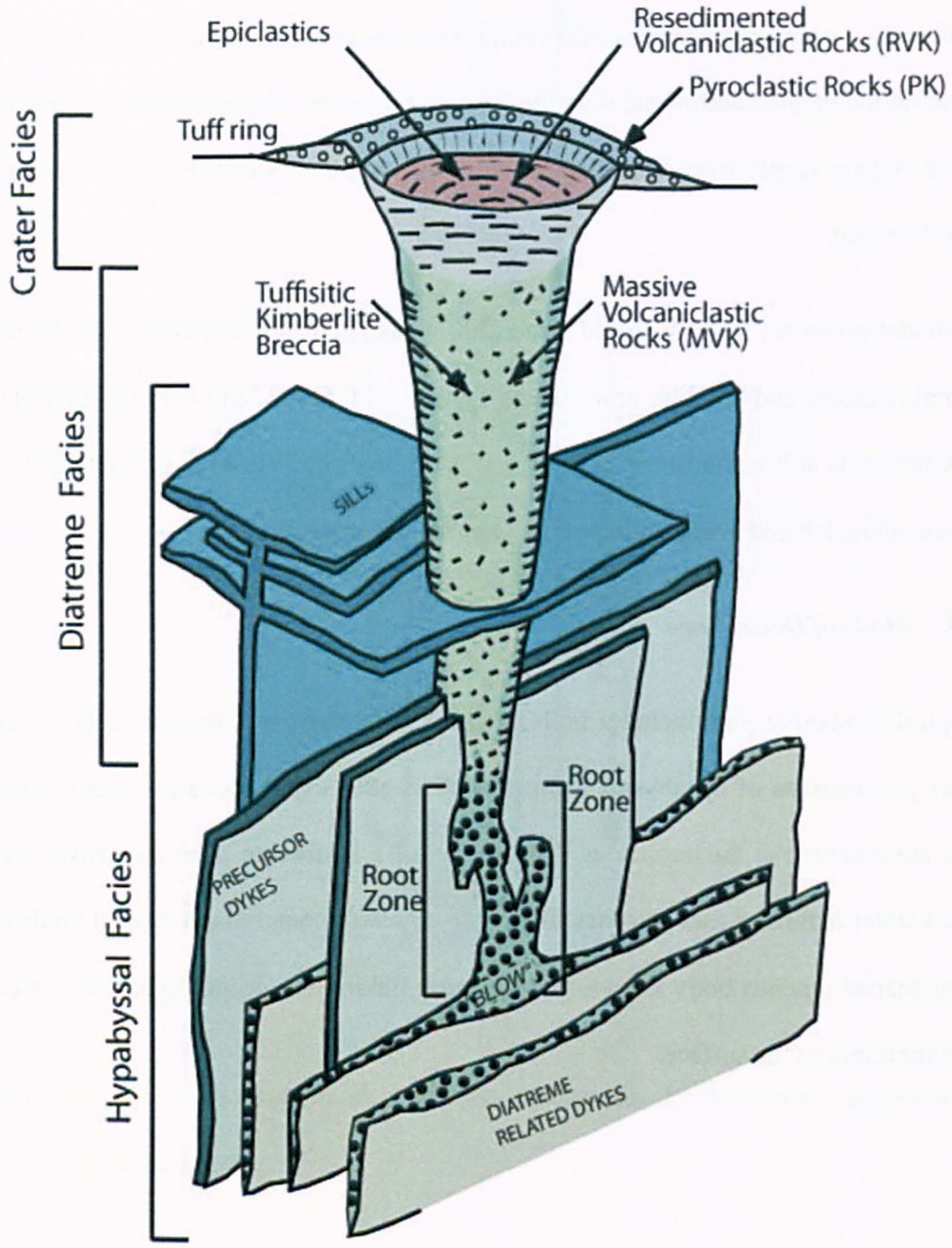

Figure 1.2. A model diagram of a typical kimberlite (after Kjarsgaard, 2003).

Kimberlites usually occur as either pipes or dykes. Kimberlite pipes do not generally exceed 1 km in diameter, whereas dykes are typically 0.5-3 m wide and can sometimes be several kilometres in length (Basson and Viola, 2003). The distribution of kimberlite pipes and dykes is characterised by clusters, fields, districts and provinces. Clusters are generally 5-10 km across, fields 30-50 km, districts a few hundred kilometres and provinces are measured in thousands of kilometres (Janse, 1984; Bassoon and Viola, 2003). Typically all the kimberlites in a cluster and a field have similar ages of intrusion within analytical uncertainties (Gregoire et al., 2006). Districts, and particularly provinces, often include a range of kimberlitic occurrences of different intrusion ages (Garanin et al., 1993).

Kimberlites have been found on every continent, with estimates of known primary rock occurrences currently at around 5000. These occurrences are thought to include approximately 500 diamondiferous deposits of which ~50 have been or are being mined (Janse and Sheahan, 1995).

Kimberlites and lamproites are predominantly found on Archons i.e. cratonic regions underlain by Achaean basement, or Protons i.e. Proterozoic mobile belts adjacent to Archons. Economically diamondiferous kimberlites have only been found on Archons, whereas economically diamondiferous lamproites have been found on some Protons as well as Archons. Archons are distributed worldwide in twelve regions across seven continents (Janse and Sheahan, 1995).

The Asian continent contains at least five cratons, the East Siberian Craton in eastern Russia, the North China, Tarim and Yangtze Cratons in China and the Indian Craton in India (Janse and Sheahan, 1995). The Indian Craton includes four Archons, separated by Mesozoic rifts and surrounded by Proterozoic mobile belts. India's only active diamond mine is located at

Majhgawan near Panna in northern Madhya Pradesh in central India. It is developed on a lamproite pipe located on the southern rim of the Aravalli Craton (Kumar et al., 2007).

The kimberlites and lamproites in this study are located in the Dharwar Craton in the state of Andhra Pradesh with some clusters considered non-diamondiferous and others diamondiferous but uneconomic (Fig. 1.3).

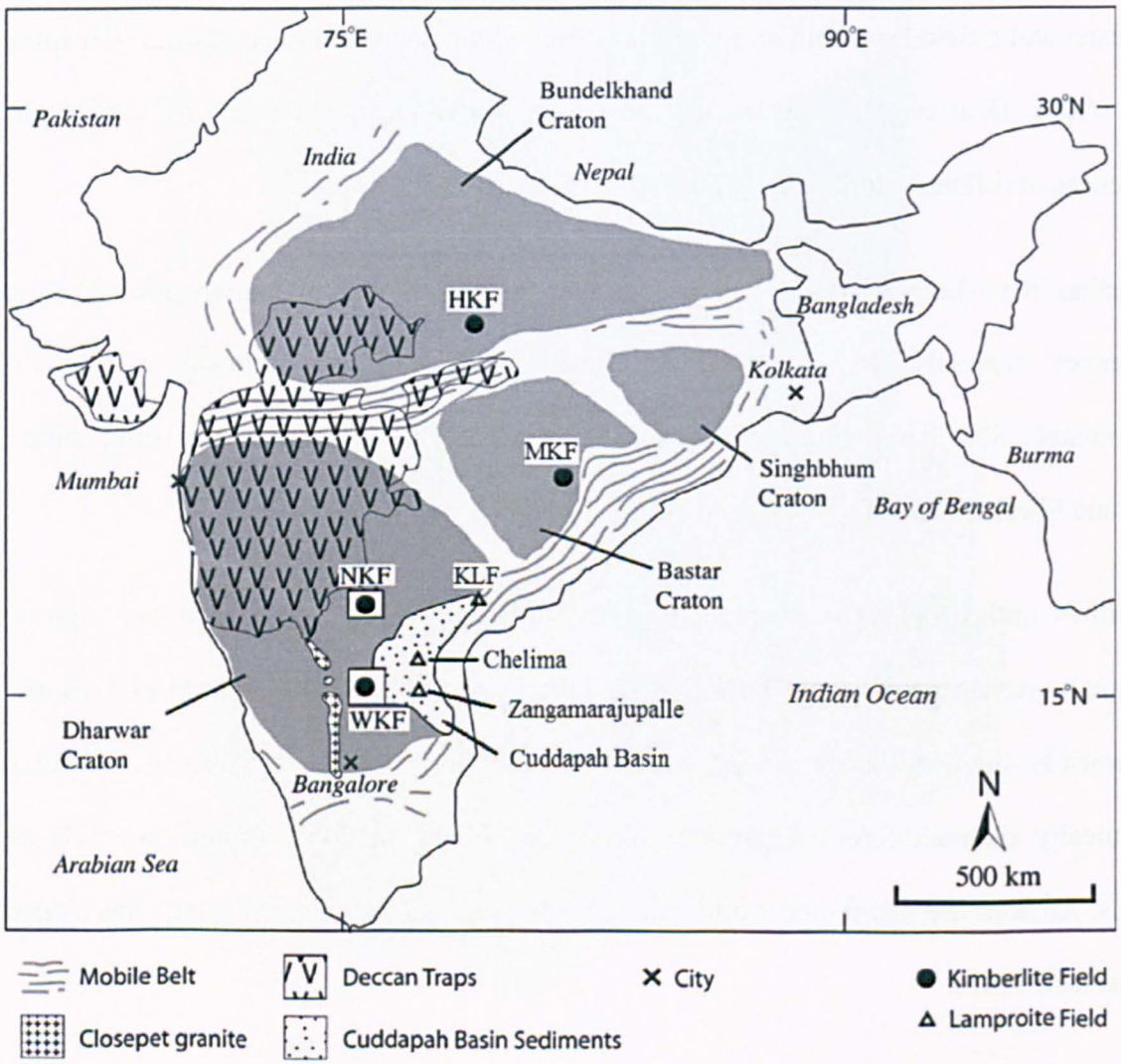

Figure 1.3. Location of kimberlites and lamproites relative to the major tectonic domains of southern India. HKF: Hinota Kimberlite Field; MKF: Mainpur Kimberlite Field; NKF: Narayanpet Kimberlite Field; WKF: Wajrakarur Kimberlite Field. Modified from Paton et al. (2009).

The lamproite pipes in the Krishna lamproite field have been suggested to be the primary host for the widespread alluvial deposits in the Krishna River near Kurnool and Kollur (Janse and Sheahan, 1995). These are postulated to have been the source of some of the most famous diamonds, most notably the Koh-I-Noor diamond currently part of the British crown jewels. However, a more recent study has proposed that these pipes should now be considered non-diamondiferous (Chalapathi Rao et al., 2011).

1.5. Classification

1.5.1. Kimberlites

Kimberlites have been subdivided into Group I and Group II (Smith et al., 1985; Skinner, 1989; Mitchell, 1986, 1995). These two groups are both volatile rich, but Group I is CO_2 dominant and Group II is H_2O dominant. Group I kimberlites have slightly lower K abundances than Group II kimberlites, with much less phlogopite and a high content of groundmass oxide minerals (e.g. perovskite, ilmenite and spinel). All the kimberlites in southern India have been classified as Group I (Chalapathi Rao et al., 2004).

In general, Group I kimberlites are porphyritic with megacrysts/macrocrysts of olivine (forsteritic), ilmenite, garnet (pyrope), pyroxene (diopside and enstatite), mica (phlogopite) and chromite in a groundmass of olivine, garnet, pyroxene, ilmenite and spinel. Woolley et al. (1996) and Mitchell and Bergman (1991) report that as well as Group I kimberlites being volatile-rich (predominantly CO_2), they are ultramafic (MgO > 12 %), and potassic (high K; high K_2O/Na_2O; high K_2O/Al_2O_3). They typically have high Ni (> 400 ppm), Cr (> 1000 ppm) and Co (> 150 ppm) concentrations. They are REE-enriched with extreme enrichment in LREEs.

1.5.2. Lamproites

Lamproites are usually fine-grained or microgranular and resemble other types of alkali igneous rocks, with many finds of K-alkalic rocks wrongly classified as lamproites. Lamproites are volcanic, subvolcanic and intrusive rocks consisting of 6 rock-forming minerals in different proportions: olivine, clinopyroxene, mica, leucite, K-alkalic amphibole, and K-feldspar (sanidine) (Mitchell and Bergman, 1991). At least three of these minerals must be present for a rock to be classified as a lamproite, and it must not contain primary plagioclase, melilite, monticellite, kalsilite, nepheline, sodalite, nosean, hauyne, melanite, scholomite or kimzeyite. The presence of glass can also be an important diagnostic mineral of lamproites (Mitchell, 1994). The chemical composition of lamproites varies widely depending on the modal proportion of different minerals (Vladykin, 2009).

Woolley et al. (1996) and Mitchell and Bergman (1991) suggest that a typical lamproite is ultramafic (MgO >12 %), ultrapotassic (high K; K_2O/Na_2O >3; high K_2O/Al_2O_3), and is also peralkaline (molar $Na_2O+K_2O)/Al_2O_3$ > 1). Lamproites typically have high Ba (> 2000 ppm), Zr (> 500 ppm), Sr (> 1000 ppm), La (> 200 ppm) concentrations. Like Group I kimberlites, they are REE-enriched with extreme enrichment of the LREEs. Relative to kimberlites they have higher concentrations of K, Si, Ti, Al, Rb, Sr, Zr, Ba and lower concentrations of CO_2, Ca, Mg, Fe, Ni, Co, Cr.

1.6. Xenoliths

Kimberlites and lamproites offer a direct window into the nature and evolution of the sub-cratonic lithospheric mantle at depths in excess of 150 km, by transporting xenoliths and xenocrysts to the surface (e.g. Gurney et al., 1991; Karmalkar et al., 2007). A group of deformed high temperature garnet peridotite mantle xenoliths have been found within

kimberlites from around the world (Nixon, 1987; Pearson et al., 2003) and are thought to be the deepest xenoliths observed and display evidence of mantle-melt reactions (e.g. Gregoire et al., 2003).

Xenoliths can be entrained by magma near the surface or deep in the mantle. Mantle xenoliths found in kimberlites and lamproites can provide snapshots of the lithospheric mantle at the time of extrusion. If the xenoliths are carried to the surface rapidly enough to avoid significant high-temperature alteration, chemical analysis can reveal the pressure (dependent on depth) and temperature at which it crystallized (Gregoire et al., 2003). Pristine xenoliths can also reveal rock textures and compositions deep in the mantle.

The sub-continental mantle is predominantly peridotitic; therefore the majority of xenolith populations found in kimberlites are dominated by peridotite (Guerney et al., 1991). Kimberlites can entrain both spinel- and garnet-facies peridotites (Karmalkar et al., 2009).

Eclogitic xenoliths also occur in many kimberlites although often to a lesser extent than peridotite xenoliths, as estimates suggest the abundance of eclogites in the upper 200 km of the sub-continental mantle to be < 1 vol % (Mitchell et al., 2004). However, in some cases eclogite xenoliths make up the majority of mantle nodules at some localities (e.g. Roberts Victor, Bellsbank, Newlands in South Africa; Zagadochnaya in Siberia) (Mitchell et al., 2004). This abundance of eclogite may reflect either local enrichment of eclogite within the predominantly peridotitic sub-continental mantle, or the effect of differences in xenolith preservation during sampling by the kimberlite (Gregoire et al., 2003).

The Wajrakarur kimberlite field (WKF) kimberlites in the Eastern Dharwar Craton (EDC), although diamondiferous, contain relatively few mantle xenoliths. Xenolith-bearing pipes include Lattavaram (pipe 3) and Kalyandurg (pipe 2). The xenoliths are represented by garnet

lherzolites, harzburgites, wehrlites and kyanite-eclogite varieties (Karmalkar et al., 2009). The Narayanpet kimberlite field (NKF) in the EDC is not diamondiferous and mantle xenoliths are rare except for the occurrence of spinel-lherzolite xenoliths from the Narayanpet kimberlite cluster (NK2 and NK3) (Karmalkar et al., 2009).

Mantle-derived xenocrysts are found in the WKF (e.g. Wajrakarur, Kalyandurg, and Chigicherla) and in the NKF (e.g. Narayanpet). The xenocrysts include garnet, spinel, ilmenite, and rare clinopyroxene, in varying proportions (Karmalkar et al., 2009).

The lamproites from the EDC in the Krishna lamproite field (KLF) and Cuddapah lamproite field (CLF) have no reported mantle xenoliths, except for a doubtful altered lherzolite xenolith (Reddy et al., 2003). Mantle xenoliths are not generally found in lamproites as primary lamproite magma is strongly alkaline and highly reactive. Therefore, deep-seated xenoliths and megacrysts simply dissolve in it (Vladykin, 2009).

1.7. Ages of world-wide kimberlites

Global kimberlite and lamproite occurrences have been reported ranging in age from the Early Proterozoic to the Quaternary (Janse and Sheahan, 1995). The oldest kimberlites are in the Pilbara craton of western Australia (~1800 Ma; Wyatt et al., 2003) while the youngest emplacement events recorded from Tanzania (Dawson, 1994) and the Kundelungu Plateau, D.R. Congo (Batumike et al., 2007) are of Quaternary age. The majority of kimberlites on the Earth (> 80 %) are Mesozoic/Cenozoic (200-50 Ma) (Kumar et al., 2007). There have been several periods in the Earth's history when global synchronous kimberlite emplacement events have occurred. These include ~ 1100 Ma (Africa, Australia, North America, India and Greenland) (Kumar et al., 2007), 450-500 Ma (Archangel in the Baltic region, China, Canada, southern Africa and Zimbabwe), 370-410 Ma (Siberia and USA), ~ 200 Ma

(Botswana, Canada, Swaziland and Tanzania), 80-120 Ma (central and western Africa, Brazil, Canada, Siberia and USA), and ~ 50 Ma (Canada and Tanzania) (Heaman et al., 2003).

These periods of kimberlite emplacement are frequently associated with mantle plumes (e.g. Gibson et al., 1995) or more often periods of continental rifting and formation of ocean basins (Kumar et al., 2007). For example, Cretaceous kimberlite and related magmatism in southern Africa (125-55 Ma; Heaman et al., 2003) closely follows the opening of the South Atlantic Ocean initiated about 130 Ma ago. The association of kimberlite and related magmatism to continental extension and rifting can also be seen with older periods of magmatism. For example the majority of kimberlites and affiliated ultramafic lamprophyres in Labrador, Quebec, West Greenland and Scandinavia were emplaced around 630-560 Ma (Doig, 1970; Scott-Smith, 1989; Heaman et al., 2004; Tappe et al., 2004) and can be linked to the Eocambrian opening of the Iapetus Ocean (Kumar et al., 2007).

Precambrian kimberlites and lamproites are relatively rare in the geological record; however, they tend to form in narrow windows of time (Fig. 1.4). Kimberlite and lamproite occurrences older than 1100-1200 Ma are rare but have been recorded in Venezuela, W. Greenland and South Africa (Appendices: Table A8). The majority of known Precambrian kimberlites and lamproites are Mesoproterozoic and have an emplacement age around 1100 Ma (Appendices: Table A9). Kimberlite activity appears to decrease significantly from 1000-630 Ma, with virtually no reported kimberlites except for several kimberlite occurrences around 800 Ma (Appendices: Table A10). Then from 630 Ma until the end of the Precambrian (540 Ma), kimberlite activity appears to become more frequent (Appendices: Table A11).

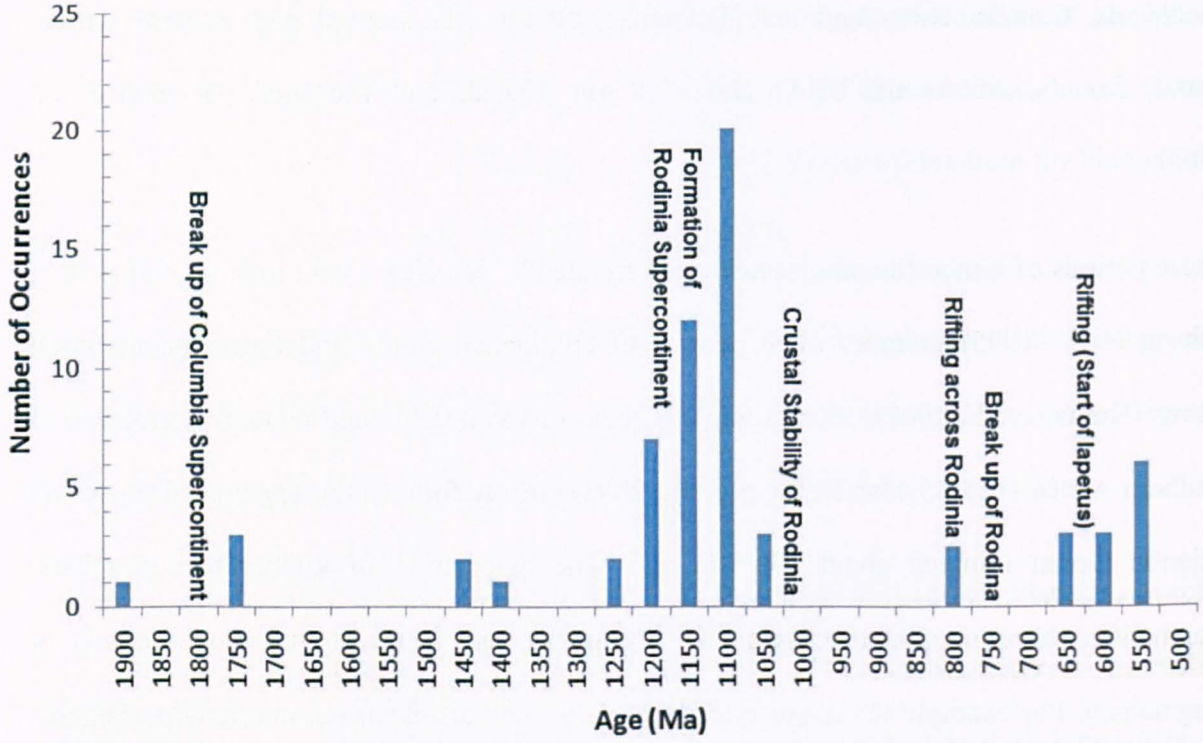

Figure 1.4. Histogram of kimberlite and lamproite occurrences through the Precambrian into the early Cambrian with global tectonic events proposed to be linked with kimberlite emplacement.

There is overwhelming evidence that the Gondwana supercontinent existed at the end of the Palaeozoic. However, evidence to support the proposed preceding supercontinent of Rodinia is more sparse and equivocal (Chalapathi Rao et al., 2005). Rodinia existed between 1100 and 750 Ma ago, in the Neoproterozoic era. It was assembled at ~ 1.0 Ga by the accretion and collision of fragments produced by the breakup of an older supercontinent, Columbia, which was assembled by global-scale 2.0-1.8 Ga collisional events (Zhao et al., 2004). Rodinia is thought to have included India, Australia and many of the present day continents of the southern hemisphere, which subsequently reorganized to form Gondwana.

The important global mantle event for kimberlite emplacement (~ 1100) is thought to have taken place during the initial assembly of Rodinia (Kumar et al., 2007). The break-up of Columbia and formation of Rodinia was taking place at this time and may have provided the

conditions for kimberlite formation across the Rodinia continent, fragments of which can now be found dispersed around the world. Recent reconstructions of Rodinia at this time (Fig. 1.5) place India near Australia and eastern Antarctica; hence correlation of mantle source data between these regions is desirable to help constrain models of Rodinia assembly (Li et al., 2008).

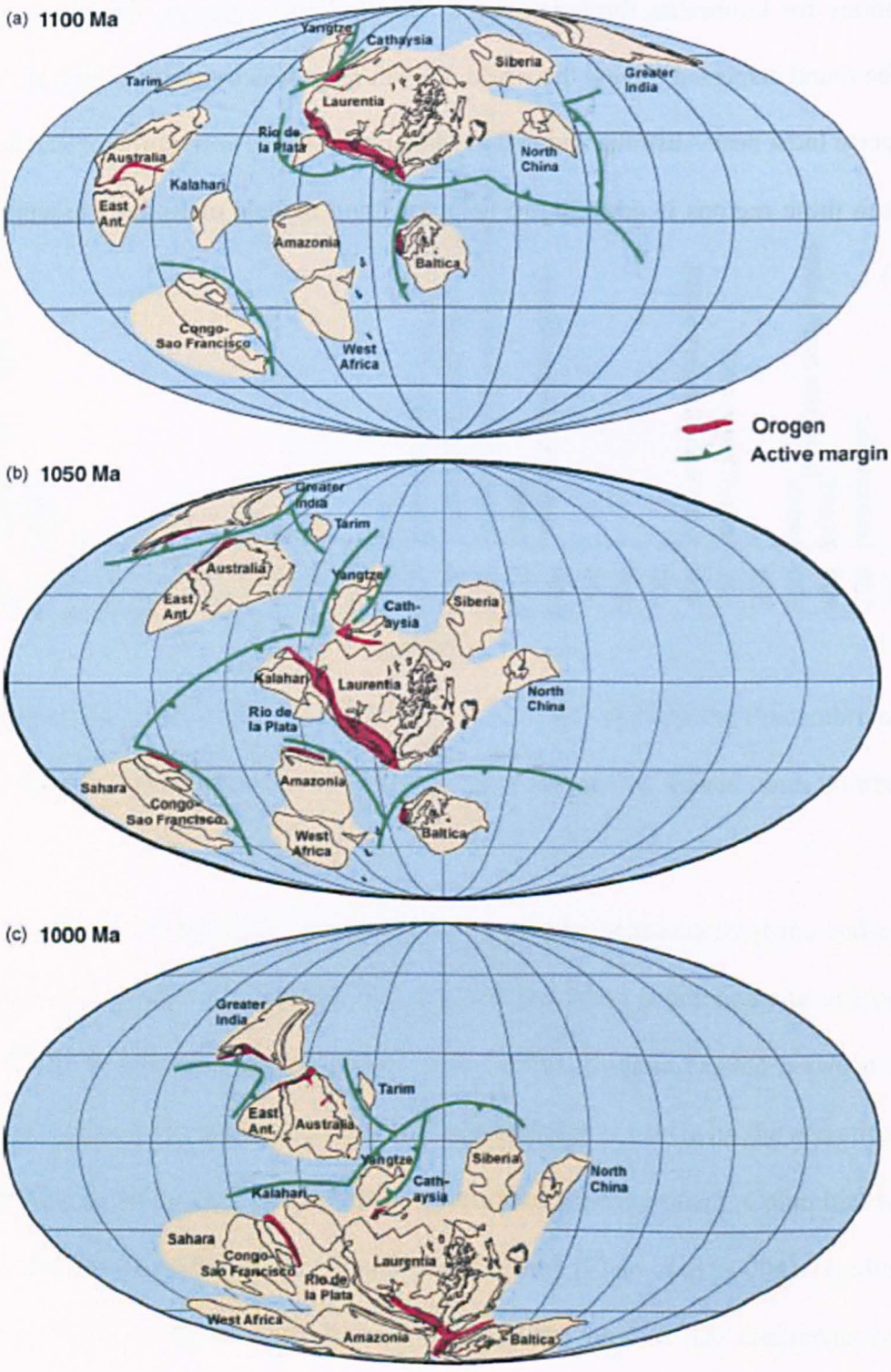

Figure 1.5. Three reconstructions for Rodinia from 1100-1000 Ma (Li, et al., 2008).

The oldest kimberlite occurrences in the Precambrian (~ 1740; Appendices: Table A8) could be linked to the break-up of the Columbia supercontinent, which is thought to have started to break up after 1800 Ma. The abundance of kimberlites reported at ~1100 Ma may have then been linked to the formation of Rodinia, with the lack of kimberlites after this time (1000-630 Ma) being the result of the relative crustal stability of the Rodinia supercontinent. Heaman et al. (2003) indicate a lack of worldwide known kimberlite occurrences between 250 and 360 Ma that may be linked to relative crustal and mantle stability during the lifetime of Gondwana. However, the Rodinian supercontinent was not thought to completely lack any crustal activity during this period of low kimberlite generation (1000-630 Ma) and the reported occurrence of several kimberlites at ~ 800 Ma, may be linked to a rift that developed on the Rodinia supercontinent (850-800 Ma) between the Australian, Antarctic, Indian, Congo and Kalahari cratons on one side and Laurentia, Baltica, Amazonia, W. Africa and Rio de La Plata on the other. This rift eventually became the Adamastor Ocean during the Ediacaran (Condie, 2003). There is also abundant evidence in northern India and China for 850-800 Ma (mainly failed) rifting and magmatism (Zhang et al., 2010).

It is thought that the Rodinia supercontinent started to break up ~ 750 Ma and the Malani volcanics in northern India attest to 750 Ma rifting (Torsvik et al., 2001). This large scale rifting is linked to the increase in kimberlite occurrences from 630 Ma until the end of the Precambrian and into the Cambrian (e.g., large scale rifting event ~ 610 Ma, which resulted in the formation of the Iapetus ocean may be linked to the kimberlite formation ~ 630-540 Ma).

1.8. Kimberlite and Lamproite mineralogy

The crystallisation of kimberlite magma after emplacement results in abundant olivine phenocrysts followed by phlogopite, perovskite, calcite, monticellite, serpentine and some other minor minerals that together compose the groundmass of hypabyssal kimberlite rocks (Kamenetsky et al., 2009). Lamproite main mineral phases include olivine (forsteritic), clinopyroxene (diopside), mica (phlogopite), amphibole (richterite), leucite, and K-feldspar (sanidine).

1.8.1. Olivine

Kimberlite is a rock dominated by olivine ($(Mg,Fe)_2SiO_4$). Lamproites often contain abundant olivine, but are dominated by mica. Olivine in most kimberlites and lamproites is highly altered and its primary textures are poorly preserved (Arndt et al., 2010). The olivine found in kimberlite and lamproite is generally forsteritic (Mg_2SiO_4). There are two types of olivine found in kimberlites and lamproites; xenocrystic olivine and 'primary' or phenocrystic olivine (Mitchell, 1970, 1986, 1995; Scott-Smith, 1992). The xenocrystic olivine occurs mainly as 'macrocrysts' (0.5-5 mm in the longest dimension). This term is used to describe large, subangular to rounded, single crystals or crystal aggregates whose habit, undulose extinction and multi-grain character suggest an origin foreign to that of the source magma (Kamenetsky et al., 2008). Phenocrystic olivine occurs as smaller grains (< 0.5 mm) that are subhedral to euhedral and have an absence of strain features. The origin of these is ambiguous but a recent study suggests that they evolved during growth, recrystallisation, transport, dissolution and regrowth in different mantle-melt and crustal melt environments (Kamenetsky et al., 2008).

1.8.2. Phlogopite

Mica is abundant in kimberlites and is the dominant phase in lamproites. The mica found in kimberlites and lamproites generally occurs as macrocrysts (0.5-5 mm) and phenocrysts (< 0.5 mm). Some macrocrysts represent high-pressure phenocrysts precipitated from the source magma; other xenocrysts formed from the fragmentation of mantle rocks (Mitchell, 1995). The most common mica found in kimberlite and lamproite is phlogopite [$KMg_3AlSi_3O_{10}(OH,F)_2$]. Phlogopite generally shows strong pleochroism under PPL from brown/dark orange to pale yellow/colourless. The mica compositions in kimberlites have been used to discriminate between kimberlites and texturally similar rocks (e.g. Mitchell and Bergman, 1991) and constrain the conditions of magma emplacement and evolution (e.g. Brod et al., 2001). The mica found in kimberlites has also been used extensively for dating the age of emplacement (e.g. Ar-Ar on phlogopite separates: Chalapathi Rao et al., 1999; this study).

1.8.3. Spinel

The majority of spinel found in kimberlites and lamproites is high-chromium chromite ($FeCr_2O_4$) and Mg-rich ulvospinel ($(Mg,Fe)_2TiO_4$)-magnetite (Fe_3O_4) (Roeder and Schulze, 2008). It is considered a primary phase that crystallises as small octahedra from the source magma. There is evidence that spinel forms throughout the kimberlite crystallisation sequence (Mitchell, 1986). Spinel xenocrysts can also be found in kimberlites derived from the break-up of upper mantle peridotite (Roeder and Schulze, 2008). The spinel can show mineralogical and compositional diversity within a single kimberlite as a result of rapidly changing pressure and temperature conditions (Roeder and Schulze, 2008).

1.8.4. Perovskite

Perovskite ($CaTiO_3$) is a common mineral in kimberlites but a rare constituent in lamproites. More details on perovskite are given in Chapter 4. It forms in the final stages of magmatic crystallisation either as discrete grains in the groundmass or as necklaces surrounding earlier-formed olivine.

1.8.5. Apatite

Apatite [$Ca_{10}(PO_4)_6(OH, F, Cl, Br)_2$] is one of the main REE-bearing minerals, along with perovskite, in kimberlites and lamproites. It generally occurs as euhedral laths or acicular crystals. Acicular crystals of apatite are thought to be indicative of relatively rapid cooling (Mitchell, 2008). Apatite is considered a late crystallising magmatic phase in kimberlites and lamproites.

1.8.6. Ilmenite

Ilmenite is a common constituent of kimberlites but is a minor phase in lamproites. It is thought to be xenocrystic in origin, derived from the break-up of mantle rocks. In kimberlites it generally occurs as Mg-rich ilmenite (picroilmenite). Ilmenite is often found as a minor phase in lamproites; however, high pressure minerals such as picroilmenite are not characteristic of lamproites, as they are thought to dissolve (along with other xenolith materials) in the strongly alkaline magma and highly reactive lamproite magma (Vladykin, 2009). Ilmenite is often used as an important diamond indicator mineral in kimberlites and lamproites.

1.8.7. Amphibole

Amphibole is a minor/absent phase in kimberlites, but a common phase in lamproites. The majority of amphiboles in lamproites are richterite, but other varieties can also be found. Richterite is a sodic, calcic, highly pleochroic (red/pink to pale yellow) amphibole. Richterite is rich in TiO_2 and K_2O, but poor in Al_2O_3 and CaO has been described as 'unique' to lamproites (Bergman, 1987).

1.8.8. Titanite

Titanite ($CaTiSiO_5$) is inferred to be a late magmatic to hydrothermal constituent of kimberlites and lamproites (Edwards et al., 1992). It is often a minor phase in kimberlites but abundant in lamproite. An abundance of titanite in a rock demonstrates the alkaline nature of the parental melt (Tiepolo et al., 2002).

1.8.9. Rutile

Rutile (TiO_2) is a common accessory phase in high-pressure and high-temperature rocks such as kimberlites and lamproites. It generally occurs as needle shaped laths in the groundmass. It is a common phase in kimberlites but is considered an uncommon mineral in lamproites (Mitchell and Bergman, 1991). However, rutile is reported to be fairly abundant in some Indian lamproites (Chalapathi Rao et al., 2004).

1.8.10. Pyroxene

Pyroxene is rarely reported as phenocryst or a groundmass phase in hypabyssal kimberlites (Mitchell, 1986). Pyroxene has been shown to be absent in high pressure liquidus experiments with inferred parental kimberlite melt compositions (Edgar and Charbonneau, 1993). Where pyroxene is found, it is thought to originate from disaggregated mantle and

crustal xenoliths (Kamentsky et al., 2009). Clinopyroxene has been reported in kimberlites from the Dharwar Craton (Scott-Smith, 1989) and Greenland (Scott, 1981). However, pyroxene xenocrysts are rare in most kimberlites, particularly orthopyroxene (Mitchell, 1986), which is unusual considering the high abundance of pyroxene in typical mantle (20-60 %) and crustal xenoliths, which can be entrained into the kimberlite magma.

Clinopyroxene is commonly present as euhedral to subhedral laths in lamproites. It is generally diopside ($MgCaSi_2O_6$) with little compositional variation, which is considered typical of lamproite clinopyroxene, and attributed to the rapid quenching of the magma after the onset of pyroxene crystallisation (Mitchell, 1985).

1.8.11. Monticellite

Monticellite ($CaMgSiO_4$-$CaFeSiO_4$) is an important mineral used in the classification of kimberlites, as it is often found as a groundmass phase in kimberlites but must not be present for a rock to be classified as a lamproite (Woolley et al., 1996). It is a product of silica-deficient magma rich in CO_2. It is thought to crystallise at low temperatures and pressures after spinel and perovskite, but before late-stage calcite and serpentine (Eggler, 1989). It is part of the olivine group with compositions generally tending towards the solid solution Mg end member.

1.8.12. Feldspar

Alkali feldspar (sanidine) is a common mineral found in lamproites. Compositionally sanidines enriched in K and Fe and depleted in Na are considered typical of lamproites (Mitchell and Bergman, 1991).

1.8.13. Serpentine

Serpentine [$(Mg, Fe)_3Si_2O_5(OH)_4$] is a common mineral in most kimberlites and lamproites. It is an alteration mineral, which often occurs as an irregular mass or replaces olivine, creating a pseudomorph.

1.8.14. Carbonate

Calcite is the most abundant carbonate in kimberlites. Calcite is an important primary and secondary phase in kimberlites, but generally only occurs as a secondary phase in lamproites (Mitchell and Bergman, 1991). However, primary groundmass carbonate has been reported in lamproites from Antarctica (Luttinen et al., 2002). It predominantly occurs as an irregular mass or replaces olivine.

1.9. Diamonds

Diamond forms deep in the mantle (> 150 km) at high temperature and pressure. The diamonds are brought close to the Earth surface via kimberlites and lamproites. The kimberlites and lamproites have been suggested to originate at depths as great as 250 km (Wilson and Head, 2007). The kimberlites can pass through the diamond stability zone, picking up diamonds and transporting them to the surface. The kimberlite magma moves rapidly to the surface and cools rapidly, which prevents the diamonds from being reabsorbed into the magma. Therefore, it is difficult to differentiate between non-diamondiferous and diamondiferous kimberlites (and lamproites), as diamonds are unrelated to their host having been inherited as a component in pre-existing mantle rocks. Mineral xenocrysts can be found in kimberlite and to a lesser extent lamproite which have identifiable geochemical signatures that link them with diamond genesis (Gurney and Zweistra, 1995). The most useful diamond

indicator minerals are Cr-diopside, picro-ilmenite and pyrope-garnet (Gurney and Zweistra, 1995).

The Wajrakarur kimberlite field (WKF) consists of 27 kimberlites with the majority of them diamondiferous (e.g. Chalapathi Rao and Srivastava, 2009). The Narayanpet kimberlite field (NKF) contains 60 kimberlites that are considered non-diamondiferous (e.g. Paul et al., 2006). A recent study by Chalapathi Rao et al. (2011) show that the low fO_2 of the NKF magma is indistinguishable from that of diamondiferous kimberlites world-wide, indicating that redox conditions were favourable for diamond preservation. However, the NKF is known to be non-diamondiferous and it is therefore thought that magmatic emplacement could have played a major role in their low diamond potential (i.e. generation at depths above diamond stability). The Raichur kimberlite field (RKF) comprises 15 kimberlites some of which are reportedly diamondiferous (e.g. Lynn, 2005). The location of Raichur kimberlites is significant since it is the only known kimberlite field located very close to the Krishna River, which is renowned for the occurrence of alluvial diamonds all along the alluvial belt (Chalapathi Rao et al., 2009). The Siddanpalle cluster kimberlites analysed in this study currently have no reported diamonds. However, a recent study by Chalapathi Rao et al. (2009) suggests that they may be diamondiferous. In general, the crater zones and uppermost portions of a kimberlite are relatively more diamondiferous compared to the root zones (e.g., Nixon 1995) with some exceptions (Gurney 1989). Chalapathi Rao et al. (2009) therefore propose that the deeply eroded nature of the Siddanpalli and other kimberlites in the RKF indicates that a substantial portion of their diamondiferous upper horizons have been removed and dispersed along the Krishna River basin and could be the elusive source of the alluvial diamonds of the Krishna valley. (The diamondiferous nature of the kimberlites in this study is shown in appendices: A.2.3).

The KLF has also been proposed as the source of the world famous (e.g. Koh-I-Noor diamond: currently part of the crown jewels) alluvial diamonds of the Krishna River (e.g. Reddy et al., 2003, Paul et al., 2007). However, no diamonds have been reported in the KLF lamproites (Rau et al., 2005). Chalapathi Rao et al. (2011b) infer the Krishna lamproites to be non-diamondiferous based on newly developed models from a global database that predict diamond potential of hypabyssal facies lamproite/kimberlite from whole-rock geochemistry. The Chelima lamproite from the CBL has been extensively mined since antiquity, though it is yet to be tested for diamonds by modern exploration techniques (The diamondiferous nature of the lamproites in this study is shown in appendices: A.2.3).

Chapter 2: Geology of the field area and sample locations.

2.1. Introduction

This chapter provides information on the fieldwork logistics, the geology of the field area and each sample location. There have been several detailed petrographic and field descriptions of the southern Indian kimberlites and lamproites (e.g. Chalapathi Rao et al., 2004, 2008, 2010; Reddy et al., 2003; Paul et al., 2006). Herein we only report a brief account of the main petrographic features of the southern Indian kimberlites and lamproites for the sake of completeness as well as for pointing out features that may be useful in interpreting the bulk-rock geochemical data and Ar-Ar age data.

2.2. Fieldwork logistics

The fieldwork for this project was undertaken in February 2008 with the aim to collect as many samples from kimberlite and lamproite localities as possible from the Eastern Dharwar Craton and Cuddapah Basin of Southern India. I was accompanied by Dr Mahesh Anand (PhD supervisor) and Dr N.V. Chalapathi Rao from Banaras Hindu University, India. Dr Chalapathi Rao led the field trip having extensively worked with the kimberlites and lamproites in this region and having a good knowledge of their location.

The fieldtrip began with a flight to Hyderabad (Fig.2.1, Point 1) in the state of Andhra Pradesh, India, where we were based at the National Geophysical Research Institute.

Figure 2.2: Map of Andhra Pradesh, India. The fieldwork route is shown in black, with sample localities numbered (http://www.indianrealtynews.com/indian-states/andhra-pradesh).

We travelled south passing through Mahbubnagar and Kurnool to the Wajrakarur Kimberlite Field (WKF) near Anantapur (Fig.2.1, Point 2) and sampled 18 different kimberlite pipes. We then travelled to the east to Cuddapah (Fig.2.1, Point 3), where we sampled one lamproite (Chelima) located within the Cuddapah Basin, before travelling to the north of the basin to the location of the Krishna Lamproite Field (KLF) (Fig.2.1, Point 4) sampling 10 lamproite pipes.

We then travelled NW back through Kurnool to Mahbubnagar, where went to the Raichur Kimberlite Field (RKF), just to the south of Mahbubnagar (Fig.2.1, Point 5), sampling 3 kimberlite pipes, then moving north to the Narayanpet Kimberlite Field (NKF) (Fig.2.1, Point 6) sampling 6 kimberlite pipes. We then returned to Hyderabad.

The kimberlite and lamproite pipes varied from good exposures to no exposure (Section 2.5). On the well exposed kimberlites and lamproites we used hammers to obtain the freshest samples possible discarding weathered exposed surfaces and collecting ~3 kg of sample at each locality. The localities that had no exposure, loose samples were collected from the site, selecting the freshest looking samples. In total 70 kg of sample was collected from 40 different known and newly discovered kimberlite and lamproite occurrences.

2.3. Regional Geology

The Indian Shield has been a single lithospheric unit since mid-Proterozoic times (Radhakrishna and Piper, 1999). An extensive supracrustal sequence of Proterozoic rocks lie above the cratons that form the core of the Indian subcontinent. The Indian Shield was initially suggested to have formed around Achaean nuclei (Mahadevan, 1995), which are thought to have developed into seven cratons (Naqvi and Rogers, 1987).

This study focuses on the Dharwar craton in southern India, which hosts most of the kimberlite and lamproite occurrences in India. The Dharwar craton can be subdivided into two broad regions; the Southern Granulite Terrane comprising ~ 2.51 Ga granulites in the south and a low-grade granite-greenstone terrain in the north (Kumar et al., 2007). The granite-greenstone terrain comprises Achaean supracrustal belts surrounded by gneisses. A N-S fault zone further divides this area into the Western Dharwar Craton (WDC) and Eastern

Dharwar Craton (EDC) blocks. The outcrop of the N-S trending Closepet granite (2.51 Ga) runs parallel to this fault for > 300 km.

The majority of kimberlite and lamproite intrusions in the region occur within the Eastern Dharwar Craton (Fig 1.3).

The Eastern Ghat orogeny (1.3-1.6 Ma) affected the EDC, resulting in a narrow, highly deformed granulite-facies belt extending from Chennai in the south to near Kolkota in the north east. The timing of the Eastern Ghat orogeny is poorly constrained, with age estimates from 500 Ma (Grasty and Leelanandam, 1965) to 2900 Ma (Paul and Barman, 1988). The present day lithospheric thickness beneath the Dharwar Craton is thought to be greater than 200 km (Gupta et al., 1991).

2.4. Local Geology

A large crescent shaped basin known as the Cuddapah Basin is located within the EDC. The Cuddapah Basin is ~ 2.0 Ga old (Anand et al., 2003) and covers an area of around 44000 km^2 (Nagaraja Rao et al., 1987). It comprises a 6 to 12 km thick succession of igneous and sedimentary rocks of Early to Late Proterozoic age. It shows increasing metamorphic grade from west to east, attributed to the effects of the Eastern Ghat orogeny. It includes two sub-basins, the Kurnool and Palnad basins (Nagaraja Rao et al., 1987). There are intrusive and extrusive rocks present throughout the Cuddapah Basin, with extensive lava flows and sills along the SW fringes of the basin (Anand et al., 2003). The crust beneath the Cuddapah Basin has been estimated to be 40-50 km thick (Kaila et al., 1979).

The Archaean basement surrounding the basin has been intruded by an extensive swarm of dolerite dykes predominantly trending ENE-WSW, but these dykes do not intrude the basin sediments. Three major episodes of dyke emplacement have been suggested at 1900-1700

Ma, 1400-1300 Ma and 1200-1000 Ma, with a minor younger event at 650 Ma. Some N-S trending mafic dykes, thought to be 1400-1300 Ma in age, were emplaced at the northern end of the Cuddapah Basin,. The dykes in the EDC can generally be classified into two broad groups: a depleted type similar to MORB and an enriched type similar to continental flood basalts (Rao and Puffer, 1996).

The kimberlites in the EDC crop out to the west of the Cuddapah Basin, while lamproites intrude the basin and its north-eastern margin. The kimberlites in the EDC predominantly occur in three spatially separated groups: the diamondiferous Wajrakarur kimberlite field (WKF), the Raichur kimberlite field (RKF) and the Narayanpet kimberlite field (NKF) (Fig. 2.2). Kimberlite samples from all three fields were collected for this study.

The WKF in the district of Anantapur consists of 27 kimberlites that intrude Archaean granites and gneisses. These kimberlites are diamondiferous and the majority of pipes have been classified as hypabyssal-facies kimberlite. The NKF in the district of Mahbubnagar consists of 60 kimberlites that intrude into migmatites and igneous intrusive rocks. These kimberlites are non-diamondiferous (Satyanarayana, 2002) and are also considered to be hypabyssal-facies kimberlites (Chalapathi Rao et al., 2004). The RKF comprises 15 kimberlites, some of which are diamondiferous (e.g., Lynn, 2005).

Lamproites occur in three fields in the EDC (Fig. 2.2). The Cuddapah Basin Lamproites (CBL) comprises two lamproites - Chelima and Zangamarajupalle. The lamproites of the CBL that are located within the Cuddapah basin intrude slates and phyllites of the Nallamalai Group (Sreeramachandra Rao, 1988). These are considered hypabyssal facies lamproites (Chalapathi Rao et al., 2004). The lamproites of the Krishna lamproite field (KLF) located to the NE of the Cuddapah Basin intrude the granites of the Peninsular Gneissic Complex of the Dharwar Craton. There are around 30 known lamproites within the KLF, covering an area of

~160 km^2. These lamproites occur mainly as dykes that intrude the early Proterozoic granites of the Peninsular Gneissic Complex of the Dharwar Craton. These lamproites have been classified as diopside lamproites, phlogopite lamproites and olivine lamproites (Chakrabarti et al., 2007).The Ramadugu lamproite field (RLF) comprises of 15 lamproite bodies. Diamonds have not been reported from any lamproites in the RLF. This field was not sampled for this study.

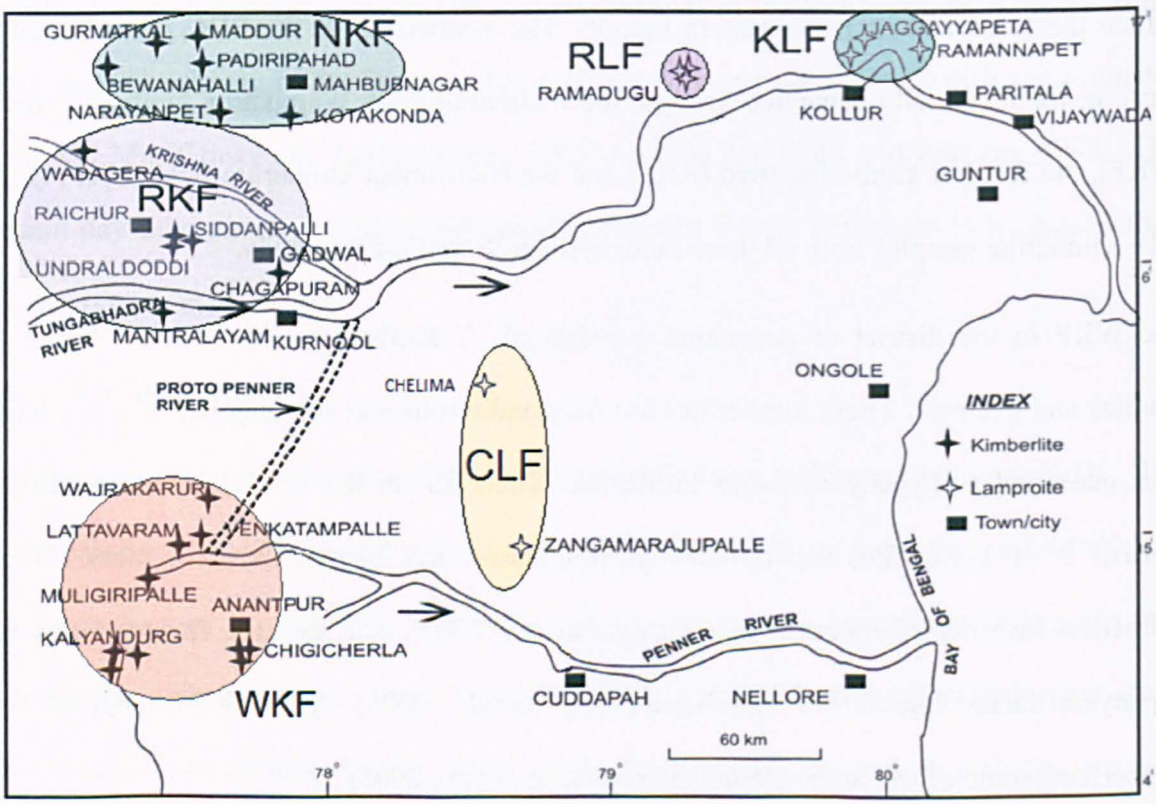

Figure 2.2. Location and extent of kimberlite and lamproite fields around the Cuddapah Basin, showing the locations of individual bodies. WKF: Wajrakarur Kimberlite Field; NKF: Narayanpet Kimberlite Field; RKF: Raichur Kimberlite Field; KLF: Krishna Lamproite Field; CLF: Cuddapah Basin Lamproite Field; RLF: Ramadugu Lamproite Field. Modified from Chalapathi Rao et al. (2009).

The Krishna lamproites are thought to be some of the oldest lamproite occurrences globally, and have been previously suggested to be the sources of several of the notable Indian diamonds (Chakrabarti et al., 2007). However recent studies suggest the Krishna lamproites to be non-diamondiferous (Chalapathi Rao et al., 2011) and that the primary source(s) for the historically renowned diamonds recovered from the Krishna valley may lie elsewhere, for instance in host rocks yet to be discovered.

2.5. Wajrakarur Kimberlite Field

The Wajrakarur Kimberlite field (KLF) includes ~25 kimberlites that intrude the Archaean granites and gneisses in the Anantapur district (Babu, 1998; Nayak et al., 2001).The kimberlites occur as either dykes or highly weathered and altered outcrops. Approximately 85% of the kimberlites are thought to be diamondiferous, which is comparable only to the Kimberlite Field in South Africa in this aspect (Satyanarayana, 2002).

In general the kimberlites show a porphyritic texture with megacrysts (>5mm), macrocrysts (1-5 mm) and microphenocrysts (<1 mm) of olivine. The modal proportion and amount of serpentinization varies between pipes in this field from completely sepentinized to fresh. Groundmass phases can include monticellite, rutile, phlogopite, perovskite, various spinels (predominantly chromite), calcite, chlorite, apatite, serpentine and clay minerals. Perovskite is particularly pervasive in the kimberlites from the WKF (5-15% vol % by mode) occurring as discrete euhedral grains. Phlogopite can also be abundant in these kimberlites but the modal proportion again varies between pipes as does the degree of alteration to chlorite. Randomly orientated clinopyroxene laths are present in some pipes, which may represent late-stage crystallization (Chalapathi Rao et al., 2004). Hazelwoodite, pectolite, melilite, richterite and sanidine have also been reported in some of the pipes (Reddy, 1987; Chalapathi Rao et al., 2004) but were not observed in this study.

2.5.1. Lattavaram kimberlite cluster

There are four main pipes in the Lattavaram cluster. In this study samples from two pipes known as Lattavaram Pipe 3 (Lat3) and Lattavaram pipe 4 (Lat4) are analysed. Lat3 is located 1 km east of Lattavaram, while Lat 4 (also known as the Lambadi Hut pipe) is located 1.6 km east of Lattavaram. Lat3 is one of the smallest pipes in the WKF, while Lat4 is the largest of the 4 Lattavaram pipes. The Lat3 pipe was poorly exposed and samples were collected from a large boulder found at the locality (Fig. 2.3).

Figure 2.3: Samples were collected from a large kimberlite boulder found at the Lat3 locality.

Lat4 was also poorly exposed and samples were collected from large pieces of kimberlite located at the site of Lat4 (Fig. 2.4).

Figure 2.4: Location of the Lat4 kimberlite.

The remaining two pipes are not well exposed and are blanketed by a soil cover. Drilling at Lat3 has revealed that the "yellow ground" continues to a depth of 10 m and is underlain by "blue ground" and the "harde banke" was encountered at a depth of 70 m (Rao et al., 1991). The pipes have been reported to contain diamonds as well as mantle xenoliths of lherzolite, harzburgite, dunite and eclogite (Karmalkar et al., 2009). Where the two pipes are exposed, the rock is relatively unweathered and dark blue in colour and contains abundant crustal xenoliths that appear felsic in composition.

In thin-section (Fig. 2.5) the pipes are porphyritic and contain subhedral macrocrysts (2-8 mm; 15 vol % by mode) and subhedral to euhedral microphenocrysts of olivine (0.1-0.4 mm; 25 vol % by mode). Olivine varies in degree of alteration to serpentine (general degree of alteration: macrocrysts 50-70%; microphenocrysts 80-100%). Macrocrysts (1-2 mm, 1-2 vol % by mode) and microphenocrysts (100-500 μm, 5 vol % by mode) of phlogopite are also

present, although the majority show alteration to chlorite (degree of alteration: 60-70 %). The groundmass olivine has nearly completely altered to serpentine. The groundmass also contains perovskite (50-100 μm; 5 vol % by mode), Cr-spinel/ilmenite (30-60 μm; 5 vol % by mode), calcite (20 vol % by mode), serpentine (25 vol % by mode), apatite and clinopyroxene. The Lat3 pipe has been classified as hypabyssal-facies-phlogopite-bearing macrocrystal kimberlite and Lat4 as a hypabyssal-facies phlogopite-kimberlite (Chalapathi Rao et al., 2004).

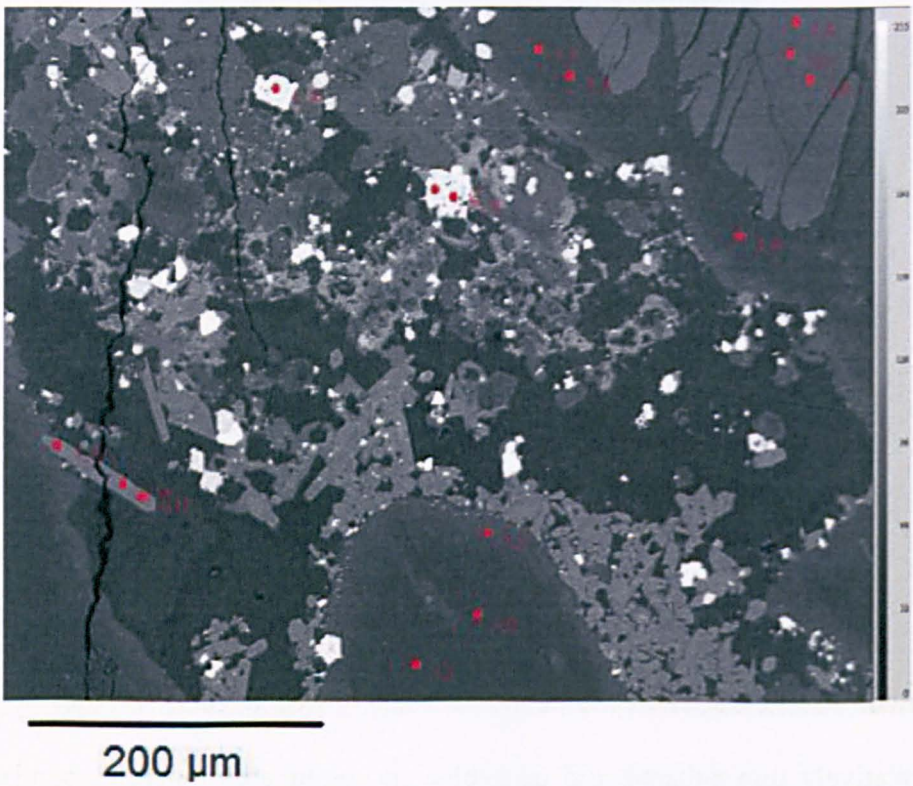

Figure 2.5: SEM image of Lat3 sample. Points 1_1 to 1_9 are located in olivine crytals that have been serpentinised to varying degrees. Points 1_10-1_12 are located in Cr-Spinel/ilmenite. Points 1_13-1_15 are located in apatite.

2.5.2. Muligiripalle kimberlite

This is one of the largest and best exposed pipes in the WKF (Fig. 2.6). It is known as Muligiripalle Pipe 5 (Mul5) in the order it was discovered in the WKF. It appears as a series

of linear outcrops and drilling has revealed that this body is an elongate diatreme in plan form (Chalapathi Rao et al., 2004). It is not diamondiferous and contains xenoliths of dolerite. An E-W dolerite dyke outcrops near the pipe (Chalapathi Rao et al., 2004).

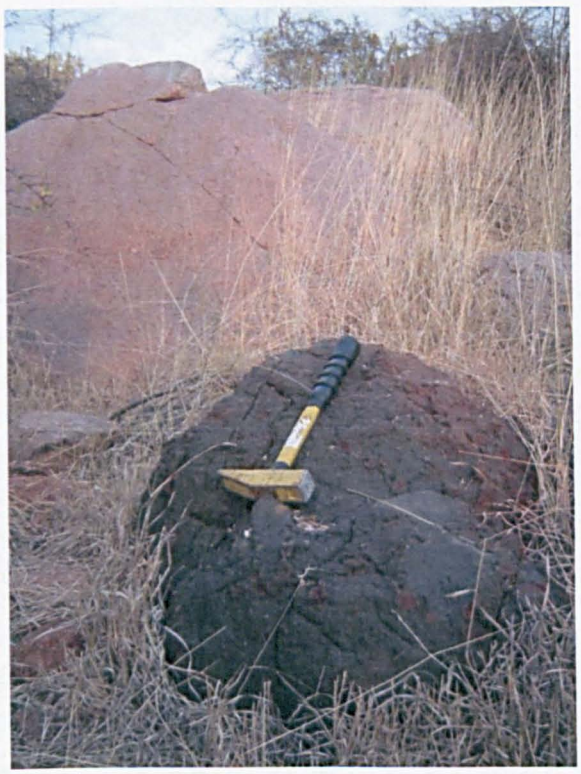

Figure 2.6: Location of the Mul5 kimberlite.

In thin-section (Fig. 2.7) the sample is porphyritic with euhedral olivine microphenocrysts (0.1-0.8 mm; 25 vol % by mode) and to a lesser extent macrocrysts (4-7 mm; 5 vol % by mode). The majority of olivine grains are altered to serpentine (general degree of alteration 80-100 %) and often rimmed by chlorite, commonly only leaving pseudomorphs of olivine. Phlogopite macrocrysts are present (1-3 mm, 5-10 vol % by mode), which are remarkably fresh with only minor alteration to chlorite on some grains (degree of alteration: 0-10 %). There is also a high proportion of phlogopite microphenocrysts (200-500 μm; 10-15 vol % by mode) in the groundmass, which sometimes show minor alteration to chlorite (degree of alteration: 0-20 %). Perovskite is abundant throughout the sample (50-200 μm; 5-10 vol % by

mode), appearing as euhedral dark brown grains. The groundmass also includes Cr-spinel/ilmenite (40-80 μm; 5 vol % by mode), calcite (5 vol % by mode), serpentine (40 vol % by mode) and minor ilmenite, clinopyroxene, monticellite, apatite. This pipe has been classified as a hypabyssal-facies phlogopite-monticellite-kimberlite.

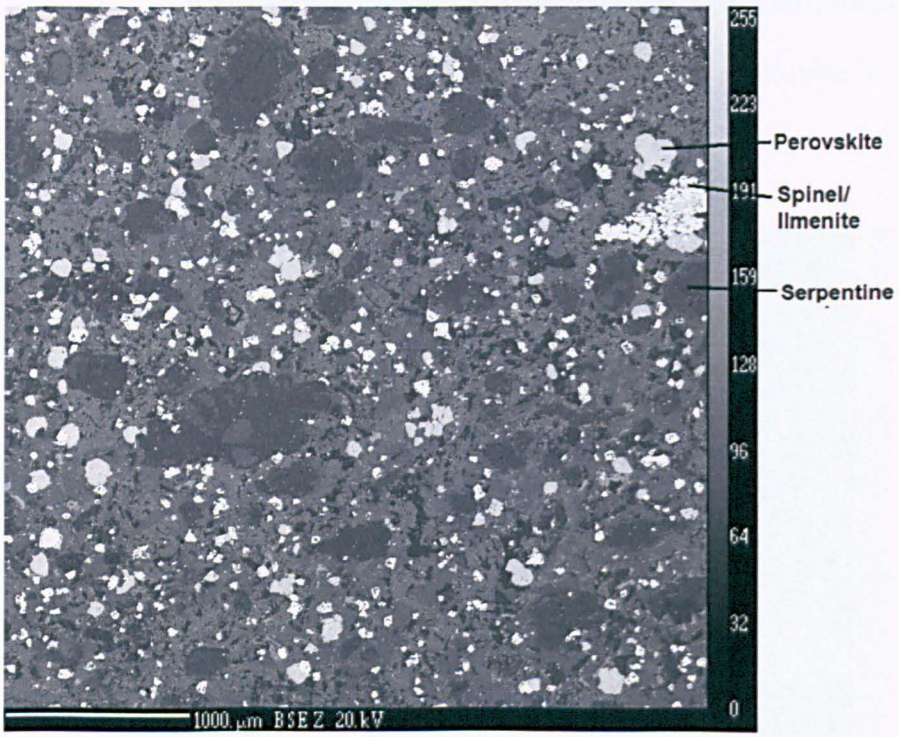

Figure 2.7: SEM image of Mul5 sample.

2.5.3. Tummatapalle Kimberlite

The Tummatapalle kimberlite (Tumm) is located in close proximity to the west of the Muligiripalle kimberlite, approximately 15 km south of the town Uravakonda. It is well exposed and appears remarkably fresh (Fig. 2.8).

Figure 2.8: Location of the Tumm kimberlite.

In thin-section (Fig. 2.9) the sample is porphyritic with macrocrysts (3-8 mm; 5 vol % by mode) and microphenocrysts (0.3-0.9 mm; 20 vol % by mode) of olivine. Almost all the olivine has been altered to serpentine (general degree of alteration: macrocrysts 80-100 %; microphenocrysts 50-100 %) often just leaving pseudomorphs of the olivine, sometimes also showing alteration by calcite (degree of alteration: macrocrysts 5-10 %; microphenocrysts 10-20 %). The sample contains a large amount of phlogopite microphenocrysts in the groundmass (100-800 μm; 30 vol % by mode). The phlogopite can appear fresh but some grains show minor alteration to chlorite and/or calcite (degree of alteration: 0-15 %). Other groundmass phases include, perovskite (25-80 μm; 5 vol % by mode), Cr-spinel/ilmenite (30-80 μm; 5 vol % by mode), serpentine (25 vol % by mode), calcite (10 vol % by mode), and apatite, and monticellite.

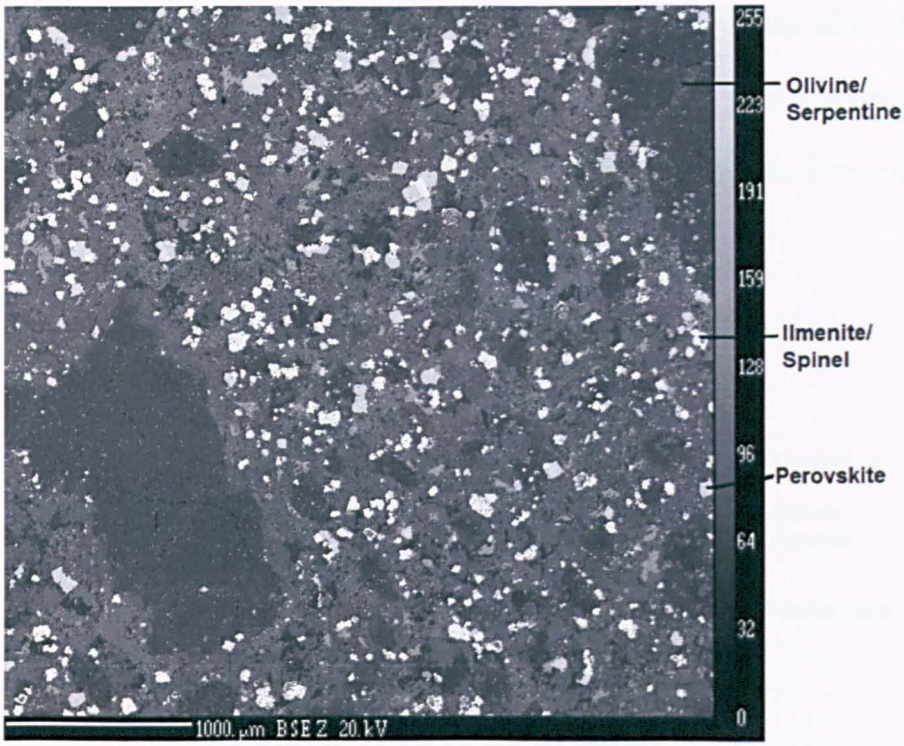

Figure 2.9: SEM image of Tumm sample.

2.5.4. Kalyandurg kimberlite cluster

The Kalyandurg cluster consists of 6 kimberlites. In this study 3 kimberlites are analysed including KL1 located 1 km north of the village of Pillalapalli, KL2 located 3 km east of Pillalapalli and KL3 located 1 km north west of the village Nagireddipalli. KL1 was well exposed (Fig. 2.10), however samples were weathered and crumbly. Eclogitic mantle xenoliths have been found in the Kalyandurg cluster (KL2) and crustal xenoliths are common (Karmalkar et al., 2009). KL2 was poorly exposed and samples were collected from loose blocks from the site (Fig. 2.11), which were extremely weathered and appeared clay-like in hand specimen. KL3 samples were collected from exposure (Fig. 2.12) and appeared less weathered but had a green altered appearance.

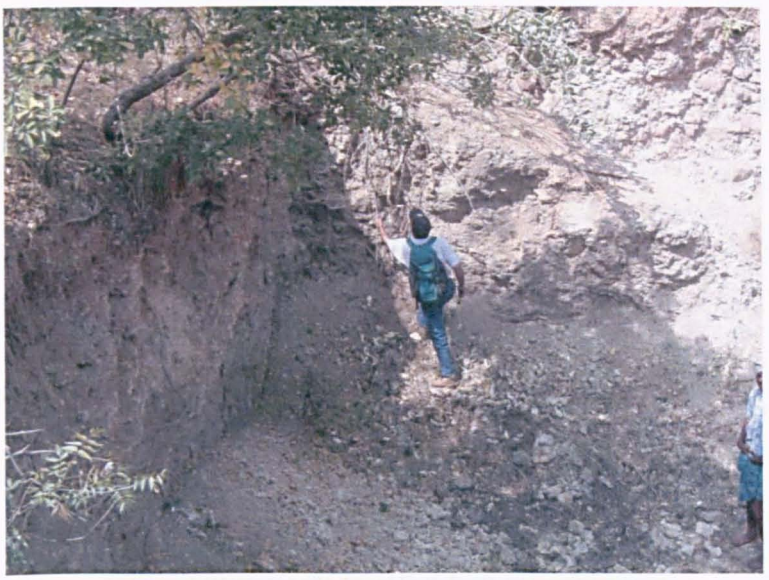

Figure 2.10: Location of the KL1 kimberlite.

Figure 2.11: Location of the KL2 kimberlite.

Figure 2.12: Location of the KL3 kimberlite.

In thin-section the Kalyandurg samples appear porphyritic with large euhedral macrocrysts (4-6 mm; 5 vol % by mode) and euhedral/subhedral microphenocrysts (0.1-0.7 mm; 20 vol % by mode) of olivine. The olivine is almost completely altered to serpentine and calcite (general degree of alteration: macrocrysts 75-100 %; microphenocrysts 55-100 %) leaving only pseudomorphs. Macrocrysts of ilmenite (5-6 mm; 5 vol % by mode) occurring as euhedral laths are also present. The samples have undergone extensive alteration with abundant alteration, with the majority of the groundmass composed of calcite (30 vol % by mode) and serpentine (40 vol % by mode). Other groundmass phases present include olivine, serpentine, phlogopite, Cr-spinel, ilmenite, perovskite, apatite, magnetite, clinopyroxene and calcite. Microprobe analysis in this study suggested some garnet megacrysts may have been present but are extremely altered. These kimberlites have been classified as macrocrystal hypabyssal serpentine calcite kimberlites.

2.5.5. Chigicherla kimberlite cluster

The Chigicherla kimberlite cluster is located in the south east of the WKF and includes 5 pipes. In this study samples from 4 pipes known as CC1, CC2, CC4 and CC5 were collected. The CC1 pipe is well-exposed (Fig. 2.13) and is located approximately 1.5 km east of the village of Chigicherla. It is a hard melanocratic greenish-black rock, which contains abundant serpentine and calcite veins. Crustal xenoliths are common and mantle xenoliths (spinel harzburgite) have been reported (Murthy et al., 1994).

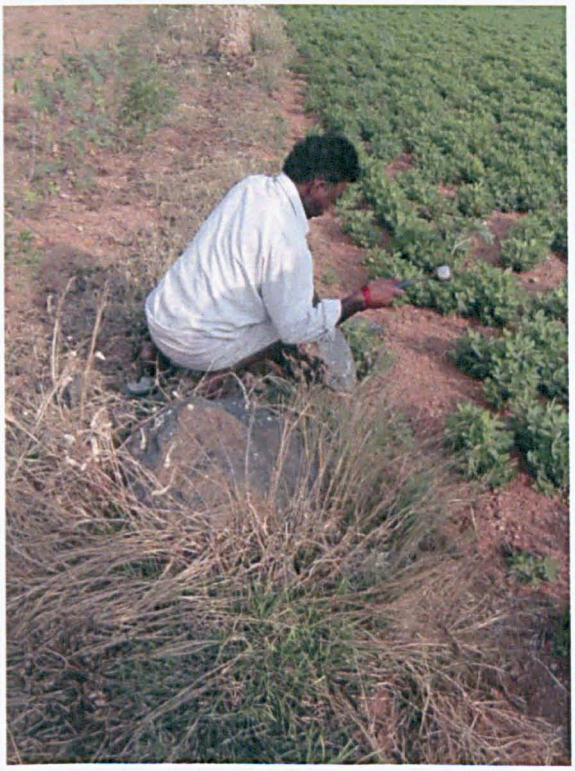

Figure 2.13: Location of the CC1 kimberlite.

The CC2 pipe (Fig. 2.14) is located 2 km west of CC1 and 0.75 km north of Chigicherla village. It is similar in appearance to CC1 but where as CC1 diamond potential is thought to be poor (Chalapathi Rao et al., 2004), CC2 is thought to be diamondiferous.

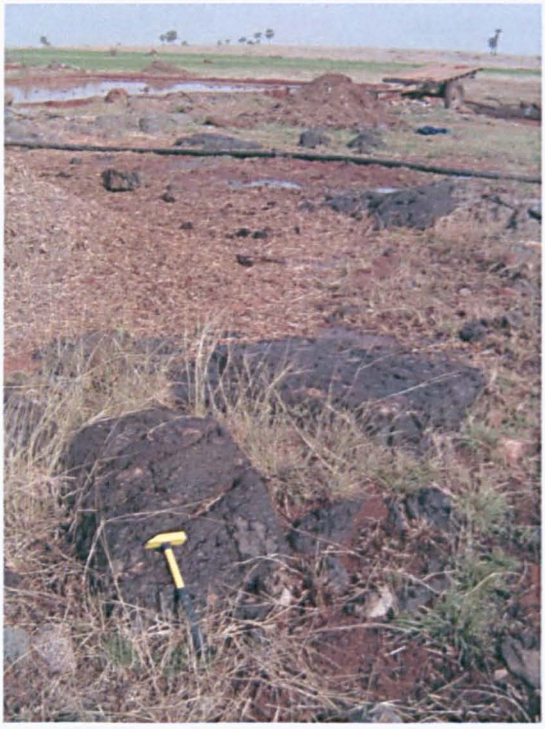

Figure 2.14: Location of the CC2 kimberlite.

The CC4 pipe is located 1.75 km west of Gollapalle village. This again has a hard, melanocratic, greenish-black appearance (Fig. 2.15) and has been reported to be diamondiferous (Fareeduddin, 2008).

Figure 2.15: Location of the CC4 kimberlite.

The CC5 pipe is located NE of Gollapalle. It is an elongated body with a ENE-WSW trend (Fig 2.16). It contains abundant crustal xenoliths and is diamondiferous (Chalapathi Rao et al., 2008). The CC5 pipe has an unusual appearance with spectacular globular segregations (Fig. 2.17).

Figure 2.16: Location of the CC5 kimberlite.

Figure 2.17: Nodules on the CC5 kimberlite.

The globules are up to 6 cm in diameter, and can show concentric or spiral structure (Fig. 2.18). These are thought to be kimberlite autoliths (Chalapathi Rao et al., 2010).

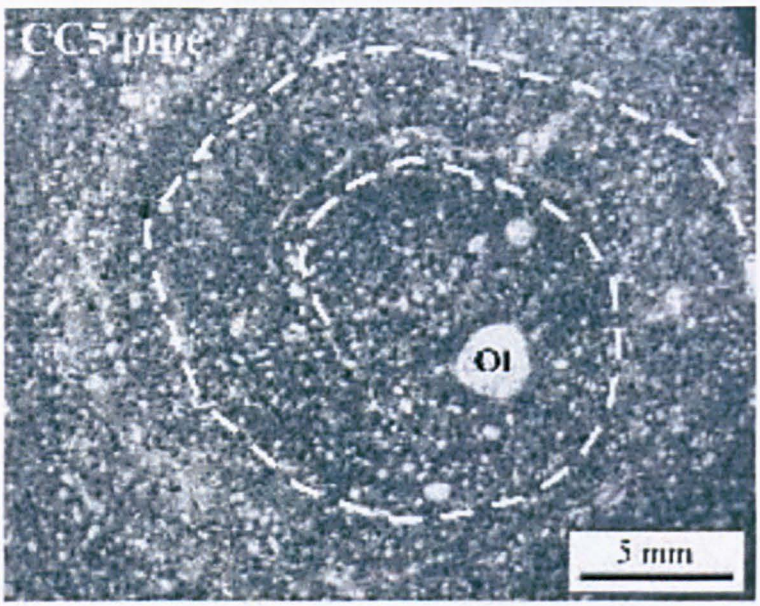

Figure 2.18: Photomicrograph in plane polarized light (PPL) of a globule in CC5 kimberlite (Patel, 2008) showing spiral trail (dashed line). The trail is defined by apatite and calcite. Olivine rarely occurs as macrocryst, and is common as microphenocryst. The groundmass comprises of serpentine, calcite, spinel and perovskite (Patel et al., 2008).

In thin-section (Fig. 2.19, Fig. 2.20, Fig. 2.21, Fig. 2.22) the samples have a porphyritic texture with rounded subhedral olivine macrocrysts (5-8 mm; 10 vol % by mode) and subhedral microphenocrysts (0.1-0.9 mm; 30 vol % by mode). The olivine is often serpentinised and sometimes overprinted by calcite (general degree of alteration: macrocrysts 60-100 % serpentine; microphenocrysts 60-100% serpentine, 0-20% calcite). Phlogopite is a common phase occurring as macrocrysts (1-2 mm, 5 vol % by mode) and microphenocrysts in the groundmass (80-150 μm; 5 vol % by mode), but often show minor to extreme chloritisation (degree of alteration: 25-85 %). Perovskite is pervasive throughout all the samples (30-100 μm; 5 vol % by mode), but particularly in CC5 where it is more abundant

and larger (80-500 μm; 15-20 vol % by mode) than in the other Chigicherla samples. The perovskite appears zoned in CC5 (Fig. 2.23) and microprobe analysis showed this to be the result of slight variations in the Fe content. The other groundmass phases include Cr spinel/ilmenite (10-50 μm; 2-5 vol % by mode), serpentine (20 vol % by mode), calcite (35 vol % by mode), clinopyroxene, and apatite. Although not found in this study, melilite and monticellite have been reported in the CC1 pipe (Murthy et al., 1994). These rocks have been classified as hypabyssal-facies phlogopite-kimberlite (Chalapathi Rao et al., 2004).

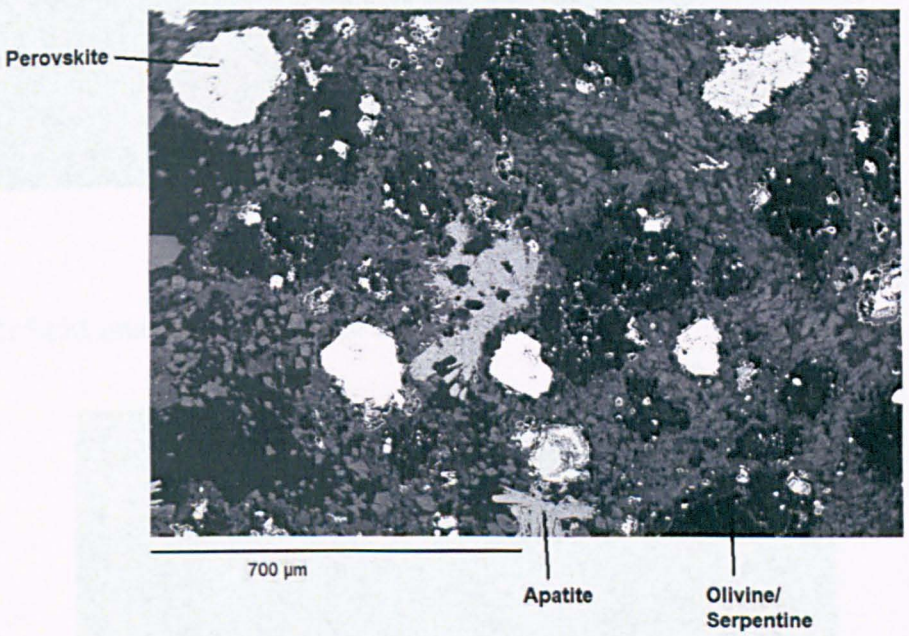

Figure 2.19: SEM image of CC5 sample.

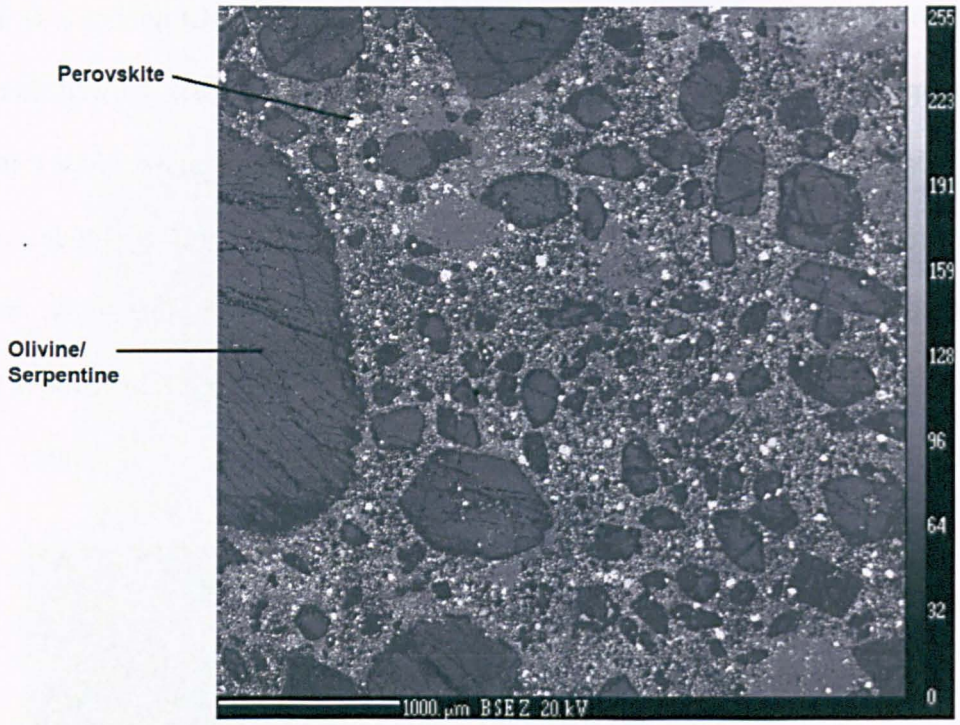

Figure 2.20: SEM image of CC1 sample.

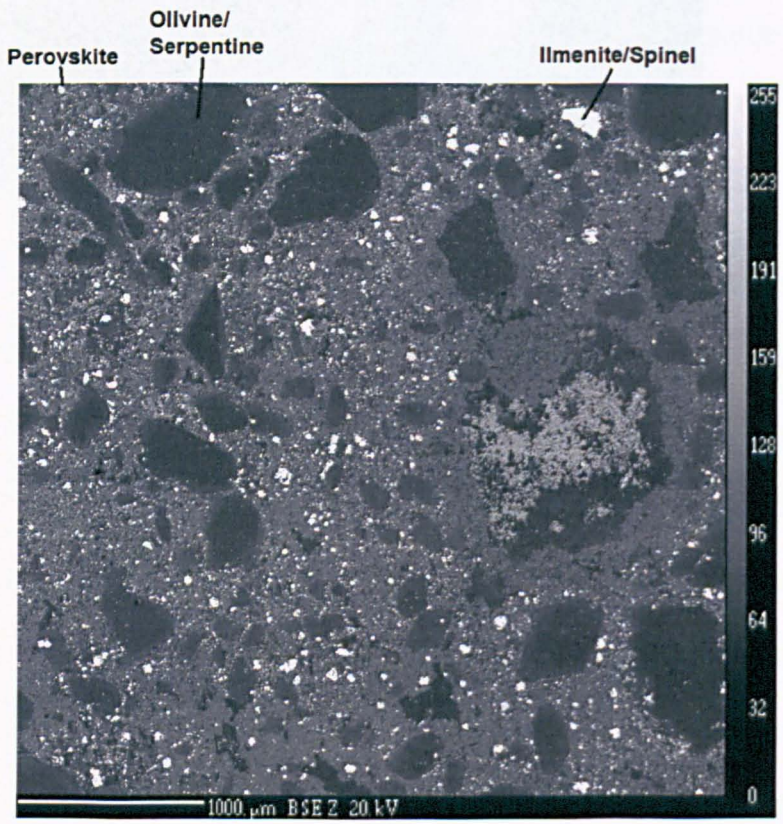

Figure 2.21: SEM image of CC2 sample.

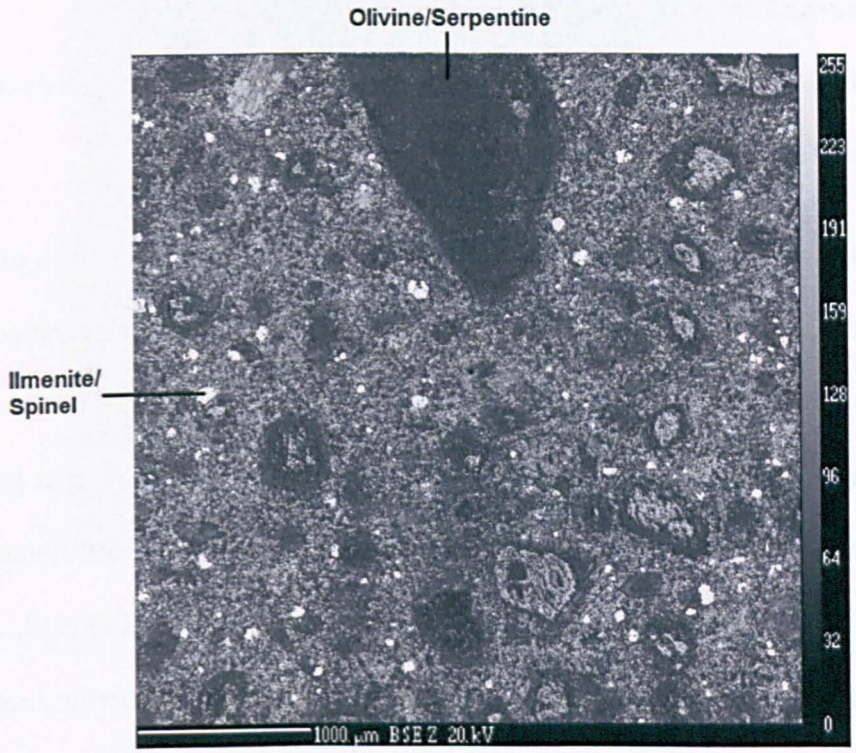

Figure 2.22: SEM image of CC4 sample.

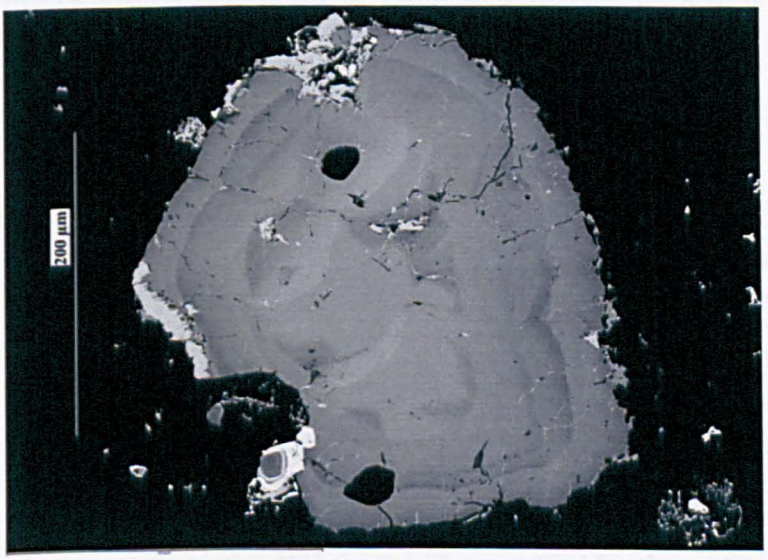

Figure 2.23: SEM image of a perovskite crystal from the CC5 kimberlite.

2.5.6. Wajrakarur kimberlite cluster

There are 7 kimberlite pipes in the Wajrakarur kimberlite cluster. In this study samples from two pipes were analysed, Waj1, Waj2 and Waj2N.

Waj1 is one of the largest pipes in the WKF and is located NW of the village of Wajrakarur. It is well exposed in places (Fig. 2.24). The rock has a weathered appearance but is dark black/blue in colour and contains numerous crustal xenoliths (Fig 2.25). The crustal xenoliths appear felsic in composition and are likely from the surrounding granite and gneiss country rocks. It has been reported to be diamondiferous and contains abundant diamond indicator minerals (Cr-diopside, picro-ilmenite and pyrope-garnet) (Chalapathi Rao et al., 2004). Waj1 has been classified as a highly-altered-diatreme facies, tuffistic kimberlite breccias (Scott-Smith, 1989).

Figure 2.24: Location of the Waj1 kimberlite.

Figure 2.25: Samples from the Waj1 kimberlite showing abundant crustal xenoliths.

Waj2 is located 3.2 km E of Wajrakarur village (Fig. 2.26, Fig. 2.27). Waj2N (Fig. 2.28) is a recently discovered exposure of kimberlite located in close proximity to the north of the Waj2 exposure and is thought to be part of the same pipe. These pipes are well exposed and again contain abundant crustal xenoliths. These pipes appear less weathered than Waj1 and are very hard and black in appearance. Diamonds have not been reported from this pipe.

Figure 2.26: Location of the Waj2 kimberlite

Figure 2.27: A hand dug well exposing the Waj2 kimberlite.

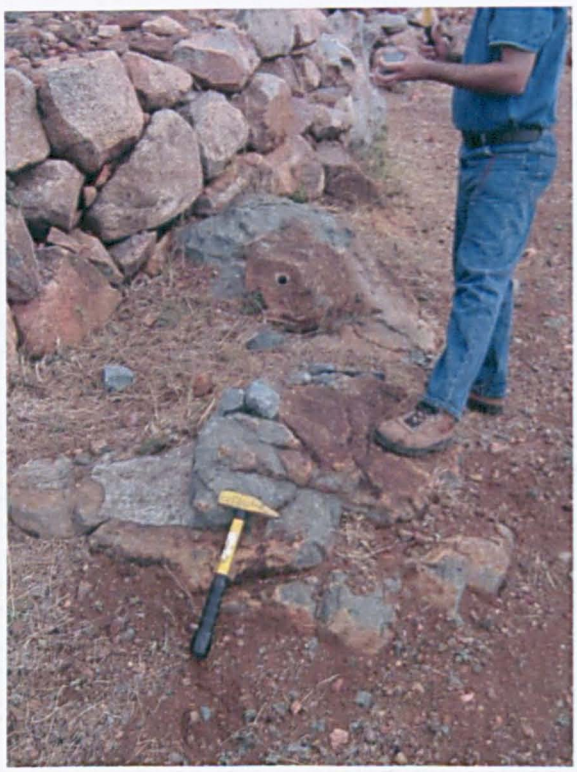

Figure 2.28: Location of the Waj2N kimberlite.

In thin-section the Waj1 sample is porphyritic with macrocrysts (2-6 mm; 5 vol % by mode) and microphenocrysts (0.1-0.8 mm; 20 vol % by mode) of olivine. The olivine has been

significantly altered (general degree of alteration: macrocryst 60 % serpentine; microphenocrysts 40 % serpentine 30 % calcite) and are now predominantly pseudomorphed by serpentine and calcite. Phlogopite microphenocryst (50-150 μm; 1-2 vol % by mode) are present, which has undergone moderate to complete alteration by chlorite (general degree of alteration: 50-100 %). The groundmass is predominantly composed of serpentine (20 vol % by mode) and calcite (40 vol % by mode) but other phases include perovskite (30-80 μm; 1-2 vol % by mode), Cr-spinel (50-100 μm; 3-5 vol % by mode) and clinopyroxene.

Waj2 and Waj2N appear fresher and less altered than Waj1 in thin section (Fig. 2.29). It is also porphyritic with rounded-subrounded olivine macrocrysts (3-6 mm; 5-10 vol % by mode) and microphenocrysts (0.1-1 mm; 20 vol % by mode). The majority of the olivine is again serpentinised only leaving pseudomorphs (general degree of alteration: macrocrysts 60-100 % serpentine; phenocrysts 50-100 % serpentine, 10-20 vol % by mode), however some rare fresh olivine can be seen. Phlogopite occurs as macrocrysts (1-3 mm, 5-10 vol % by mode) and microphenocrysts (100-250 μm, 5 vol % by mode), which show varying degrees of chloritisation (general degree of alteration: 40-80 %). The other groundmass phases include perovskite (40-90 μm, 5 vol % by mode), Cr spinel/ilmenite (50-100 μm, 5-10 vol % by mode), serpentine (10 vol % by mode), calcite (40 vol % by mode), and apatite. Minor monticellite is also present in the groundmass. Carbonate veins can be seen cross cutting the other mineral phases. The Waj2 pipe has been classified as a hypabyssal-facies phlogopite-rich monticellite-kimberlite (Chalapathi Rao et al., 2004).

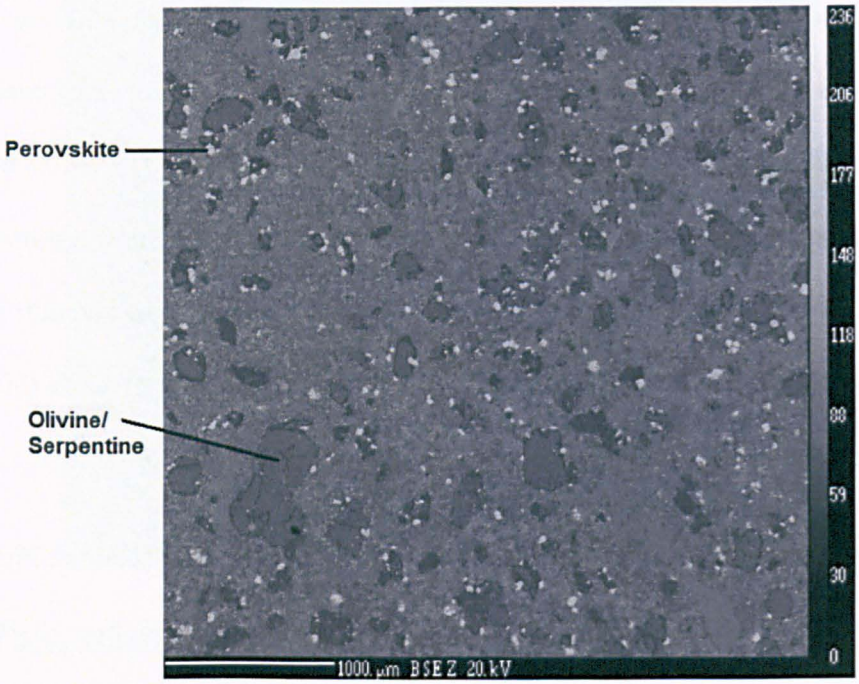

Figure 2.29: SEM image of Waj2 sample.

2.5.7. Chintalampalle kimberlite

The Chintalampalle kimberlite (Chin12) is located about 0.75 km north of the Chintalampalle village and has dimensions of 130 m x 50 m (Chalapathi Rao et al., 2004). It is a NE-SW trending body emplaced in granitoids along NE-SW trending faults (Fig. 2.30).

Figure 2.30: Location of the Chin12 kimberlite.

In thin-section (Fig. 2.31) the sample is porphyritic with rounded macrocrysts (2-6 mm; 5 vol % by mode) and microphenocrysts (0.5-1.5 mm; 15 vol % by mode) of olivine. Almost all the olivine has been altered to serpentine (general degree of alteration: macrocrysts 75-100 %; phenocrysts 40-60 %) often just leaving pseudomorphs after olivine, sometimes also showing alteration by calcite (degree of alteration: macrocrysts 25-30 %; phenocrysts 20-25 %). Phlogopite macrocrysts (1-2 mm, 2-4 vol % by mode) and microphenocrysts (100-200 μm; modal 5 vol % by mode) are present. The phlogopites often show moderate to complete alteration to chlorite and/or calcite (degree of alteration: 50-100 %). Other groundmass phases include perovskite (40-80 μm; 5-10 vol % by mode), Cr-spinel/ilmenite (50-100 μm; 5 vol % by mode), serpentine (30 vol % by mode), calcite (25 vol % by mode), apatite, monticellite and magnetite.

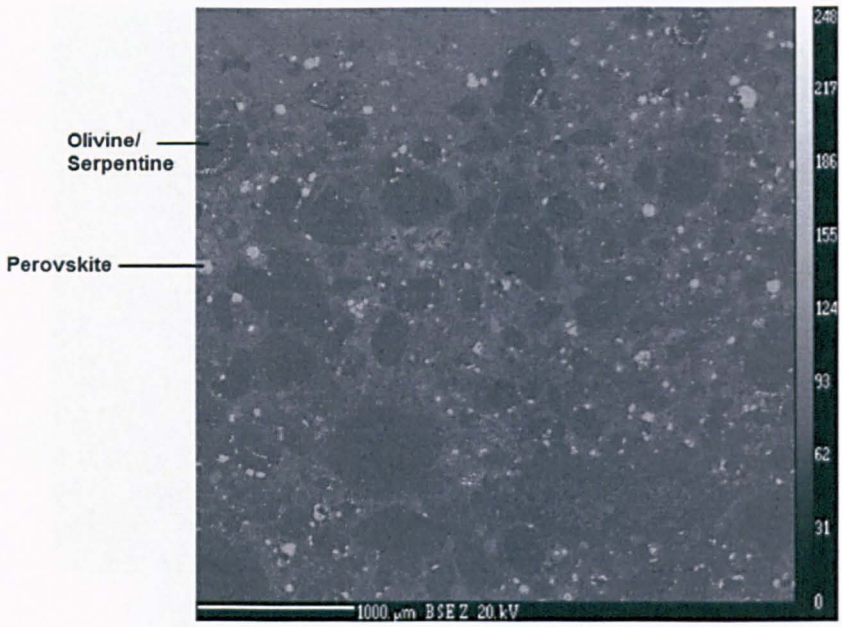

Figure 2.31: SEM image of Chin12 sample.

2.5.8. Timmasamudram kimberlite cluster

The Timmasamudram kimberlite cluster consists of 6 kimberlites (TK1, TK2, TK3, TK4, TK5 and TK6). It is located on the bank of the Penner River about 1.5 km WSW of Timmasamudram village. The kimberlites vary in size from 20 m x 25 m to 30 m x 50 m and are emplaced in Archaean granite-gneisses. In this study samples of TK4 (Fig. 2.32) and a sample named TKO (Fig. 2.33) (located in close proximity to TK4) were collected. They are generally poorly exposed, concealed under a thick soil cover (0.5-1 m thick). A sample collected from the site of TK3 was given to us by a colleague. These pipes are reported to be diamondiferous with the TK-4 kimberlite considered to have the highest grade (65 cpht) of diamonds among all the WKF.

Figure 2.32: Location of the TK4 kimberlite.

Figure 2.33: Location of the TKO kimberlite.

In thin section the kimberlite is porphyritic with macrocrysts (5-10 mm; 5 vol % by mode) and microphenocrysts (0.4-1 mm; 20 vol % by mode) of olivine. The olivine is predominantly serpentinised and carbonated (general degree of alteration: macrocryst 90-100%; microphenocrysts 90-100 %). Phlogopite macrocrysts (0.5-1mm; 5 vol % by mode) and microphenocrysts (200-300 μm, 5-10 vol % by mode) are present, but are predominantly

completed carbonated or chloritised (general degree of alteration: 90-100%). Groundmass phases also include perovskite (20-70 μm; 1-2 vol % by mode), Cr-spinel/ilmenite (30-50 um; 2-5 vol % by mode), serpentine (30 vol % by mode), calcite (25 vol % by mode), apatite and clinopyroxene. Carbonate veins are pervasive throughout the sample.

2.6. Narayanpet Kimberlite Field

The Narayanpet Kimberlite Field (NKF) includes ~48 kimberlites, half of which are not exposed (Chalapathi Rao et al., 2009). The kimberlites occur near Maddur, Kotakonda, Narayanpet and Padiripahad. They are emplaced into migmatites and younger intrusive. Those exposed occur either as highly weathered and altered outcrops or exposed in well sections. The kimberlites are generally small (~ 100 m x 20 m), with the exception of a kimberlite at Kotakonda, which is a dyke of ~2 km in length.

The NKF kimberlites are considered non-diamondiferous (Satyanarayana, 2002). In general the NKF contain olivine macrocrysts/phenocrysts varying in degree of serpentinization and calcite alteration between pipes. Long euhedral grains of phlogopite (0.2-8 mm) occur in the groundmass varying in the degree of alteration to chlorite between pipes. The groundmass phases can include calcite, serpentine, apatite, clinopyroxene and spinel. Perovskite is abundant in these kimberlites occurring as discrete euhedral grains.

2.6.1. Kotakonda kimberlite

The Kotakonda kimberlite cluster is located 4 km NE of the Kotakonda village in the Kotakonda Reserve forest. In this study samples were collected from two exposures of the Kotakonda kimberlite, KK1 (Fig. 2.34) and KK6 (Fig. 2.35).The KK1 kimberlite is a discontinuous 1 km long dyke that trends E-W. The exposed rock is hard, blue-black in colour and contains a moderate amount of crustal xenoliths.

Figure 2.34: Location of the KK1 kimberlite.

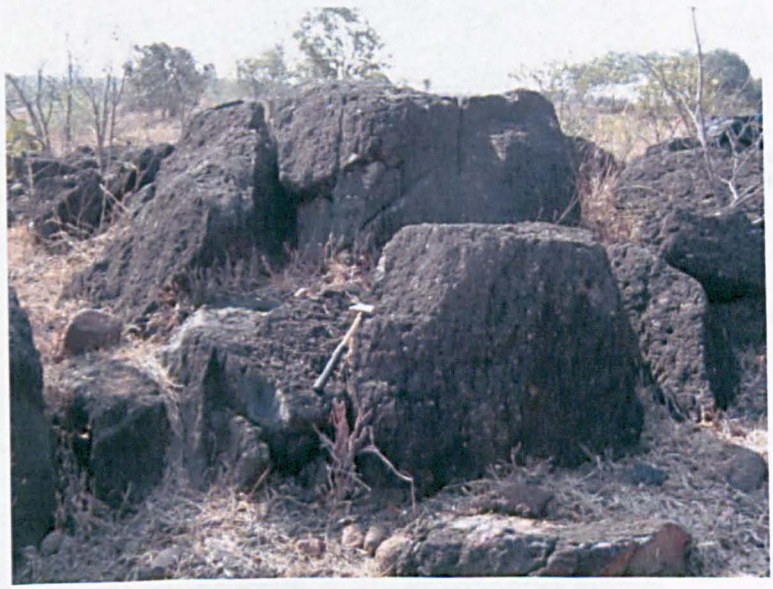

Figure 2.35: Location of the KK6 kimberlite

In thin-section (Fig. 2.36) the rock is porphyritic with subhedral olivine macrocrysts (1-5 mm; 5 vol % by mode) and phenocrysts (0.1-0.5 mm; 20 vol % by mode). The olivine has

undergone extensive serpentinisation particularly in the groundmass (general degree of alteration: macrocryst 80-100 % serpentinised; phenocrysts 80-100 % serpentinised, 0-20 % carbonised). Phlogopite phenocrysts (0.5-1 mm, 5 vol % by mode) are present and it is also abundant in the groundmass (200-300 μm, 10 vol % by mode), but shows varying degrees of alteration to calcite and chloritisation from relatively fresh to completely altered (general degree of alteration: 30-100 %. Perovskite is pervasive throughout the sample (40-100 μm, 5-10 vol % by mode) occurring as dark brown euhedral crystals. Other groundmass phases include Cr-spinel/ilmenite (20-70 μm, 5 vol % by mode), serpentine (20 vol % by mode), calcite (30 vol % by mode), rutile, titanite, barite and monticellite. Calcite veins cross cut other phases throughout the sample. This pipe has been classified as a hypabyssal-facies phlogopite-rich monticellite-bearing kimberlite.

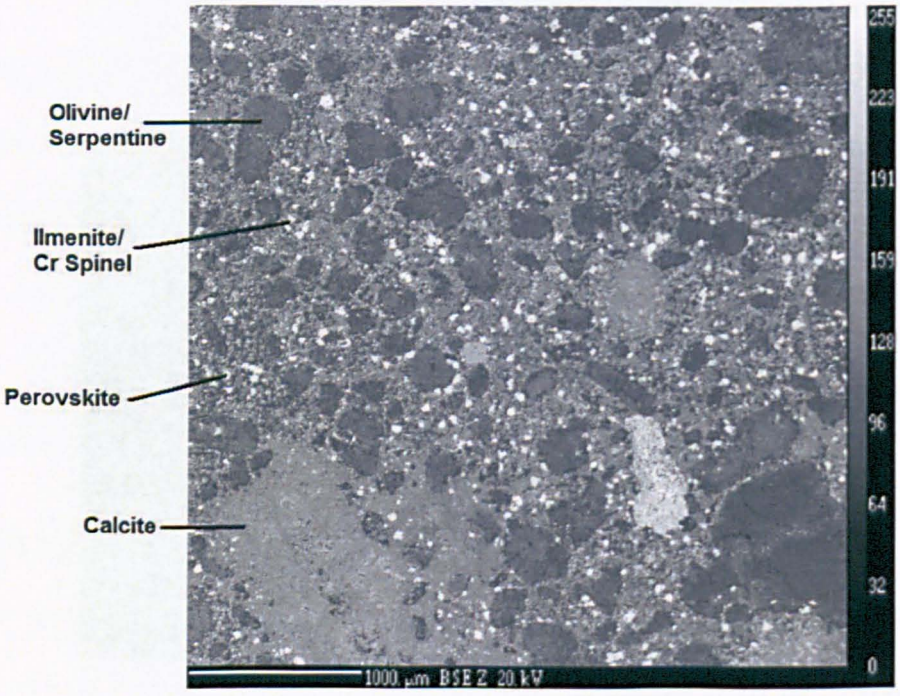

Figure 2.36: SEM image of KK6 sample.

2.6.2. Narayanpet kimberlite

The Narayanpet kimberlite cluster is located 2.6 km NW of the Narayanpet village. It is the smallest kimberlite in the NKF and the exposed rock is the diatreme part of the kimberlite (Chalapathi Rao et al., 2004). It contains large (> 5 mm) macrocrysts of olivine and mica that are visible in hand specimen. The rock has a black appearance, is hard and contains few crustal xenoliths. In this study samples were collected from two exposures of the Narayanpet kimberlite, NK1 (Fig. 2.37) and 1 km to the east, NK2 (Fig. 2.38). They appear similar in hand and thin-section except for NK2 containing a greater abundance of crustal xenoliths.

Figure 2.37: Location of the NK1 kimberlite.

Figure 2.38: Location of the NK2 kimberlite.

In thin section (Fig. 2.39) the samples are porphyritic with sub rounded macrocrysts (2-6 mm, 5-10 vol % by mode) and subhedral microphenocrysts (0.1-0.5 mm, 15 vol % by mode) of olivine. The olivine varies from relatively fresh to completely serpentinised (general degree of alteration: macrocrysts 40-100 % serpentinised, microphenocrysts 40-100 % serpentinised, 0-20 % carbonatised). Macrocrysts of phlogopite are present (1-3 mm, 5 vol % by mode) as euhedral laths and microphenocrysts of phlogopite are also common in the groundmass (100-200 μm, 10 vol % by mode). Much of the phlogopite has undergone chloritisation (general degree of alteration: 40-100 %). Perovskite is abundant in these samples and larger than most other EDC kimberlites (100-200 μm, 15-20 vol % by mode). Other groundmass phases include Cr-spinel/ilmenite (40-100 μm, 5 vol % by mode), serpentine (15 vol % by mode), calcite (20 vol % by mode), apatite and clinopyroxene. There are small calcite veins throughout the samples, which cross cut all other mineral phases. These pipes have been classified as a hypabyssal-facies perovskite-rich micaceous kimberlite.

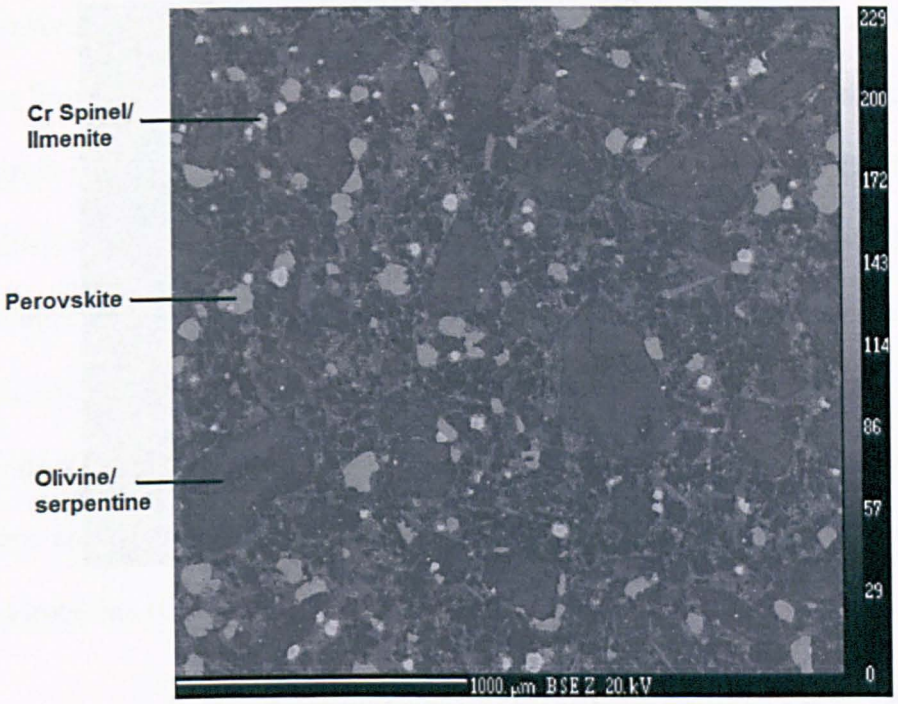

Figure 2.39: SEM image of NK1 sample.

2.6.3. Maddur kimberlite

The Maddur kimberlite pipe is located ~6 km SE of the Maddur village. It is exposed in seven small outcrops, with the largest being 4 m x 2 m. The kimberlite occupies a total area of ~40m^2. In this study samples were collected from two exposures of the Maddur kimberlite, MK1 (Fig. 2.40) and MK5 (Fig. 2.41). It is the diatreme part of the kimberlite, which is oval in shape (Chalapathi Rao et al., 2004). The outcrops appear weathered and contain serpentine veins throughout, but the rock is hard and blue/black in colour.

Figure 2.40: Location of the MK1 kimberlite.

Figure 2.41: Location of the MK5 kimberlite.

In thin section (Fig. 2.42) the samples are porphyritic with olivine macrocrysts (4-7 mm, 5 vol % by mode) and microphenocrysts (0.1-0.9 mm, 15-20 vol % by mode). The olivine is predominantly highly altered leaving only pseudomorphs of serpentine and calcite (general degree of alteration: macrocrysts 75-100 % serpentinised; microphenocrysts 80-100 % serpenitinsed, 0-15 % carbonatised). Phlogopite microphenocrysts (100-250 μm, 10 vol % by

mode) and macrocrysts (0.1-6 mm, 5 vol % by mode) are also present as elongated subhedral laths that are brown/orange in colour and show moderate pleochroism. The phlogopite shows varying degrees of alteration to chlorite from relatively fresh to complete (general degree of alteration: 20-100 %). Euhedral crystals of perovskite (40-110 μm, 5-10 vol % by mode) are present throughout sample. The groundmass predominantly contains serpentine as large irregular masses up to 1mm (30 vol % by mode). Other groundmass phases include Cr-spinel/ilmenite (20-80 μm, 5 vol % by mode), calcite (30 vol % by mode), apatite, clinopyroxene and ilmenite. This pipe has been classified as a hypabyssal-facies calcite-rich phlogopite-kimberlite (Chalapathi Rao et al., 2004).

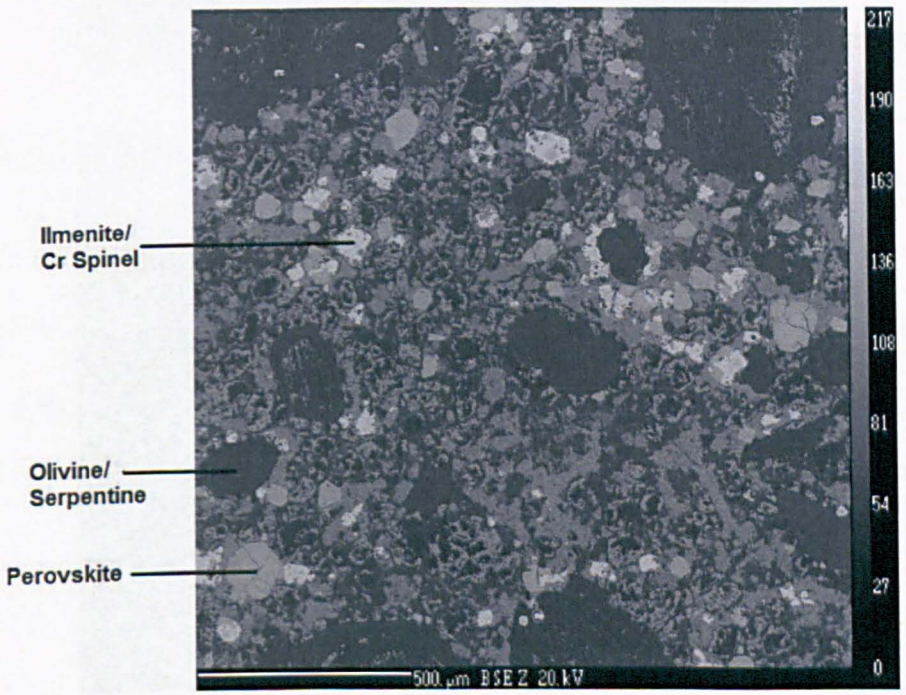

Figure 2.42: SEM image of MK5 sample.

2.7. Raichur Kimberlite Field

The Raichur Kimberlite Field includes ~15 kimberlites near the villages of Siddanpalli, Undraldoddi, Chagapuram and Wadegera. The RKF is located between the WKF and NKF close to the confluence of Krishna and Bhima rivers. The majority of the pipes are well

exposed and occur as hypabyssal facies dykes (Chalapathi Rao et al., 2009). Diamonds have been reported in the Wadegera pipes (Lynn, 2005). In this study samples have been collected from the Siddanpalle kimberlite cluster in the RKF.

2.7.1. Siddanpalle Kimberlite Cluster

The Siddanpalle cluster includes 3 kimberlites occurrences known as SK1, SK2 and SK3, which are emplaced within an area of 2.5 km^2. In this study samples from SK1, SK2 and SK3 were collected. SK1 (Fig. 2.43) is located 2 km NE of the Siddanpalle village and is the best exposed of the Siddanpalle body measuring about 100 m x 60 m. Crustal xenoliths are abundant and several carbonate xenoliths are visible, which are predominantly composed of crystalline calcite with minor chert (Chalapathi Rao et al. 2009).

Figure 2.43: Location of the SK1 kimberlite.

SK2 (Fig. 2.44) is located 1.7 km NE of the Siddanpalle village. It is reported to be a twin body measuring 100 m x 60 m with a satellite body measuring 10 m x 10 m. It appears more weathered than SK1 but also contains abundant granitic xenoliths and several carbonate

nodules. Limestone xenoliths have also been reported in this kimberlite, which have important geological implications for the regional geology of the area (Dongre et al., 2008).

Figure 2.44: Location of the SK2 kimberlite.

SK3 (Fig. 2.45) is located 1.2 km NE of Siddanpalle and measures about 25 m x 10 m. It is similar in appearance to SK1 and appears less weathered than SK2. It contains an abundance of granitic xenoliths and several carbonate xenoliths. The carbonate xenoliths in the three Siddanpalle kimberlites occur as irregular enclaves or as recrystallized rhombohedral crystals.

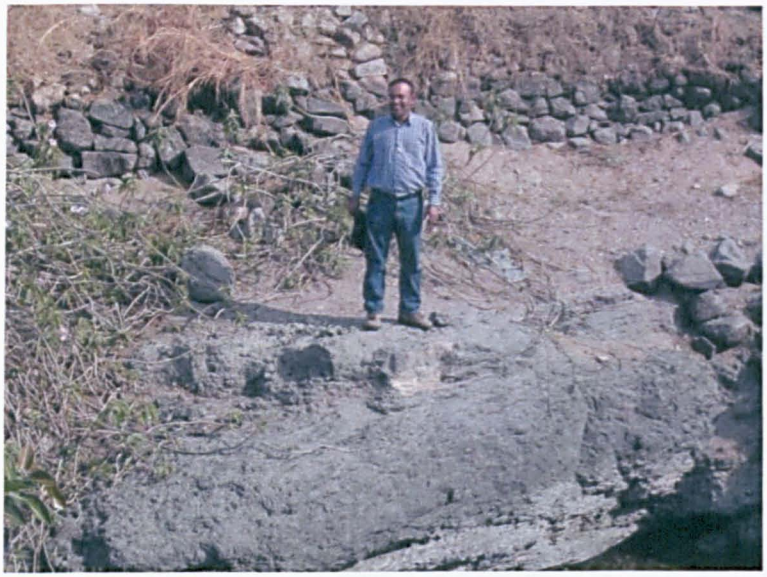

Figure 2.45: Location of the SK3 kimberlite.

In thin section the samples are porphyritic with large rounded macrocrysts (2-5mm, 5-10 vol % by mode) and euhedral microphenocrysts (0.1-0.8 mm, 15 vol % by mode) of olivine. The olivine is generally completely altered to serpentine leaving only pseudomorphs of the olivine (general degree of alteration: macrocrysts 80-100 % serpentinised; microphenocrysts 75-100 % serpentinised, 0-20 % carbonatised). Phlogopite is common as macrocryst (1-2 mm, 5 vol % by mode) and as microphenocrysts in the groundmass (200-300 μm, 5-10 vol % by mode), but is often strongly altered to chlorite (general degree of alteration: 50-100 %). Perovskite is pervasive throughout the samples (30-90 μm, 5-10 vol % by mode). Other groundmass phases include Cr spinel, calcite, serpentine, ilmenite and clinopyroxene. Pyrope garnet has also been reported in these rocks (Sridhar et al., 2007) but was not found in this study.

2.8. Krishna Lamproite Field

The Krishna Lamproite Field (KLF) is located at the north-eastern margin of the Cuddapah Basin (Fig. 6). It includes over 30 lamproite bodies, which occur as dykes and plugs. They

vary in size from 10-500 m x 1-20 m (Chalapathi Rao et al., 2008). They are not thought to be diamondiferous. (Chalapathi Rao et al., 2011).

The lamproites of the KLF contain varying modal proportions of phlogopite, clinopyroxene (diopside), amphibole, alkali feldspar, sphene, apatite, calcite, ilmenite and rutile. Chlorite, carbonate and quartz are also present as secondary phases in varying proportions. Olivine was probably present, identified by the shape of the grain, but appears to have been completely altered and is pseudomorphed by carbonate or secondary quartz (Chalapathi Rao et al., 2010).

The lamproites display heteromorphism, where a bulk-magma of similar composition can give rise to rock types of varied modal mineralogy and diverse petrographic aspects (Rock, 1991). The majority of the lamproites observed in this study appear porphyritic with uniformly distributed phenocrysts, predominantly phlogopite and pseudomorphs of what was once olivine. However, flow texture, pyroclastics (tuffistic) texture and equigranular texture has also been observed (Chalapathi Rao et al., 2010).

These lamproites have been classified as diopside lamproites (Ramannapeta, Vedadri South, Tirumalgiri), phlogopite lamproites (Pochampalle, Jayanthipuram) olivine lamproites (Nallabandlagudem, Vedadri North) (Chalapathi Rao et al., 2010).

2.8.1. Ramannapeta lamproite

The Ramannapeta lamproite (Rampet) is located 1 km south of the village of Ramannapeta in the Krishna valley. It contains crustal xenoliths (predominantly felsic) (Fig. 2.46).

Figure 2.46: Location of the Ramannapeta lamproite.

In thin section (Fig. 2.46) the lamproite contains phlogopite macrocrysts (2-4 mm, 5-10 vol % by mode) occurring as euhedral to subhedral elongated laths, as well as microphenocrysts (150-300 μm, 10-20 vol % by mode). The phlogopite is orange/brown in colour and shows strong pleochroism to pale yellow/colourless. The phlogopite show varying degrees of alteration to chlorite (general degree of alteration: 40-100 %). A few rare olivine macrocrysts (1-2 mm, <1 vol % by mode) and more microphenocrysts (100-250 μm, 2-3 vol % by mode) are present. Strongly pleochroic (pink to yellow) amphibole is present in the sample (200-300 μm, 2-3 vol % by mode), which has been reported to be a titanian potassic richterite (Chalapathi Rao et al., 2004). Clinopyroxene is abundant in the groundmass (100-300 μm, 10-20 vol % by mode). The other groundmass phases include serpentine (15 vol % by mode), carbonate (10-15 vol % by mode), titanite (75-150 μm, 10 vol % by mode) and Cr-spinel (35-90 μm, 2-4 vol % by mode). This rock has been classified as a diopside-lamproite (Chalapathi Rao et al., 2010).

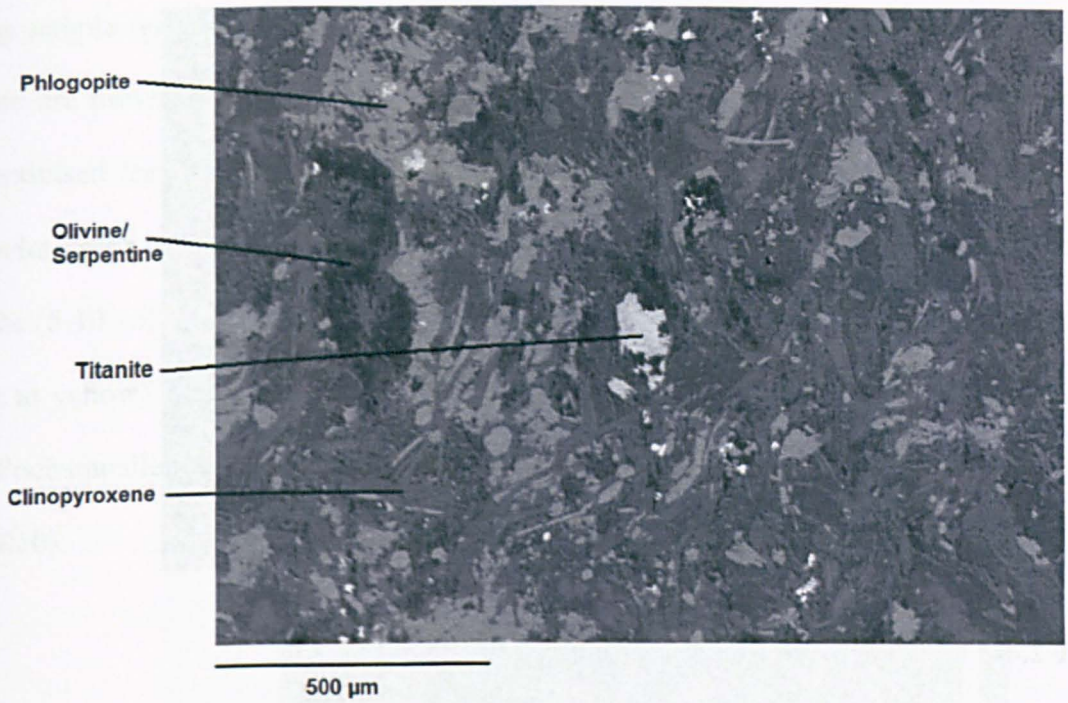

Figure 2.47: SEM image of the Ramannapeta lamproite.

2.8.2. Pochampalle lamproite

The Pochampalle lamproite is a NW-SE trending dyke, approximately 20 m in length, 1-2 m wide. It is located on a granitic hill, 2.5 km west of the Pochampalle village. In this study we collected two samples; one from the top of the hill (POC) (Fig. 2.48) and one from the bottom (POCg) (Fig.2.49). It appears a fresh, dark rock, but most noticeably is highly micaceous.

Figure 2.48: Location of the POC lamproite.

Figure 2.49: Location of the POCg lamproite

In thin section (Fig. 2.50) the Pochampalle lamproite is porphyritic with abundant phlogopite macrocrysts (1-6 mm, 25-30 vol % by mode). These are strongly pleochroic from brown/orange to pale yellow/colourless. Phlogopite is also abundant in the groundmass (100-300 μm, 25 vol % by mode). The sample POCg appears fresher and less altered than POC, particularly with regards to the phlogopite macrocrysts, which are less chloritised in the

POCg sample (general degree of alteration: POC 20-40 %; POCg 0-20 %). Phenocrysts of olivine are present (0.5-1.5 mm; 5-10 vol % by mode), but have mostly been completely serpentinised leaving only pseudomorphs (general degree of alteration: 80-100 %). Other groundmass phases include euhedral laths of apatite (150-500 μm, 10 vol % by mode), titanite (5-10 vol % by mode) and alkali feldspar (2-3 vol % by mode). Strongly pleochroic (pink to yellow) richterite is also present in the sample (100-200 μm, 1-2 vol % by mode). The Pochampalle lamproite has been classified as a phlogopite-lamproite (Chalapathi Rao et al., 2010).

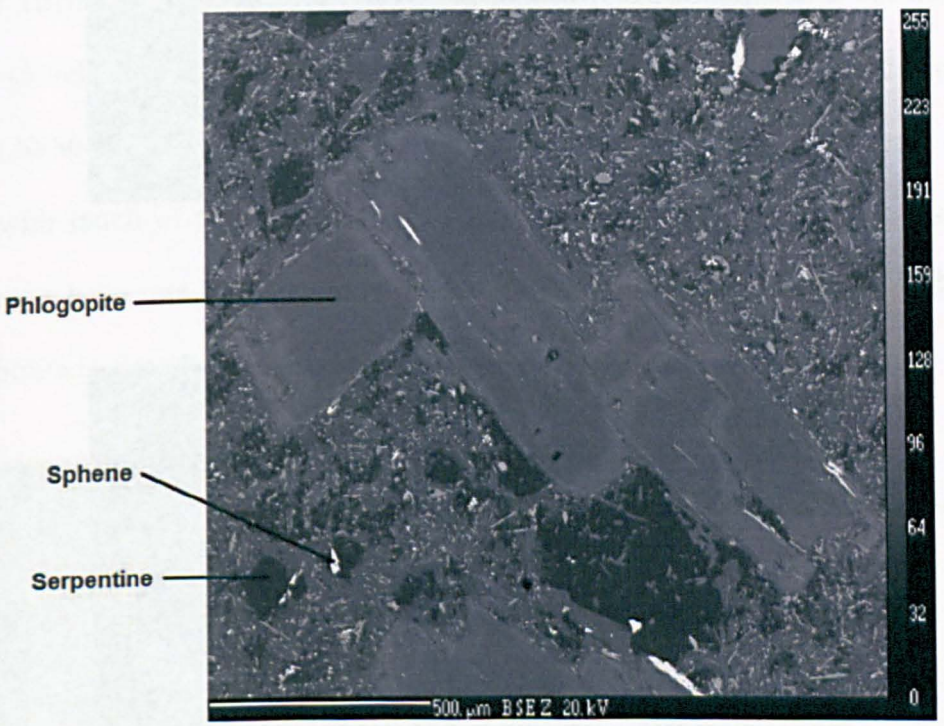

Figure 2.50: SEM image of POCg sample.

2.8.3. Vedadri lamproite

Two samples were collected from the Vedadri lamproite, known as Vedadri North (VedN) and Vedadri South (VedS). Vedadri North is located on a hilltop approximately 2.5 km NE of the Vedadri village (Fig. 2.51). It is a NW-SE trending dyke approximately 20 m long and

0.5-1 m wide. Vedadri South is located on a hilltop approximately 2 km east of the Vedadri village (Fig 2.52). It is a dyke striking E-W and is approximately 500 m long and 0.5-1 m wide.

Figure 2.51: Location of the VedN lamproite.

Figure 2.52: Location of the VedS lamproite.

In thin section (Fig. 2.53) the Vedadri lamproite is porphyritic with phlogopite phenocrysts (1-2 mm, 10-15 vol % by mode). Phlogopite microphenocrysts (200-500 μm, 15 vol % by

mode) are common in the groundmass. The phlogopite varies in alteration to chlorite (general degree of alteration: 20-60 %). Olivine phenocrysts are also present, but are more abundant in Vedadri North (Vedadri North: 100-500 µm, 20 vol % by mode; Vedadri South: 100-500 µm, 10 vol % by mode). The olivine has been extensively altered to silica, serpentine and calcite, leaving only pseudomorphs (general degree of alteration: silica 80-100 %, serpentine 10-20 %, calcite 10-20 %). Euhedral laths of clinopyroxene are abundant, but are more common in Vedadri South (Vedadri North: 100-500 µm, 20 vol % by mode; Vedadri South: 100-500 µm, 30-35 vol % by mode). Euhedral laths of apatite are present (100-300 µm, 5 vol % by mode). Amphibole (richterite) is strongly pleochroic from pink to yellow and occurs as platy aggregates (5 vol % by mode). Titanite is pervasive throughout the sample and occurs as an aggregate (20-80 µm, 5 vol % by mode). The sample appears to have undergone extensive alteration with much of the groundmass chlorite or carbonate (30 vol % by mode). The Vedadri South lamproite has been classified as a diopside-lamproite, whereas the Vedadri North lamproite is classified as a olivine lamproite (Chalapathi Rao et al., 2010).

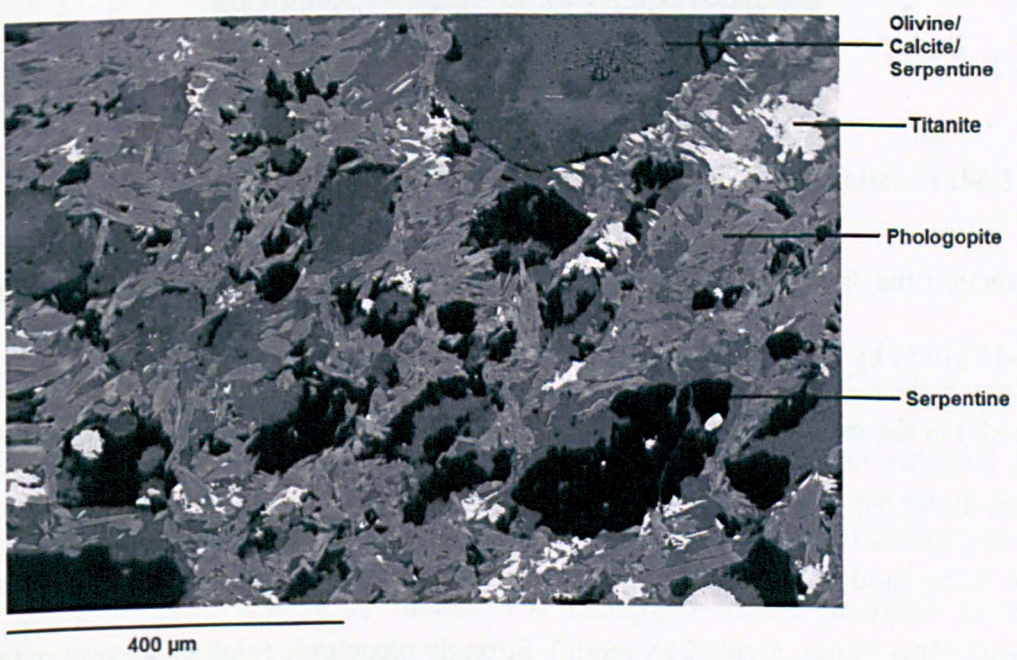

Figure 2.53: SEM image of VedN sample.

2.8.4. Jayanthipuram lamproite

The Jayanthipuram lamproite (JAY) is located on a granite hill 1.5 km east of the village Jayanthipuram. It is intruded into granitic rocks and lies parallel between 2 parallel dolerite dykes. It is associated with a small plug of vesicular and amygdaloidal lamproite (Chalapathi Rao et al., 2010). It is approximately 120 m in length and 0.3-0.5 m in width (Fig. 2.54).

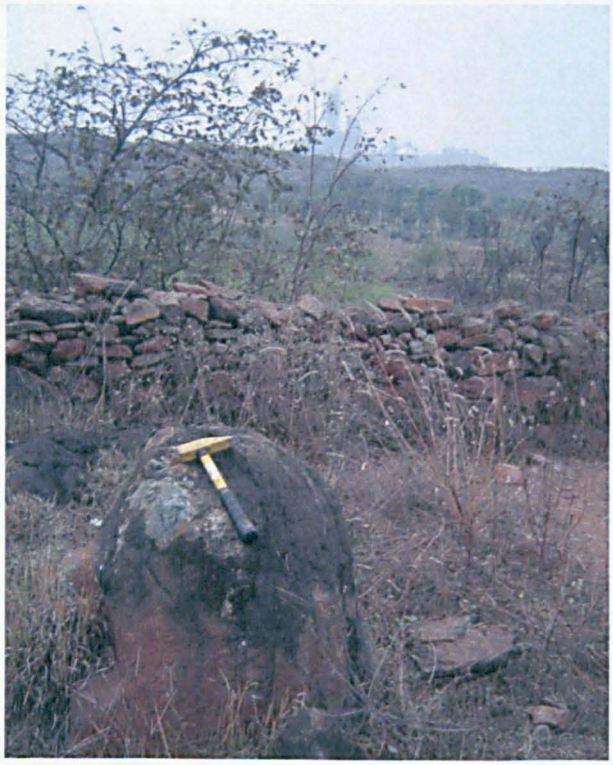

Figure 2.54: Location of the JAY lamproite.

In thin section the Jayanthipuram lamproite is porphyritic with phlogopite phenocrysts (1-3 mm, 10-15 vol % by mode). Phlogopite also occurs as microphenocrysts (100-250 μm, 15 vol % by mode) in the groundmass. The phlogopite is often altered to chlorite (general degree of alteration: 40-80 %). Titanite is pervasive throughout the sample as an aggregate (30-80 μm, 5-10 vol % by mode). Subhedral laths of alkali feldspar (sanidine) are also present in the groundmass (50-150 μm, 5 vol % by mode). Strongly pleochroic (pink to yellow) richterite is also present in the sample (100-250 μm, 1-2 vol % by mode). The sample appears to have

been extensively altered with abundant carbonate in the groundmass (30-45 vol % by mode). The Jayanthipuram lamproite has been classified as a phlogopite-lamproite (Chalapathi Rao et al., 2010).

2.8.5. Tirumalgiri lamproite

The Tirumalgiri lamproite (T1) is located on a granite hill 1-2 km north of the Tirumalgiri village. It is a dyke approximately 15-20 m in length and 0.5-1.5 m wide (Fig. 2.55).

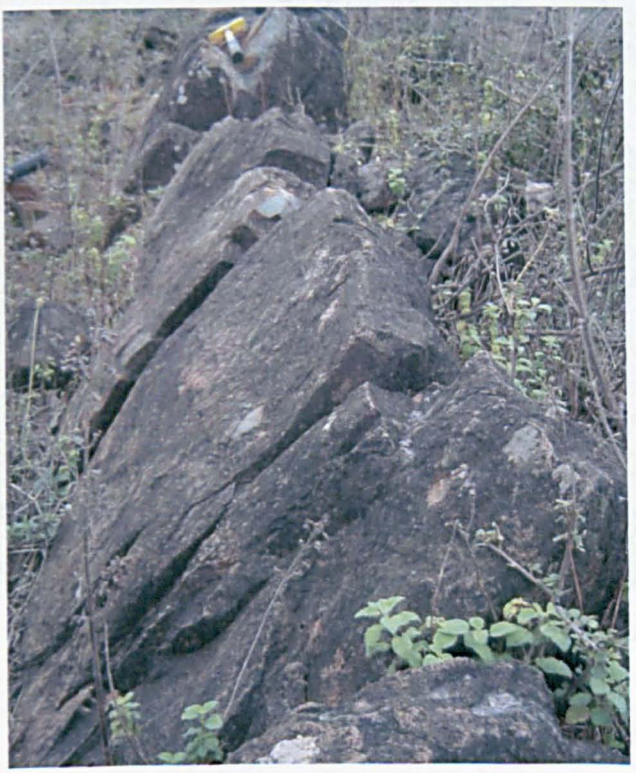

Figure 2.55: Location of the T1 lamproite.

In thin section (Fig. 2.56) the sample is porphyritic with abundant K-feldspar (sanidine) aggregates (100-350 μm, 15-20 vol % by mode). There are abundant euhedral laths of clinopyroxene (50-150 μm, 10 vol % by mode). Euhedral phenocrysts of phlogopite are also present (50-200 μm, 5 vol % by mode). The phlogopite shows moderate to complete alteration to chlorite (general degree of alteration: 40-100 %). Olivine pseudomorphs are present, which have been completely altered to silica (general degree of alteration: 100 %).

Other groundmass phases include titanite (20-40 μm, 1-3 vol % by mode) and apatite (10-30 μm, 1-3 vol % by mode). Strongly pleochroic (pink to yellow) richterite is also present in the sample (100-200 μm, 1-2 vol % by mode). Carbonate is abundant as irregular masses in the groundmass (10 vol % by mode). The Tirumalgiri lamproite has been classified as a diopside-lamproite (Chalapathi Rao et al., 2010).

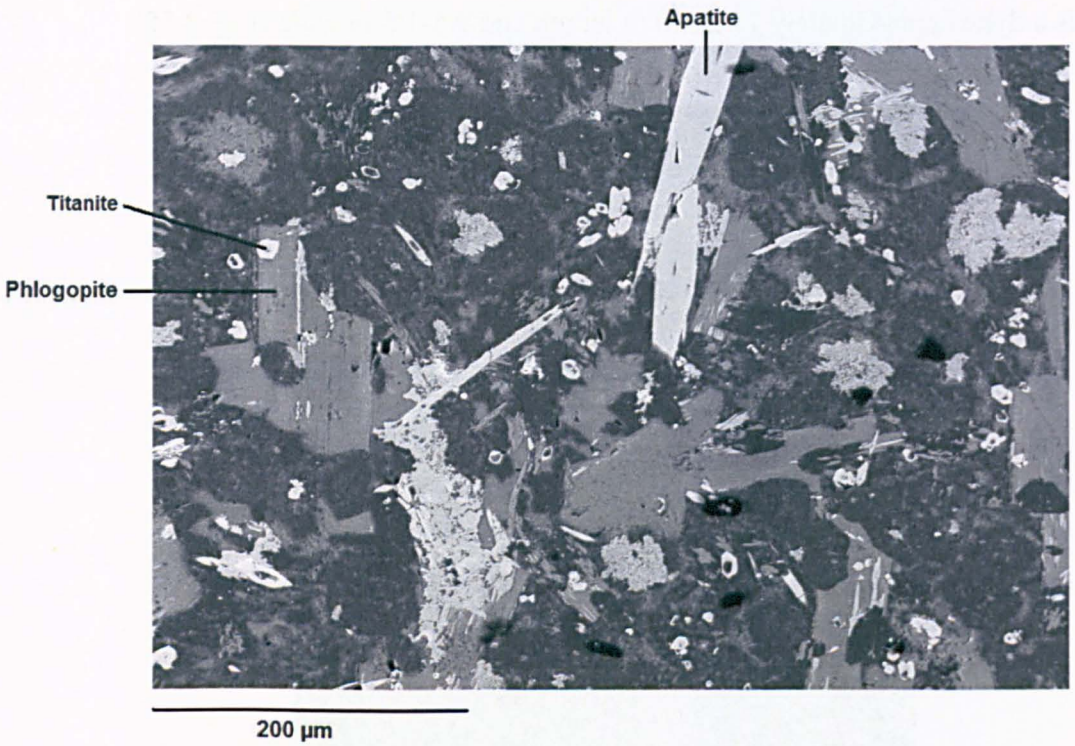

Figure 2.56: SEM image of T1 sample.

2.8.6. Nallabandlagudem lamproite

The Nallabandlagudem lamproite (Nalla) is located 700 m E-SE of the Nallabandlagudem village. It is a dyke approximately 600 m in length and 0.5-1 m wide (Fig. 2.57).

Figure 2.57: Location of the Nalla lamproite.

In thin section (Fig. 2.58) the Nallabandlagudem lamproite appears porphyritic. Olivine phenocrysts are common but are now pseudomorphs as have been completely altered to silica (100-200 μm, 10-15 vol % by mode). Phlogopite phenocrysts (1-2 mm, 5 vol % by mode) are present. Phlogopite also occurs as microphenocrysts (100-200 μm, 10 vol % by mode) in the groundmass. The phlogopite is often altered to chlorite (general degree of alteration: 60-80 %). Titanite is pervasive throughout the sample as an aggregate (40-90 μm, 5-10 vol % by mode). Other groundmass phases include apatite (15-40 μm, 1-3 vol % by mode) and richterite (100-250 μm, 1-2 vol % by mode). Carbonate is abundant as irregular masses in the groundmass (10 vol % by mode). Perovskite is also a minor phase (10-50 μm, 1-2 vol % by mode). The Nallabandlagudem lamproite has been classified as an olivine lamproite (Chalapathi Rao et al., 2009).

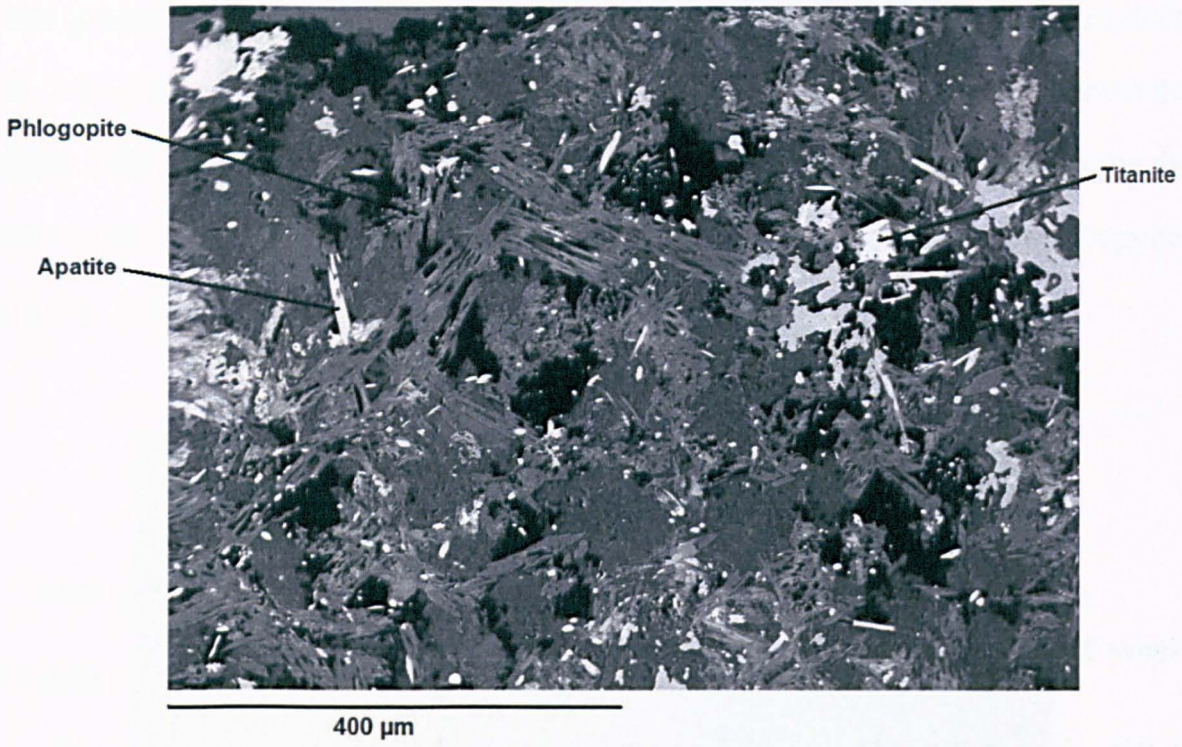

Figure 2.58: SEM image of Nalla sample.

2.8.7. Reddikunta lamproite

The Reddikunta lamproite (RED) is located approximately 2 km south-east of the Nallabandlagudem village. It is intruded into granites and gneisses (Fig. 2.59).

Figure 2.59: Location of the RED lamproite.

In thin section the Reddikunta lamproite is porphyritic with abundant euhedral laths of clinopyroxene (40-120 μm, 10 % modal) and K-feldspar (sanidine) aggregates (100-300 μm, 10 % modal). Phenocrysts of phlogopite are also present (50-150 μm, 5 % modal). The phlogopite is shows moderate to complete alteration to chlorite (General degree of alteration: 50-100 %). Olivine pseudomorphs are present (200-400 μm, 5 % modal), which have been completely altered to silica (general degree of alteration: 100 %). Groundmass phases include titanite (30-50 μm, 2-3 % modal) and apatite (15-45 μm, 2-4 % modal). Strongly pleochroic (pink to yellow) richterite is also present in the sample (80-150 μm, 1-2 % modal). Carbonate is abundant as irregular masses in the groundmass (15 % modal). Minor leucite is also present (30-80 μm, 1-2 %).

The Reddikunta lamproite has not been classified, but appears to show mineralogy similar to those classified as diopside-lamproites.

2.8.8. Ramapuram lamproite

The Ramapuram lamproite (Ramapu) is located close to the Reddikunta lamproite. It is intruded into granites and gneisses (Fig. 2.60)..

Figure 2.60: Location of the Ramapuram lamproite.

In thin section the Ramapuram lamproite is porphyritic with abundant euhedral laths of clinopyroxene (50-140 μm, 15 vol % by mode) and phenocrysts of phlogopite (800-130 μm, 5-10 vol % by mode). The phlogopite is shows high to complete alteration to chlorite (general degree of alteration: 70-100 %). K-feldspar (sanidine) aggregates are also present (80-260 μm, 5 vol % by mode). Olivine pseudomorphs are present (100-200 μm, 5 vol % by mode), which have been completely altered to silica (general degree of alteration: 100 %). Groundmass phases include titanite (40-80 μm, 2-4 vol % by mode) and apatite (20-70 μm, 2-5 vol % by mode). Richterite is also present in the sample (100-250 μm, 1-2 vol % by mode). Carbonate is abundant as irregular masses in the groundmass (20 vol % by mode). The Ramapuram lamproite has not been classified, but appears to show mineralogy similar to those classified as diopside-lamproites.

2.9. Cuddapah Basin Lamproites

The Cuddapah Basin Lamproites Field includes two clusters which intrude the Cuddapah Basin sediments at Chelima and Zangamarajupalle. These vary in width from 1-5 m. They are considered to be diamondiferous (Chalapathi Rao et al., 2007). The petrographic information is given here on the Chelima lamproite as samples from Zangamarajupalle were not collected in this study. However, a striking similarity between the 2 lamproites in the CBL has been noted by earlier workers (Sreeramachandra Rao, 1988).

2.9.1. Chelima lamproite

The Chelima lamproite (CHE) is located near the centre of the Cuddapah intra-cratonic basin, 1 km south of the Chelima village. It consists of lamproite dykes approximately 1-5 m wide, intruded into slates and phyllites (Fig. 2.61, Fig.2.62). The lamproite dykes have been extensively mined since antiquity but are yet to have their diamond potential assessed by modern day techniques (Chalapathi Rao et al., 2004).

Figure 2.61: Location of the Chelima lamproite.

Figure 2.62: Location of the Chelima lamproite.

In thin-section (Fig. 2.63) the Chelima lamproite shows a porphyritic texture. Olivine macrocrysts (500-800 μm, 2-4 vol % by mode) and phenocrysts (200-400 μm, 15 vol % by mode) are completely altered and replaced by calcite and less often serpentine (general degree of alteration: 100 %). It contains abundant phlogopite phenocrysts (0.5-1 mm, 10-15 vol % by mode). The phlogopite has moderate alteration to chlorite and calcite (general degree of alteration: 20-40 %). Groundmass phases include rutile, ilmenite, Cr-spinel, apatite, chlorite, serpentine, talc and titanite. Amphibole is absent unlike the majority of KLF samples.

The Chelima lamproite has been previously classified as a minette, lamprophyre, carbonatite-kimberlite and lamproite (Bergman, 1987; Scott-Smith, 1989), however, its current accepted classification is as a lamproite (Chalapathi Rao et al., 2004). It is most similar to those classified as phlogopite-lamproites.

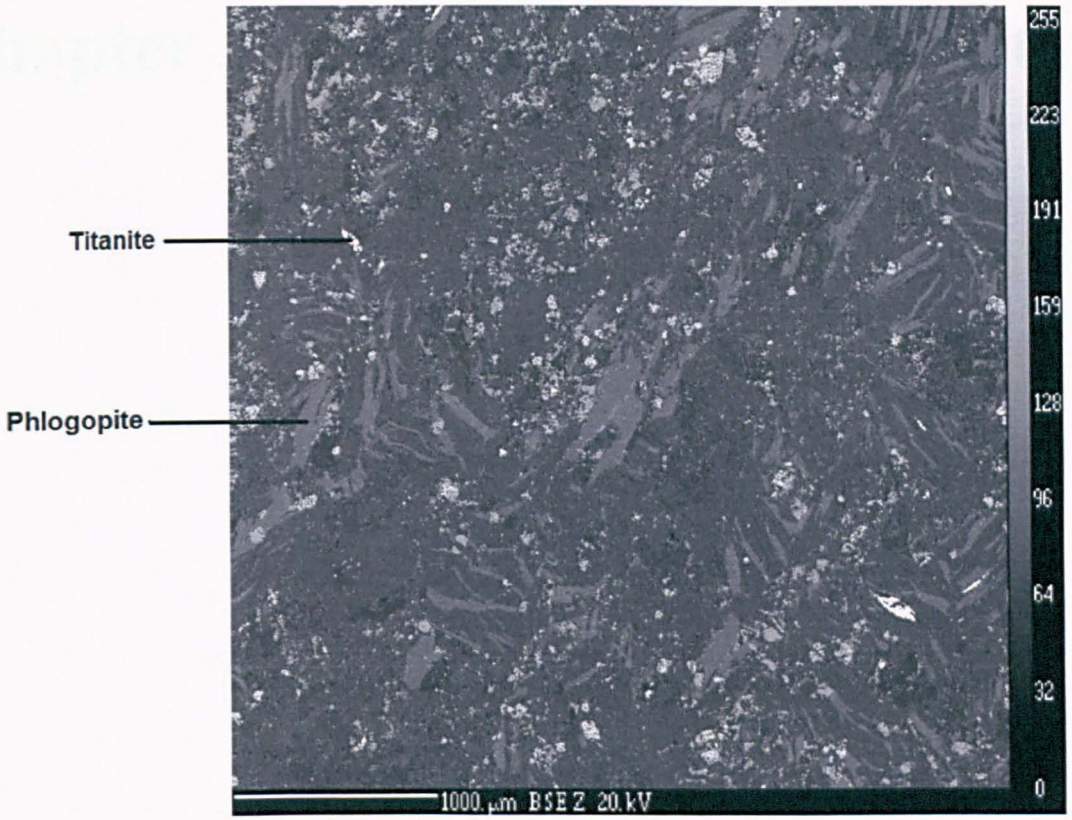

Figure 2.63: SEM image of Chelima sample.

Chapter 3: Bulk-Rock Geochemistry

3.1. Introduction

The bulk-rock major-, trace-, REE- and Nd-isotopic compositions of the southern Indian kimberlites and lamproites were measured to confirm their classification, evaluate their petrogenesis and also to understand possible deep subcontinental mantle processes involved in the generation of the partial melts of kimberlites and lamproites during the Proterozoic. In addition, major- and trace-element data on the kimberlite and lamproite suite also helped in the identification of contaminated samples, using a range of contamination indices employed in current literature.

Several previous investigations have measured the major- and trace-element compositions of kimberlites and lamproites from the Dharwar Craton. Some examples of recent studies of the EDC kimberlites include Paton et al. (2009), Chalapathi Rao and Srivastava (2009), Chalapathi Rao et al. (2004), Paul et al. (2006) and Haggerty and Birkett (2004). Examples of studies of the EDC lamproites include Chakrabarti et al. (2007), Paul et al. (2007), Chalapathi Rao et al. (2010) and Reddy et al. (2003).

This chapter presents data for 27 kimberlites and 11 lamproites from the EDC in southern India. The kimberlites are located in three fields: 6 from the Narayanpet Kimberlite Field (NKF), 18 from the Wajrakarur Kimberlite Field (WKF) and 3 from the Raichur Kimberlite Field (RKF). The lamproites are located in two fields: 10 in the Krishna lamproites field (KLF) and one (Chelima) from the Cuddapah Basin Lamproite Field (CLF).

3.2. Contamination

Many kimberlites contain a diverse assemblage of entrained mantle and crustal fragments, and are usually subject to extensive post-emplacement alteration (Berg and Allsopp, 1972; Mitchell, 1986). Hence, there is considerable uncertainty regarding whether measured bulk-

rock analyses have been affected by processes such as contamination and alteration, or instead preserve a true record of kimberlite magma variability (Paton et al., 2007). Considering the Proterozoic ages of the rocks in this study, any interpretation of geochemical data must first consider the potential effect of these processes on the samples.

In most cases, where significant exposures of kimberlites and lamproites existed, samples were collected from near the centre of the exposure, after breaking a large (10-20 kg) block. This procedure ensured collection of samples visibly free of any surficial alteration, with fresh looking mica grains under a hand lens.

Clement (1982) introduced a method of assessing contamination in kimberlites, where the oxides SiO_2, Al_2O_3, and Na_2O are used because they are characteristically elevated in weathered and crustally contaminated kimberlites (Fairbairn and Robertson, 1966). The contamination index (CI) is a measure of the proportions of clay minerals and tectosilicates relative to ferromagnesian minerals, e.g. olivine, phlogopite. It is used to identify alteration in samples analysed in this study, where a CI value of < 1.5 is considered uncontaminated for kimberlites (Mitchell, 1986).

$$CI = (SiO_2 + Al_2O_3 + Na_2O) / (MgO + K_2O)$$

Loss on ignition (LOI) is also used as a proxy for alteration (Chalapathi Rao et al., 2004). Samples with high LOI (> 15 %) are considered indicative of secondary alteration, commonly manifested in thin sections through increased abundances of secondary carbonate minerals and talc.

Gd/Lu ratios of samples were also considered, where low values are indicative of HREE-enriched crustal contaminants (Le Roex et al., 2003). Samples with a Gd/Lu ratio < 58 were considered contaminated (Paton et al., 2009).

The Ilmenite Index of Taylor et al. (1994) is also used in this study to identify kimberlites and lamproites that may have accumulated or assimilated ilmenite megacrysts and xenocrysts. This index was developed by Taylor et al. (1994) as it can prove difficult to remove abundant ilmenite xenocrysts entirely from samples. In this study the mineral perovskite was separated from crushed samples for analysis and an assessment of ilmenite contamination was useful when selecting samples for mineral separation to avoid excessive problems when removing ilmenite. This is because ilmenite has density and magnetic properties similar to perovskite, potentially compromising the magnetic and density separation techniques used to separate perovskite from sieved bulk-rock crushates.

$$\text{Ilm.I.} = (FeO_t + TiO_2) / (2K_2O + MgO)$$

Samples with an ilmenite index > 0.52 for kimberlites and > 0.47 for lamproites were considered contaminated with ilmenite (Taylor et al., 1994).

Table 3.1a: Summary of contamination indices for kimberlite and lamproites from EDC.

Sample	Contamination Index (C.I)	Loss On Ignitions (% wt loss)	Ilmenite Index	Gd/Lu	
WKF					
Lat 3	1.06	12.78	0.27	64.31	
Lat4	1.20	8.69	0.29	59.66	
Mul5	1.34	6.24	0.59	74.50	
Tumm	1.19	8.62	0.67	80.64	
KL2	**2.75**	**28.12**	1.07	87.99	X
KL1	**2.94**	**27.55**	0.65	52.80	X
KL3	1.10	12.87	0.59	89.18	
CC2	1.35	6.34	0.40	75.34	
CC1	1.20	4.87	0.40	77.62	
CC5	0.98	17.99	0.41	102.86	
CC4	0.98	13.36	0.37	105.58	
Waj1	**2.41**	5.42	0.46	87.81	X
Waj2	1.69	5.09	0.54	65.36	
Waj2N	1.46	11.45	0.68	82.97	
Chin12	1.43	7.69	0.44	102.13	
TK4	1.77	**24.16**	0.43	131.32	X
TK0	**3.27**	6.10	0.48	52.72	X
TK3	**3.32**	15.41	1.47	75.09	X

Sample	Contamination Index (C.I)	Loss On Ignitions (% wt loss)	Ilmenite Index	Gd/Lu	
RKF					
SK1	0.95	16.56	0.43	102.05	
SK2	1.94	**33.73**	0.71	16.14	X
SK3	1.05	16.36	0.36	104.03	

Sample	Contamination Index (C.I)	Loss On Ignitions (% wt loss)	Ilmenite Index	Gd/Lu	
NKF					
NK1	1.19	7.24	0.54	94.89	
NK2	1.32	7.62	0.47	78.87	
KK6	1.45	4.65	0.53	65.41	
KK1	1.17	8.96	0.54	92.96	
MK1	1.62	4.86	0.69	65.12	
MK5	1.34	9.12	0.67	86.48	

Sample	Contamination Index (C.I)	Loss On Ignitions (% wt loss)	Ilmenite Index	Gd/Lu	
Lamproites					
Chelima	1.42	**25.06**	0.57	153.33	
Ramman	3.87	4.49	0.85	65.04	
Poc	5.09	3.91	1.23	92.69	
PocG	4.41	3.40	0.62	74.44	
VedN	3.79	5.96	0.93	66.15	
VedS	4.57	5.87	1.40	89.66	
Jay	4.30	5.36	1.18	71.20	
T1	9.23	6.66	1.56	85.35	
Nalla	4.60	5.64	1.09	66.81	
Red	4.35	2.90	0.92	69.39	
Ramapu	5.51	3.55	1.34	50.09	

Table 3.1b: Guidelines for assessing alteration/contamination in this study.

Contamination Index (C.I)	Loss On Ignitions (% wt loss)	Ilmenite Index	Gd/Lu
Kimberlites			
Uncontaminated (< 1.4)	% Wt loss < 15	**Kimberlite**	Uncontaminated > 58
		> 0.52 contaminated	
Moderate Contamination (1.4-2)	% Wt loss 15-20		Contaminated < 58
		Lamproite	
High contamination (> 2)	**% Wt loss > 20**	> 0.47 contaminated	

Kimberlites were considered contaminated and therefore unsuitable for inclusion in an overall analysis of the data if they had a high contamination index (> 2), or a moderate contamination index (1.4-2) coupled with a high LOI (> 20%). Therefore, KL2, KL1, WAJ1, TKO, TK3, TK4 and SK2 were all considered contaminated (marked **X** in right-hand column of Table 3.1a). In the field these samples visibly showed signs of contamination and alteration. Samples KL2, KL1, TKO, TK3 and TK4 all appeared to be more weathered and altered than other samples in this study (Fig. 3.1a-b).

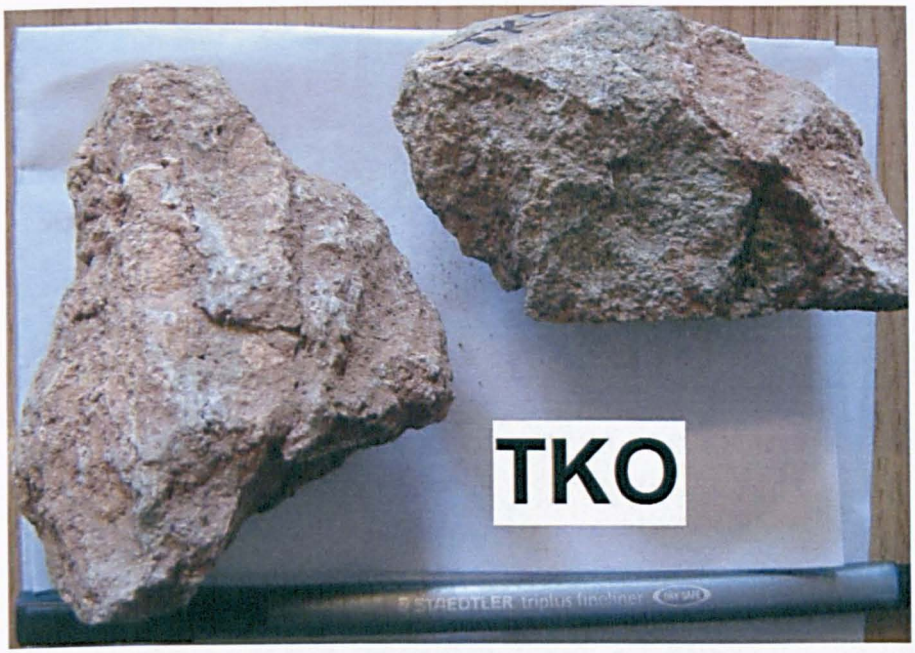

a)

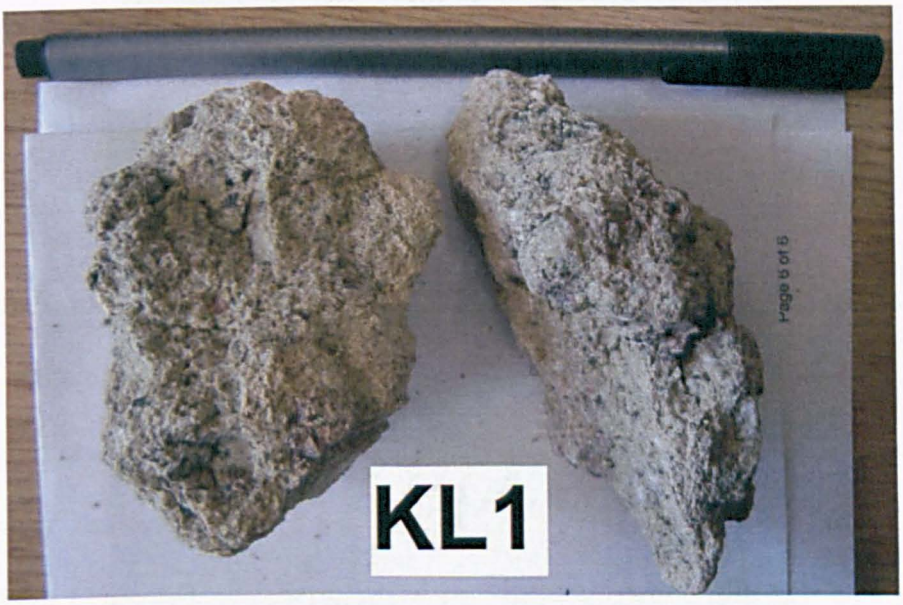

b)

Figure 3.1. Hand-specimens of the TKO kimberlite (a) and KL1 kimberlite (b). The pen is 16.5 cm long.

WAJ1 contained a high abundance of crustal xenoliths and SK2 contained a large number of calcite nodules and limestone xenoliths (Fig. 3.2a-c).

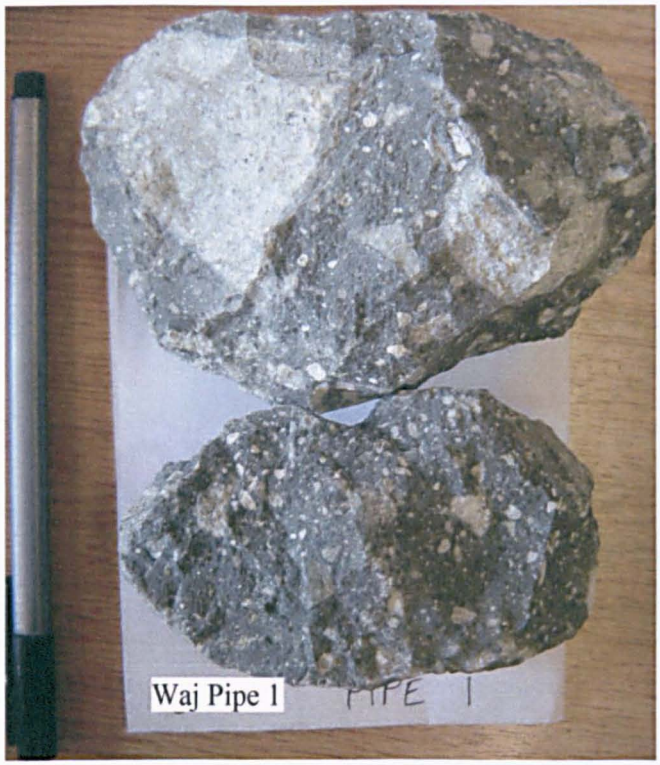

a)

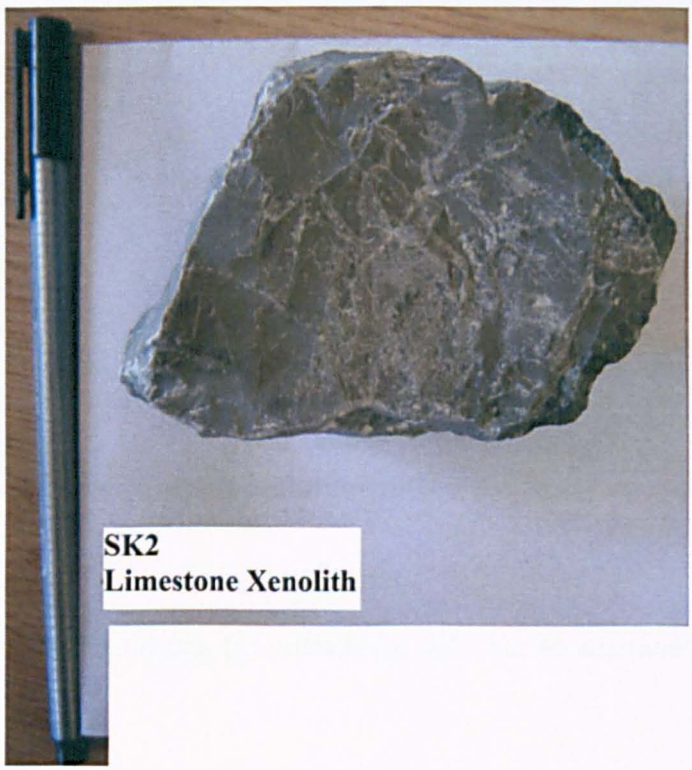

b)

c)

Figure 3.2. Hand-specimens of the Waj1 kimberlite (a), the limestone xenolith found in the SK2 kimberlite (b) and the SK2 kimberlite (c).

The lamproites all showed high CI values, which by kimberlite standards would be considered contaminated. However, this is not unusual for such mica-rich rocks (e.g. Chalapathi Rao et al., 2004). Therefore, lamproite samples were not ruled out based on their CI values alone, as such values might just reflect high mica content. However, samples showing a high LOI value (% wt loss > 20) in conjunction with a high CI (> 2) may be considered to reflect contamination. The majority of lamproites in this study do not show high LOI, except for the Chelima lamproite, but conversely it has the lowest CI. Therefore all the lamproites were included in this study.

The Gd/Lu ratio highlighted four samples that could be considered to have HREE-enriched crustal contaminants. Three kimberlites (KL1, TKO and SK2) were already considered

contaminated on the basis of their CI and LOI, and so were excluded from this study. However, although the Ramapuram lamproite has a low Gd/Lu ratio, it does not show excessively high CI for a lamproite and has low LOI. Therefore, Ramapuram was cautiously retained in this study, subject to careful scrutiny of any subsequent anomalous geochemical data.

The ilmenite index was only employed in this study to help decide which of the kimberlites would undergo mineral separation techniques to isolate perovskite. However, although samples with high ilmenite index were avoided where possible, sample selection was predominantly focused on samples with larger percentages of perovskite.

3.3. Major-Element Chemistry

(Description of analytical techniques and instrumentation used for major element analysis are described in appendices A1.2.1 and A1.2.2)

Major-element abundances are variable and few correlations exist between these elements in the EDC kimberlites and lamproites. Figure 3.3 illustrates the lack of correlation among the major-element oxides but also highlights the differences between kimberlites and lamproites. In general, the NKF and WKF have similar major-element chemistry, with the WKF having a greater overall variability in elemental abundances.

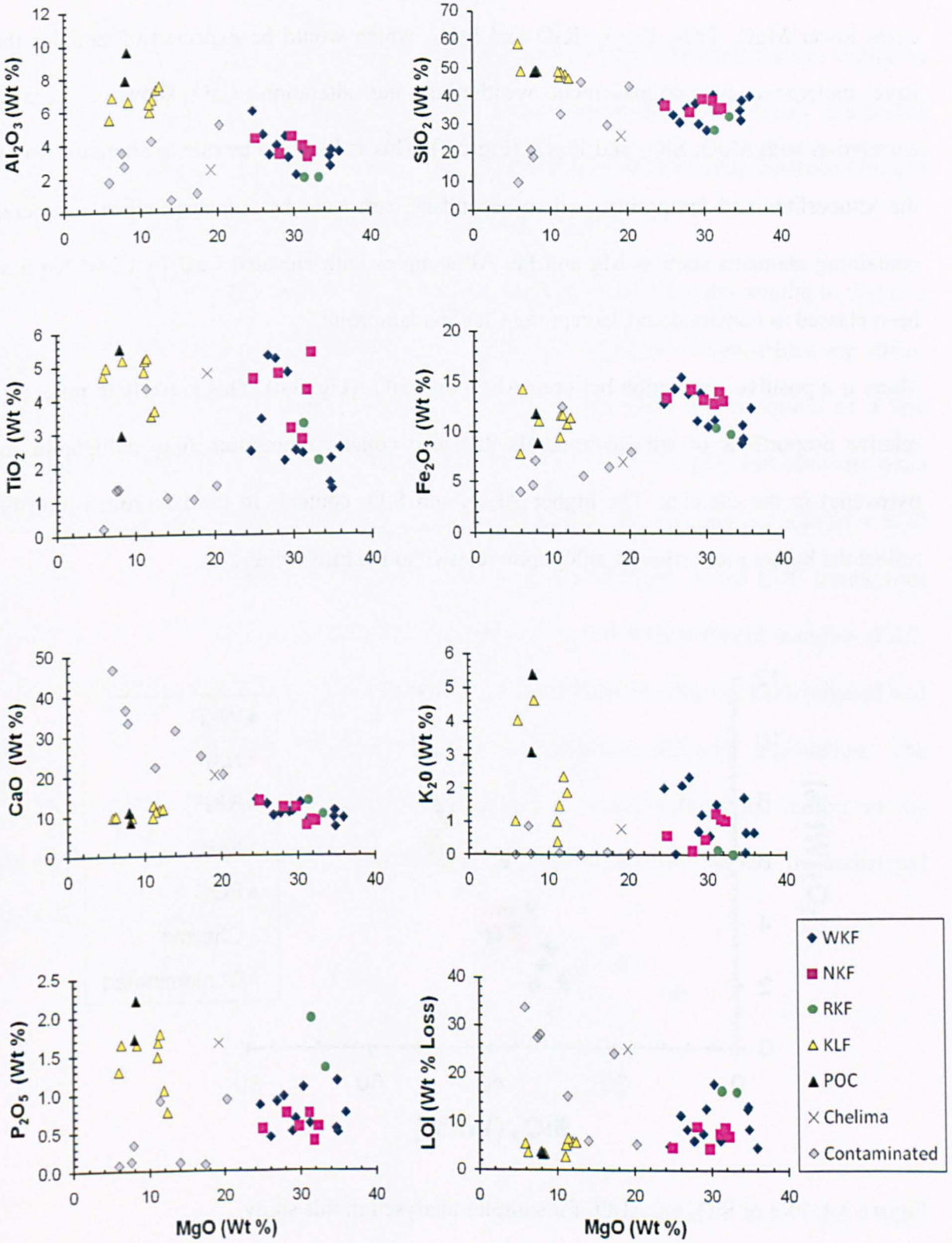

Figure 3.3. Major-element oxides vs. MgO (wt. %) in samples analysed in this study. Coloured symbols represent uncontaminated samples; grey symbols represent contaminated samples.

The samples identified as contaminated (Section 3.2) generally have lower silica and in most cases lower MgO, TiO_2, Fe_2O_3, K_2O and P_2O_5, which would be expected of samples that have undergone post-emplacement weathering and alteration. CaO shows a negative correlation with MgO, SiO_2 and Fe_2O_3 (Fig 2.3). This is likely to be due to alteration within the kimberlites and lamproites, where secondary carbonate has replaced silicate minerals containing elements such as Mg and Fe. All samples with elevated CaO (> 17 wt %) have been classed as contaminated, except the Chelima lamproite.

There is a positive correlation between Al_2O_3 and SiO_2 (Fig. 3.4). This is likely to reflect the relative proportions of silicate minerals that also contain aluminium (e.g. phlogopite and pyroxene) in the samples. The higher Al_2O_3 and SiO_2 contents in the lamproites probably reflect the higher proportion of phlogopite relative to the kimberlites.

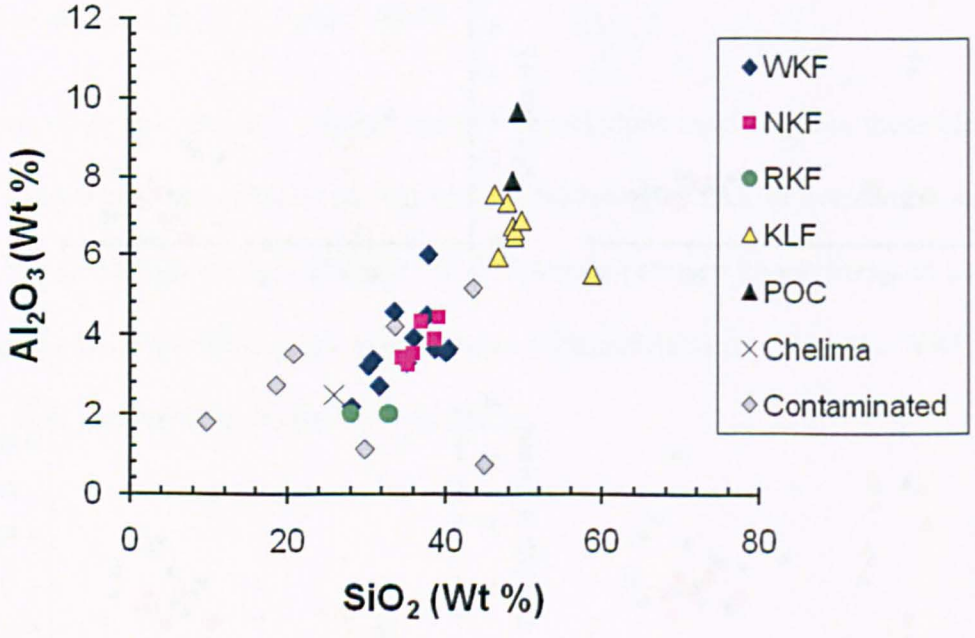

Figure 3.4. Plot of SiO_2 vs. Al_2O_3 for samples analysed in this study.

3.3.1. Kimberlites

Recent studies have revealed that although the majority of the EDC kimberlites are similar to the Group I kimberlites of southern Africa in terms of petrology, geochemistry and Sr-Nd isotope systematic, others show traits of Group II kimberlites or an overlap between Group I and Group II kimberlites (Chalapathi Rao and Srivastava, 2009).

The EDC kimberlites analysed in this study show major element chemistry similar to that of a typical kimberlite as described by Mitchell (1995). The majority of kimberlites are silica-undersaturated (< 41wt %) and ultramafic (> 12 % MgO), with the exception of a few samples (KL2, KL1, TK3 and SK2) that are not ultramafic (< 12 % MgO), but have also been shown to be contaminated (Section 3.2). Typical kimberlites are also potassic and have K_2O exceeding Na_2O abundances (K_2O/Na_2O values > 1). The majority of the EDC kimberlites are potassic (Table 3.2), again with the exception of a few contaminated samples (KL2, WAJ1, TKO, TK3, SK2). The SK3 kimberlite is not potassic but also not contaminated and therefore the geochemistry of this sample may require a different explanation. The peralkaline (molar $Na_2O+K_2O)/Al_2O_3$) and perpotassic (molar K_2O/Al_2O_3) indices of the kimberlites of the EDC are all < 1 (Table 3.2.), similar to those shown by archetypal kimberlite (≤ 1; Mitchell, 1995).

Table 3.2: Mg#, peralkaline and perpotassic indices of the uncontaminated EDC kimberlites

WKF	K_2O/Na_2O	K_2O/Al_2O_3	Molar Na_2O+K_20/Al_2O_3	Mg#
Lat 3	18.40	0.52	0.55	90
Lat 4	2.50	0.18	0.26	89
Mul5	6.90	0.60	0.69	82
Tumm	9.04	0.62	0.69	79
KL3	15.66	0.38	0.40	82
CC2	5.45	0.42	0.49	86
CC1	2.34	0.19	0.27	86
CC5	21.75	0.26	0.27	86
CC4	2.68	0.03	0.04	88
Waj2	1.89	0.34	0.51	81
Waj2N	2.46	0.01	0.01	80
Chin12	3.99	0.16	0.20	85

NKF	K_2O/Na_2O	K_2O/Al_2O_3	Molar Na_2O+K_20/Al_2O_3	Mg#
NK1	18.40	0.29	0.30	84
NK2	11.67	0.32	0.34	84
KK6	4.16	0.10	0.13	83
KK1	50.28	0.33	0.34	83
MK1	2.65	0.13	0.18	80
MK5	6.60	0.04	0.04	81

RKF	K_2O/Na_2O	K_2O/Al_2O_3	Molar Na_2O+K_20/Al_2O_3	Mg#
SK1	9.17	0.07	0.08	87
SK3	0.11	0.00	0.01	88

Mg# ((Mg/Mg+Fe)*100) values of the EDC kimberlites (excluding contaminated samples) are high (79-90) and show the mafic-ultramafic nature of the samples (Table 3.2). These values are similar to those reported in previous studies of the EDC kimberlites (72-83; Chalapathi Rao et al., 2008). The EDC kimberlites show a decrease in TiO_2 with increasing Mg# (Fig.3.5), which suggests fractionation of parental magma (Chalapathi Rao et al., 2008). On a plot of Mg# against TiO_2 (Fig. 235), all of the EDC kimberlites considered uncontaminated lie within the field of Group I kimberlites from South Africa.

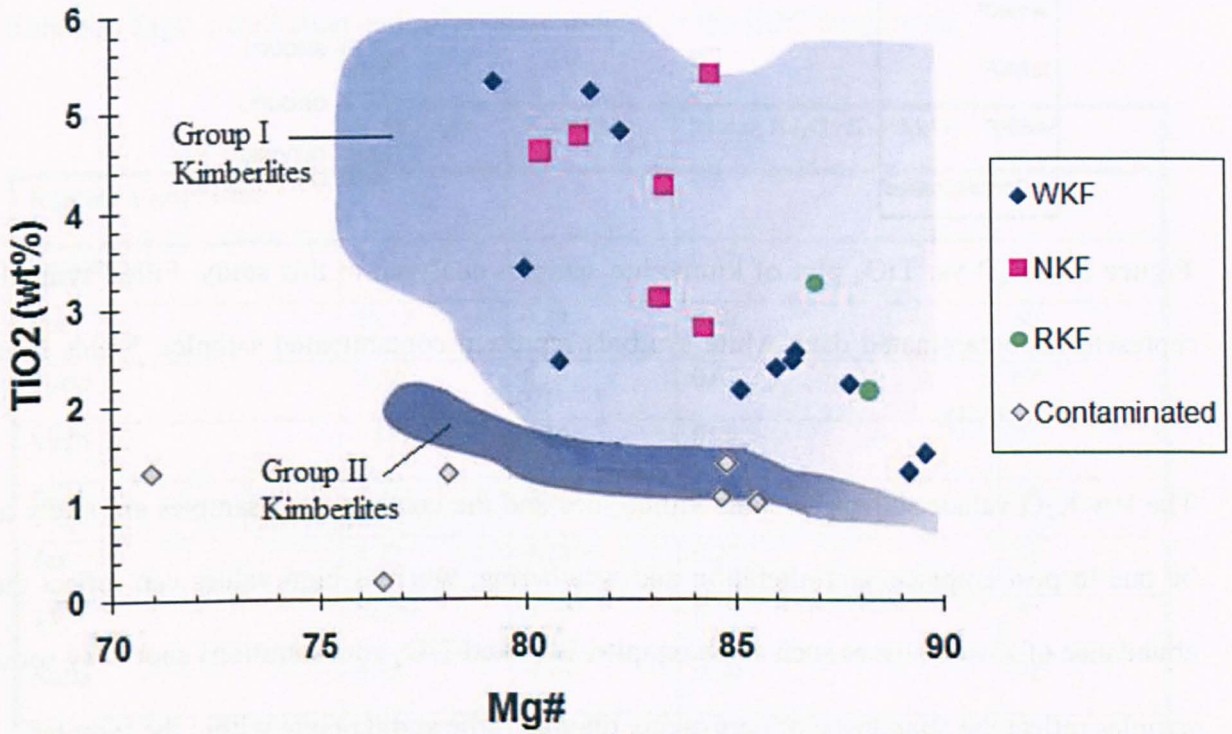

Figure 3.5. Plot of Mg# vs. TiO_2 for kimberlite data analysed in this study. Typical Group I and II kimberlite fields from South Africa shown are taken from Chalapathi Rao et al. (2009).

A plot of K_2O against TiO_2 was devised by Taylor et al. (1994) specifically to distinguish between Group I kimberlites and other ultramafic rocks (Fig 3.6). The southern Indian kimberlites lay in and around the southern African Group I kimberlite field with some samples dispersed around its margins.

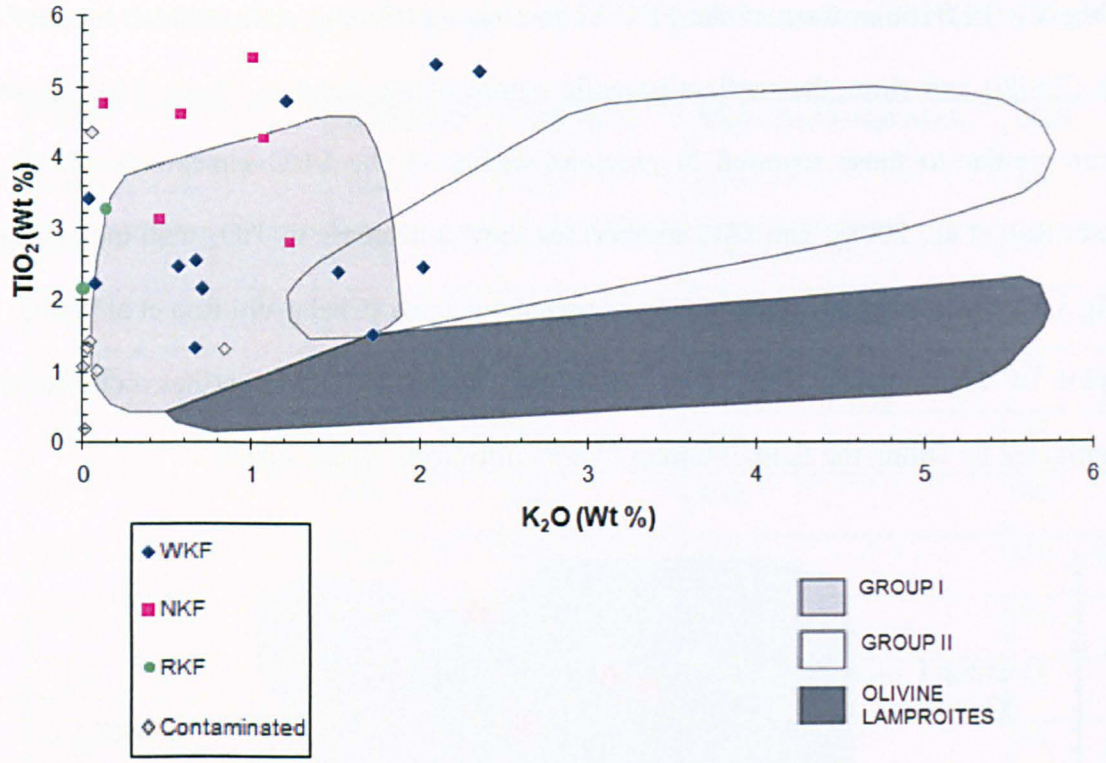

Figure 3.6. K_2O vs. TiO_2 plot of kimberlite samples analysed in this study. Filled symbols represent uncontaminated data; white symbols represent contaminated samples. Fields from Taylor et al. (1994).

The low K_2O values shown by some kimberlites and the contaminated samples are likely to be due to post-emplacement alteration and weathering, whereas high values can reflect the abundance of K rich phases such as phlogopite. Elevated TiO_2 concentrations shown by some samples reflect the abundance of perovskite, titanite, rutile and ilmenite within the samples.

It would seem that based on major-element chemistry the EDC kimberlites show a close affinity with typical Group I kimberlites from South Africa.

3.3.2. Lamproites

Relative to the kimberlites in the EDC, the lamproites show higher average abundances of K, Si, Ti and Al, but lower Ca, Mg, and Fe as would be expected. A typical lamproite is ultrapotassic (K_2O/Na_2O values > 3), peralkaline $(Na_2O+K_2O)/Al_2O_3$ > 1) and perpotassic

(K_2O/Al_2O_3 values > 1) (Mitchell and Bergman, 1991). All the lamproites in the EDC can be considered ultrapotassic, with Chelima and Pochampalle displaying significantly higher values (Table 3.3). However, the lamproites of the EDC all have peralkaline and perpotassic indices < 1, indicating they are neither peralkaline nor perpotassic (Table 3.3). This was also found in the study by Chalapathi Rao et al. (2010) who attribute these low values to the effects of low degree hydrothermal alteration and the resulting carbonation and silicification of the EDC lamproites.

Table 3.3: Mg#, peralkaline and perpotassic indices of the EDC lamproites.

	K_2O/Na_2O	K_2O/Al_2O_3	Molar Na_2O+K_20/Al_2O_3	Mg#
Krishna Lamproites				
Ramman	7.41	0.32	0.37	71
Poc	45.12	0.39	0.40	60
PocG	5.22	0.56	0.67	67
VedN	7.18	0.25	0.28	71
VedS	3.01	0.07	0.09	68
Jay	4.73	0.22	0.27	68
T1	28.90	0.19	0.19	63
Nalla	4.05	0.16	0.20	72
Red	4.83	0.70	0.85	62
Ramapu	20.46	0.59	0.62	49
Cuddapah Lamproites	K_2O/Na_2O	K_2O/Al_2O_3	Molar Na_2O+K_20/Al_2O_3	Mg#
Chelima	60.90	0.31	0.32	86

The KLF lamproites show lower Mg# values than the EDC kimberlites, with the Ramapuram lamproite at a significantly lower value, suggesting a more evolved nature (Table 3.3). This

data is similar to previously published Mg# data for the EDC lamproites (59-73, Paul et al., 2007; 56-73, Chalapathi Rao et al., 2010). The Mg# highlights the ultramafic nature of the lamproites and is similar to those of primary magmas equilibrated with a peridotitic mantle source (Chalapathi Rao et al., 2008).

The major-element chemistry of the EDC lamproites show many characteristics of worldwide lamproites. However, on a plot devised by Taylor et al. (1994) designed specifically to distinguish between Group I kimberlites and other ultramafic rocks (Fig 3.7), the EDC lamproites predominantly lie outside the olivine lamproite field having elevated TiO_2 concentrations.

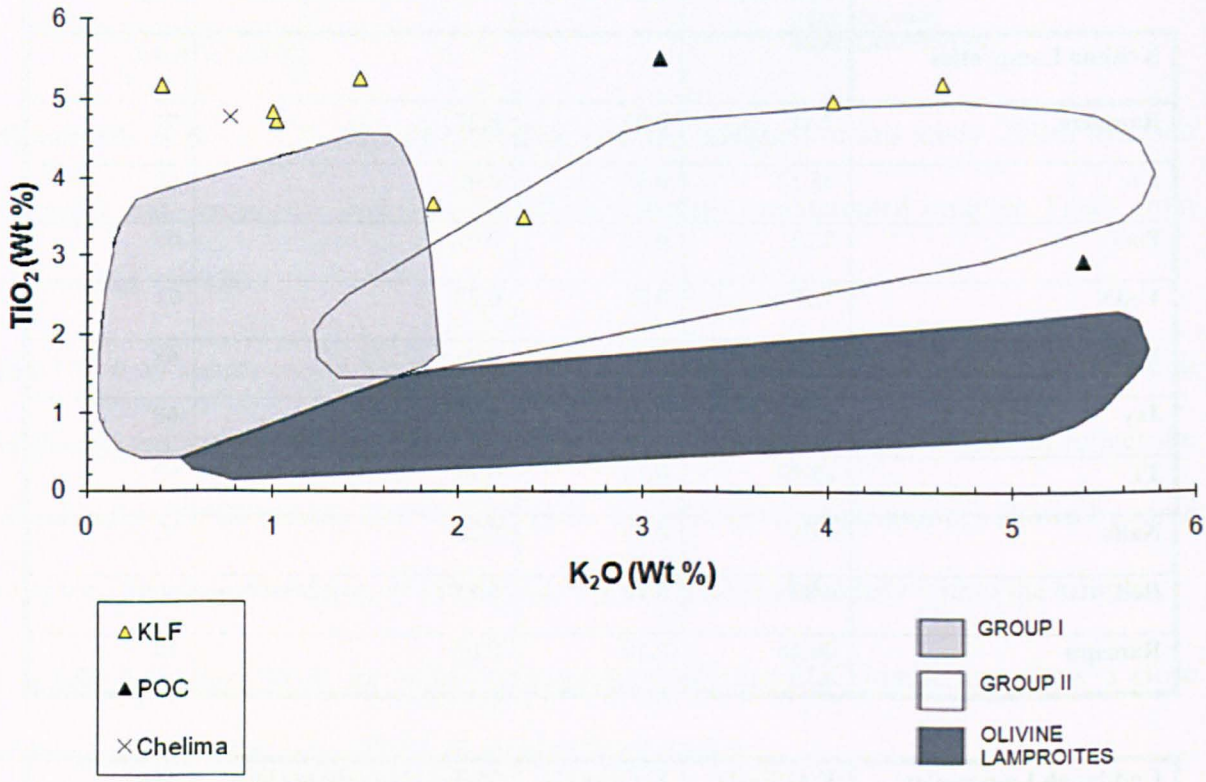

Figure 3.7. K_2O vs. TiO_2 plot of lamproite samples analysed in this study. Fields from Taylor et al. (1994).

Mitchell and Bergman (1991) suggest that a typical lamproite can contain higher TiO_2 (1-7 wt %) than shown on figure 3.7. If the lamproite field from Taylor et al. (1994) were

extended to show this greater TiO_2 range, all the EDC lamproites would fall within this extended lamproite field. The enriched TiO_2 concentrations of the EDC lamproites have been suggested to reflect the abundance of titanite, rutile and ilmenite within the samples (Chalapathi Rao et al., 2010).

The Chelima lamproite has significantly different major element chemistry from that of the lamproites located in the KLF. Chelima has a significantly higher Mg# (Table 3.2), MgO and CaO contents than the KLF samples, but lower SiO_2, Al_2O_3, and Fe_2O_3 (Fig.3.3). K_2O is towards the lower range of the KLF samples, which is surprising given that there is a high modal proportion of phlogopite in the Chelima lamproite relative to many of the KLF lamproites that would be expected to result in higher K_2O and Al_2O_3 values; for example Pochampalle has high modal phlogopite content and the highest Al_2O and K_2O contents (Fig 3.8).

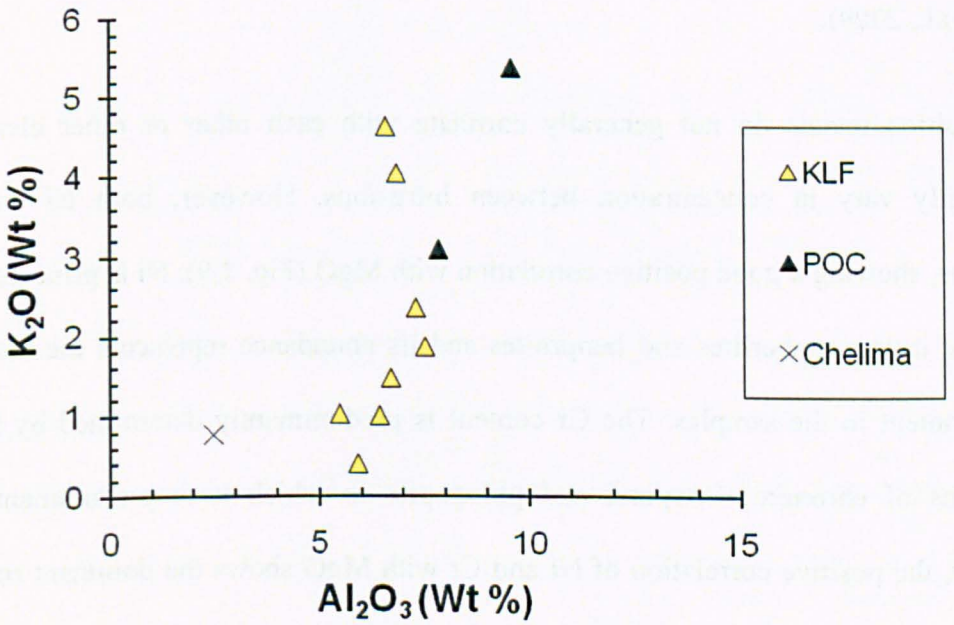

Figure 3.8. A plot of Al_2O_3 vs. K_2O for the EDC lamproite samples.

The differences between the major element chemistry of Chelima and the KLF lamproites may be due to post emplacement weathering and alteration of the Chelima lamproite. Significant secondary alteration is visible in the Chelima sample in thin section and Chelima also has a much higher LOI than the lamproites of the KLF, suggesting increased carbonate alteration.

3.4. Trace Element Chemistry

(Description of analytical techniques and instrumentation used for trace-element analysis are described in appendix A1.2.1 and A1.2.2)

Incompatible pairs such as K-Rb and Zr-Hf (Fig. 3.9), which should behave coherently, show good positive correlations in the EDC kimberlites and lamproites. The compositional range of the large-ion lithophile elements (LILE) can be extreme in many cases. This is attributed to the effects of post-emplacement alteration processes on the abundances of these elements. (Paton et al., 2009).

The transition metals do not generally correlate with each other or other elements and significantly vary in concentration between intrusions. However, both Ni and Cr are exceptions, showing a good positive correlation with MgO (Fig. 3.9). Ni is principally hosted by olivine in the kimberlites and lamproites and its abundance represents the macrocrystal olivine content in the samples. The Cr content is predominantly determined by the modal proportions of chromite, Cr-spinel and phlogopite in which it is predominantly found. Therefore, the positive correlation of Ni and Cr with MgO shows the dominant role of Mg-rich phases in their distribution.

The high-field strength elements (HFSE) vary in behaviour. For example, Zr and Hf correlate strongly with each other (Fig. 3.9) but both display a weak negative correlation with Ni and

MgO and no correlation with other HFSE. The HFSE also vary in behaviour with the REEs. Zr shows a weak positive correlation with La, but Nb shows no correlation with La. (Fig. 3.9). The LILE also vary in behaviour with the REEs and Th having a strong positive correlation with La, while Rb shows no correlation (Fig. 3.9).

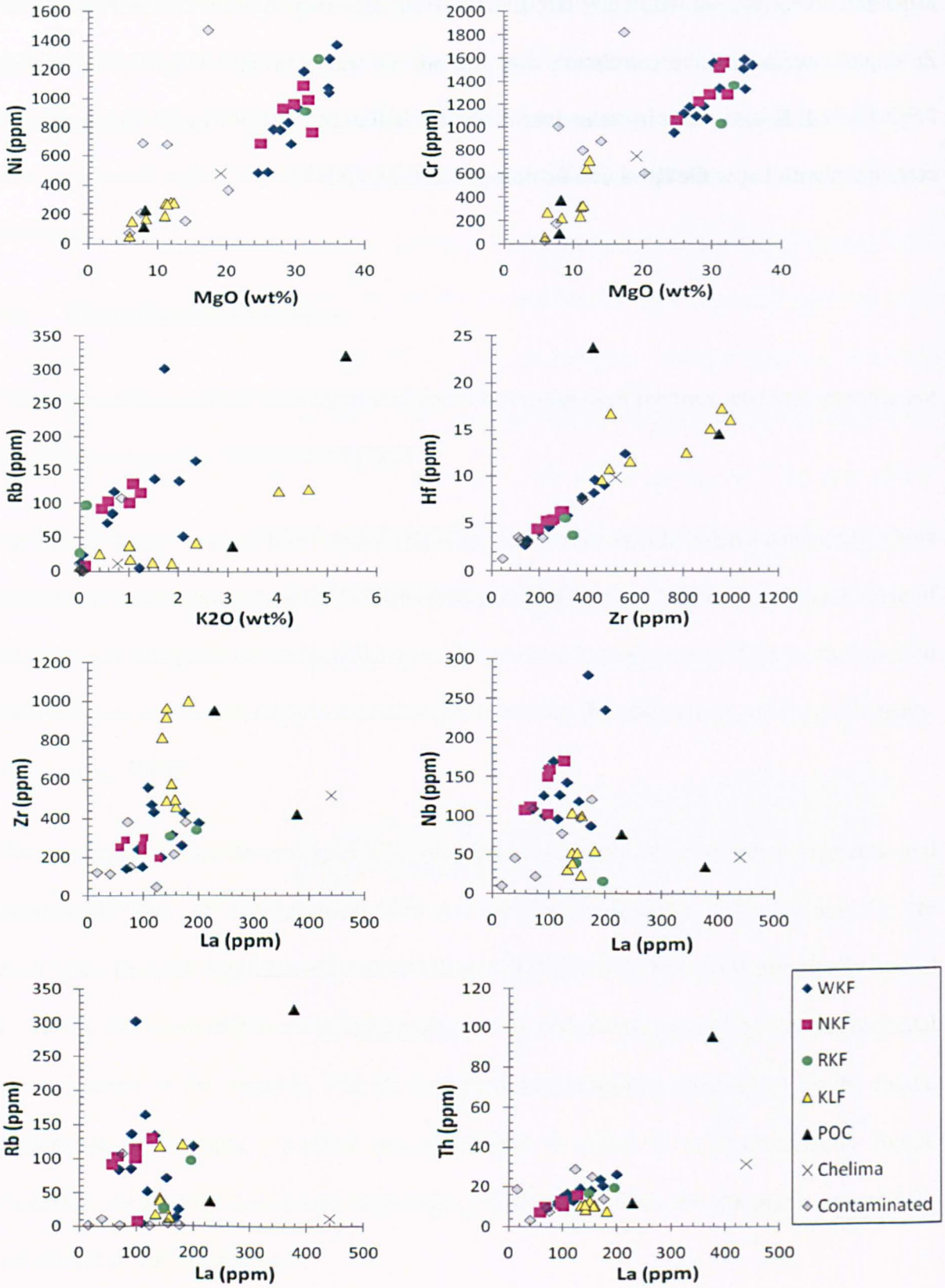

Figure 3.9. Trace element plots of samples analysed in this study.

3.4.1. Kimberlites

Archetypal kimberlites typically have high concentrations of the transition metals Ni (> 400 ppm), Cr (> 1000 ppm), and Co (> 150 ppm) (Mitchell, 1986). The majority of kimberlites in this study show typical Ni concentrations (486-1473 ppm). However, some of the samples thought to be contaminated show lower values, including KL1 (208 ppm), WAJ1 (366 ppm), TKO (154 ppm) and SK2 (74 ppm). The kimberlites show typical Cr abundances (1007-1818 ppm), again with the exception of some of the contaminated samples, including KL1 (179 ppm), WAJ1 (600 ppm), TKO (877 ppm), TK3 (796 ppm) and SK2 (31 ppm).

The kimberlites of the EDC show lower concentrations of Co than expected for a typical Group I kimberlite (79-108 ppm), with the samples classified as contaminated showing even lower concentrations (17-65 ppm). V, Cr, Co and Ni are hosted by phlogopite, chromite, diopside and olivine in kimberlites and lamproite (Reddy et al., 2003). These minerals show a high degree of alteration in most samples (particularly phlogopite and olivine), which may have resulted in the lower elemental concentrations, implying either depletion of these trace elements in the bulk rock, and/or dilution by other elements. The EDC kimberlites also show high Sc contents, which probably reflect the high modal phlogopite and/or clinopyroxene content seen in these samples, since these are the main Sc-bearing minerals in kimberlites (Mitchell and Bergman, 1991).

Zr and Nb are considered to be the least mobile incompatible elements during hydrothermal alteration, and are also relatively unaffected by small amounts of crustal contamination (Price et al., 2000). On a plot of Zr against Nb (Fig. 3.10) the majority of EDC kimberlites fall within the Group I kimberlite field of South Africa, with two samples falling just outside.

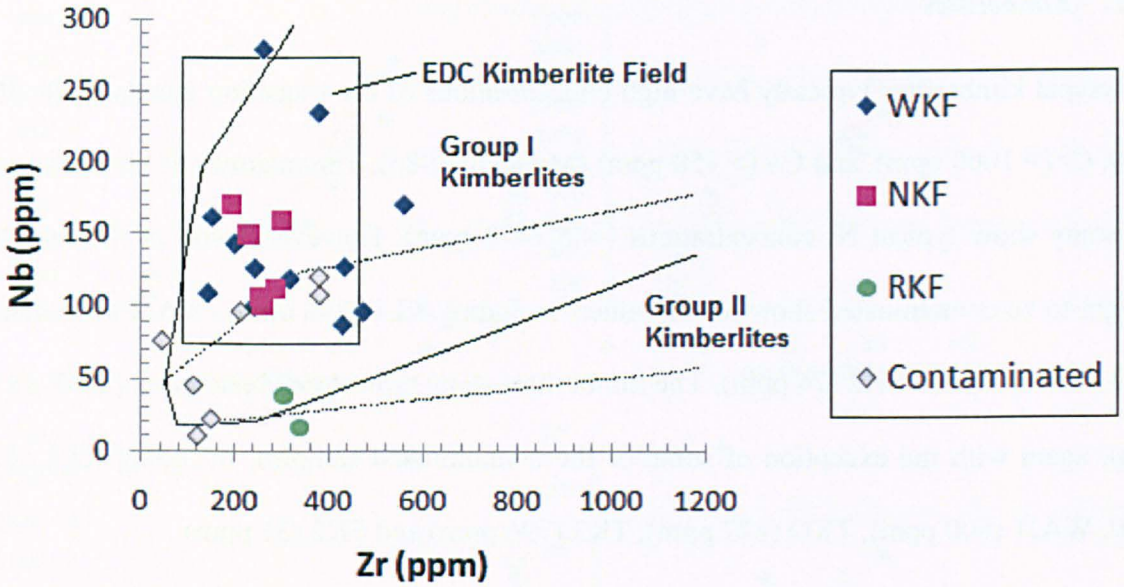

Figure 3.10. Plot of Nb against Zr for kimberlite samples analysed in this study. The EDC kimberlite field is from Chalapathi Rao et al. (2004) and the other fields are from Caro et al. (2004).

On a primitive mantle-normalized, multi-element 'spidergram' plot (Fig.3.11), the EDC kimberlites show enrichments relative to primitive mantle. However, strong negative anomalies can be seen for K and Sr. Ti and Hf also show low to moderate depletion.

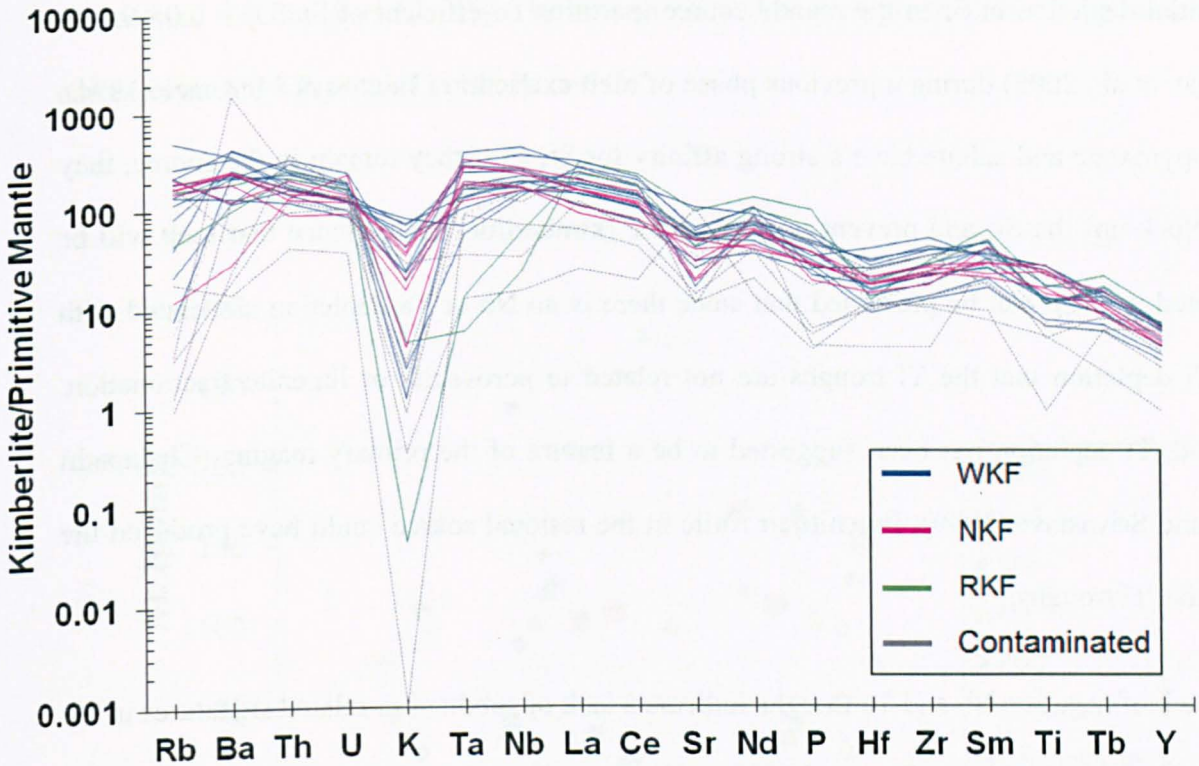

Figure 3.11 Primitive mantle-normalized (McDonough & Sun, 1995) multi-element patterns of the EDC kimberlites.

Negative K, Sr and Ti depletions have also been reported in Group I kimberlites from southern Africa (e.g. Harris and Le Roex, 2004) and Brazil (e.g. Gibson et al., 1995). As these negative anomalies are also independent of Mg#, it has been suggested that fractional crystallisation is unlikely to be responsible and they are related to the mantle source (Chalapathi Rao and Srivastava, 2009).

The K anomalies have been interpreted to be primary features of kimberlite source regions (Le Roex et al., 2003) and are most likely the result of alteration. A small Sr depletion is common in kimberlites and lamproites worldwide (Chalapathi rao et al., 2004) and can be attributed either to the presence of residual clinopyroxene (Smith et al., 1985), residual phosphate (Mitchell, 1995) or residual calcite (Keshav et al., 2005) in the mantle source, or to

an initial depletion in Sr in the mantle source (partition co-efficient of Sr (D) = 0.05-0.066; Keshav et al., 2005) during a previous phase of melt extraction (Tainton & McKenzie 1994). Clinopyroxene and calcite have a strong affinity for Sr, so if they remain in the source, they will 'lock up' the Sr, and prevent it entering the (kimberlitic) melt. Hence that melt will be depleted in Sr. It can be presumed that since there is no Nb or Ta depletion associated with the Ti depletion that the Ti troughs are not related to perovskite or ilmenite fractionation. Instead, Ti depletion has been suggested to be a feature of the primary magma (Chalapathi Rao and Srivastava, 2009); ilmenite or rutile in the residual source could have produced the negative Ti troughs.

The lack of negative Nb and Ta troughs indicate a lack of subduction-related signatures in the kimberlite source regions (Coe at al., 2008). However, it can be seen that the 2 samples from the RKF (SK1 and SK3) do show Ta and Nb abundances much lower than that of the rest of the kimberlites. This could be attributed to the large amount of carbonate and crustal material seen in these samples in hand specimen and thin-section.

A strong negative P trough has also been reported for kimberlite samples from the EDC (Chalapathi Rao and Srivastava, 2009). This has been attributed to a residual phosphate-bearing phase such as apatite (Chalapathi Rao and Srivastava, 2009) or the presence of a complex K-Ba-P-rich metasomatic mineral phase (Mitchell, 1995). However, a negative P anomaly was not found in this study.

It has been reported that the geochemical characteristics of kimberlites are directly related to the presence and amount of the minerals of metasomatic phlogopite-ilmenite assemblages (Lapin et al., 2007). Rocks that are almost free of ilmenite have shown anomalously low

contents of Ti, but also Nb, Zr, Th, U, and Ce, whereas high ilmenite contents usually correspond with enrichment in Nb, Zr and Ce.

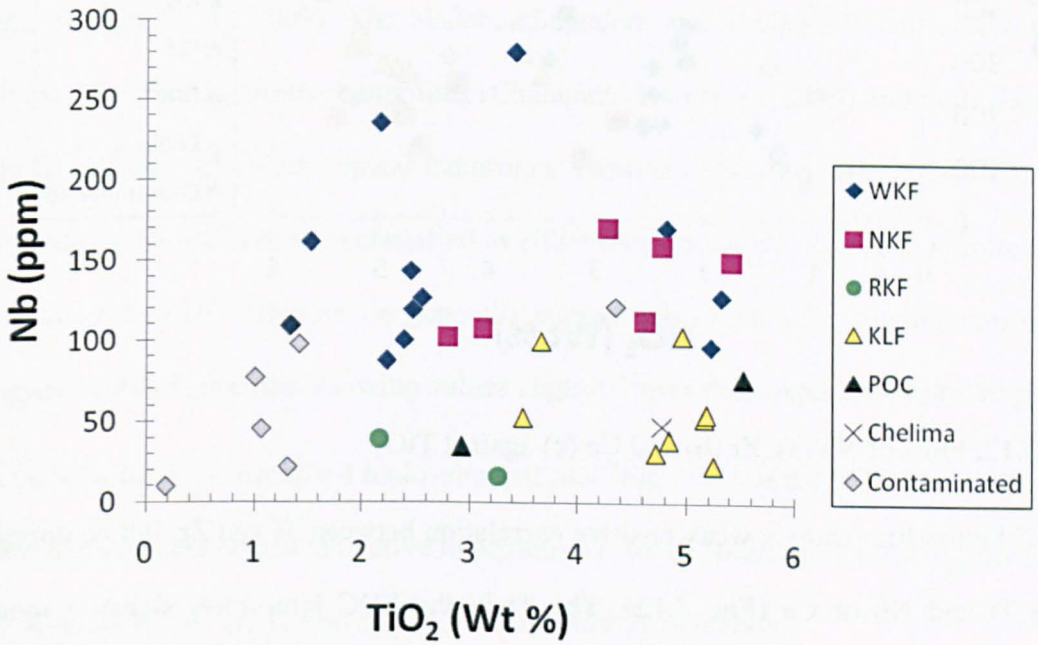

a)

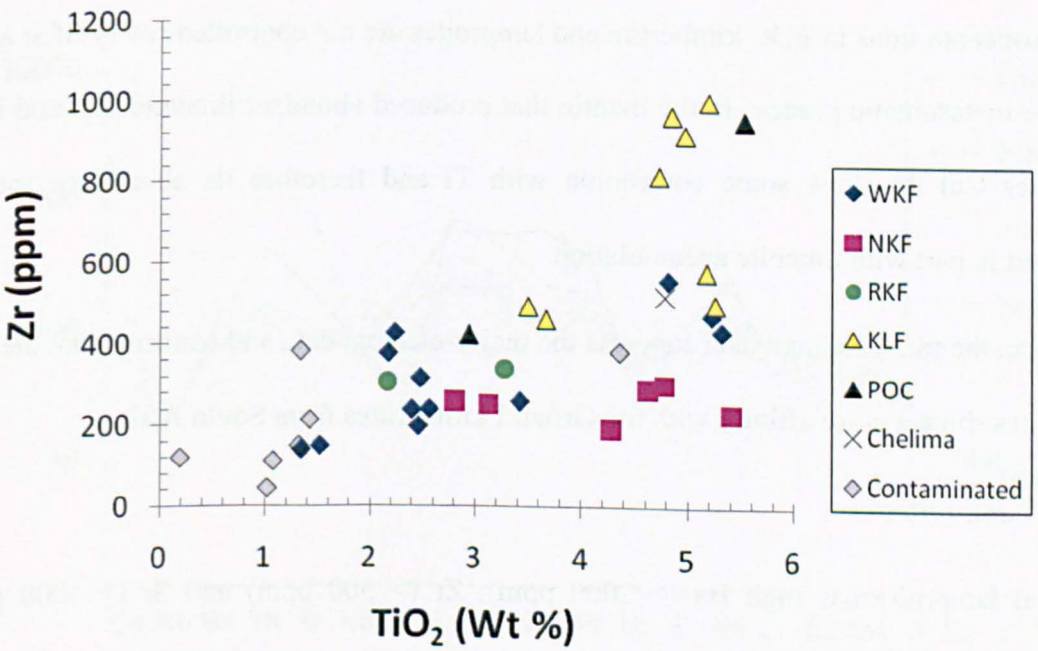

b)

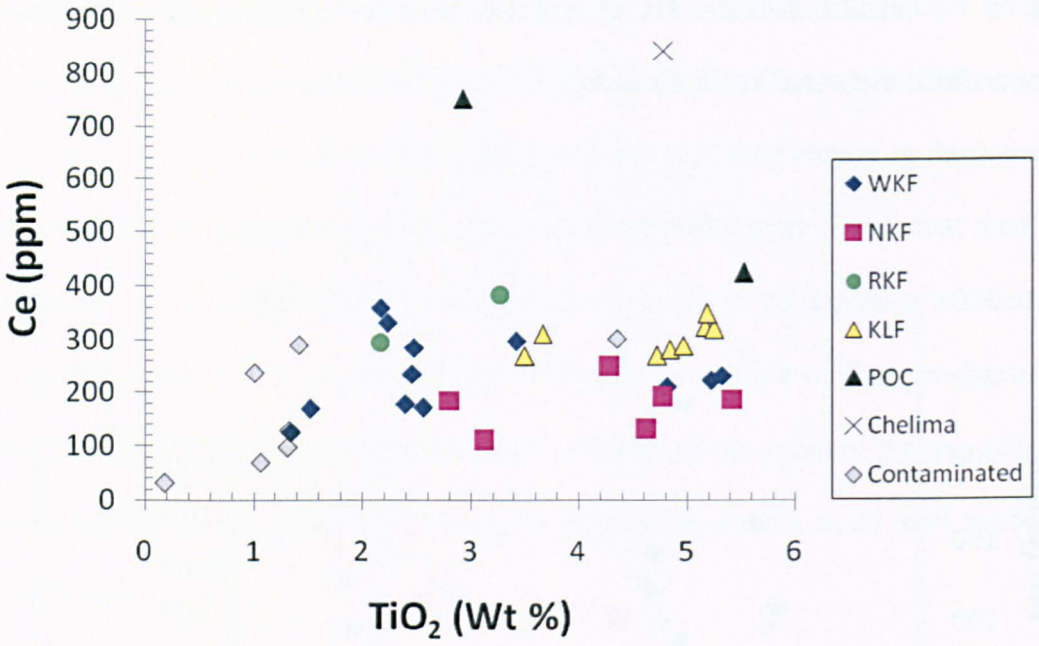

c)

Figure 3.12. Plots of Nb (a), Zr (b) and Ce (c) against TiO_2

The EDC kimberlites show a weak positive correlation between Ti and Zr, but no correlation between Ti and Nb or Ce (Fig. 3.12). The Ti in the EDC lamproites shows a moderate positive correlation with Zr and Ce, but no correlation with Nb. Therefore it would seem that the Nb concentrations in EDC kimberlite and lamproites are not controlled solely (if at all) by the same metasomatic process in the mantle that produced abundant ilmenite. Zr (and in the lamproites Ce) do show some correlation with Ti and therefore its abundance may be associated in part with ilmenite accumulation.

In essence, the trace-element data supports the major-element data and confirms that the EDC kimberlites show a close affinity with the Group I kimberlites from South Africa.

3.4.2. Lamproites

A typical lamproite has high Ba (> 2000 ppm), Zr (> 500 ppm) and Sr (> 1000 ppm), concentrations (Mitchell and Bergman, 1991). The lamproites in the EDC show a wide range of Ba abundances, but all appear lower than expected for a typical lamproite (254-1528 ppm).

Ba is hosted by phlogopite, sanidine, apatite and K-Ba-titanosilicates. The Sr abundance is also variable, with 6 lamproites showing typical lamproite abundances (1009-2144 ppm), while 5 show lower than expected abundances (494-953 ppm). It has been reported that relative to other types of lamproite, olivine lamproites can have significantly lower Ba and Sr contents (Reddy et al., 2003). The Nallabandlagudem and Vedadri North lamproites have both been classified as olivine lamproites (Chalapathi Rao et al., 2010) and both show lower Ba and Sr contents relative to typical lamproites. However, the other lamproites with low Ba and Sr concentrations have been classified as either diopside or phlogopite lamproites. The Zr abundance of the EDC lamproites is generally comparable to that of a typical lamproite (519-1001 ppm) with 4 lamproites showing values slightly lower than expected (424-499 ppm).

It can be seen from a normalised multi-element plot (Fig.3.13) of the EDC lamproites that all the trace elements are enriched relative to primitive mantle. However, strong negative troughs can be seen for K and Sr. Ti also shows low to moderate depletion.

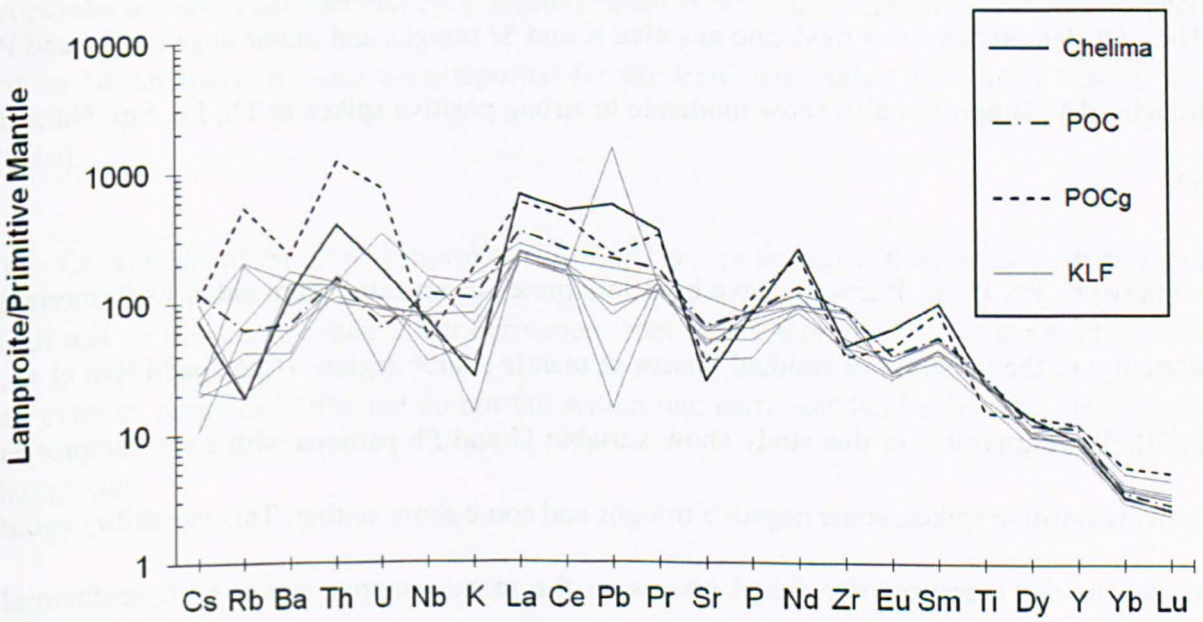

a)

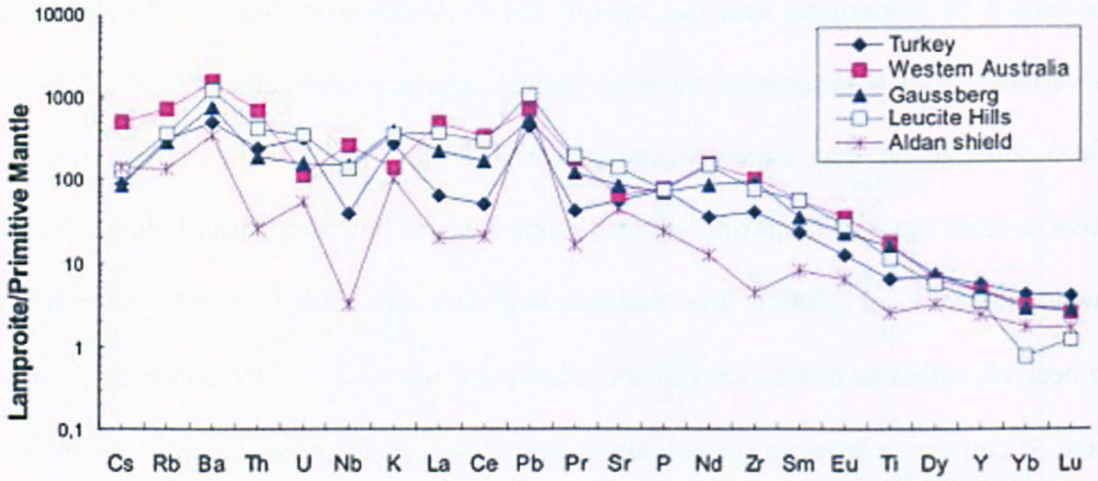

b)

Figure 3.13. Primitive-mantle-normalized (McDonough & Sun, 1995) multi-element patterns of the Krishna lamproites (a) (Data from this study), compared with other world-wide lamproites (b) (Figure from Chalapathi Rao et al., 2010; Data sources for global lamproites: Nixon et al., 1984; Jaques et al., 1986; Murphy et al., 2002; Davies et al., 2006; Mirnejad and Bell, 2006; Akal, 2008.)

The EDC lamproites show moderate negative K and Sr troughs and minor negative Eu and P troughs. The lamproites also show moderate to strong positive spikes in Th, La, Sm, Nd and Yb.

Negative K, Pb, U, Sr, P troughs have been interpreted as resulting from either hydrothermal alteration or the presence of residual phases in mantle source regions (Chalapathi Rao et al., 2010). The lamproites in this study show variable U and Pb patterns with some lamproites showing positive spikes, some negative troughs and some show neither. This variability could be due to the presence of residual phases in the mantle source region or hydrothermal alteration. It has been reported that in the case of U and Pb the contribution of hydrothermal

alteration towards the magnitude of negative depletions cannot be ruled out, as U and Pb are regarded as some of the most fluid-mobile trace-elements. (Chalapathi Rao et al., 2010).

The negative K anomaly may be the result of a K-bearing phase such as phlogopite or K-richterite in the source not melting entirely. It has been reported that even though lamproites show high K_2O abundances, depletions in K relative to primitive mantle are characteristic of lamproites (Foley et al., 1987) and other mafic potassic-ultrapotassic rocks (Coe et al., 2008). The negative Sr anomalies in the lamproites can be attributed to either the presence of residual phases such as clinopyroxene (Smith et al., 1985) in the source or the depletion of Sr in the mantle source during a previous phase of melt extraction (Chalapathi Rao et al., 2004). Negative P troughs are likely to be due to residual apatite in the source (Chalapathi Rao et al., 2010).

The Nb content of the EDC lamproites is variable, but generally shows a minor negative anomaly. The majority of the other world-wide lamproites with the exception of Western Australia are also characterized by a negative spike at Nb (Fig. 3.13b); however the absence of an Nb anomaly has also been reported for the EDC lamproites (Chalapathi Rao et al., 2010).

The Ce contents of the EDC lamproites (Fig.3.14) are much higher than that for MORB and OIB and do not suggest their direct derivation from the asthenosphere. The lamproites show an extreme range in Ce/Pb and do not fall within one particular field shown by other world lamproites.

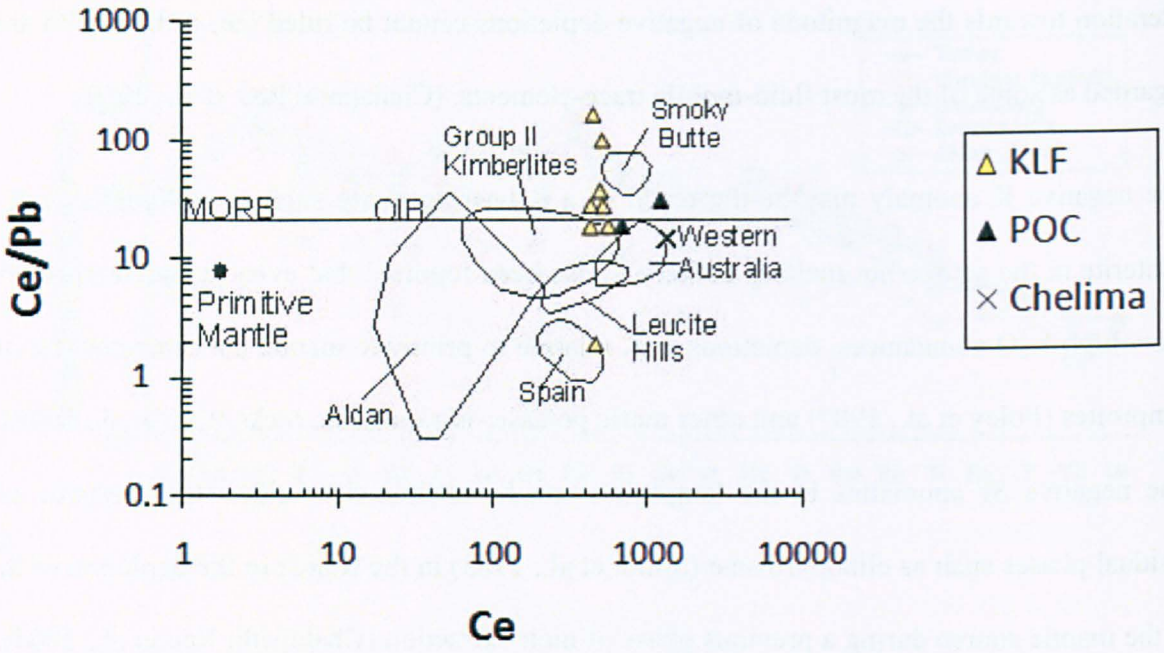

Figure 3.14. Plot of Ce against Ce/Pb. Adapted from Chalapathi Rao et al., 2010. Data sources for global lamproites: Nixon et al., 1984; Jaques et al., 1986; Murphy et al., 2002; Davies et al., 2006; Mirnejad and Bell, 2006; Akal, 2008.) As Ce does not show a large range in concentration, it can be assumed that the large range in Ce/Pb is at least in part due to the fluid mobile nature of Pb compared to the highly immobile Ce during weathering or alteration.

As well as showing distinctive major-element abundances, the Chelima lamproite also shows anomalous trace-element abundances relative to the other EDC lamproites (Fig. 3.9). It has the highest Ni and Cr concentrations among the lamproites, which is likely to be due to higher modal olivine. The Pochampalle (POCg) lamproite also shows differences in its trace element abundance from that of the rest of the KLF. Most notably it has higher Ba, Bi, Hf, Mo, Pb, Rb, Th and U. The elevated concentration of these elements could be due to greater enrichment in the source, however, some of these elements are the more mobile trace elements and may have been affected by hydrothermal alteration. Elevated concentrations of other trace elements such as Th may have been the result of crustal contamination. It can be

seen that Chelima and Pochampalle both show high La and low Nb contents (Fig. 3.9) another indication of crustal contamination.

The nomenclature and classification of the EDC lamproites is difficult due to their distinct petrologically complex mineral assemblages and diverse igneous forms and facies (Reddy et al., 2003). Haggerty and Birkett (2004) suggest that there are neither archetypal kimberlites nor typical lamproites in India. The data in this study show that the EDC lamproites although show many trace-element characteristics of more established lamproites (Fig 3.13b) also show some variability from typical lamproites.

3.5. Rare Earth Element Chemistry

Description of analytical techniques and instrumentation used for rare earth element analysis are described in appendices A.1.2.1 and A.1.2.2

3.5.1. Kimberlites

Perovskite and apatite are the main REE-bearing phases in kimberlites. The kimberlites of Southern India are strongly enriched in LREEs with La abundances of 248 to 855 times that of chondrite. HREEs are much less enriched than the LREEs, ranging from 3-8 times chondrite. Consequently La/Yb ratios are high and show a wide range of values from 48-121 with an average of ~ 88. All samples are enriched in LREEs relative to MREEs with La/Sm ratios from 4-8. Kimberlites in the NKF, WKF and RKF show similar LREE abundances but the samples from the NKF and RKF have slightly higher HREE abundances than the WKF, resulting in a slightly steeper REE pattern for the WKF (Fig. 3.15). The extreme enrichment of LREEs and less enriched HREEs creating a steep REE pattern is typical of Group I kimberlites and also suggests derivation from the garnet stability fields (Le Roex et al., 2003; Gaffney et al., 2007).

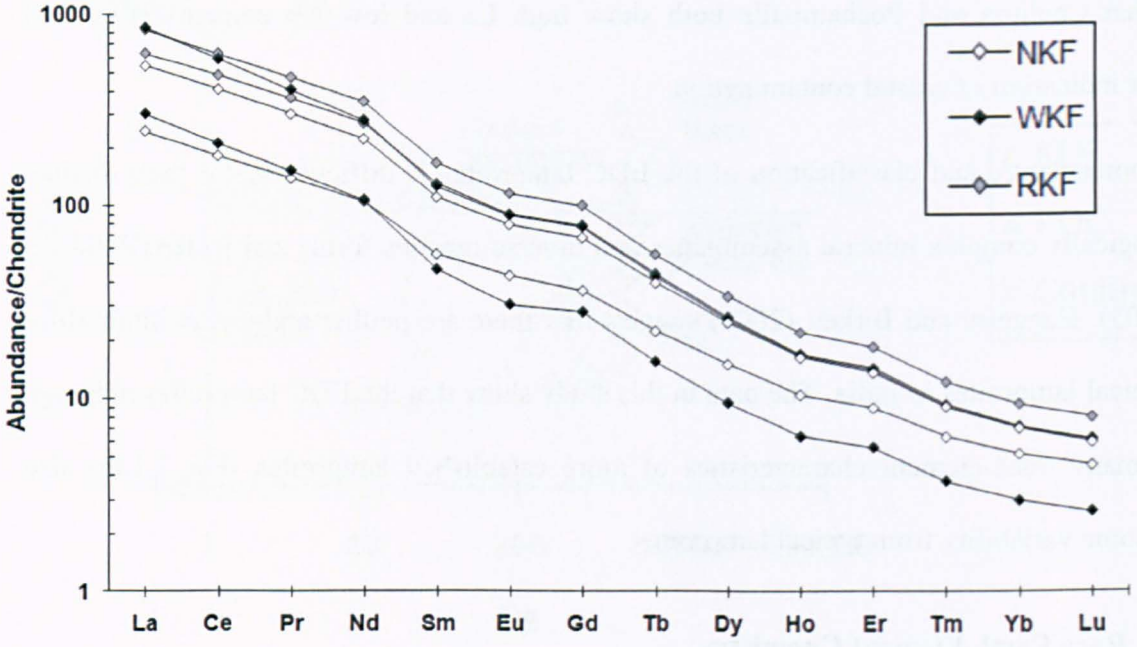

Figure 3.15. Rare earth element (REE) patterns (normalized to chondrite; values from Anders and Grevesse, 1989) of the EDC kimberlites. The upper and lower values from the data in this study are shown for the WKF and NKF.

3.5.2. Lamproites

The EDC lamproites generally show greater enrichment in REEs than the EDC kimberlites in this study. On a chondrite-normalized REE plot (Fig. 3.16) the majority of lamproites from the KLF display similar REE-enriched patterns showing only subtle differences. As with the kimberlites the low HREE abundance and steep slope of the REE patterns of the lamproites suggest derivation from the garnet stability fields (Gaffney et al., 2007). The Pochampalle and Chelima REE patterns show a different trend from that of the other EDC lamproites on the chondrite-normalized REE plot (Fig. 3.16).

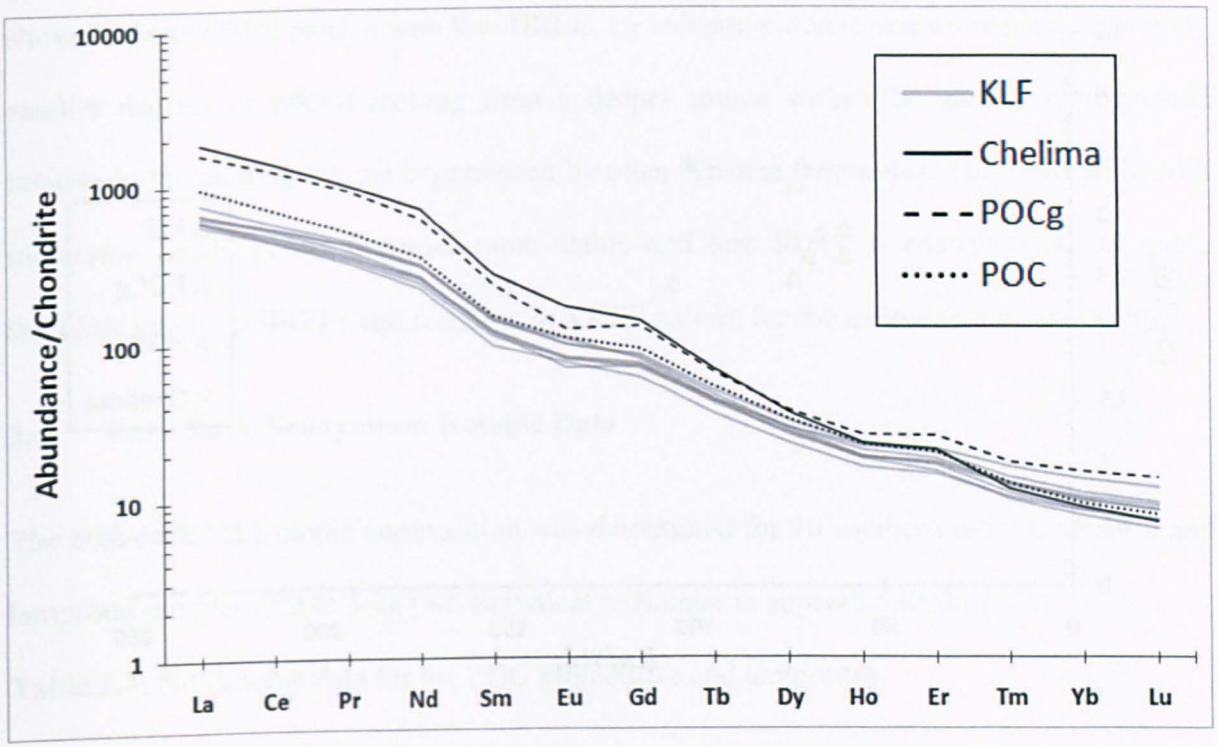

Figure 3.16. Rare earth element (REE) (normalized to chondrite; values from Anders and Grevesse, 1989) patterns of the EDC lamproites.

The EDC lamproites show extreme LREE enrichment illustrated by elevated $(La/Yb)_N$ values (Fig 3.17). The Krishna lamproites $(La/Yb)_N$ values generally range from 45 to 75, but the Pochampalle lamproite shows the greatest LREE enrichment within the KLF at $(La/Yb)_N = \sim 100$. The Chelima lamproite has the highest degree of LREE enrichment among the sample suite analyzed in the present study, with $(La/Yb)_N = \sim 200$.

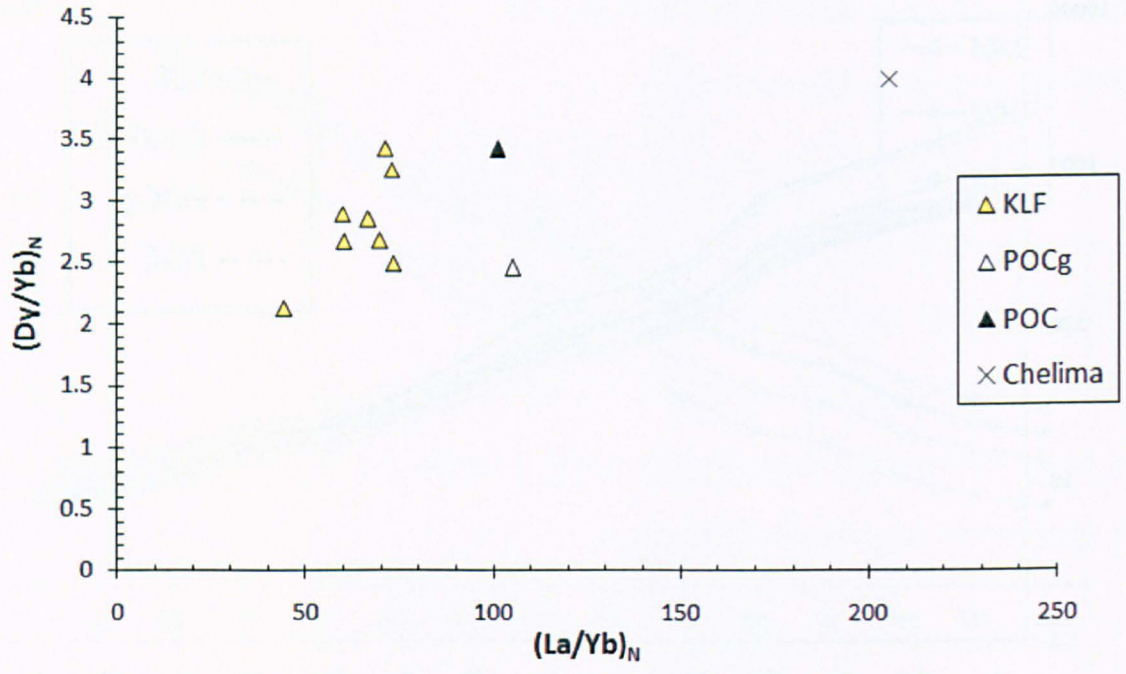

Figure 3.17. Plot of Dy/Yb against La/Yb (normalized to chondrite; values from Anders and Grevesse, 1989) of the lamproites of Southern India.

Two samples were collected from different locations from the Pochampalle lamproite and both show REE patterns distinct from those of the rest of the KLF (Fig 3.17). The POC sample shows a closer trend to that of the KLF, with similar Dy/Yb ratios and HREE contents, but with a higher La/Yb ratio due to greater LREE enrichment. The POCg sample also has an elevated La/Yb ratio but is characterized by a low Dy/Yb ratio (POCg has the highest HREE contents among all the lamproite samples investigated in this study) such that it plots off the trend defined by other KLF samples (Fig. 3.17). The elevated HREE contents in POCg may be an indication of crustal contamination, a hypothesis supported by the large negative Nb anomaly shown by the POCg sample (Fig. 3.12).

The Chelima lamproite shows a different REE signature than the KLF (Fig. 3.17), with higher La/Yb and Dy/Yb ratios due to its extreme LREE enrichment. The Chelima lamproite

shows a steeper REE pattern with low HREE, an indication that it may have been derived by smaller degrees of partial melting from a deeper source within the garnet stability field relative to the melting regime experienced by other Krishna lamproites. This is because with increasing depth, garnet becomes more stable and less likely to contribute to the melt, therefore retaining HREEs and resulting in a REE pattern for the melt with a steeper slope.

3.6. Bulk-Rock Neodymium Isotopic Data

The bulk-rock Nd isotopic composition was determined for 20 southern India kimberlite and lamproite samples (Table 3.4). (Nd analytical technique in appendix A1.2.4)

Table 3.4: Nd isotopic data for the EDC kimberlites and lamproites

	Age (Ma)	Sm (ppm)	Nd (ppm)	$^{147}Sm/^{144}Nd$	$^{143}Nd/^{144}Nd(m)$	ε(Nd)t
WKF						
Chin 12	1100	18.7	129	0.0873	**0.511944**	**1.9**
Mul 5	1100	13.7	88.3	0.0934	**0.512072**	**3.5**
KL3	1100	12.9	83.7	0.0928	**0.511979**	**1.8**
Waj 2	1100	12.9	84.8	0.0916	**0.511970**	**1.8**
Lat 3	1100	8.11	58.7	0.0832	**0.511839**	**0.4**
Tumm	1100	14.5	92.7	0.0942	**0.512046**	**2.9**
CC1	1100	10.2	68.2	0.0900	**0.511909**	**0.8**

	Age (Ma)	Sm (ppm)	Nd (ppm)	$^{147}Sm/^{144}Nd$	$^{143}Nd/^{144}Nd(m)$	ε(Nd)t
NKF						
NK2	1100	11.7	73.9	0.0953	**0.512015**	**2.1**
MK1	1100	8.83	53.4	0.0995	**0.512016**	**1.6**
KK6	1100	8.32	48.2	0.1039	**0.512144**	**3.4**

	Age (Ma)	Sm (ppm)	Nd (ppm)	$^{147}Sm/^{144}Nd$	$^{143}Nd/^{144}Nd(m)$	ε(Nd)t
RKF						
SK3	1100	19.3	124	0.0937	**0.512001**	**2.1**

	Age (Ma)	Sm (ppm)	Nd (ppm)	$^{147}Sm/^{144}Nd$	$^{143}Nd/^{144}Nd(m)$	ε(Nd)t
KLF						
PocG	1500	34.3	280	0.0737	**0.511059**	**-7.2**
Jay	1225	21.3	142	0.0903	**0.511459**	**-6.3**
Ramapu	1225	17.6	119	0.0890	**0.511358**	**-8.1**
VedN	1225	17.2	119	0.0870	**0.511364**	**-7.7**
Ramman	1225	14.2	101	0.0846	**0.511348**	**-7.6**
T1	1225	16.4	110	0.0898	**0.511413**	**-7.1**
Red	1225	20.5	144	0.0857	**0.511379**	**-7.2**
Nalla	1225	17.4	116	0.0903	**0.511391**	**-7.7**
CBL						
Chelima	1350	39.8	319	0.0751	**0.511129**	**-8.4**

Reproducibility of the La Jolla Nd standard over the analysis period was 0.511849 ± 0.000002 (8 ppm, 2SD). The initial ratios were calculated using an age of: 1100 Ma - kimberlites; 1225 Ma - KLF; 1500 Ma - Pochampalle; 1350 Ma - Chelima lamproite. (Chapter 4; Table 4.1).

3.6.1. Kimberlites

Calculated initial εNd values are quite similar for both the WKF (0.4-3.5) and the NKF (1.6-3.4). $^{143}Nd/^{144}Nd_m$ ratios are also similar between the WKF (0.511839-0.512072) and the NKF (0.512001-0.512144). These data are in good agreement with published data (Chalapathi Rao et al., 2004; Paton et al., 2009; Chakrabarti et al., 2007) (Fig. 3.18).

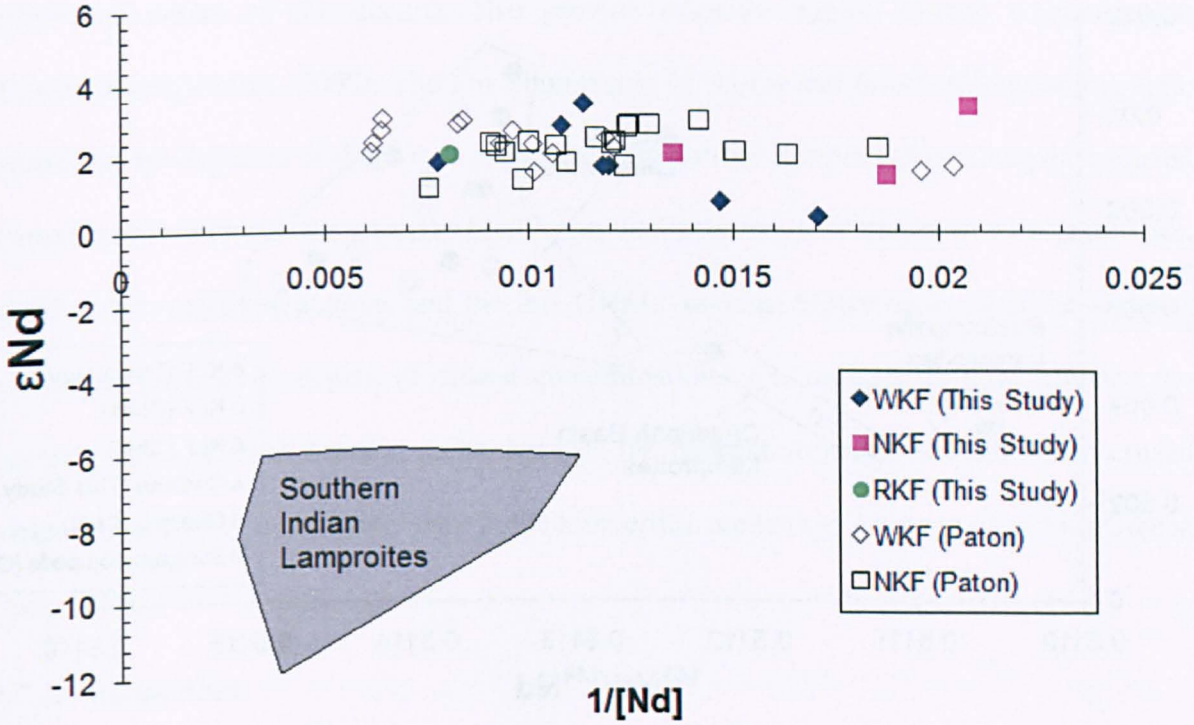

Figure 3.18. Plot of 1/[Nd] against εNd for kimberlites and lamproites from the Eastern Dharwar Craton (For detail of lamproite data, see figure 3.19).

3.6.2. Lamproites

The EDC lamproites have negative initial εNd values (-8.4 to -6.3), with $^{144}Nd/^{143}Nd_m$ ratios in a fairly narrow range (0.511059- 0.511459). These values are significantly lower than that of the kimberlites, which is thought to be due to much earlier metasomatic enrichment in the lamproite mantle source. These data are in good agreement with published data (Chalapathi Rao et al., 2004; Chakrabarti et al., 2007) (Fig. 3.19).

The Pochampalle and Chelima lamproites show Nd isotopic values that are distinct from the rest of the lamproites in the KLF. In contrast to the REE data, the $^{143}Nd/^{144}Nd$ isotopic ratio of Pochampalle is not intermediate between that of Chelima and the Krishna lamproite group on a 1/[Nd] vs. $^{143}Nd/^{144}Nd$ plot (Fig. 3.19).

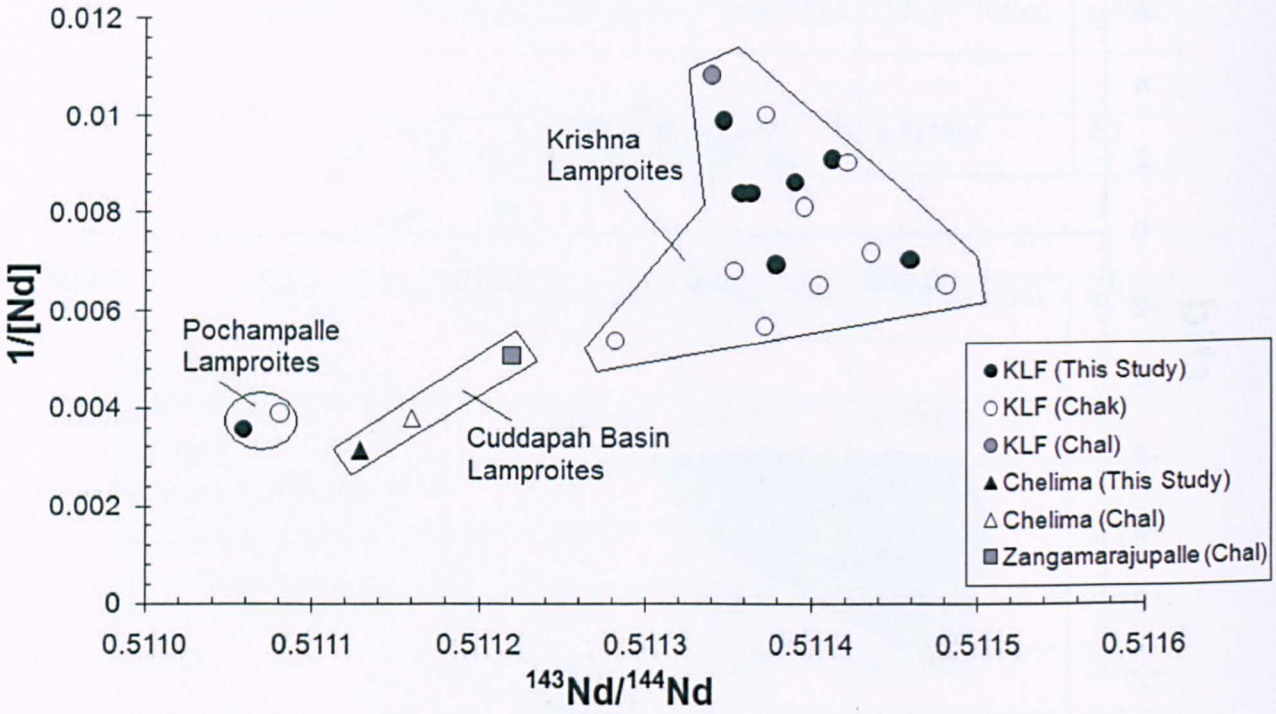

Figure 3.19. Plot of 1/[Nd] against $^{143}Nd/^{144}Nd$ ratios for the Krishna lamproites (including Pochampalle) and the CLF (including Chelima). Data from this study, Chakrabarti et al. (2007) (Chak) and Chalapathi Rao et al. (2004) (Chal).

The lower $^{143}Nd/^{144}Nd$ ratio of the Pochampalle lamproite suggests a closer affinity with the CLF, particularly Chelima, than with the rest of the KLF samples. The broad spread of the KLF Nd data precludes robust interpretations of a mixing array involving the Cuddapah Basin Lamproites (CBL), Pochampalle and the Krishna lamproites. However, the difference in Nd isotopic signature between Pochampalle and the other Krishna lamproites is striking.

3.7. Discussion

3.7.1. Contamination

The contamination indices applied in this study show that contamination in most of the samples used is minimal, and those samples deemed to be contaminated were excluded from further analysis. High Mg# and Ni contents, which are often regarded as indicating the

'primitive' nature of the magma, also provide evidence against crustal contamination (Chalapathi Rao et al., 2008). The low abundances of Al_2O_3 and Na_2O of this sample suite would not be expected if there was crustal contamination. Further evidence against crustal contamination includes the strongly LREE-enriched patterns, lack of positive Eu anomalies, negative Nb and Zr depletions and the low HREE contents. However, even if the samples have undergone some degree of crustal contamination, it is unlikely to have affected the isotopic ratios of small-fraction melts, because the concentrations of Sm and Nd in crustal rocks is likely to be much lower than in the kimberlitic melts (e.g. Fraser et al., 1985; Gibson et al., 1996).

3.7.2. Kimberlites

The kimberlites of southern India located in the EDC were all previously classified as Group I kimberlites (Chalapathi Rao et al., 2004). However, due to their diverse nature, the classification of kimberlites is difficult and it has been suggested that there are neither archetypal kimberlites nor typical lamproites in India (Haggerty and Birkett, 2004). Recent studies have revealed that although the majority of the EDC kimberlites are similar to the Group I kimberlites of southern Africa in terms of petrology, geochemistry and Sr-Nd isotope systematics, others show traits more typical of Group II kimberlites, or an overlap between Group I and Group II kimberlites (Chalapathi Rao and Srivastava, 2009).

The bulk-rock major-, trace-, REE- and Nd-isotopic composition of the EDC kimberlites is consistent with their classification as Group I kimberlites. This inference is also in agreement with Paton et al., (2009) who proposed that the incompatible trace element compositions and Sr, Nd and Hf isotopic compositions of the EDC kimberlites are indistinguishable from South African Group I kimberlites.

Group I kimberlites are considered to be the product of extremely low degree partial melting of a primitive peridotite (Arndt, 2003) that had previously experienced both *depletion* via early melt extraction (e.g. Tainton and McKenzie, 1994) and also subsequent *enrichment* in trace elements (e.g. Foley et al., 1992).

The petrogenesis of the southern Indian kimberlites is currently still debated and several theories have been put forward. There is strong support for the model of Tainton and McKenzie (1994) that proposed formation of the kimberlites via a two stage process involving the partial melting of metasomatically enriched SCLM (e.g. Chalapathi Rao et al., 2004; Becker and le Roex, 2006). This model contended that a SCLM source initially undergoes ~ 20 % melting within the garnet stability field, which leaves the residual SCLM depleted, but with relatively high abundances of the HREEs. The depleted SCLM subsequently experienced metasomatic enrichment caused by the migration of low-temperature small fraction melts from the asthenosphere. The small degree of melting (~0.4 %; Paton et al., 2009) of an asthenospheric source with residual garnet would result in melts with high LREEs, which would subsequently metasomatise the depleted SCLM by raising its LREE concentrations while leaving HREE abundances relatively unchanged. The kimberlites would then be generated from the partial melting (0.3-0.4 %) of the metasomatised SCLM source within the garnet stability field, resulting in a LREE-enriched melt. The model also indicates that the kimberlites are the products of low-degree partial melting of a garnet peridotite mantle source, extensively depleted prior to metasomatic enrichment and subsequent partial melting. Based on perovskite Sr and bulk-rock Hf and Nd isotopic data, Paton et al. (2009) suggested that the asthenospheric component must have originated from within or below the transition zone, and may represent ancient subducted oceanic crust.

The EDC kimberlites have high La/Yb ratio that could be produced by very small (< 1 %) degrees of partial melting of a phlogopite-garnet lherzolite (Tainton and McKenzie, 1994). In addition, to generate melts with such high REE abundances the mantle source must have been previously enriched. The degree of partial melting can be estimated from the SiO_2 content of a melt and its Nb/Y ratio, which is not thought to be greatly affected by metasomatic processes (Beard et al., 1998); (Fig 3.20).

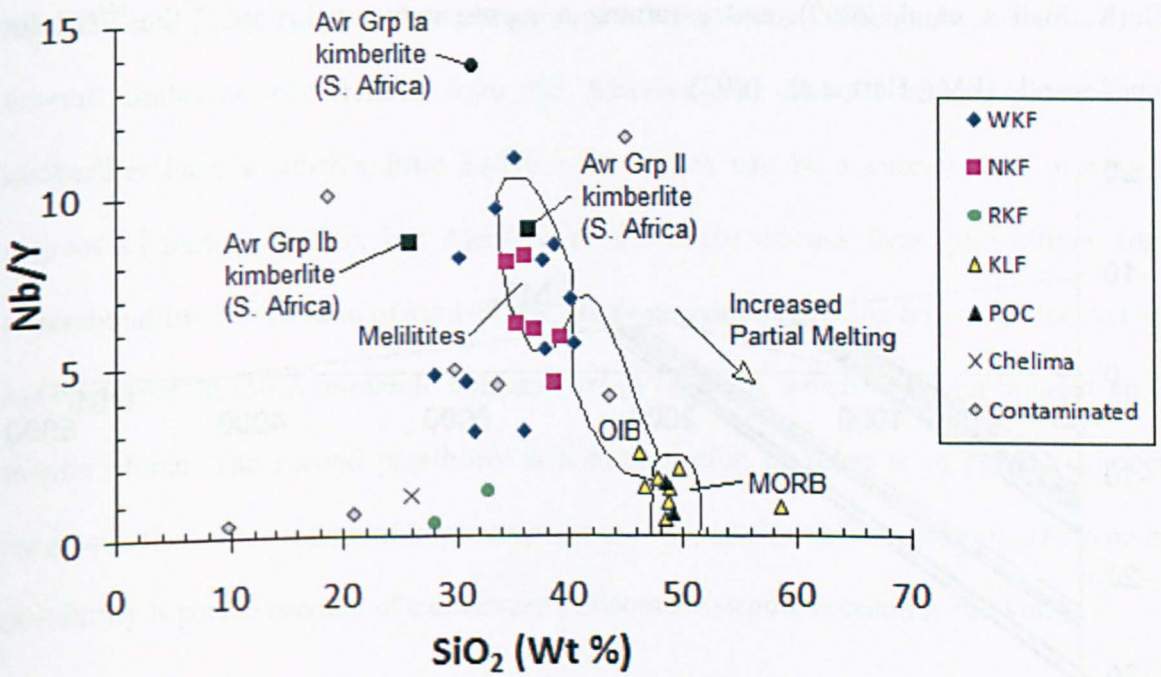

Figure 3.20. Plot of SiO_2 against Nb/Y for samples analysed in this study, illustrating the degree of partial melting. Fields are from Beard et al. (1998).

The EDC kimberlites appear to be predominantly the products of much smaller degrees of partial melting than OIB or MORB. The amount of partial melting appears similar to that of melilitites. However, it can also be seen that they display a wide range of values on the SiO_2 against Nb/Y plot, which may reflect variation in the degree of partial melting. This is supported by experimental studies of near-solidus melts produced at 30 kbar and at 30-70 kbar in carbonated mantle peridotite, which proposed that it is possible to generate a

continuous spectrum of melts ranging in composition from kimberlite to melilitites (Gudffinsson and Presnell, 2005).

The Nd isotope evolution through time of the southern Indian kimberlites and lamproites in this study is summarised in figure 3.21, and compared with model evolution curves for depleted mantle (DM; Workman and Hart, 2005), and enriched mantle (EM*x). The enriched mantle is modelled using the εNd value of a xenolith from the Lattavaram kimberlite in the EDC (Karmalkar et al. 2009), and assuming a representative value of $^{147}Sm/^{144}Nd$ for enriched mantle (EMI; Hart et al., 1992).

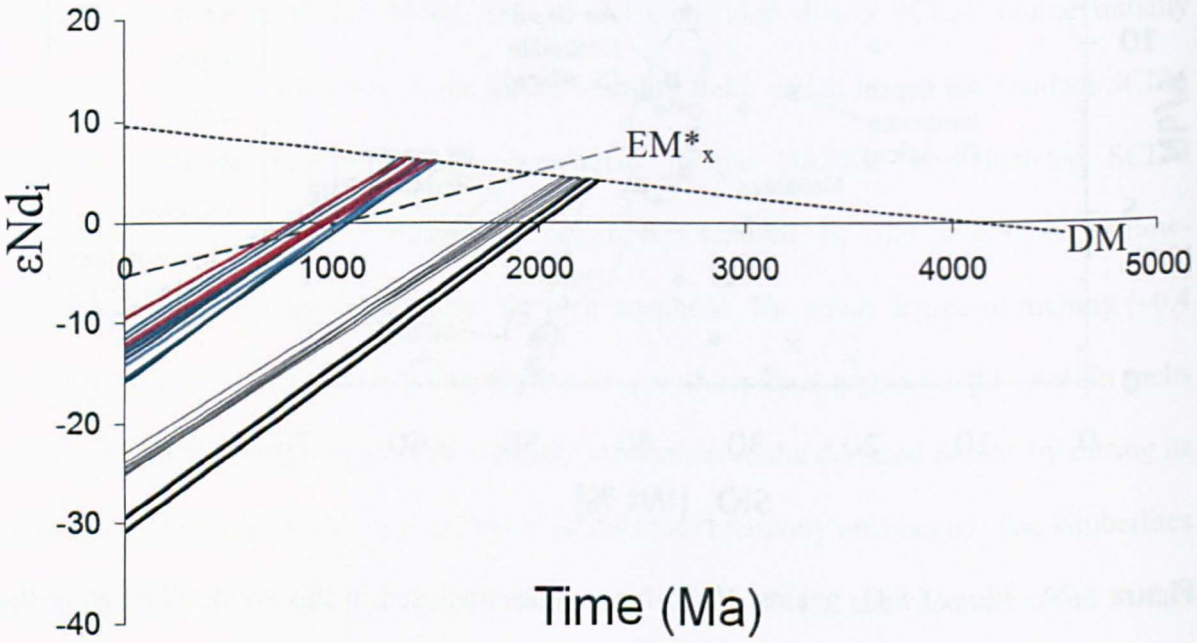

Figure 3.21. Plot of εNd_i against time for the EDC kimberlites (coloured lines) and lamproites (black lines). The single bold dashed line represents the potential Nd evolution of enriched mantle (EM^*_x) beneath India, modelled using the εNd of a xenolith from the Lattavaram kimberlite in the EDC (Karmalkar et al. 2009), and assuming a representative value of $^{147}Sm/^{144}Nd$ (0.5116) for EM (EMI; Hart et al., 1992). The depleted mantle (DM) trend (dotted line) is based on data from Workman and Hart (2005).

The εNd evolution trajectory of the kimberlites intersects the EM model evolution line at around 1 Ga, which corresponds to the emplacement age of the EDC kimberlites. However, the DM and EM model evolution lines intersect much earlier (1.9-2.0 Ga). One model for petrogenesis of the EDC kimberlites consistent with these Nd evolution data is that the kimberlite magmas were derived at around 1 Ga from an initially depleted mantle source that had been previously enriched at around 1.9-2.0 Ga.

Agashev et al., (2010) report superchondritic Nb/Ta ratios and subchondritic La/Nb ratios in several kimberlite occurrences from the Siberian and Slave (Canada) provinces. All kimberlites have a subchondritic La/Nb ratio, which can be a consequence of very low degrees of partial melting, but Agashev et al. (2010) discuss three possibilities for the superchondritic Nb/Ta ratio of kimberlites. They propose a "missing reservoir" located in the lower mantle, at the core-mantle boundary or in the core, which has been brought up by a mantle plume. The second possibility is a fractionation of ilmenite in primary kimberlite magma in the source region of kimberlites (at the base of lithospheric mantle). The remaining possibility is partial melting of carbonated peridotite at depths exceeding 300 km.

The Nb/Ta against La/Nb ratios of the EDC kimberlites (Fig. 3.22) scatter widely between primitive mantle composition and that of a proposed "missing reservoir" suggested by Agashev et al. (2010) to account for the superchondritic Nb/Ta ratios.

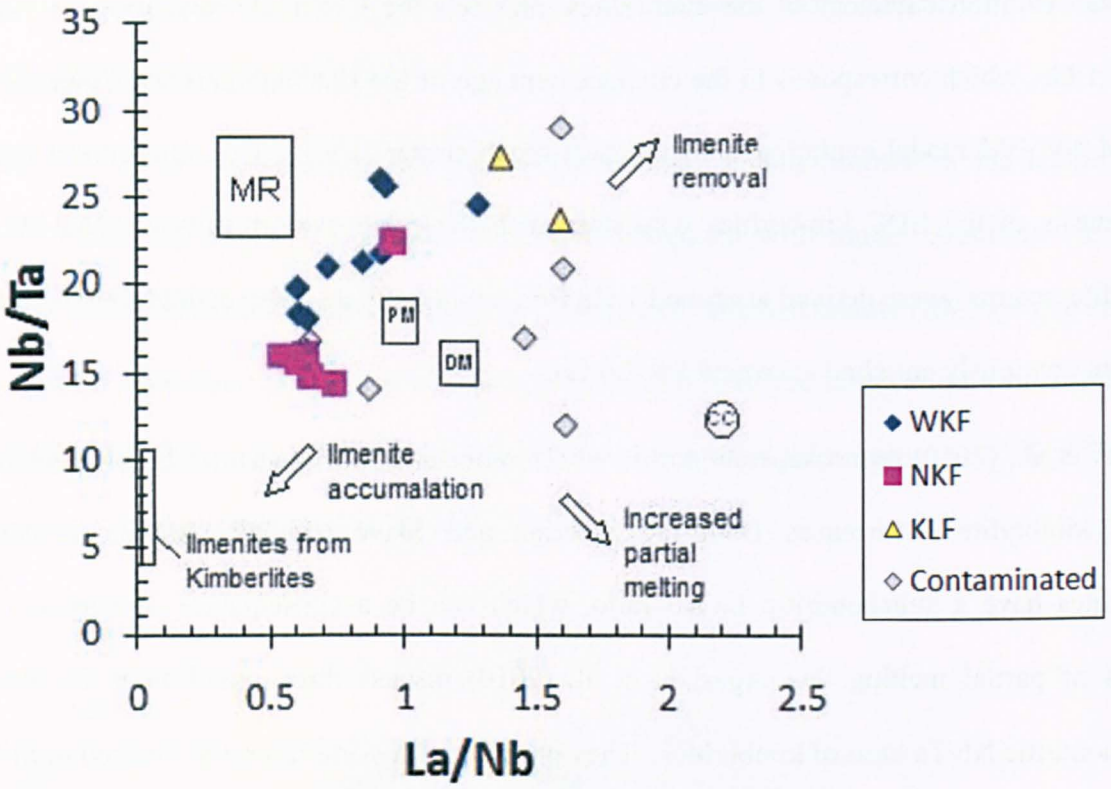

Figure 3.22. Graph of Nb/Ta against La/Nb for the EDC kimberlite and lamproite samples. MR: Missing reservoir; PM: Primitive mantle; DM: Depleted mantle; CC: Continental crust. Most EDC lamproite samples plot at much higher Nb/Ta and La/Nb values. Adapted from Agashev et al., (2010).

The NKF kimberlites show an ambiguous distribution, with a negative trend in a tight cluster of data, and a single outlier falling on the WKF trend towards ilmenite removal. The negative trend may reflect partial melting (Agashev et al., 2010). The positive trend shown by the WKF kimberlites can be explained by the fractional crystallization of ilmenite from the primary kimberlite melt as ilmenite megacrysts from kimberlites have a low Nb/Ta (4-10) ratio (Griffin et al., 1997) and a nearly zero La/Nb ratio (Agashev et al., 2010). This can be corroborated by plotting Nb/Ta against TiO_2 (Fig. 3.23).

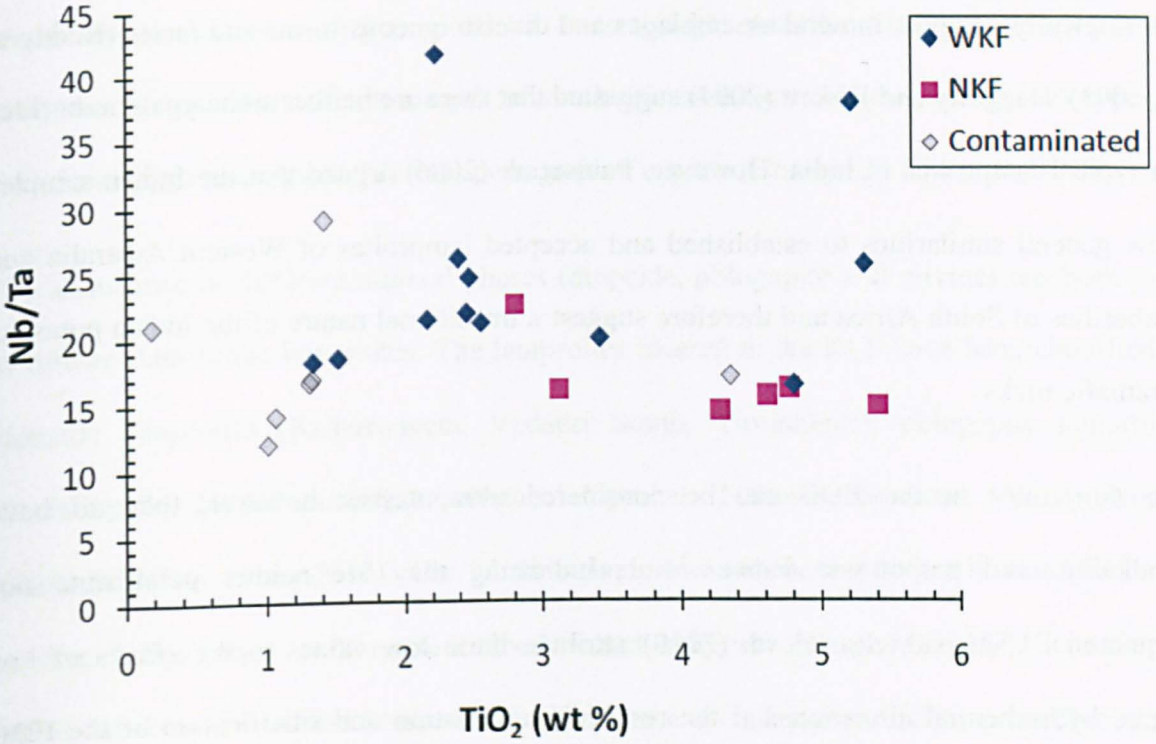

Figure 3.23. Plot of Nb/Ta against TiO_2 for the EDC kimberlite samples.

It can be seen that for the majority of EDC kimberlites Nb/Ta appears to gradually decrease as TiO_2 increases, which is consistent with ilmenite removal. However, there are 3 WKF samples that have higher Nb/Ta ratio and/or TiO_2 which plot off this trend.

3.7.3. Lamproites

The similarities observed in mineralogy, geochemistry and tectonics of ultramafic rocks from various localities around the world (e.g. Kimberly Craton, Western Australia; Prairie creek, Leucite Hills and Smoky Butte, USA; Murcia Almeria, Spain; South Africa; West Africa; Zambia) prompted several authors (Atkinson et al., 1984; Jaques et al., 1984; Nixon et al., 1984, Scott Smith and Skinner, 1984; Mitchell and Bergman, 1991) to classify these rocks as lamproites.

The nomenclature and classification of the EDC lamproites is difficult due to their distinct petrologically complex mineral assemblages and diverse igneous forms and facies (Reddy et al., 2003). Haggerty and Birkett (2004) suggested that there are neither archetypal kimberlites nor typical lamproites in India. However, Paul et al. (2006) argued that the Indian samples show general similarities to established and accepted lamproites of Western Australia and kimberlites of South Africa and therefore suggest a transitional nature of the Indian potassic, ultramafic rocks.

The lamproites in the EDC can be considered ultrapotassic; however, they all have peralkaline and perpotassic indices < 1, indicating they are neither peralkaline nor perpotassic. Chalapathi Rao et al. (2010) attribute these low values to the effects of low degree hydrothermal alteration and the resulting carbonation and silicification of the EDC lamproites. The EDC lamproites contain elevated TiO_2 concentrations that are characteristic of a lamproite (Mitchell and Bergman, 1991).

A typical lamproite has high Ba (> 2000 ppm), Zr (> 500 ppm) and Sr (> 1000 ppm), concentrations (Mitchell and Bergman, 1991). The Sr abundance of the lamproites in the EDC is variable with lamproites showing either typical or lower than expected abundances. The lamproites also show a wide range of Ba abundances but all appear lower than expected for a typical lamproite. However, it has been reported that relative to other types of lamproite, olivine lamproites can have significantly lower Ba and Sr contents (Reddy et al., 2003). The Zr abundance is generally that of a typical lamproite.

The data in this study show that the EDC lamproites show similar geochemistry to that of established lamproites. However, the lamproites of the EDC contain varying modal proportions of phlogopite, clinopyroxene (diopside), amphibole, alkali feldspar, titanite,

apatite, calcite, ilmenite and rutile. Chlorite, carbonate and quartz are also present as secondary phases in varying proportions. It is thought that the EDC lamproites display heteromorphism, where a bulk-magma of similar composition can give rise to rock types of varied modal mineralogy and diverse petrographic aspects (Chalapathi Rao et al., 2010).

The abundance of different mineral phases (diopside, phlogopite and olivine) has been used to further classify the lamproites. The lamproites located in the KLF have been classified as diopside lamproites (Ramannapeta, Vedadri South, Tirumalgiri), phlogopite lamproites (Pochampalle, Jayanthipuram) or olivine lamproites (Nallabandlagudem, Vedadri North) (Chalapathi Rao et al., 2010). The Chelima lamproite has been previously classified as a minette, lamprophyre, carbonatite-kimberlite and lamproite (Bergman, 1987; Scott-Smith, 1989), however, its current accepted classification is as a lamproite (Chalapathi Rao et al., 2004). The data from this study support the classifications of Chalapathi Rao et al. (2010) and suggest that the Reddikunta and Ramapuram lamproites show mineralogy similar to those classified as diopside-lamproites, while the Chelima lamproite is most similar to those classified as phlogopite-lamproites.

The complex geochemistry of lamproites, like kimberlites, suggests a mantle source region that experienced both depletion and enrichment. For the Krishna lamproites there are currently three main theories put forward for their generation.

- Chalapathi Rao et al. (2004) suggested that the source region underwent an extensive initial depletion involving komatiitic type melt extraction, followed by subsequent enrichment by a depleted MORB-type source. The lamproites were proposed to have been derived from a metasomatised harzburgite near the base of the mechanical boundary layer (~ 145 km). (Chalapathi Rao et al., 2004).

- Paul et al. (2007) proposed that they were derived from partial melting of a mantle source that was metasomatically enriched in Ti and Fe. This same study also suggested that the lamproites were derived from depths shallower than the garnet stability field and their source regions were shallower than those of the kimberlites in the EDC.

- Chakrabarti et al. (2007) maintained that the Krishna lamproites were derived by partial melting of metasomatized subducted Achaean komatiite in a peridotite mantle-source assemblage, based on Sr-Nd-Hf-Pb isotopes, major and trace elemental ratios. In this study, their Pb-isotopic signatures (high ^{207}Pb low ^{206}Pb) and superchondritic Nb/Ta ratios ruled out the lamproites' derivation from a metasomatized sub continental lithospheric mantle source and indicated an Archaean crustal component in the source (Chakrabarti et al., 2007).

The EDC lamproites show much lower Nb/Y ratio and higher SiO_2 contents than the EDC kimberlites and therefore appear to be the products of much greater degrees of partial melting (Fig. 3.20). This has been attributed to the location of the KLF at the margin of the craton where the lithosphere has been thinned more compared to its core, so that the lamproites reflect more extensive melting at shallower levels (Chalapathi Rao et al., 2010).

The mantle source from which the lamproites were derived is not tightly constrained by the evolution curves in Figure 3.21. Their enriched geochemistry indicates that they did not originate directly from a depleted mantle source, but clearly they have a different source to that of the kimberlites. It is also apparent that the Pochampalle and Chelima lamproites followed a separate evolution from the other Krishna lamproites. It is possible that Pochampalle and Chelima were derived from a different source from that of the KLF. However, they may merely have been derived from the same source as the KLF but at an earlier time (as shown by the age data in this study- Chapter 4).

The source of the EDC lamproites could have been depleted mantle that was enriched earlier; however, more definite conclusions are difficult to draw from Nd evolution modelling of the lamproites due to the isotopic heterogeneity of the sub-continental lithospheric mantle, even on relatively small length scales.

Chapter 4: Geochronology

This chapter presents the Ar-Ar age dating of southern Indian kimberlites and lamproites. The bulk of this chapter is comprised of a manuscript which has been published in the journal 'Precambrian Research':

Osborne, I., Sherlock, S., Anand, M., Argles, T., 2011. New Ar–Ar ages of southern Indian kimberlites and a lamproite and their geochemical evolution. Precambrian Research 189, 91-103. doi:10.1016/j.precamres.2011.05.004

Article history: Received 18 June 2010; Received in revised form 24 March 2011; Accepted 6 May 2011; Available online 19 May 2011.

The age dating aspect of this project developed from a pilot investigation involving U-Pb age dating of perovskites in the EDC samples. The result from this work was presented as a poster at the 9th International Kimberlite Conference in Frankfurt, Germany, 2008:

Anand, M., Terada K, **Osborne, I.**, Chalapathi Rao, N. V., Dongre, A. (2008) SHRIMP U-Pb dating of Perovskites from southern Indian kimberlites. 9th International Kimberlite Conference Extended Abstract No. 9IKC-A-00222. (Appendix 3)

New Ar–Ar ages of southern Indian kimberlites and a lamproite and their geochemical evolution

Ian Osborne[a], Sarah Sherlock[a], Mahesh Anand[a,b], Tom Argles[a]

[a] Department of Earth and Environmental Sciences, CEPSAR, The Open University, Walton Hall, Milton Keynes MK7 6AA, UK

[b] Department of Mineralogy, The Natural History Museum, Cromwell Road, London, SW7 5BD

Abstract

The kimberlites and lamproites of southern India are thought to have formed in the most prolific known period of Precambrian ultramafic/ultrapotassic magmatism at around 1100 Ma. This study reports new age data for southern Indian ultrapotassic rocks (kimberlites and lamproites), a controversial topic due to the wide range of published age data and disagreements over the reliability of previously published ages. In this study we obtained new high-precision Ar–Ar data that better constrain the ages of southern Indian ultrapotassic rocks. Dates from three samples are presented, including two kimberlites from Wajrakarur kimberlite field and one lamproite from the Krishna lamproite field. These age data are then combined with bulk-rock geochemical and Nd isotopic data to provide further constraints on the source region and primary magma composition of southern Indian kimberlites and lamproites. Previously, the Chelima lamproite (ca. 1400 Ma) was considered to be one of the oldest lamproites in the world. However, our age data suggest that at least one lamproite (Pochampalle) was generated in the same region 100 Ma before the Chelima event. The Pochampalle lamproite was emplaced around ~1500 Ma as shown by the Ar–Ar data in this study, roughly 250 Ma before the other Krishna lamproites. It would seem that the Pochampalle lamproite was also derived from an isotopically distinct source region with a lower $^{143}Nd/^{144}Nd$ ratio than other lamproites in the Krishna field. These findings not only have implications for regional ultramafic/ultrapotassic magmatism, but also demonstrate that the mantle processes for producing lamproitic melts existed earlier than previously thought.

Keywords: Kimberlite Lamproite Eastern Dharwar Craton Southern India Proterozoic Ar–Ar dating

4.1. Introduction

Kimberlites and lamproites represent ultramafic magmas that travel rapidly from source regions in the deep mantle (>100 km) to the shallowest crustal levels at speeds of up to 0.1–4.0 ms−1 (Kelley and Wartho, 2000). In effect, they provide snapshots of the geochemical and isotopic nature of the deep lithospheric or asthenospheric mantle at the time of their emplacement. Because their petrogenesis has critical implications for large-scale pro-cesses (e.g., subduction, rifting, mantle plumes, and lithospheric enrichment), accurate determination of their ages is important in order to investigate the evolution of the deep mantle through time.

The majority of known kimberlite and lamproite occurrences (>80%) globally are Mesozoic or Cenozoic in age and are often associated with periods of continental rifting and formation of ocean basins. For example, Cretaceous kimberlite and related magmatism in Southern Africa (125–55 Ma) closely follows the opening of the South Atlantic Ocean, which initiated around 130 Ma ago; similarly the majority of kimberlites and related ultramafic lamprophyres in Labrador, Quebec, West Greenland and Scandinavia were emplaced 630–560 Ma ago and linked to the Eocambrian opening of the Iapetus Ocean (Kumar et al., 2007). Heaman et al. (2003) indicate a lack of worldwide known kimberlite occurrences between 250 and 360 Ma that may be linked to relative crustal and mantle stability during the lifetime of the Gondwanaland supercontinent. It could therefore be proposed that a similar lack of kimberlite and lamproite occurrences of Proterozoic age is also due to crustal and mantle stability.

Proterozoic kimberlite and lamproites are relatively rare by comparison with Phanerozoic occurrences. The kimberlites and lamproites of southern India are thought to have formed in the most prolific known period of Precambrian ultramafic magmatism at around 1100 Ma. Kimberlites, lamproites and related alkalic rocks with emplacement ages of ~1100–1200 Ma

have been reported from India, Canada, Greenland, Australia, Liberia, N. America, Scandinavia and South Africa (Kumar et al., 2007). Consequently this period of magmatism has been suggested to represent a global 'mantle event', when mantle conditions must have been favourable for kimberlite and lamproite emplacement (Skinner et al., 1985).

The kimberlites and lamproites of India have been proposed to be related to the formation of the Rodinia supercontinent (Kumar et al., 2007), which existed between 1000 and 750 Ma ago (Dalziel et al., 2000). The supercontinent began to form at ~1 Ga by accretion and collision of fragments produced by breakup of the older supercontinent, Columbia, which was assembled by global-scale 2.0–1.8 Ga collisional events (Zhao et al., 2004). Rodinia is thought to have included India, Australia and many of the present day continents of the southern hemisphere, which subsequently reorganized to form Gondwana.

The break-up of Columbia and initial assembly of Rodinia occurred ~1100 Ma ago, which may have provided favourable conditions for generation and emplacement of kimberlitic magmas across the Rodinian continent, producing many of the known Proterozoic kimberlites (~1100 Ma). During the formation of Rodinia ~1100 Ma ago, intracontinental rifting was taking place, resulting in the formation of several Large Igneous Provinces; e.g., 1109–1086 Ma in Laurentia (Ernst and Buchan, 2001) and 1112–1102 Ma in the Kalahari Craton (Hanson et al., 2004). Kumar et al. (2007) also proposed an enhanced period of mantle plume activity, approximately 100 Ma prior to the formation of Rodinia.

The petrogenesis of the southern Indian kimberlites is currently still debated and several theories have been put forward. Chalapathi Rao et al. (2004) suggested that they are the result of lithospheric extension during the Mid-Proterozoic. This model proposes a sub-continental lithospheric source that experienced metasomatic enrichment caused by the migration of volatile-rich small fraction melts from the convecting mantle. The model also indicates that

the kimberlites are the products of small-degree partial melting of a garnet peridotite mantle source, extensively depleted prior to metasomatic enrichment and subsequent partial melting (Chalapathi Rao et al., 2004). In contrast, Paton et al. (2009) suggested that the southern Indian kimberlites were derived directly from asthenospheric depths. Based on perovskite Sr and bulk-rock Hf and Nd isotopic data, these authors proposed that the asthenospheric component must have originated from within or below the transition zone, and may represent ancient subducted oceanic crust. Kumar et al. (2007) proposed that the southern Indian kimberlites located in the Eastern Dharwar craton (EDC) are likely to be linked to the impingement of a short-lived mantle plume beneath the Dharwar Craton, or that a major change and re-organization of the mantle convection regime occurred at the time of their formation.

There is also debate over whether lamproites are derived from the lithospheric (Davies et al., 2006) or convecting mantle (Murphy et al., 2002). Their complex geochemistry suggests a mantle source region that experienced both depletion and enrichment. For the Krishna lamproites there are currently three main theories put forward for their formation. Chalapathi Rao et al. (2004) suggested that the source region underwent an extensive initial depletion involving komatiitic type melt extraction, followed by subsequent enrichment by a depleted MORB-type source. Paul et al. (2007) proposed that they were derived from partial melting of a mantle source that was metasomatically enriched in Ti and Fe. This same study also suggested that the lamproites were derived from depths shallower than the garnet stability field and their source regions were shallower than those of the kimberlites in the Eastern Dharwar Craton (EDC). Chakrabarti et al. (2007) maintained that the Krishna lamproites were derived by partial melting of metasomatized subducted Achaean komatiite, in a peridotite mantle-source assemblage. In their study, Chakrabarti et al. (2007) argued that the Pb-isotopic signatures (high 207Pb low 206Pb) and superchondritic Nb/Ta ratios in Krishna

lamproites ruled out their derivation from a metasomatized sub-continental lithospheric mantle source and instead suggested an Archaean crustal component in the source (Chakrabarti et al., 2007).

There are relatively few known kimberlite and lamproite occurrences before ~1100 Ma, e.g., lamproite in Karelia, Russia 2.74 Ga (Sergreev et al., 2007); Kimberlite located in the Guyana Craton, Venezuela age dated at 1732 ± 82 using Rb–Sr chronometry (Nixon et al., 1992). The Proterozoic kimberlites and lamproites of southern India (Fig. 4.1) therefore provide a rare opportunity to study some of the oldest known occurrences of these rock types.

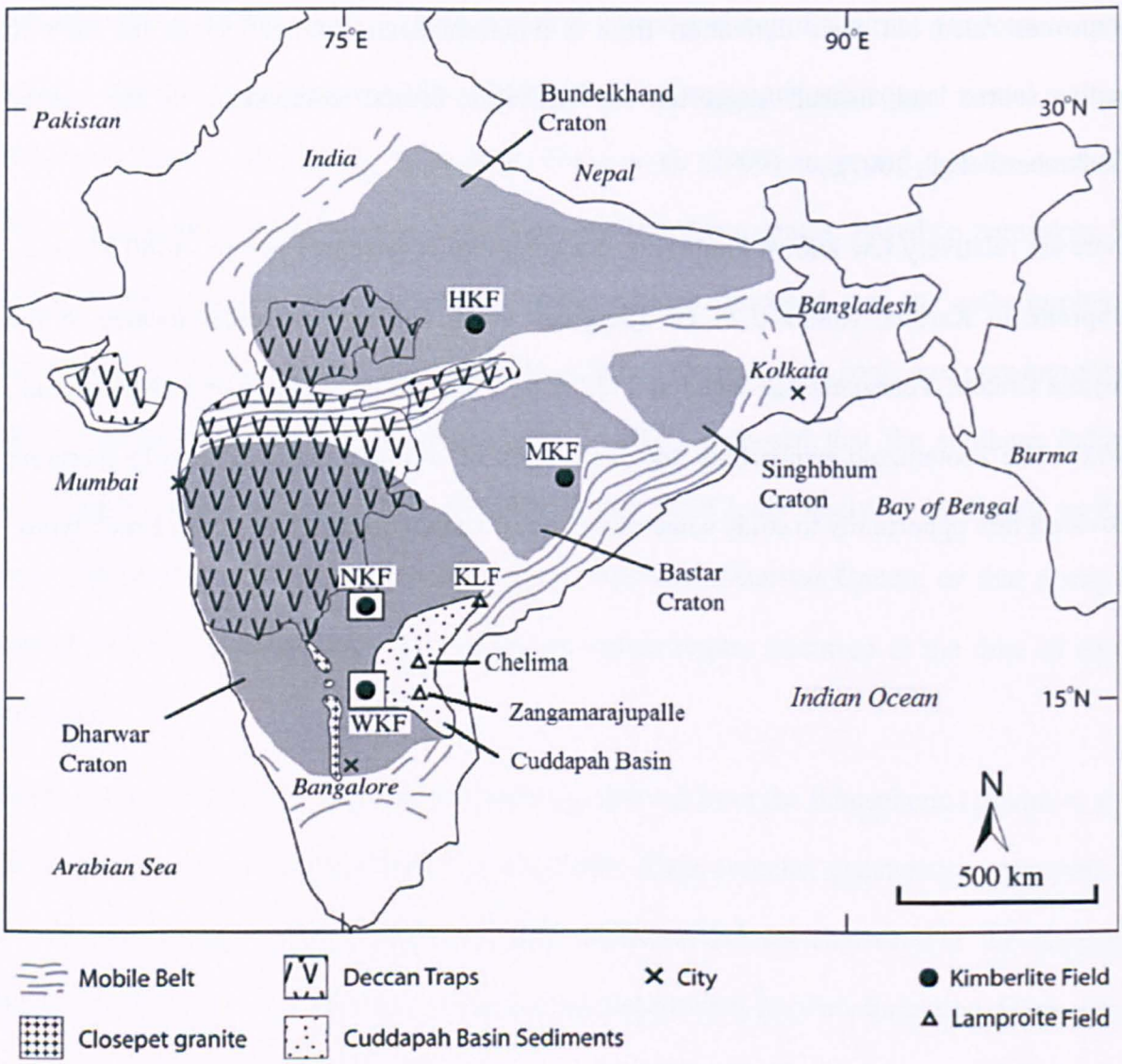

Figure 4.1. Location of the Krishna lamproites (KLF) relative to the major tectonic domains of southern India. HKF: Hinota Kimberlite Field; MKF: Mainpur Kimberlite Field; NKF: Narayanpet Kimberlite Field; WKF: Wajrakarur Kimberlite Field. Modified from Paton et al. (2009).

Previously published age data for the southern Indian kimberlites has been controversial, with different dating techniques showing wide ranges in age, whilst several individual pipes remain undated. It has been proposed that the kimberlites in the EDC had a contemporaneous emplacement at around 1.1 Ga (Kumar et al., 2007). The age of the Majhgawan lamproite body (1067 ± 31 Ma) located 1000 km to the north of the Wajrakarur kimberlite field, fuelled

speculation that ultrapotassic, alkaline and mafic magmatism at this time occurred on a greater scale across India. Kumar et al. (2007) suggested that the 1.1 Ga potassic–ultrapotassic and alkaline mafic-magmatism in India was a part of a global geo-dynamic event as kimberlites and lamproites of similar ages are recognized worldwide in countries such as Australia, Greenland, Liberia, North America, Scandinavia and South Africa.

This study presents robust new ages for the emplacement of some southern Indian kimberlites and lamproites and uses Ar–Ar age dating techniques on phlogopite separates. Our work focuses predominantly on the Krishna lamproites, which in particular lack reliable data to constrain their emplacement age(s). These age data are then combined with geochemical data from the kimberlites and lamproites to provide further constraints on the source region, and primary magma composition, prior to kimberlite and lamproite emplacement. Our new age data for the kimberlites and lamproites also provides insight into the geodynamic evolution of this region.

4.2. The southern Indian kimberlites and lamproites

The majority of kimberlite and lamproite intrusions in the region occur within the Eastern Dharwar craton (EDC) (Fig. 4.1). Kimberlites crop out to the west of the Cuddapah Basin, whilst lamproites intrude the basin and its north-eastern margin. Among these are the Krishna lamproites (Fig. 4.1), which are thought to be some of the oldest lamproite occurrences globally (Chalapathi Rao et al., 2004), and speculated to be the sources of several of the notable Indian diamonds (Chakrabarti et al., 2007).

The EDC is primarily composed of ancient (>2 Ga), greenschist-to granulite-facies schists and gneisses (Chalapathi Rao et al., 2004). The Eastern Ghat orogeny (1.3–1.6 Ga) affected the EDC, resulting in a narrow, highly deformed granulite-facies belt extending from Chennai to near Kolkota. The ~2.0 Ga old Cuddapah Basin (Anand et al., 2003) covers an area of

around 44,000 km^2 (Nagaraja Rao et al., 1987) and lies within the EDC. It comprises a 6–12 km thick succession of igneous and sedimentary rocks of Early to Late Proterozoic age.

The kimberlites in the EDC predominantly occur in two spatially separated groups: the diamondiferous Wajrakarur kimberlite field (WKF) and the Narayanpet kimberlite field (NKF) (Fig. 4.2).

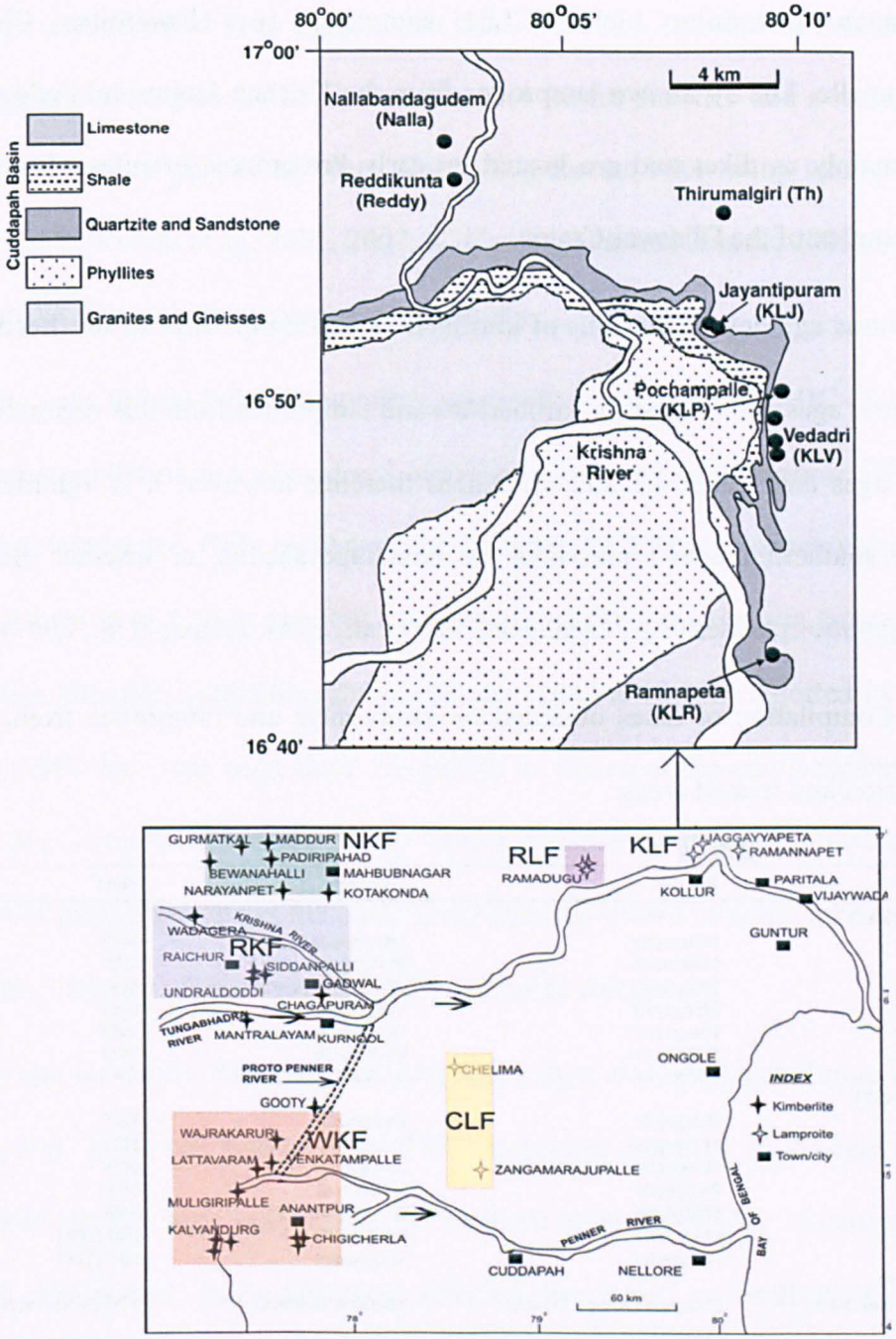

Figure 4.2. Location and extent of kimberlite and lamproite fields around the Cuddapah Basin, showing the locations of individual pipes. Modified from Chalapathi Rao and Srivastava (2009). The inset shows the location of the KLF expanding north to provide a more detailed map of the Krishna lamproite field (KLF) showing the location of the individual lamproite pipes including Pochampalle (KLP on diagram). Modified from Chakrabarti et al. (2007).

The Cuddapah Lamproite Field (CLF) comprises two lamproites Chelima and Zangamarajupalle. The 30 known lamproites from the Krishna Lamproite Field (KLF) (Fig. 3.2) occur mainly as dikes and are hosted by early Proterozoic granites of the Peninsular Gneissic Complex of the Dharwar Craton.

4.3. Previous age determinations of kimberlites and lamproites in southern India

All radiometric ages determined for kimberlites and lamproites from this region have yielded Proterozoic ages (see Table 4.1 and references therein); however, it is vigorously debated whether the southern Indian kimberlites are contemporaneous, or whether they represent separate magmatic episodes (e.g., Chalapathi Rao et al., 2004; Kumar et al., 2007).

Table 4.1: Compilation of dates obtained on kimberlites and lamproites from the Eastern Dharwar Craton and related areas.

Date (Ma)	Method	Material	Samples[a]	Field	Authors[b]
Wajrakarur kimberlite field (WKF)					
1093±20	Rb–Sr	Phlogopite	Muligiripalle pipe 5	WKF	K et al. 93
1153±17	K–Ar	Phlogopite	Muligiripalle pipe 5	WKF	CR et al. 96
1091±20	Rb–Sr	Phlogopite	Wajrakarur pipe 1	WKF	K et al. 93
1092±15	Rb–Sr	Phlogopite	Wajrakarur pipe 2	WKF	K et al. 93
1102±23	Rb–Sr	Phlogopite	Wajrakarur	WKF	K et al. 07
1124±5	U–Pb	Perovskite	Wajrakarur	WKF	K et al. 07
1091±10	Rb–Sr	Phlogopite	Venkatampalle pipe 7	WKF	K et al. 93
Narayanpet kimberlite field (NKF)					
1363±48	K–Ar	Phlogopite	Kotakonda	NKF	CR et al. 96
1401±5	Ar–Ar	Phlogopite	Kotakonda	NKF	CR et al. 99
1085±14	Rb–Sr	Phlogopite	Kotakonda	NKF	K et al. 01
1099±12	Rb–Sr	Phlogopite	Mudalabad	NKF	K et al. 01
1167±86	K–Ca	Phlogopite	Narayanpet	NKF	G & K 08
1093±4	Rb–Sr	Phlogopite	Siddanpalle	NKF (SKF)	K et al. 07
1063±41	K–Ca	Phlogopite	Siddanpalle	NKF (SKF)	G & K 08
Mainpur kimberlite field (MKF)					
60–65	Ar–Ar and U–Pb	Phlogopite and perovskites	Behradih Kodomali	MKF (~700 km N)	L et al. 2010
Hinota kimberlite field (KKF)					
1067±31	Rb–Sr	Phlogopite	*Majhgawan*	HKF (1000 km N)	K et al. 93
Cuddapah basin lamproites (CB)					
1350±52	K–Ar	Phlogopite	*Chelima*	CB	CR et al. 96
1418±8	Ar–Ar	Phlogopite	*Chelima*	CB	CR et al. 99
1354±17	Rb–Sr	Phlogopite	*Chelima*	CB	K et al. 01
1090	Rb–Sr	Phlogopite	*Zangamarajupalle*	CB	K et al. 01
Krishna lamproite field (KLF)					
1384±18	K–Ar	Phlogopite	*Ramannapeta*	KLF	CR et al. 96
1224±14	Rb–Sr	Phlogopite	*Ramannapeta*	KLF	K et al. 01

[a] Kimberlites: plain type; *lamproites: italics.*
[b] K et al. 93: Kumar et al. (1993); CR et al. 96: Chalapathi Rao et al. (1996); CR et al. 99: Chalapathi Rao et al. (1999); K et al. 01: Kumar et al. (2001); K et al. 07: Kumar et al. (2007); G & K 08: Gopalan and Kumar (2008); L et al., 2010: Lehmann et al. (2010).

Kumar et al. (2007) argued for a contemporaneous emplacement at around 1.1 Ga for all the kimberlites in the Eastern Dharwar Craton. In contrast, Chalapathi Rao et al. (1996, 1999)

used their age data (Table 4.1) to suggest that there were two episodes of Proterozoic mafic potassic magmatic activity in the EDC: one at ca. 1.4 Ga for the NKF and a second at 1.1 Ga for the WKF. However, further age data (Table 3.1) for the NKF using various techniques (Rb–Sr and U–Pb; Kumar et al., 2001, 2007; K–Ca; Gopalan and Kumar, 2008) indicated that the NKF and WKF were both emplaced at ~1100 Ma.

There are few ages for the Indian lamproites, especially for those from EDC (Table 4.1) and those that are published are considered unreliable because of alteration effects in the kimberlite and lamproites. Only one lamproite from the KLF (Ramannapeta) has been dated previously. Kumar et al. (2001) reported a Rb–Sr age for the Ramannapeta lamproite (1224 ± 14 Ma), which although contradicts the K–Ar age (1384 ± 18 Ma) reported by Chalapathi Rao et al. (1996), has been used more frequently to represent the emplacement age of the entire KLF (e.g., Chakrabarti et al., 2007). This is because the possibility that excess Ar in mantle-derived phlogopite causes the older K–Ar ages (as shown by some Siberian and South African kimberlites, e.g., Pearson et al., 1995) cannot be ruled out.

For the Chelima lamproite, the ages of Chalapathi Rao et al. (1996) and Kumar et al. (2001) are in agreement. However, Kumar et al. (2001) suggested that their Rb-Sr ages for Chelima and Zangamarajupalle were only tentative, as these samples display extensive secondary carbonation, which may have adversely affected the "true" crystallization ages of the lamproites. The K–Ar age reported by Chalapathi Rao et al. (1996) has also been considered unreliable (Kumar and Gopalan, 2005) due to the possibility of excess Ar in mantle-derived phlogopite leading to the older K–Ar ages.

From Table 4.1 and the preceding discussion it is apparent that the recent age determinations provide a compelling argument for contemporaneous kimberlite emplacement in the EDC at around 1100 Ma. However, little reliable data exists for the lamproites from Southern India,

and in particular the KLF; the published ages (Table 4.1) suggest that the kimberlites are not contemporaneous with the older lamproites.

In this study we employed the Ar–Ar method to determine new age data to better constrain the age of the KLF. Whilst the use of the K–Ar and Ar–Ar methods to date the kimberlites and lamproites of southern India has been questioned (Kumar et al., 2007), studies elsewhere have successfully dated kimberlites and lamproites through applying the Ar–Ar dating technique to phlogopite (Phillips, 1991), yielding ages which were consistent with previous age determinations using different methods. Lehmann et al. (2010) recently used the Ar–Ar age dating technique on phlogopite separates as well as U–Pb on perovskites to date kimberlites in the MKF, with both methods providing a similar age. We have also obtained new dates on some kimberlites from the EDC which agree with well-constrained published ages (Chalapathi Rao et al., 1999; Kumar et al., 2007). Comparison of our data with previously published ages allows us to assess the reliability of our age data for the KLF.

4.4. Samples, methodology and analytical techniques

4.4.1. Samples analysed and assessment of alteration

Samples were collected from the interior of each exposure (locations listed in Table 3.2). The kimberlites are classified as 'Group I' kimberlites on the basis of their mineralogy, in agreement with previous studies (e.g., Chalapathi Rao et al., 2004). Kimberlites and lamproites are susceptible to alteration processes and crustal contamination, and given the Proterozoic age of the rocks in this study, any interpretation of geochemical data must first consider the potential effect of these processes on the samples.

To assess any contamination or alteration effects, we first used the Ilmenite index of Taylor et al. (1994), which identifies kimberlites and lamproites that may have accumulated or assimilated ilmenite megacrysts and xenocrysts. We also used loss on ignition (LOI) data as a

proxy for alteration (Chalapathi Rao et al., 2004). Samples with high LOI are considered indicative of secondary alteration, commonly manifested in thin sections through increased abundances of secondary carbonate minerals and talc. Gd/Lu ratios of samples were also considered, where low values are indicative of HREE-enriched crustal contaminants (Le Roex et al., 2003). A cut-off value of <58 was considered contaminated (Paton et al., 2009). The contamination index (CI, a measure of the proportions of clay minerals and tectosilicates relative to ferro-magnesian minerals – olivine, phlogopite) of Clement (1982) was used in this study, where a CI value of <1.5 is considered uncontaminated for kimberlites (Mitchell, 1986). The kimberlite samples used in this study are below this cut-off value; however the lamproites show higher values, which are not unusual for such mica-rich rocks (Chalapathi Rao et al., 2004). CI values in the whole suite of samples from the Krishna lamproites ranged from 3.79 to 9.23.

Care was taken to ensure that all the samples we collected from the EDC were as fresh as possible. Those chosen for dating in this study are among the freshest and showed minimal contamination and alteration as identified by CI, LOI, Gd/Lu and Ilmenite index determinations for our sample suite (Table 4.2).

Table 4.2: Location and contamination/alteration of samples.

Name	Longitude (°N)	Latitude (°E)	CI	LOI (%wt loss)	Ilmenite index	Gd/Lu
Muligiripalle (K)	14°85'74"	77°32'06"	1.34	6.24	0.59	74.50
Tummatapalle (K)	14°84'55"	77°30'09"	1.19	8.62	0.67	80.64
Pochampalle (L)	16°83'79"	80°16'61"	5.09	3.91	1.23	92.69
Pochampalle G (L)	16°84'59"	80°16'38"	4.41	3.40	0.62	74.44

4.4.2. Ar–Ar dating technique

Age data for three samples are presented here, including two kimberlites (Muligiripalle Pipe 5 and Tummatapalle pipe 13) from the WKF and one lamproite (Pochampalle) from the KLF. The Pochampalle lamproite is a NW-SE trending body located 2.5 km west of the

Pochampalle village. Petrographic analysis of thin sections identified samples with the most suitable phlogopite grains for dating. The samples with freshest phlogopite were selected, with several samples discounted on the basis of high calcite content and alteration of phlogopite to chlorite. Once selected, microprobe analysis of phlogopite within each selected sample was used to determine the mineral chemistry (Fig. 4.3).

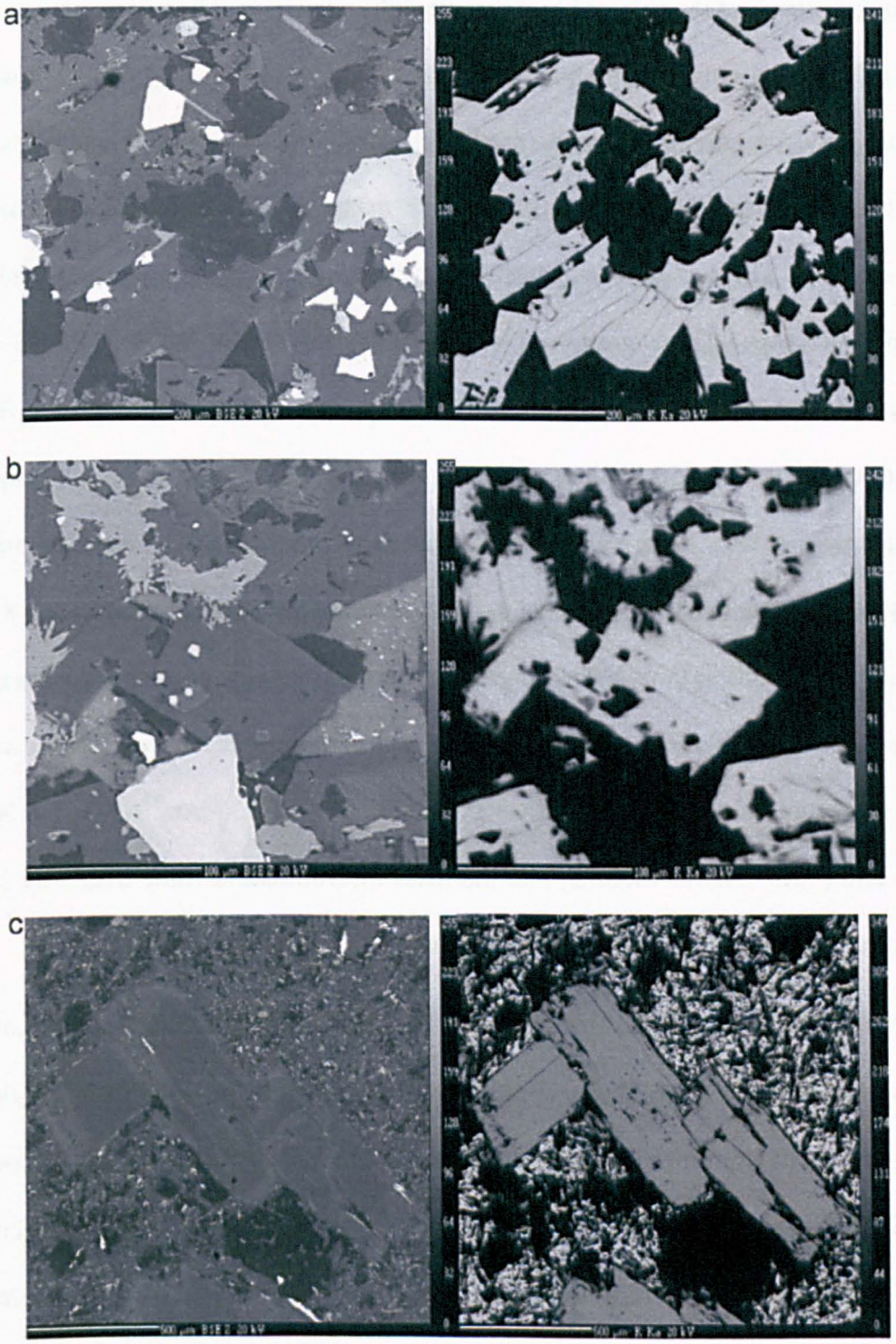

Figure 4.3. Typical microtextures of phlogopite in the analysed samples. Each set shows a back-scattered electron image (left) and an element map for potassium (right). (a) Muligiripalle kimberlite (pipe 5, WKF), scale bars 200 μm; (b) Tummatapalle kimberlite (pipe 13, WKF), scale bars 100 μm; (c) Pochampalle lamproite (KLF), scale bars 500 μm.

Small blocks of each of the selected samples were then sawn, avoiding any crustal xenoliths, and crushed in a jaw crusher. The fragments were then sieved into fractions from which the phlogopite could be carefully picked (predominantly 300–500 μm in length). The picked phlogopite grains were then washed in ace-tone using an ultrasonic bath to remove any adhering material. The visibly fresh grains with fewest inclusions were then selected using a binocular microscope. These grains were then packaged in aluminium foil and sent for sample irradiation at McMaster University in Ontario, Canada. Irradiation flux was monitored using the GA1550 biotite standard with an age of 98.79 ± 0.54 Ma (Renne et al., 1998). Sample J values were calculated by linear interpolation between two bracketing standards and are included in Table 3; a standard was included between every 8 and 10 samples in the irradiation tube. Blanks were measured either side of each measurement and used to correct each unknown, and ^{37}Ar decay and neutron-induced interference reactions using the correction factors $(^{39}Ar/^{37}Ar)Ca = 0.00065 \pm 0.000033$. $(^{36}Ar/^{37}Ar)Ca = 0.000264 \pm 0.000013$ and $(^{40}Ar/^{39}Ar)K = 0.0085$, and the mass discrimination value used was 283. The decay constant of Steiger and Jager (1977) was used.

Samples were loaded into an ultra-high-vacuum laser port and placed under a heat lamp for 8 h to reduce atmospheric blank levels. Samples were analysed by total fusion of single grains using Nd- YAG 1064 nm infrared laser, or Nd-YAG 213 nm UV laserprobe, both coupled to a MAP 215-50 mass spectrometer. Gases were gettered for 5 min using two SAES getters one at 450 °C and one at room temperature, and a liquid nitrogen cold trap, before inlet to the mass spectrometer. Peaks between ^{35}Ar and ^{41}Ar were scanned 10 times and amounts extrapolated back to the inlet time. Each analysis was background corrected using blank measurements bracketing every 1–2 samples.

The infrared-laser single-grain-fusion technique was applied to Muligiripalle Pipe 5 (Mul) and Tummatapalle pipe 13 (Tum) and Pochampalle (POCg) samples. Here individual mineral grains were fused to yield a single age, and the final age is a weighted mean aver-age, error and MSWD as calculated using Isoplot 3a (Ludwig, 2003) and reported at 2σ level. The UV intragrain laserprobe technique was applied to POC and POCg samples, in which mineral grains were large enough to enable several measurements within each grain in order to test for heterogeneity (Fig. 4.4) (e.g., Kelley and Wartho, 2000; Sherlock et al., 2002). Each age determination was derived from a rastered laser pit measuring 75 μm × 75 μm, with a 10 μm diameter beam and reported at 2σ level. In addition, grain margins were analysed using trenches parallel to the grain margins with a beam size of 10 μm. The number of analysis on each grain depended on its size, but can be seen in Fig. 4.4. (The full dataset is available in the appendices: A.2.4).

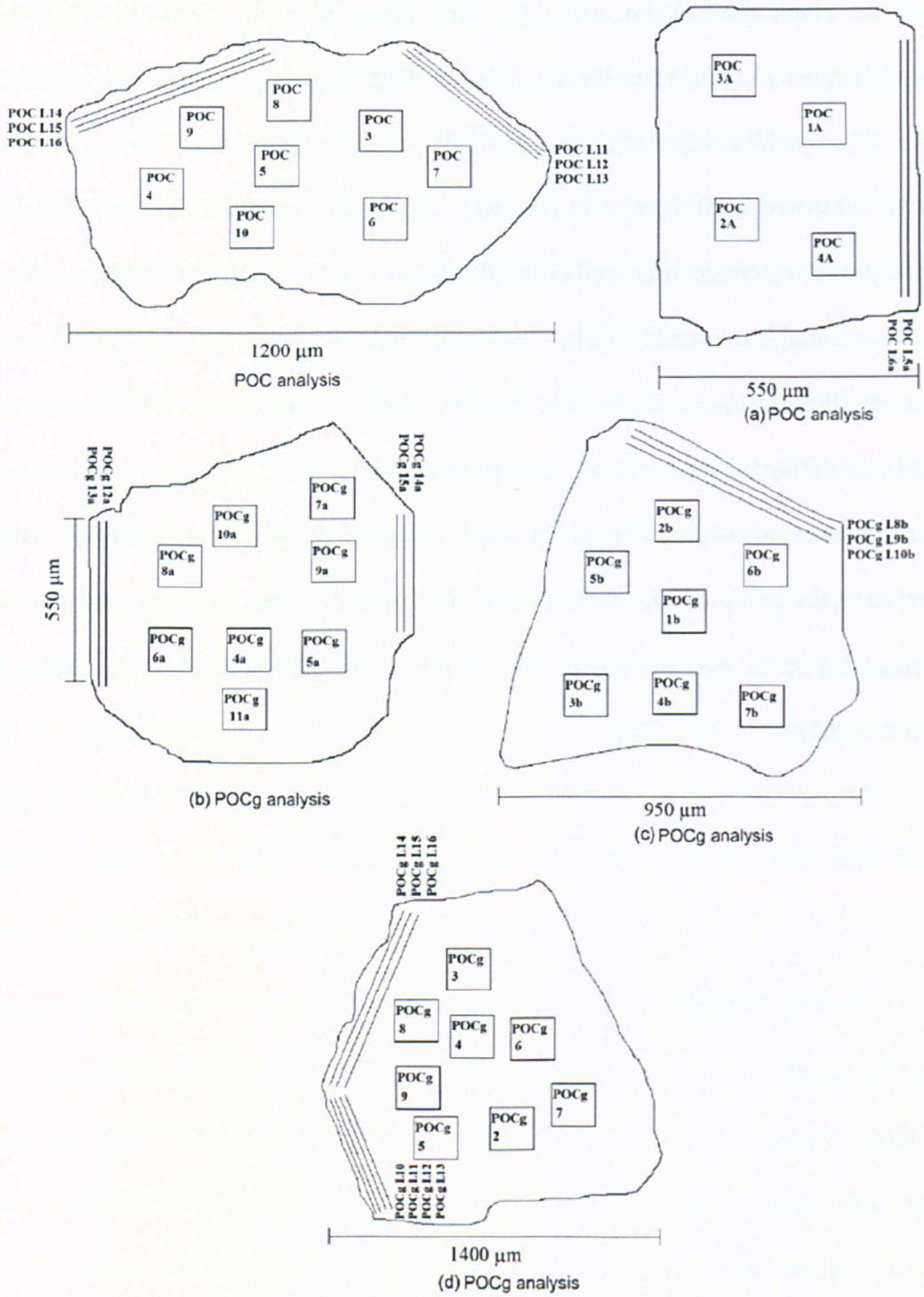

Figure 4.4. Sketches of phlogopite grains analysed using UV intragrain laserprobe technique. Each age determination was derived from a rastered laser pit measuring 75 µm × 75 µm, with a 10 µm diameter beam. The number of analyses on each grain depended on its size.

4.4.3. Bulk-Rock and Isotopic measurements protocol

1–2 kg of visibly unaltered kimberlite and lamproite samples were cut on a rock saw to remove any weathered portions and then reduced to small fragments in a jaw-crusher. These fragments were then crushed to powder in an agate ring mill to produce the powders used in all bulk-rock geochemical analysis. The bulk-rock major-, trace- and REE data was determined at the NHM in London, where as the bulk rock Nd data was obtained at a later date at the Open University.

Two methods were used to obtain bulk-rock major-, trace- and REE data. Major and some minor elements (Al, Ca, Fe, K, Mg, Mn, Na, P, Si, Ti, Ba, Cr, Ni, Sr, Y, and Zr), were analysed using Inductively Coupled Plasma Atomic Emission Spectroscopy (ICP-AES). 100 mg of powdered sample was fused with 300 mg $LiBO_2$ (lithium metaborate) flux, and then dissolved in dilute HNO_3. The concentrations of selected major- and trace-elements were then determined by ICP-AES at the Natural History Museum, London. These solutions were not spiked. Reference materials were selected based on their similarities to the samples to be analysed and included BCR-1 (major and trace) and GA (trace and REE).

$HF/HClO_4$ (hydrofluoric acid/perchloric acid) digestion was used for other minor-, trace- and REE analyses. In each case, 500 mg of powdered sample underwent a total digestion in $HF/HClO_4$. The resulting solution was evaporated to dryness, and the residue was then dissolved in dilute nitric acid. The concentrations of trace-elements were then determined by ICP-AES and ICP-MS, as required, at the Natural History Museum, London. Solutions for ICP-MS were diluted a further 10 times and were spiked with 1 ppb In and 1 ppb Rh as internal standards prior to analysis. ICP-AES solutions were not spiked. To monitor instrumental drift and precision the standard BCR-1 was used. Major, trace and REE element analysis were found to be better than ±20% (2 s.d.) to that of the certified values, with the

exception of Ni, Cr, Sn and Be which were found to be better than ± 30% (2 s.d.) to that of the certified values and Bi, Cd, and Ta which showed slightly greater deviation to that of certified values.

The four dated samples underwent Nd isotope analysis. 50 mg of powdered sample was weighed in each case and spiked with a $^{150}Nd/^{144}Nd$ solution. These samples underwent a total digestion in HF/HNO_3. Nd and Sm were separated from the dissolved samples by standard ion-exchange techniques (Cohen et al., 1988), using cation columns to collect the REE fraction, which was then passed through HDEHP columns to collect Nd and Sm fractions, which were evaporated to dryness. 1 µl of 2M HCl was added to the Nd collected for each sample and then loaded with 0.6 µl of 0.01M H_3PO_4 onto the centre of an outgassed Re filament. Nd isotopic ratios were measured in the static mode using a Triton thermal ionization mass spectrometer at the Open University. Reproducibility of the La Jolla Nd standard over the analysis period was $^{143}Nd/^{144}Nd = 0.511849 \pm 0.000002$ (8 ppm, 2SD).

Results

4.1.1. Ar–Ar dating

The Ar–Ar dating results are summarised in Table 3.3 and reported to 2σ. Where infrared laserprobe analysis is performed on mineral separates each age is derived from the total fusion of an individual mineral grain.

Table 4.3: Ar-Ar Results

Sample	Rock type	Method[a]	Wtd mean (Ma)	Error (±)	MSWD	Number of analyses
Muligiripalle	Kimberlite	TF	1109	6	2.7	12 grains fused
Muligiripalle	Kimberlite	TF	1115	4	0.78	6 grains fused
Tummatapalle	Kimberlite	TF	1105	12	0.24	10 grains fused
Pochampalle	Lamproite	UV	1575	20	1.3	14 points on single grain (Fig.4.4a)
Pochampalle	Lamproite	UV	1568	55	11.3	6 points on single grain (Fig.4.4b)
Pochampalle	Lamproite	TF	1523	110	16.3	6 grains fused
Pochampalle G	Lamproite	UV	1563	25	6.8	12 points on single grain (Fig.4.4c)
Pochampalle G	Lamproite	UV	1564	51	0.52	8 points on single grain (Fig.4.4d)
Pochampalle G	Lamproite	UV	1583	16	2.5	15 points on single grain (Fig.4.4e)

[a] TF: total fusion analysis; UV: ultraviolet laser *in situ* analysis.

Kimberlites: Muligiripalle Pipe 5 and Tummatapalle Pipe 13

For the Muligiripalle Pipe these ages range from 1088 ± 5 to 1149 ± 21 Ma (n = 18) with a weighted mean age of 1113 ± 3 Ma (MSWD = 0.96; n = 17). For the Tummatapalle Pipe the age range from 1098 ± 16 to 1138 ± 29 Ma (n = 10), with a weighted mean age of 1105 ± 12 (MSWD = 0.24; n = 10).

Lamproite: Pochampalle

Infrared laserprobe analysis yields individual mineral ages in the range 1408 ± 5 to 1614 ± 8 Ma (n = 6). With such a scatter in age data it is important to assess the spatial variation of ages within individual mineral grains which is achievable using the ultraviolet intra-grain technique. Five different mineral grains from two samples have been analysed using this technique (Fig. 3.4). From sample POC ages within the internal parts of the mineral grains range from 1543 ± 39 to 1611 ± 32 Ma, and from the grain margins range from 1480 ± 35 to 1625 ± 15 Ma (n = 8). From sample POCg ages within the internal parts of the mineral grains range from 1463 ± 71 to 1646 ± 100 Ma (n = 24) and from the grain margins range from 1507 ± 38 Ma to 1698 ± 30 Ma (n = 11).

4.1.2. Geochemical and isotopic data on the Krishna lamproites

Major, trace and REE data were obtained on lamproites from 9 different locations (the full dataset is available in the appendices: A.2.6. and A.2.7). Two samples were analysed from two of the lamproites, Vedadri (VEDN and VEDS) and Pochampalle (POC and POCg); in each case, the two samples were collected from different locations within the same lamproite body. 8 of the lamproite samples are from the KLF, whilst one (Chelima) is located within the Cuddapah Basin (Fig. 4.1).

All of the lamproites in this study are LREE enriched, as shown by elevated $(La/Yb)_N$ values (Fig. 4.5).

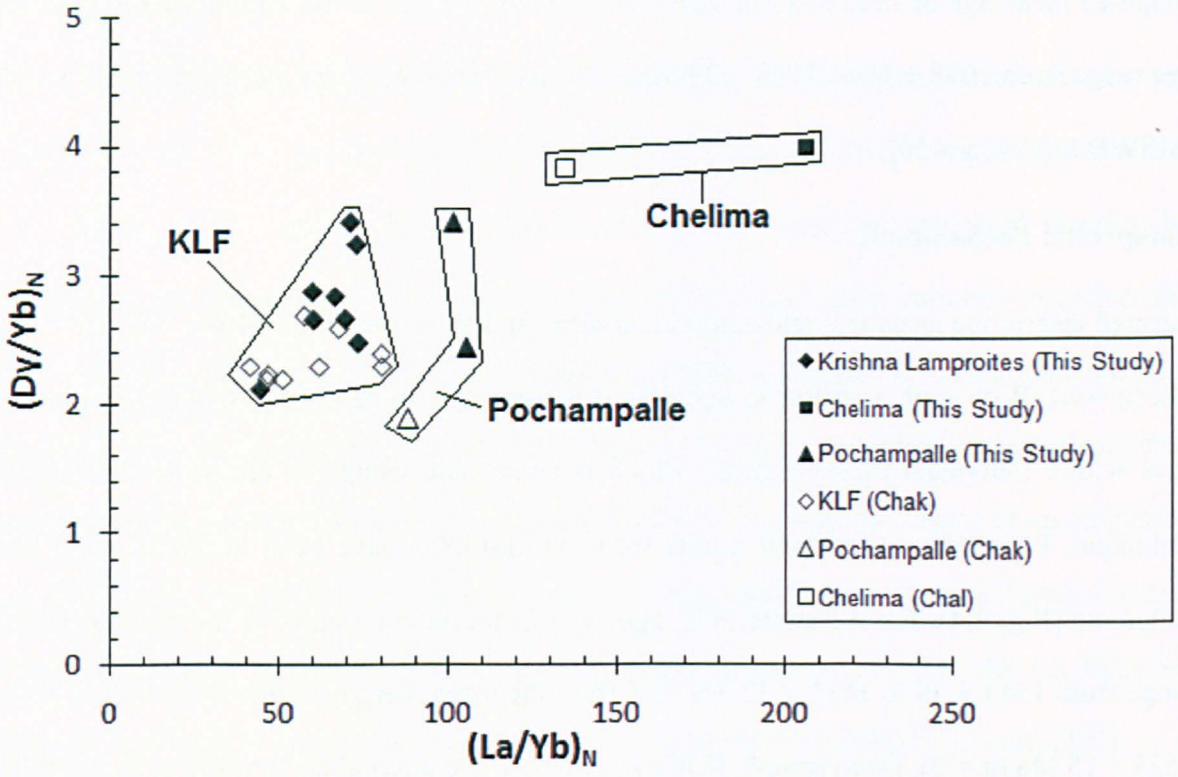

Figure 4.5. Plot of Dy/Yb_N against La/Yb_N (normalized to chondrite; values from Anders and Grevesse, 1989) for the Krishna lamproites and Chelima lamproite.

For the Krishna lamproites, $(La/Yb)_N$ = ~45–75. The Pochampalle lamproite shows even greater LREE enrichment compared to the rest of the KLF samples with $(La/Yb)_N$ = ~100. The Chelima lamproite has the highest degree of LREE enrichment among the sample suite analysed in the present study, with $(La/Yb)_N$ = ~200. These values are comparable to other published ratios for the KLF $(La/Yb)_N$ = 51–173 (Chalapathi Rao et al., 2010) and Chelima $(La/Yb)_N$ = 72–247 (Chalapathi Rao et al., 2004).

On a chondrite-normalized REE plot (Fig. 4.6), all lamproites from the EDC display similar LREE-enriched patterns.

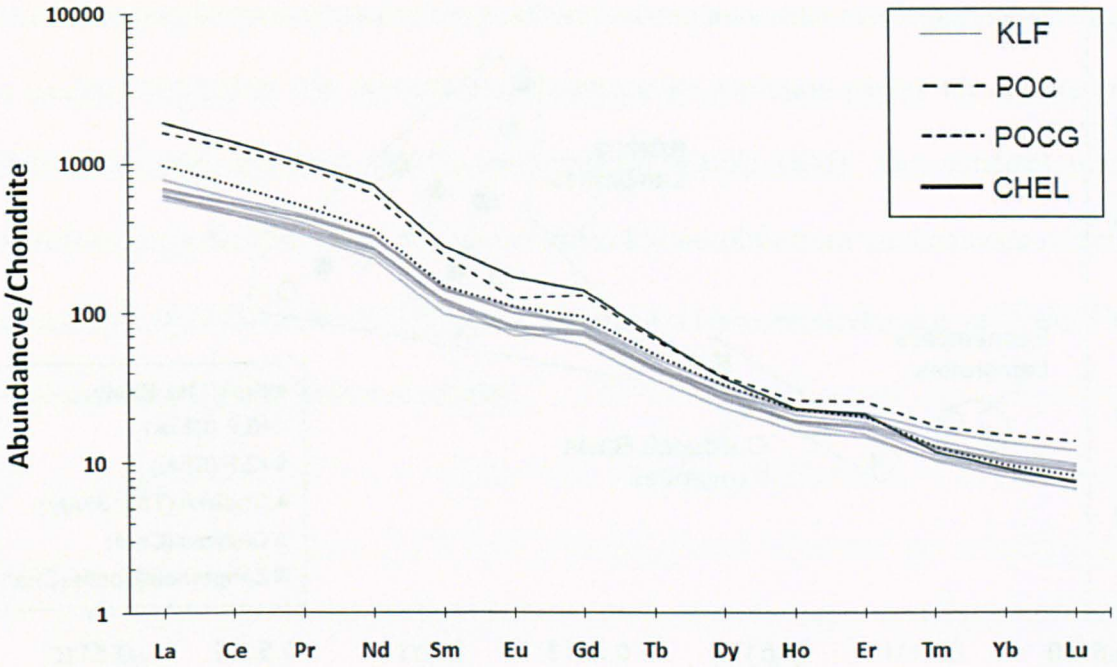

Figure 4.6. Chondrite-normalized (values from Anders and Grevesse, 1989) REE plot for the Krishna lamproites (average abundance), the Chelima lamproite (solid line), and the two Pochampalle lamproite samples (dashed lines).

The Chelima lamproite shows the steepest REE pattern. Two samples were collected from different locations from the Pochampalle lamproite and show slightly different REE patterns (Fig. 4.6). The POC sample shows a trend closer to those of the KLF, especially for the HREE, though with a higher La/Yb ratio due to greater LREE enrichment. The POCg sample has an even higher La/Yb ratio due to its extreme LREE enrichment (similar to that of Chelima), but has higher HREE con-tents than Chelima. The HREE enrichment may be due to variations in the source but can also be attributed to crustal contamination. However, even if the samples have undergone some degree of crustal contamination, it is unlikely to have affected the isotopic ratios of small-fraction melts, because the concentrations of Sm and Nd in crustal rocks is likely to be much lower than in the kimberlitic melts (e.g., Fraser et al., 1985; Gibson et al., 1995).

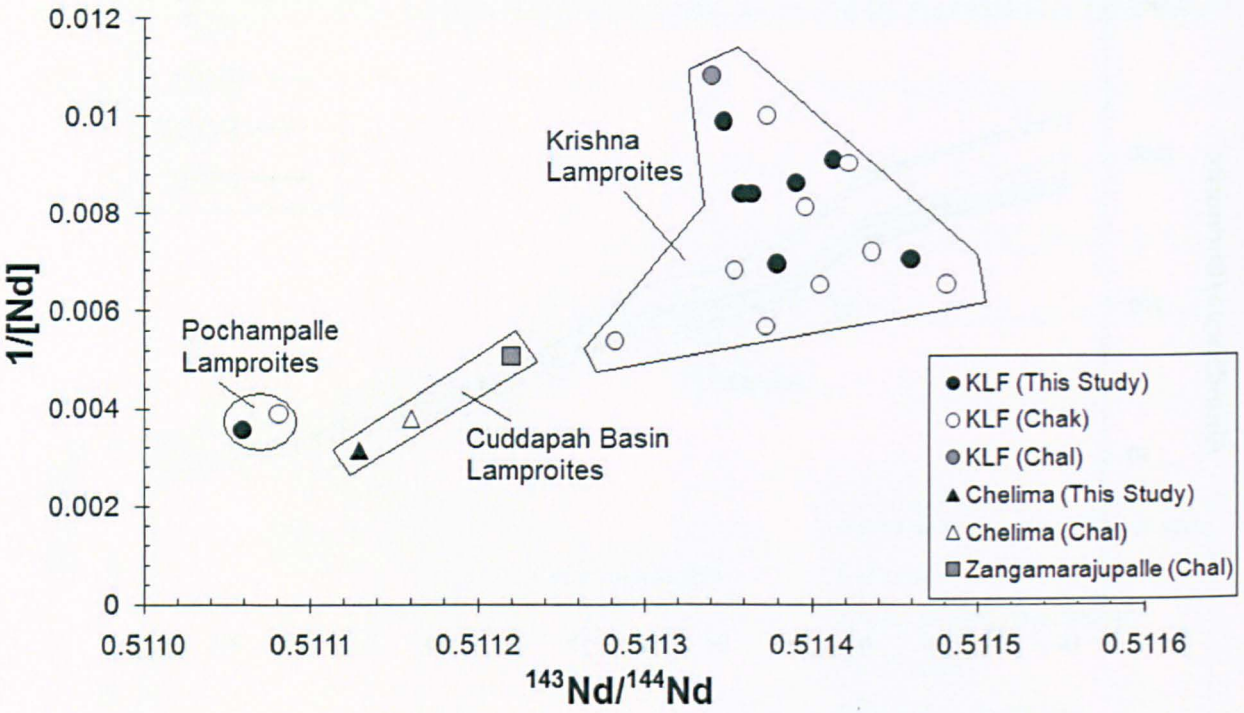

Figure 4.7. Plot of 1/[Nd] against $^{143}Nd/^{144}Nd$ ratios for the Krishna lamproites (including Pochampalle) and the CLF (including Chelima). Data are from this study, Chakrabarti et al. (2007) (Chak) and Chalapathi Rao et al. (2004) (Chal).

The Pochampalle ($^{143}Nd/^{144}Nd(m)$ = 0.511059) and Chelima ($^{143}Nd/^{144}Nd(m)$ = 0.511129) lamproites also show lower Nd isotopic values than the rest of the lamproites in the KLF ($^{143}Nd/144Nd(m)$ = 0.511348–0.511459) (Fig. 4.7). In contrast to the REE data, the $^{143}Nd/^{144}Nd$ isotopic ratio of Pochampalle is not intermediate between that of Chelima and the Krishna lamproite group.

The lower $^{143}Nd/^{144}Nd$ ratio of the Pochampalle lamproite suggests a closer affinity with the CLF, particularly Chelima, than with the rest of the KLF samples. The broad spread of the KLF Nd data precludes robust interpretations of a mixing array involving the Cuddapah Basin Lamproites (CBL), Pochampalle and the Krishna lamproites. However, the difference in Nd isotopic sig-nature between Pochampalle and the other Krishna lamproites is striking.

The Nd evolution through time of the southern Indian kimberlites and lamproites in this study is summarised in Fig. 4.8, and compared with model evolution curves for depleted mantle (DM; Workman and Hart, 2005), and enriched mantle (EM). The enriched mantle is modelled using the εNd value of a garnet lherzolite xenolith from the Lattavaram kimberlite in the EDC (Karmalkar et al., 2009), and assuming a representative value of $^{143}Nd/^{144}Nd$ for enriched mantle (EMI; Hart et al., 1992).

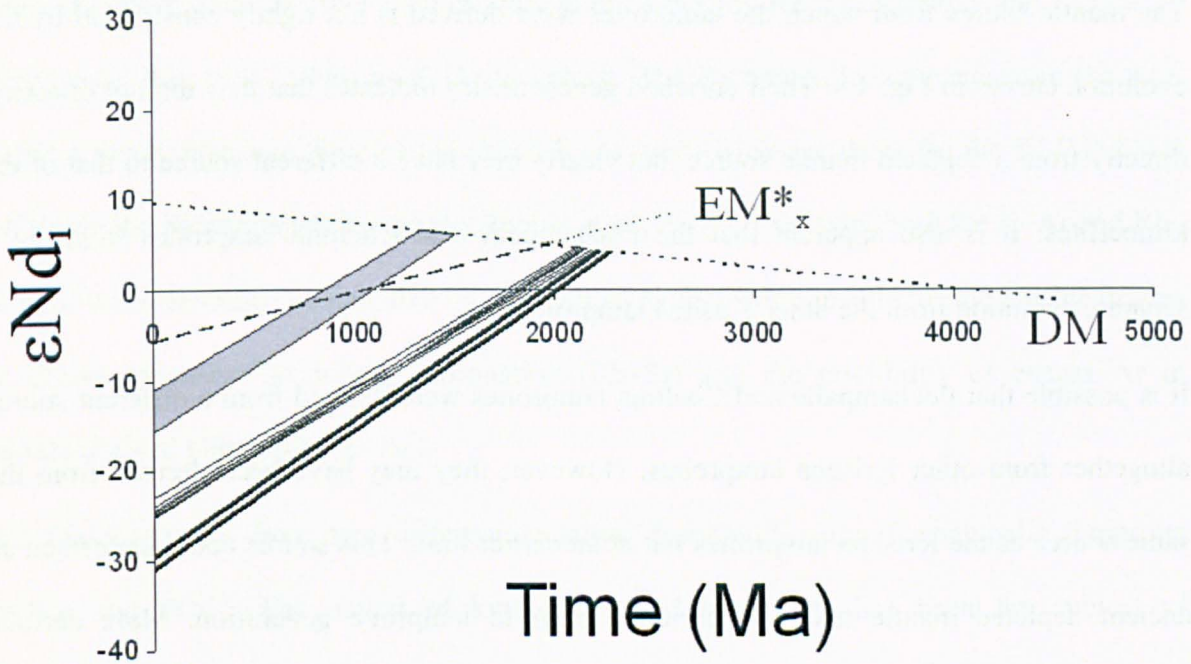

Figure 4.8. Plot of εNd against time for the lamproites (solid lines) from the EDC (data from this study). The Pochampalle and Chelima lamproites are shown as bolder solid lines. Also shown is the range of kimberlites data from the EDC (shaded field; Paton et al., 2009). The single bold dashed line represents the potential Nd evolution of enriched mantle (EM*x) beneath India, modelled using the εNd of a garnet lherzolite xenolith from the Lattavaram kimberlite in the EDC (Karmalkar et al., 2009), combined with a representative value of $^{147}Sm/^{144}Nd$ (0.5116) for EMI (Hart et al., 1992). The depleted mantle (DM) trend (dotted line) uses data from Workman and Hart (2005).

The εNd evolution trajectory of the kimberlites intersects the EM*x model evolution line at around 1 Ga, which corresponds to the emplacement age of the EDC kimberlites. However, the DM and EM*x model evolution lines intersect much earlier (1.9–2.0 Ga). One model for petrogenesis of the EDC kimberlites consistent with these Nd evolution data is that the kimberlite magmas were derived at around 1 Ga from an initially depleted mantle source that had been enriched at around 1.9–2.0 Ga.

The mantle source from which the lamproites were derived is not tightly constrained by the evolution curves in Fig. 4.8. Their enriched geochemistry indicates that they did not originate directly from a depleted mantle source, but clearly they have a different source to that of the kimberlites. It is also apparent that the Pochampalle and Chelima lamproites followed a separate evolution from the other Krishna lamproites.

It is possible that Pochampalle and Chelima lamproites were derived from a different source altogether from other Krishna lamproites. However, they may have been derived from the same source as the Krishna lamproites but at an earlier time. This source could have been an ancient depleted mantle that was enriched prior to lamproite generation. More definite conclusions are difficult to draw from Nd evolution modelling of the lamproites due to the isotopic heterogeneity of the sub-continental lithospheric mantle, even on relatively small length scales.

4.5. Discussion

Despite the recent increase in scientific interest in the kimberlites and lamproites of the Dharwar Craton in southern India, the ages of the kimberlites and in particular lamproites are poorly con-strained. An age of around 1.1 Ga for both the kimberlites in the WKF and NKF appears to be well supported, although many pipes within these fields are yet to be dated. The only lamproite previously dated from the KLF is the Ramannapeta lamproite, even though

there are many lamproites in the KLF; it would seem presumptuous to assume an age for the entire field based on one age from one lamproite. However, this age has been used in several studies to represent an age for the KLF mainly because of a lack of any other reliable age data (Reddy et al., 2003; Paul et al., 2007; Chakrabarti et al., 2007).

The Ar–Ar ages for Muligiripalle of 1113 ± 3 Ma and for Tummatapalle of 1105 ± 12 are consistent with previous age determinations for the WKF and in particular Muligiripalle, which has been dated at 1093 ± 20 (Kumar et al., 1993) by Rb–Sr technique and 1153 ± 17 (Chalapathi Rao et al., 1996) by K–Ar technique. The Pochampalle lamproite from the KLF yields a much older age than the published K–Ar and Rb–Sr age dates for the KLF (1224 ± 14 Ma on the Ramannapeta lamproite; Kumar et al., 2001). However, both the K–Ar and Rb–Sr ages were described as tentative by the authors as they were unable to rule out the effects of excess extensive secondary carbonation (Rb–Sr) and the possibility of excess Ar in mantle-derived phlogopite (K–Ar).

We dated samples from two different locations from within the Pochampalle lamproite (POCg and POC). The dating of kimberlites and lamproites has been the subject of discussion, because in many cases phlogopite cores are older than their rims, which is true of the Pochampalle lamproite. In rocks formed and cooled in mid- and upper-crustal settings this is usually attributed to either prolonged cooling imparting an 'age' gradient or partial resetting of a mineral and argon-loss occurring at the rims (e.g., Sherlock et al., 2002). In kimberlites and lamproites the same observed age patterns are argued to be due to a pervasive and uniformly distributed excess argon component derived from a deep fluid source (e.g., Phillips and Onstott, 1988; Phillips, 1991; Phillips et al., 1999) that is then partially outgassed to the grain boundary network during incorporation into the magma chamber (Pearson et al., 1997).

Phillips and Onstott (1988) compared step-heating spectra of two sets of phlogopite mineral separates with in situ data obtained from a single large phlogopite grain using a continuous wave infrared Nd-YAG laser. The step-heating spectra identify the range of ages preserved within the mineral separates but without identifying the spatial distribution of the ages, whilst the laserprobe data identifies the position of the ages within the grain. The resolution of the laserprobe data is limited by the area outside the point of laser-sample interaction that is outgassed due to heat conduction during lasing; Phillips and Onstott (1988) report a resolution of 80–150 μm diameter pits separated by distances of 20–100 μm, which gave sufficient confidence that the individual age measurements were not affected by adjacent laser pits. The age range of ca. 1200 to ca. 1540 Ma from low- to high-temperature steps in the heating spectra indicate a range of ca. 1200 Ma to ca. 2200 Ma (Phillips and Onstott, 1988), the oldest age represented by a single laser spot. The differences were difficult to reconcile but it was considered that the old ages could be 'masked' during physical mineral decrepitation during step-heating and the mixing of different aged reservoirs within the mineral separates. Notably, the volume of phlogopite preserving old apparent ages is a small fraction of the grain and so it is conceivable that during the preparation of the mineral separates by crushing and sieving this low-volume component might not be well represented. The study raised more questions about the behaviour of argon in such high pressure and high temperature minerals.

Phillips (1991) also compared step-heating and laserprobe Ar–Ar data, and analysed matrix and macrocryst phlogopites. The former yielded plateau ages that were consistent with eruption ages and the latter yielded complex release patterns concurring with those reported by Phillips and Onstott (1988). In contrast the laserprobe data (spatial resolution of 100 × 200 μm sized pits in the internal parts of the grain and up to 160 × 400 μm at the rim, separated by 30–80 μm) reveal older cores and younger rims, with similar conclusions to Phillips and

Onstott (1988), in that a high concentration of excess argon was trapped in the macrocrysts prior to eruption, the rims record the eruption age, and the matrix phlogopites record the eruption age (Phillips, 1991). This model dictates that radiogenic argon is retained in minerals in the upper mantle at temperatures of 700 °C or more (Pearson et al., 1997). Kelley and Wartho (2000) were able to test this by analysing well-characterised xenoliths from two different settings, with robust age constraints, using the high spatial resolution ultra-violet laserprobe approach to assess core-rim age differences in detail. The results showed old cores and young rims, and in both settings the older core ages corresponded to magmatic/metasomatic events that were recorded by other isotope systems (Kelley and Wartho, 2000). The rims were also younger than the cores, with argon-loss profiles of 200–300 μm in length decreasing to the known eruption age at the grain edge (Kelley and Wartho, 2000). This study identified that the phlogopites retained argon at temperatures hundreds of degrees higher than the phlogopite closure temperature (ca. 450 °C) and that argon loss at the grain margins represents the integrated time–temperature history as the xenolith travels from depth to emplacement at the surface (Kelley and Wartho, 2000). The key difference between this study and the conclusions of Phillips (1991) and Phillips et al. (1999) is in the interpretation of the core-rim age differences: Phillips (1991) and Phillips et al. (1999) interpret old cores due to excess argon whilst Kelley and Wartho (2000) interpret them as retained radiogenic argon because of a lack of transfer of argon to the grain boundary network because the grains behave as 'closed systems' under the high pressures experienced in the mantle and lower crust.

In terms of our new data for the Pochampalle lamproite, macrocrystic phlogopite yielded single grain fusion ages that spanned ca. 200 Myr, and the intra-grain ultraviolet laserprobe analysis revealed a complex age structure with older internal parts and varied rim ages. Individually the five grains are different, in size and shape, but the age ranges for each of the

grains are very similar, most notably for sample POC. Contouring is not appropriate in this case because there are two analytical approaches – ablating squares in internal parts of the grains and margin-parallel trenches – and taking the approach of plotting age versus distance from the centre of the laser pit to the nearest grain margin can reveal information on the age structure (Fig. 4.9).

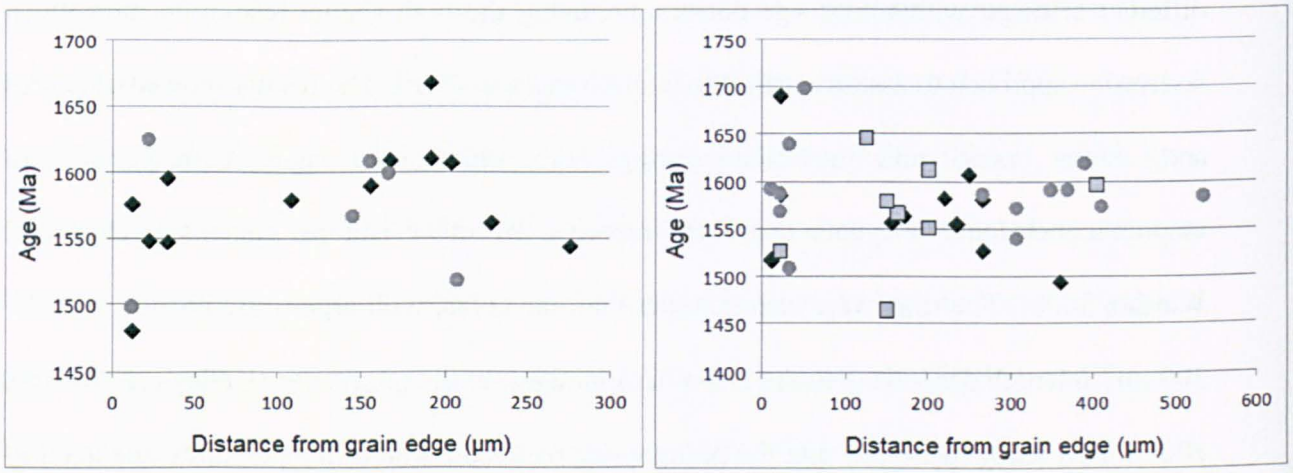

a. **b.**

Figure 4.9. Age versus distance from grain edge for all UV laserprobe data points from phlogopite macrocrysts from: (a) sample POC; (b) sample POCg.

Sample POC preserves cores of ca. 1560 Ma to ca. 1610 Ma with a single data point that is much higher (ca. 1660 Ma). In both grains the measurements actually at the grain margins are the youngest – ca. 1500 Ma and ca. 1480 Ma. In POCg the same age pattern is observed though with more scatter, and the key point is that in plotting data in this way it assumes that the distance from laser pit to grain margin now, is the same as it was at the time of mineral growth, a likely false assumption given the difficulty in recovering intact mineral grains. Notably for POCg the grain margins are consistently the youngest with ages of ca. 1493 Ma, ca. 1463 Ma and ca. 1507 Ma, although there is notable scatter in the third grain from sample POCg in which two grain margins are measured, one of which is significantly older than the

other and may not represent an original grain margin. The internal parts of the grain are consistently in the range ca. 1530 Ma to ca. 1630 Ma. The key points to note are: (1) in five mineral grains from samples POC and POCg the grain margins are the youngest parts of the grains and are all within error of 1500 Ma; (2) the internal parts of the mineral grains are significantly older and in the region of ca. 1550–1650 Ma. These observations are in keeping with those of Phillips and Onstott (1988), Phillips (1991), Phillips et al. (1999) and Kelley and Wartho (2000). Whether the older core regions of the minerals reflect excess argon or retention of radiogenic argon under mantle-lower crust conditions is difficult to discern, but by and large this is a moot point. It is the ages recorded by the rims of the minerals that are of importance since these are considered to represent the timing of eruption by all the previously cited studies.

To summarise the new Ar–Ar data, ages from the two kimberlite pipes derived from matrix phlogopites are consistent and yield an age of ca. 1100 Ma for their eruption. The Pochampalle lamproite preserves old ages in internal parts of the grain that could be due to either excess argon retention or quantitative retention of radiogenic argon, whilst the rims record an eruption age of ca. 1500 Ma.

Based on these Ar–Ar age data, we propose that the Pochampalle lamproite was emplaced ~1500 Ma ago, roughly 250 Myr before the rest of the KLF. It would seem that the Pochampalle magma was also derived from an isotopically distinct mantle source from the rest of the KLF with a lower $^{143}Nd/^{144}Nd$ ratio. Trace-element geochemistry implies that it may have been derived by relatively smaller degrees of partial melting from within the garnet stability field compared to the rest of the KLF. The Nd isotopic signature and the bulk-rock REE pattern in the Pochampalle lamproite appear to be consistent with a hypothesis that a heterogeneous mantle source was sampled by the Krishna lamproites during the Proterozoic.

Insight into the possible tectonic setting for emplacement of the Pochampalle lamproite could come from recent work by Hou et al. (2008). Citing a giant radiating dyke swarm and LIPs at ~1.85 Ga, they propose that the North China Craton and the Indian Craton were united together in a single landmass before its extension and break-up (Fig. 2.10).

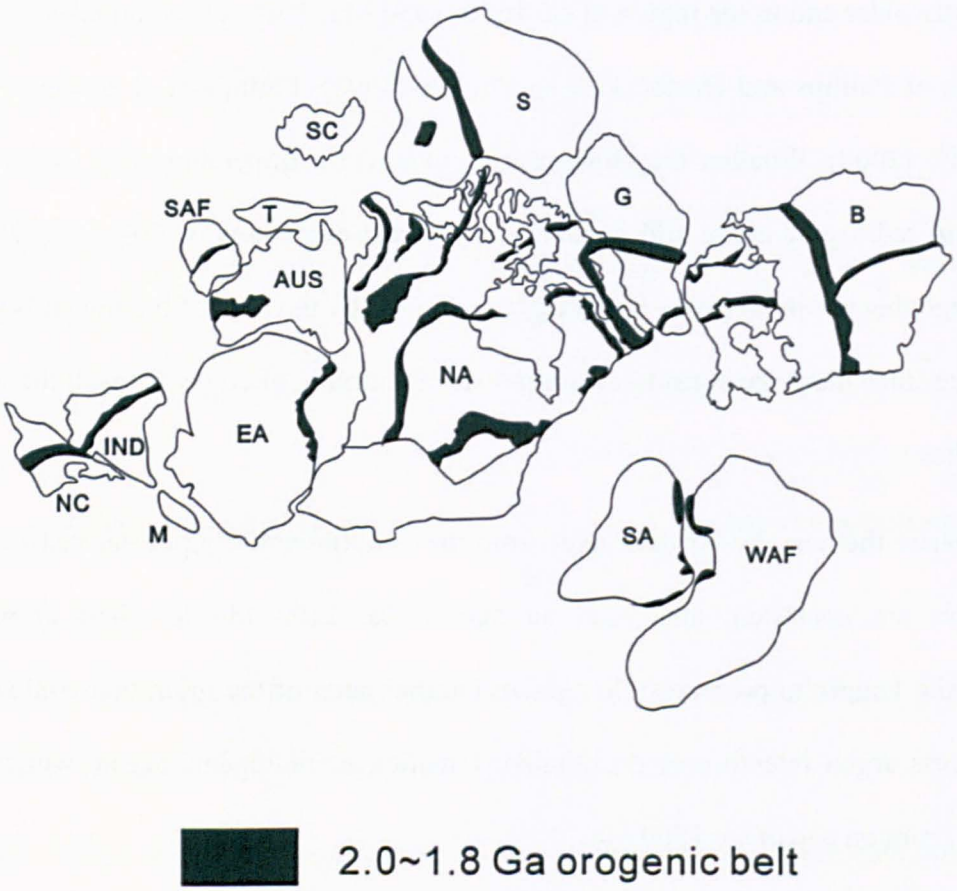

Figure 4.10: A proposed pre-Rodinian supercontinent (Hou et al., 2008).

Abbreviations:AM-Amazonia; AUS-Australia; B-Baltica; C-Congo Craton; EA-East Antarctica; G-Greenland; IND-India; K-Kalahari Block; M-Madagascar; NA-North America; NC-North China; RP-Rio de la Plata; S-Siberia; SC-South China; T-Tarim; SAF-South Africa; SA-South America; WAF-West Africa.

The Mesoproterozoic Belt–Purcell–Uinta rift system (1470–1440 Ma) (Sears et al., 1998) along the west margin of the Canadian Shield suggests that the North China Craton and the Indian Craton were ultimately separated from the Laurentia continent by around 1.5 Ga

onwards. This is close to the emplacement age of the Pochampalle lamproite, which could therefore be linked to this period of continental rifting.

The older age and smaller degrees of mantle partial melting inferred for the Pochampalle lamproite may correspond to initiation of lithospheric stretching beneath the southern Indian craton at ~1500 Ma. The continuation or pre-existence of such a weakness in the lithosphere may have been exploited by later emplacement of the Krishna lamproites, by which time the mantle source region had acquired modified isotopic signatures through melt percolation from the asthenospheric mantle.

Previously, the Chelima lamproite (ca. 1400 Ma) was thought to be one of the oldest recorded lamproites in the world (Chalapathi Rao, 2007). However, our age data suggest that at least one lamproite (Pochampalle) was generated in the same region 100 Ma before the Chelima lamproite. This not only has implications for regional ultramafic magmatism, but also demonstrates that the mantle mechanism for producing lamproitic melts existed earlier than previously thought. It seems likely that further age determinations on Indian lamproites may extend their age range even further.

4.6. Other Ar-Ar Dating Techniques

In this study we successfully dated samples (MUL5, TUMM, POC and POCg) using total fusion and UV Ar-Ar dating techniques. However, further analyses were attempted with results rejected as unreliable.

4.6.1. Step-heating

We attempted to date 3 samples (CC1, CC4 and KK6) using $^{40}Ar/^{39}Ar$ step-heating technique. A sample is heated in steps of increasing temperature until all the argon is released. The argon released at each step is measured and a "step age" is calculated. At the

end of the experiment the step ages are plotted against the cumulative amount of ^{39}Ar released. This technique is designed to look at the gas released from sites of increasing argon retentivity. When a reasonable number of consecutive steps, carrying a substantial amount of the total argon released, give the same age, the resulting average value carries geological significance, representing the crystallisation age. A plateau is where sections of the age spectra contain at least three consecutive steps, carrying > 50 % of the total ^{39}Ar released, whose ages "overlap".

The data obtained via step heating in this study showed no clear plateau's (Fig 4.11) and it was thought that alteration (chloritsation and carbonation) of the phlogopite, made this technique unsuitable.

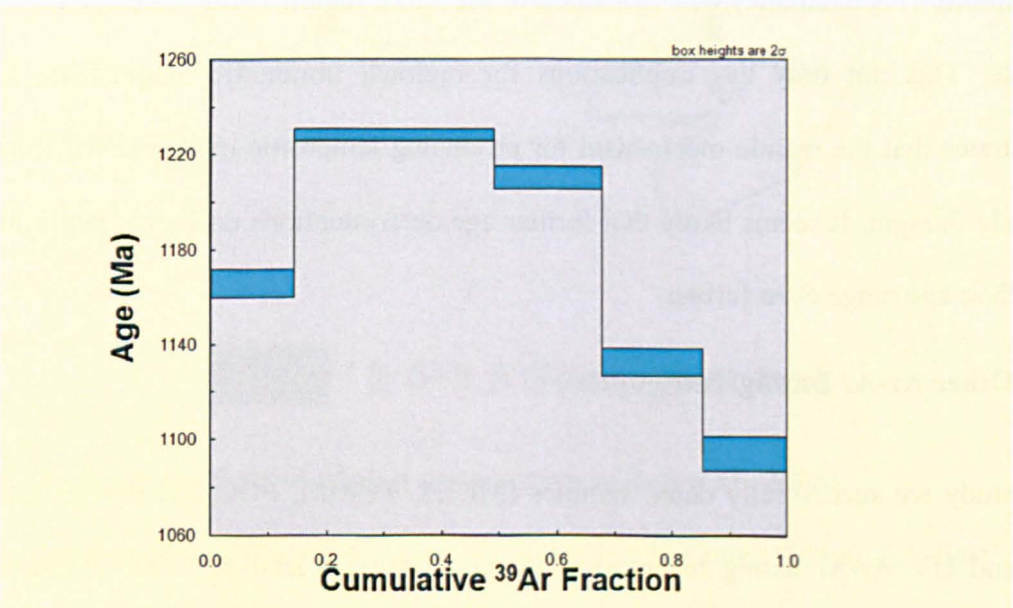

a) CC1

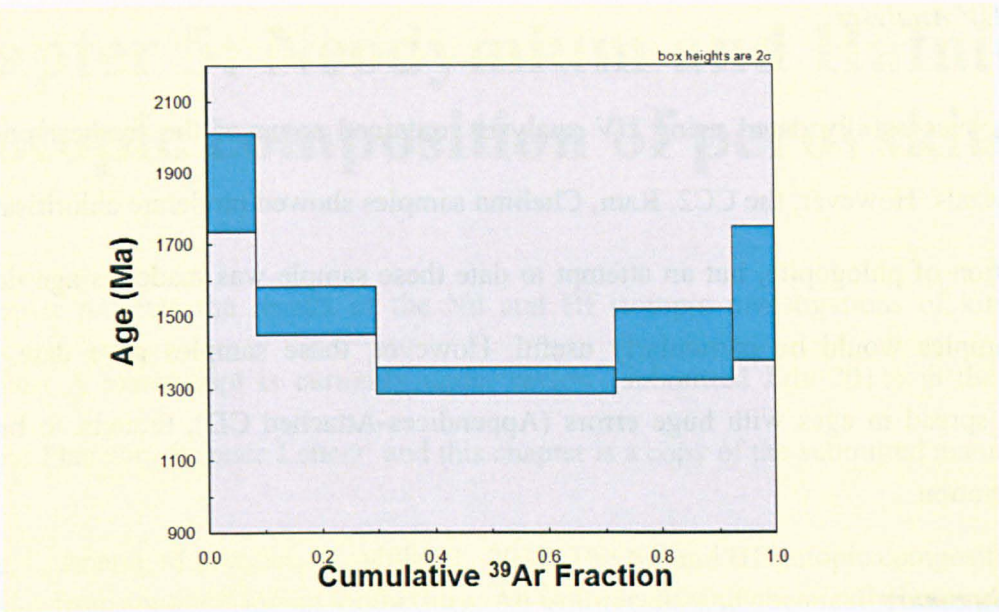

b) CC4

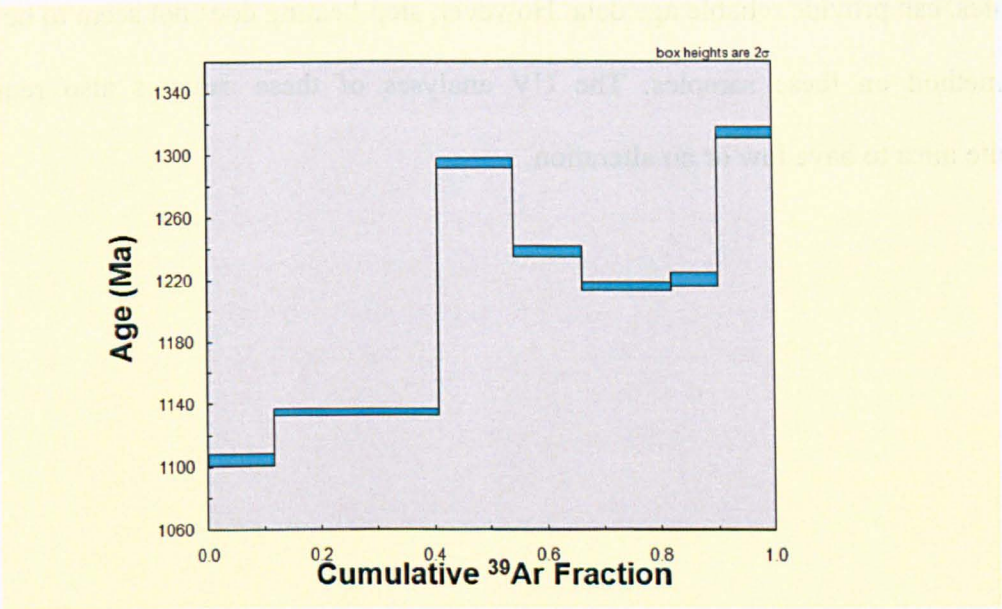

c) KK6

Figure 4.11. Some examples of the step-heating data: a) CC1 b) CC4 c) KK6.

4.6.2. UV Analyses

Samples successfully dated using UV analysis contained some of the freshest phlogopite mica crystals. However, the CC2, Ram, Chelima samples showed moderate chloritisation and carbonation of phlogopite, but an attempt to date these sample was made, as age data from these samples would be particularly useful. However, these samples gave data with an extreme spread in ages with huge errors (Appendices-Attached CD), thought to be due to their alteration.

4.6.3. Summary

In summary, it would seem that total fusion and UV analyses of phlogopite mica in kimberlites, can provide reliable age data. However, step-heating does not seem to be a viable dating method on these samples. The UV analyses of these samples also require the phlogopite mica to have low or no alteration.

Chapter 5: Neodymium and Hafnium isotopic composition of perovskites

This chapter presents the results of the Nd and Hf isotopic investigations of kimberlitic perovskites. A manuscript is currently under review (submitted July 2011) in the journal 'Earth and Planetary Science Letters' and this chapter is a copy of the submitted manuscript:

Osborne, I., Anand, M., Argles, T., Millar, I., 2011. The Nd and Hf isotopic composition of perovskites from southern Indian kimberlites: An isotopically and chemically heterogeneous sub continental lithospheric mantle (in review), Earth and Planetary Science Letters.

The Nd and Hf isotopic composition of perovskites from southern Indian kimberlites: An isotopically and chemically heterogeneous sub continental lithospheric mantle

Ian Osborne[a*], Mahesh Anand[a,b], Tom Argles[a], Ian Millar[c]

[a] *Department of Earth and Environmental Sciences, CEPSAR, The Open University, Walton Hall, Milton Keynes MK7 6AA, UK*

[b] *Department of Mineralogy, The Natural History Museum, Cromwell Road, London, SW7 5BD, UK*

[c] NERC Isotope Geosciences Laboratory, Kingsley Dunham Centre, Keyworth, Nottingham, NG12 5GG

Abstract

This study presents the first Hf isotopic analyses of perovskites from kimberlites. Magmatic perovskite is considered to be largely immune to the late stage crustal contamination and alteration that tends to affect kimberlitic bulk-rock compositions. Perovskites were analysed from six kimberlites located in the Eastern Dharwar Craton (EDC) of southern India. The perovskites were separated using a combination of magnetic and density separation techniques. Perovskites fall into two distinct groups in Hf isotope space, suggesting a degree of heterogeneity in the source of the kimberlites in the EDC. The kimberlites are all found in such close proximity that lateral variations in the source are unlikely, but this does not preclude vertical heterogeneity in the source region(s). We propose a model of kimberlite generation with a vertically heterogeneous source that has undergone separate periods of enrichment and depletion before kimberlite melt generation and emplacement at ~1100 Ma. In this model there was an early asthenospheric melting event linked with the initial depletion in the SCLM at ~ 2Ga, which coincides with the time of recorded magmatism in the Cuddapah basin. The next stage of the model is enrichment of the residual SCLM at ~1.5 Ga. It could be that the two groups of kimberlites with distinct Hf isotope signatures are derived from varying degrees of partial melting. However, the two groups of kimberlites could also be inferred to have been derived from source regions located at different depths, manifested in terms of one group being diamondiferous and the other non-diamondiferous.

Keywords: Perovskite; Kimberlite; Southern India; Neodymium isotopes; Hafnium isotopes

* Corresponding author. Tel.: +44-1908-653023; Fax: +44-1908-655151.

E-mail address: I.Osborne@open.ac.uk

5.1. Introduction

Kimberlites represent ultramafic magmas that travel rapidly from source regions in the deep mantle (>100 km) to the shallowest crustal levels at speeds of up to 0.1 to 4.0 ms^{-1} (Kelley & Wartho, 2000). In effect, they provide snapshots of the geochemical and isotopic nature of the deep lithospheric or asthenospheric mantle at the time of their emplacement.

Many kimberlites contain a diverse assemblage of entrained mantle and crustal fragments, and are usually subject to extensive post-emplacement alteration (Berg and Allsopp, 1972; Mitchell, 1986). Hence, there is considerable uncertainty regarding whether an observed kimberlite bulk-rock composition has been affected by processes such as contamination and alteration, or instead preserves a true record of kimberlite magma variability (Paton et al., 2007).

Perovskite ($CaTiO_3$) is a common primary groundmass phase in kimberlites and is considered to be a more faithful recorder of primary magmatic compositions than the bulk-rock composition of the same samples (Paton et al., 2007). Perovskite is thought to crystallise directly from a kimberlitic magma prior to entrainment of crustal material, and is robust during weathering (Mitchell, 1972). Magmatic perovskite is therefore considered to be largely immune to the late stage crustal contamination and alteration that tends to affect kimberlitic bulk-rock compositions (Paton et al., 2009). However, a recent study by Malarkey et al. (2010) uses high precision TIMS data show a significant range in $^{87}Sr/^{86}Sr_i$ in perovskite and other minerals in a kimberlite and olivine melilitite that they indicate reflects the effects of progressive crustal contamination. Therefore, although perovskite may provide a closer approximation to the kimberlite source region than bulk-rock analysis, in some cases, it may also have been affected by contamination.

Perovskite is abundant in trace-elements (including REEs) and is therefore an ideal target mineral for trace-element and isotopic studies of kimberlites, as it has the potential for recording the primary geochemical and isotopic composition relating to the origin of these rocks and the nature of their source regions (Heaman, 1989). However, until recently perovskite has not been widely used for isotopic studies because of its grain size: typically 40 to 80 μm, and rarely exceeding 100 μm (Kinny, 1997). Separation of such small grains from other kimberlite matrix minerals and purification for isotope dilution analysis is therefore very difficult. Smith (1989) used a combination of chemical and magnetic separation methods for separating perovskites from kimberlites. In these early studies perovskite was analysed using multi-grain composites to produce model ages (Hamilton, 2003). Recent advances in analytical techniques (e.g. laser-ablation MC-ICP-MS) have allowed *in situ* investigations of perovskite for their chemical and isotopic compositions (e.g. Paton et al., 2007). However, these studies are limited to isotopic analysis for elements that occur in sufficient abundances (e.g., Nd and Sr) allowing both accurate and precise measurements. To determine the isotopic composition of elements which are not sufficiently concentrated in a single perovskite grain, measurement of separated perovskites is the only available option.

This study presents the first determination of the Hf isotopic composition of perovskites from Indian kimberlites. We use a combination of magnetic and density separation techniques to separate perovskites from the southern Indian kimberlites for chemical and isotopic analysis. Nd and Hf isotopic analyses on separated perovskites are used to better constrain the nature of the mantle source region(s) and to determine whether previous bulk-rock analyses of these samples were affected by crustal contamination and/or alteration.

5.2. The southern Indian kimberlites

The majority of kimberlites and other mafic intrusives in the region occur within the Eastern Dharwar craton (EDC) (Fig.5.1).

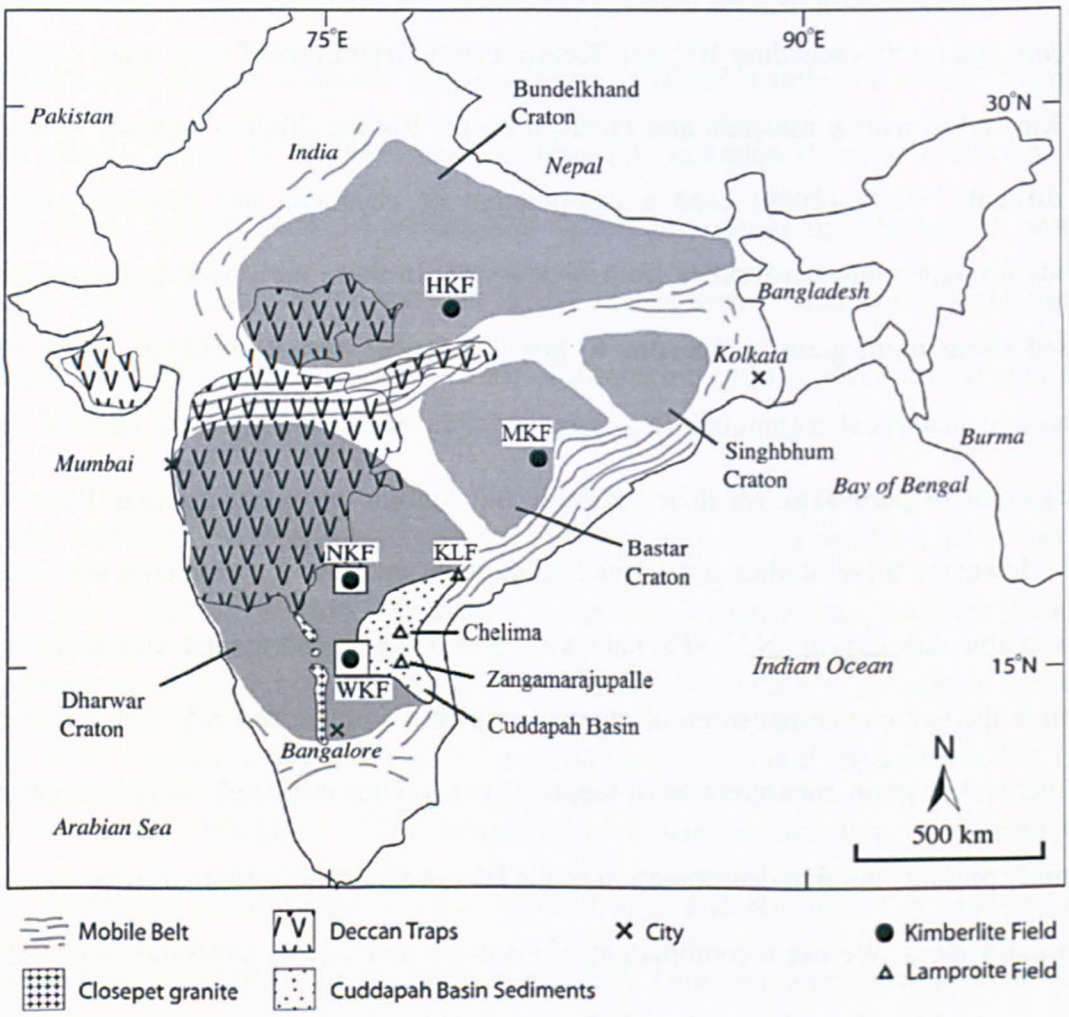

Figure 5.1. Location of the eastern Dharwar Craton (EDC) kimberlites relative to the major tectonic domains of southern India. HKF: Hinota Kimberlite Field; MKF: Mainpur Kimberlite Field; NKF: Narayanpet Kimberlite Field; WKF: Wajrakarur Kimberlite Field. Modified from Paton et al. (2009)

The EDC is primarily composed of ancient (>2 Ga), greenschist- to granulite-facies schists and gneisses (Chalapathi Rao et al., 2004). The Eastern Ghat orogeny (1.3-1.6 Ga) affected

the EDC, resulting in a narrow, highly deformed granulite-facies belt extending from Chennai to near Kolkota. The ~2.0 Ga old Cuddapah Basin (Anand et al., 2003) covers an area of around 44000 km^2 (Nagaraja Rao et al., 1987) and lies within the EDC. It comprises a 6 to 12 km thick succession of igneous and sedimentary rocks of Early to Late Proterozoic age.

The kimberlites in the EDC crop out to the west of the Cuddapah Basin and occur in three spatially separated groups: the diamondiferous Wajrakarur kimberlite field (WKF), the non-diamondiferous Narayanpet kimberlite field (NKF) and the Raichur kimberlite field (RKF) (Fig. 5.2).

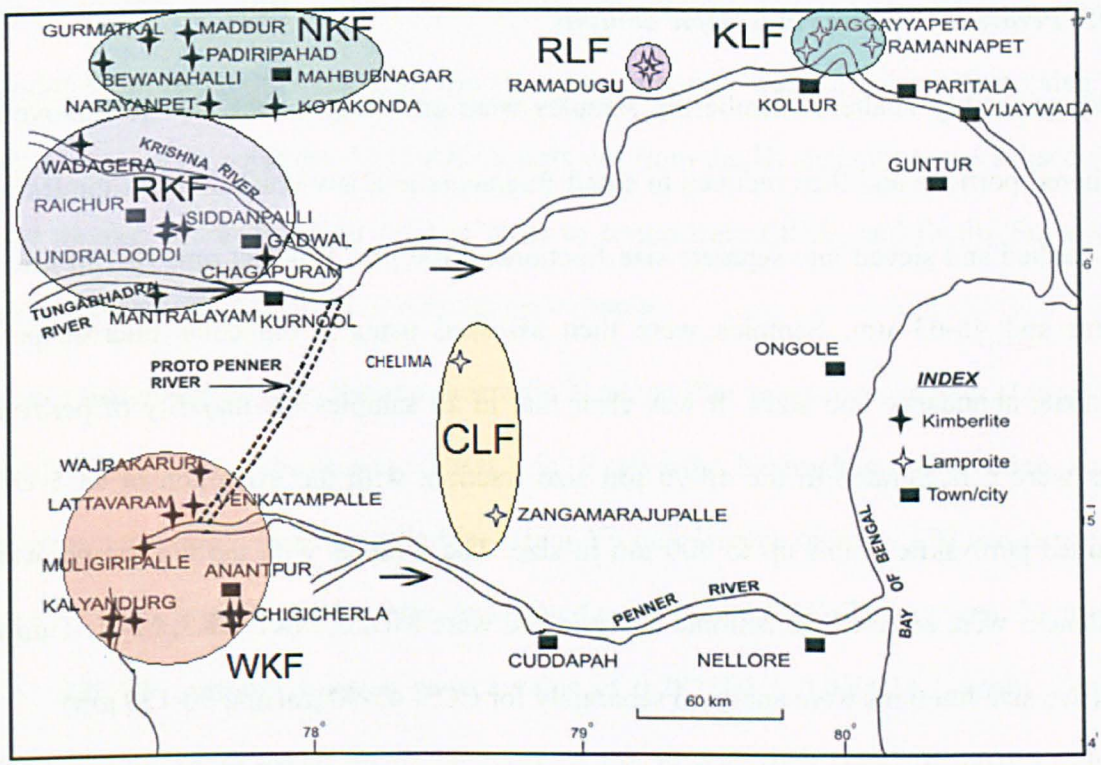

Figure 5.2. Location and extent of kimberlite and lamproite fields around the Cuddapah Basin, showing the locations of individual pipes. Modified from Chalapathi Rao et al. (2009). NKF: Narayanpet Kimberlite Field; RKF: Raichur Kimberlite Field; WKF: Wajrakarur Kimberlite Field; CLF: Cuddapah Lamproite Field; RLF: Ramadugu Lamproite Field; KLF: Krishna Lamproite Field.

This study presents the Hf isotopic data from kimberlitic perovskites, with mineral separates analysed from six kimberlites located in EDC. Three of the kimberlites are located in WKF: Muligiripalle (Mul5), Tummatapalle (Tum- located in close proximity just to the west of the Muligiripalle kimberlite) and Chigicherla pipe 5 (CC5). Two kimberlites are from the NKF: Narayanpet (NK1) and Maddur (MK1). One kimberlite is from the RKF: Siddanpalle (SK3). The CC5 kimberlite has the largest and most abundant perovskite, so two size fractions were analysed separately for CC5: 45-90 μm and 90-150 μm).

5.3. Methodology

5.3.1. Perovskite Hf and Nd isotopic analysis

1-2 kg of visibly unaltered kimberlite samples were cut using a rock saw to remove any weathered portions and then reduced to small fragments in a jaw-crusher. The samples were then washed and sieved into separate size fractions: >300 μm, 150-300 μm, 90-150 μm, 63-90 μm and 45-63 μm. Samples were then assessed using a binocular microscope for perovskite abundance and sizes. It was clear that in all samples the majority of perovskite grains were concentrated in the 45-90 μm size fraction, with the exception of CC5 which contained perovskite grains up to 400 μm in size. The samples with the highest perovskite abundances were selected for isotopic analysis and were MUL5, NK1, SK3, MK1, Tum and CC5 (two size fractions were analysed separately for CC5: 45-90 μm and 90-150 μm).

In the first step, a simple bar magnet was passed over the samples to remove the most magnetic phases (e.g. ilmenite and spinel). Dense liquid separation was then carried out on the remaining fraction. Perovskite density is ~ 4 g/cm^3 (http://webmineral.com).

Initially Na heteropolytungstate (Fastflow™) was used, with a density of 2.9 g/cm^3. This removed much of the less dense material, particularly the silicates, leaving a separate 10-50 % (by volume) perovskite. To improve the percentage of perovskite these samples were then

passed through a higher density liquid (methylene iodide: density 3.3 g/cm^3), which removed additional less dense minerals. Further magnetic separation was carried out on the samples using a Frantz magnetic separator. After this step, the samples (0.001-0.026 g) contained ~ 75-80 % by volume perovskite. The final step involved removal of any visible impurities by handpicking, leaving perovskite separates with an estimated purity of 95 % by volume.

For isotopic analysis, perovskite samples were dissolved in HF-HNO_3 and spiked with mixed ^{176}Lu-^{180}Hf and ^{149}Sm-^{150}Nd isotopic tracers, dried down and then subsequently converted to chloride by dissolution in 3M HCl. Hafnium was separated using the method of Münker et al. (2001), modified in order to elute more Zr from the sample prior to Hf collection. Lu was separated from the HREE cut from the Hf separation, and was further purified using LN-SPEC ion exchange columns. The LREE/matrix cut from the Hf separation was subsequently passed through Eichrom AG50 resin in order to concentrate LREE, and finally Sm and Nd were separated using LN-SPEC ion exchange columns.

Hafnium was analysed on a Thermo Scientific Neptune Plus mass spectrometer at the NERC Isotope Geoscience Laboratories (NIGL) in Keyworth, Nottingham. Correction for Lu interference on mass 176 was negligible. Minor Yb interference on mass 176 was carried out using ^{173}Yb/^{176}Yb values empirically determined using doped JMC475 solutions. 54 analyses of the JMC475 standard solution gave a value of 0.282160 ± 0.000014 (46ppm, 2-sigma) across the time of analysis. Seven analyses of the BCR-2 rock standard gave a value of 0.282867 ± 0.000010 (32ppm, 2-sigma) at the time of analysis, with a hafnium concentration of 4.92 ± 0.04 ppm. Lu concentration was also measured on a Thermo Scientific Neptune Plus mass spectrometer. Lu samples were doped with sufficient natural Yb to allow mass bias correction. Correction of the ^{176}Lu peak for ^{176}Yb was carried out using the natural ^{176}Yb/^{173}Yb of 0.79622 (Chu et al. 2002), corrected for exponential mass bias using the

measured $^{172}Yb/^{173}Yb$ ratio relative to the natural ratio of 1.35274 (Chu et al., 2002). Correction of the ^{176}Lu peak for ^{176}Hf used the measured $^{176}Hf/^{177}Hf$ for each sample, corrected using the measured Yb mass bias.

Nd was loaded on Re-Re double filament assemblies and analysed on a Thermo Scientific Triton mass spectrometer using a multidynamic algorithm. Three analyses of the La Jolla standard run with the Nd samples gave $Nd^{143}/Nd^{144} = 0.511854 \pm 0.000016$ (2-sigma).

4.3.2. LA-ICP-MS measurements protocol

Laser-ablation ICP-MS analysis was performed on polished thin sections (250 μm) at the Open University on the Agilent 7500s ICP-MS coupled with a New Wave 213Nd:YAG deep (213 nm) laser system. Instrumental operating conditions are summarised in Table 5.1.

Table 5.1 LA-ICP-MS operating conditions

SCAN PARAMETERS	**Detection modes**	**Dwell time**	**Integration time**	
	Dual[1]	10-100 ms	10 ms	
LASER	**Laser**	**Type**	**Wavelength**	**Repetition rate**
	UP-213 (New Wave)	Nd:YAG frequency quintupled	213 nm	10 Hz
SPOTS	**Ablation duration**	**Spot size**	**Energy**	
	60 s	80 μm	0.8 mJ	

[1] Analogue and pulse detector are cross-calibrated prior to each session

Samples were ablated in a pure He atmosphere, and the analyte was carried in the He and then mixed with Argon via a "y" connector before entering the plasma. The use of He gives a 2-3 fold increase in sensitivity and significantly reduces background intensity (e.g. Günther and Heinrich, 1999). Data were acquired across the mass range from ^{7}Li to ^{208}Pb. The total time for each analysis was 240s. During the first 120s the gas blank was measured, during

which the laser beam was blocked by a shutter. The shutter was then removed, the sample ablated for 60s and the transient signals from the analyte were acquired for a further 60s. A further 60s wash out period was carried out between analyses. Data reduction was carried using the GLITTER software (Van Achterbergh et al., 2001).

A glass standard (NIST 612) was used to provide external calibration. The standard was analysed twice at the start of each run and then after every 8 or 9 samples. The standard was also analysed twice at the end of each run. The trace element measurements of the standard were all found to be within ± 30 % (2 s.d.), Mn was higher at ± 40 % (2 s.d.). Detection limits are usually between 1 and 10 ppb range (Hathorne et al., 2004).

4.3.3. Bulk-Rock and Isotopic measurements protocol

1-2 kg of visibly unaltered kimberlite samples were cut on a rock saw to remove any weathered portions and then reduced to small fragments in a jaw-crusher. These fragments were then crushed to powder in an agate ring mill to produce the powders used in all bulk-rock geochemical analysis.

Two methods were used to obtain bulk-rock major-, trace- and REE data. Major and some minor elements (Al, Ca, Fe, K, Mg, Mn, Na, P, Si, Ti, Ba, Cr, Ni, Sr, Y, Zr) were analysed using Inductively-Coupled Plasma Atomic Emission Spectroscopy (ICP-AES). 100 mg of powdered sample was fused with 300 mg $LiBO_2$ (lithium metaborate) flux, and then dissolved in dilute HNO_3. The concentrations of selected major- and trace-elements were then determined by ICP-AES at the Natural History Museum, London. These solutions were not spiked. Reference materials were selected based on their similarities to the samples to be analysed and included BCR-1 (major and trace) and GA (trace and REE).

$HF/HClO_4$ (hydrofluoric acid/perchloric acid) digestion was used for other minor-, trace- and REE analyses. In each case, 500 mg of powdered sample was digested in $HF/HClO_4$. The

resulting solution was evaporated to dryness, and the residue was then dissolved in dilute nitric acid. The concentrations of trace-elements were then determined by ICP-AES and ICP-MS at the Natural History Museum, London. Solutions for ICP-MS were diluted a further 10 times and were spiked with 1 ppb In and 1 ppb Rh as internal standards prior to analysis. ICP-MS solutions were not spiked. To monitor instrumental drift and precision the international rock standard, BCR-1, was used. Major, trace and rare earth element analyses were found to be within ± 20 % (2 s.d.) to that of the certified values, with the exception of Ni, Cr, Sn and Be which were found to be within ± 30 % (2 s.d.) to that of the certified values and Bi, Cd, and Ta which showed slightly greater deviation to that of certified values.

Nd isotope analysis was performed on twenty one samples (12 kimberlites and 9 lamproites). 50 mg of powdered sample was weighed in each case and spiked with a $^{150}Nd/^{144}Nd$ solution. These samples were digested in HF/HNO_3. Nd and Sm were separated from the dissolved samples by standard ion-exchange techniques (Cohen et al., 1988), using cation columns to collect the REE fraction. This fraction was then passed through HDEHP columns to collect Nd and Sm fractions, which were evaporated to dryness. 1µl of 2M HCl was added to the Nd collected for each sample and then loaded with 0.6µl of 0.01M H_3PO_4 onto the centre of an outgassed Re filament. Nd isotopic ratios were measured in the static mode using a Triton thermal ionization mass spectrometer at the Open University. Reproducibility of the La Jolla Nd standard over the analysis period was $Nd^{143}/Nd^{144} = 0.511849 \pm 0.000002$ (8 ppm, 2SD).

5.4. Perovskite characteristics

The crystallisation of kimberlite magma results in abundant olivine phenocrysts followed by phlogopite, perovskite, calcite, monticellite, serpentine and some other minor minerals that together comprise the groundmass of hypabyssal kimberlite rocks (Kamenetsky et al., 2009).

Perovskite is particularly abundant in the EDC kimberlites and occurs as subhedral, dark brown, pseudo-cubic crystals with a metallic lustre (Fig. 5.3).

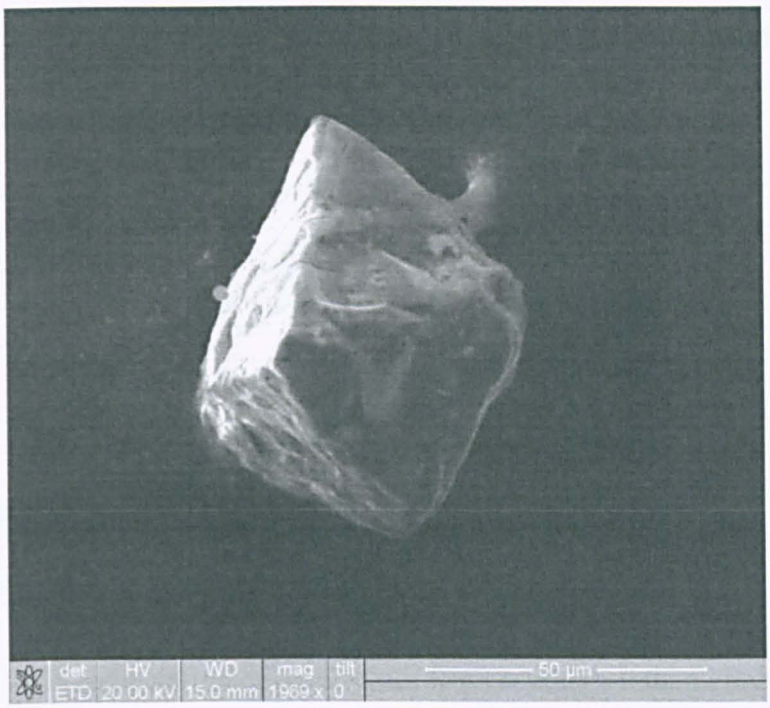

Figure 5.3. Secondary Electron Microscope (SEM) image of a perovskite crystal from the Kotakonda kimberlite pipe in the NKF of the EDC.

In our samples, the perovskite crystals are small and generally occur within the 45-90 μm fraction, except in one sample (CC5) where they can be up to 400 μm in size. On Back Scatter Electron (BSE) images, the perovskite crystals appear zoned because of slight variations in their Fe content, which is likely to be related to varying fO_2 conditions during perovskite crystallization (Canil and Bellis, 2007).

5.5. Results

5.5.1. Major and trace-element geochemistry

Microprobe and LA-ICP-MS analysis of perovskite grains show that these grains approach the ideal formula for perovskite ($CaTiO_3$), with < 2% substitution by other elements (predominantly LREEs and Nb). Perovskite from two NKF samples (MK1 and KK6) and

three WKF samples (MUL5, CC1 and CC5) were analysed using LA-ICP-MS for their REE abundances (Fig. 5.4).

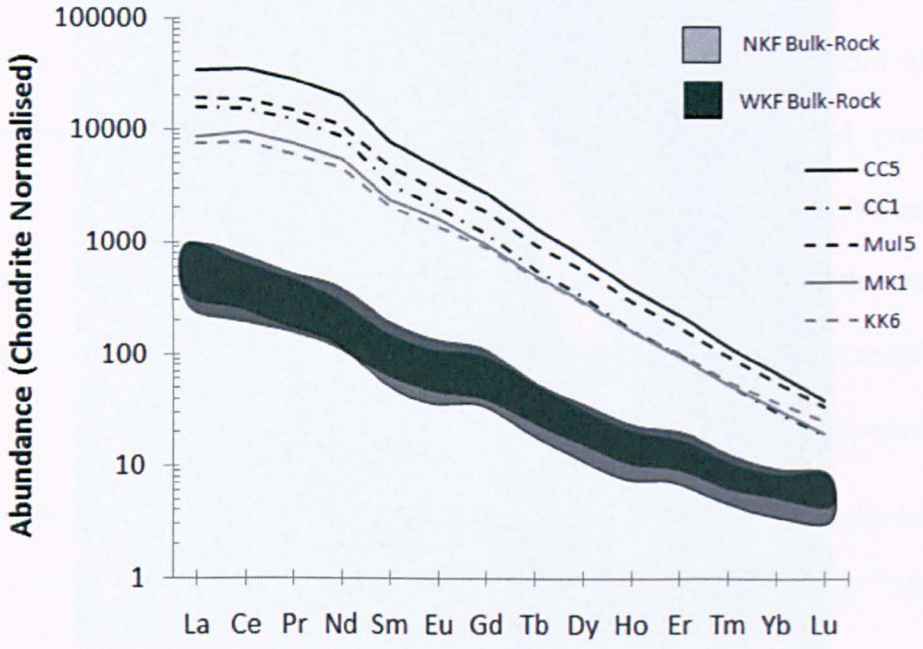

Figure 5.4. Rare earth element (REE) patterns of the kimberlites of southern India (normalized to chondrite; values from Anders and Grevesse, 1989). The black lines represent WKF perovskite REE data. The grey lines represent NKF perovskite data. The shaded areas represent bulk-rock data for kimberlites from WKF and NKF.

All perovskites show extreme LREE enrichments, with La in the NKF 7500-8500 times chondrite and in the WKF 16000-34000 times chondrite. The HREEs are much less enriched with Lu in NKF samples at 20-25 times chondrite whereas Lu in WKF samples at 20-40 times chondrite. This is illustrated by the high $(La/Yb)_N$ values (200-260 NKF; 340-520 WKF). Although more enriched than the bulk-rock, the perovskites show a similar pattern to that shown by the bulk-rock REE abundances but with a steeper trend, illustrated by the lower $(La/Yb)_N$ ratio of the bulk-rock samples (48-89 NKF; 69-121 WKF). (Bulk-rock REE (A.2.6; A.2.7) and perovskite LA-ICP-MS (A.2.9) full dataset are available in the appendices).

5.5.2. *Isotope geochemistry*

Table 5.2. Nd Isotopic composition of perovskites from southern Indian kimberlites

Sample	[Sm] (ppm)	[Nd] (ppm)	$^{147}Sm/^{144}Nd$	$^{143}Nd/^{144}Nd$	± 2SE	T_{DM}	T_{DM}*	εNd (1100)
Mul5	235	1531	0.0928	0.512010	0.000004	1301	1469	2.39
NK1	174	1129	0.0934	0.511963	0.000006	1362	1552	1.39
CC5 45-90 μm	X	3763	X	0.511922	0.000003	X	X	X
CC5 90-150 μm	X	3958	X	0.511915	0.000002	X	X	X
MK1	172	996	0.1045	0.512016	0.000005	1422	1596	0.86
SK3	145	964	0.0911	0.511969	0.000014	1331	1516	1.83
Tum	281	1909	0.0889	0.512005	0.000006	1268	1430	2.85

X: Not analysed for Sm
T_{DM}*: 2-stage model ages calculated using the method of Depaolo et al. (1991).

Table 5.3 Hf isotopic composition of perovskites from southern Indian kimberlites

Sample	[Lu] (ppm)	[Hf] (ppm)	$^{176}Lu/^{177}Hf$	$^{176}Hf/^{177}Hf$	±2SE	T_{DM}	T_{DM}*	εHf (1100)
Mul5	0.69	26	0.0038	0.282270	0.000004	1496	1619	3.8
Mul5 (rpt)	0.69	26	0.0038	0.282263	0.000005	1506	1633	3.6
NK1	0.59	13	0.0066	0.282293	0.000006	1587	1687	2.6
NK1 (rpt)	0.59	13	0.0066	0.282284	0.000005	1602	1705	2.3
CC5 45-90 μm	0.79	47	0.0024	0.282093	0.000005	1694	1910	-1.4
CC5 90-150 μm	0.51	30	0.0024	0.282103	0.000004	1681	1891	-1.1
MK1	0.51	9	0.0079	0.282317	0.000017	1617	1696	2.4
SK3	0.74	185	0.0006	0.281999	0.000026	1744	2021	-3.4
Tum	1.1	38	0.0042	0.282032	0.000008	1875	2103	-4.9

T_{DM}*: 2-stage Hf model ages were derived using a method derived from the Nd model age of Liew & Hoffman (1988), using an average crustal $^{176}Lu/^{177}Hf$ ratio of 0.012 (average passive margin mud, Vervoort et al., 1999).

5.6. Discussion

5.6.1. Nd Isotopic Data

Many kimberlites contain abundant crustal xenoliths and are prone to alteration, which may affect data obtained on bulk-rock samples. Direct analyses of isotopes in magmatic perovskite should provide a closer approximation to the kimberlite source region than bulk-rock analysis, assuming the perovskite equilibrated with the primary kimberlite melts at an early stage before contamination or alteration.

The data in this study (Fig. 5.5; Table 5.2) show that the perovskite has higher concentrations of Nd than the bulk-rock, as would be expected since perovskite is the main sink for REEs in kimberlites. The bulk-rock and perovskite analyses show remarkably similar isotopic data with almost indistinguishable εNd and $^{143}Nd/^{144}Nd$ values, though the bulk-rock isotopic data are slightly more scattered.

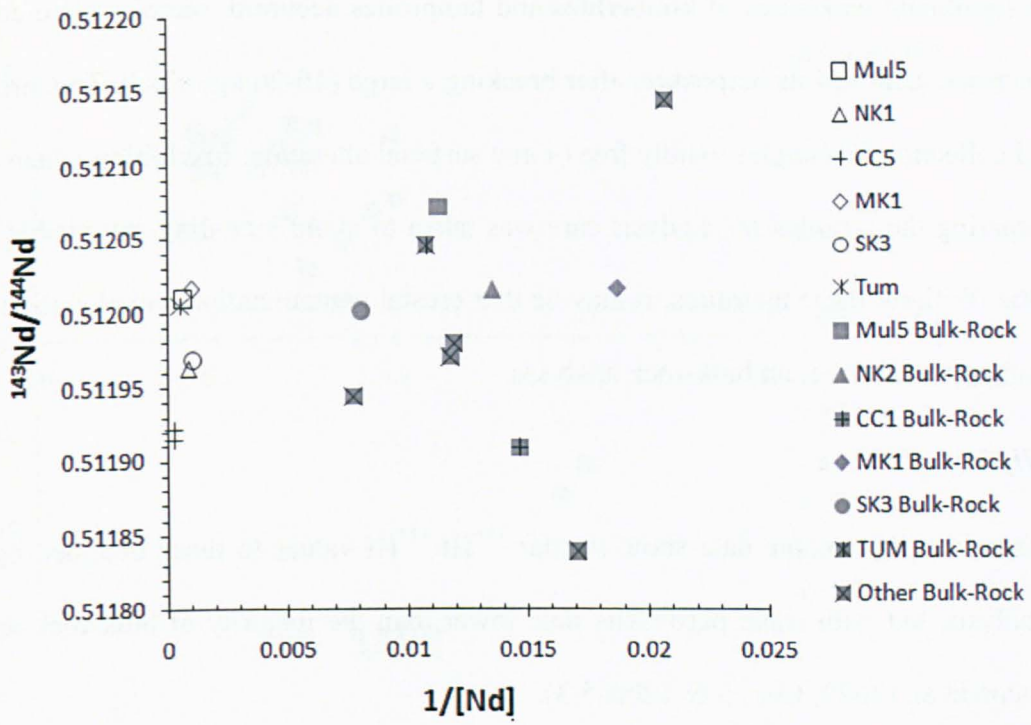

Figure 5.5. Plot of $^{143}Nd/^{144}Nd$ vs 1/[Nd] comparing perovskite separates (clear symbols) with their corresponding bulk-rock analyses (grey symbols). Plotted uncertainties on the data lie within the symbols.

The scatter of the bulk-rock data may reflect contamination. However, assuming that perovskite provides a closer approximation to the kimberlite source region than bulk-rock analysis, the close correspondence of bulk-rock with perovskite Nd isotopic values suggests that for these EDC kimberlite samples, crustal contamination and alteration have not significantly affected their bulk-rock composition. Hence, in this case, the bulk-rock compositions represent the true isotopic signatures of the kimberlite sources, as recorded by the perovskite analyses. It should be noted that in this study great care was taken to ensure that only the freshest bulk-rock samples were collected and only a subset of these samples were then selected for the further geochemical investigations presented here.

Where significant exposures of kimberlites and lamproites occurred, samples were collected from near the centre of the exposure, after breaking a large (10-20 kg) block. This procedure ensured collection of samples visibly free of any surficial alteration. In addition, when cutting and preparing the samples for analysis care was taken to avoid including any visible crustal xenoliths. Without these measures, it may be that crustal contamination and alteration would have had a greater effect on bulk-rock analyses.

5.6.2. Hf Isotopic Data

The perovskite Hf isotopic data show similar $^{176}Hf/^{177}Hf$ values to those obtained by bulk-rock analysis, but with some perovskite data lower than the majority of bulk-rock analyses from Paton et al. (2009) (Fig. 5.6; Table 5.3).

Unlike the Nd isotopic data, the perovskite εHf isotopic data appear to be split into two groups; one with positive εHf_i (+2 to +4) and one with negative εHf_i (-1 to -4) (Fig. 5.6).

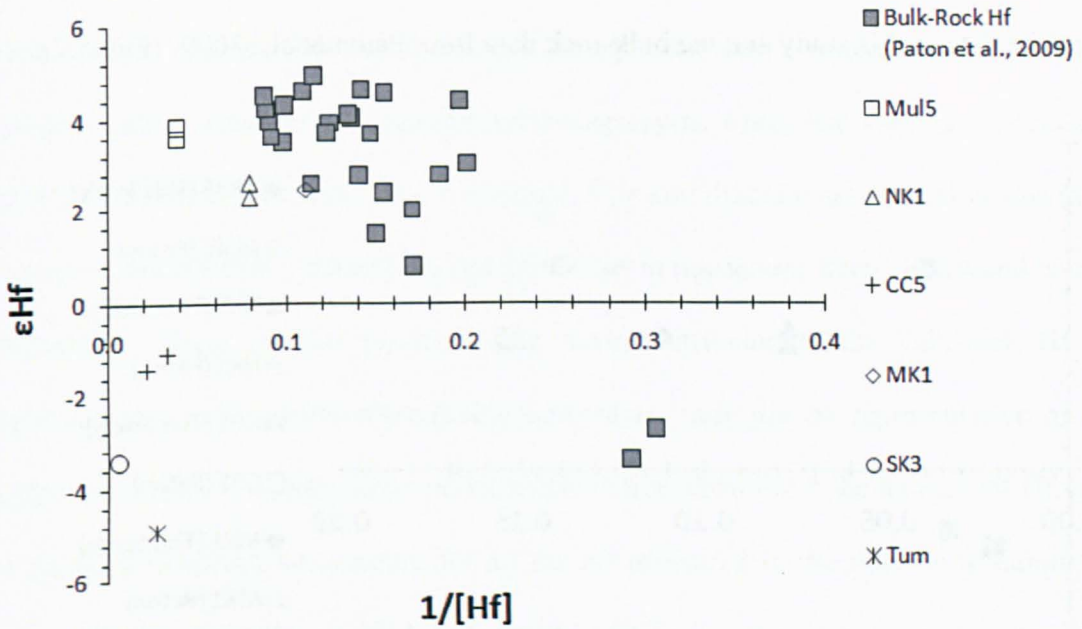

Figure 5.6. Plot of εHf_i vs 1/[Hf] comparing perovskite separates with bulk rock analyses from Paton et al. (2009) (grey filled symbols). Plotted uncertainties on the data lie within the symbols.

The two groups are not obvious from the bulk-rock isotopic data from Paton et al. (2009). However, Paton et al. (2009) did obtain negative εHf_i values from sample CP17 of kimberlite X116 ($\varepsilon Hf_i = -6.5$) and from samples of the Lattavaram-P4 kimberlite ($\varepsilon Hf_i = -2.71$ and -3.39). The CP17 sample had a C.I. of ~2.4, a correspondingly low εNd_i value, and very different Nd and Hf isotopic compositions to another sample from the same intrusion; hence its anomalous composition was attributed to the effects of crustal contamination by Paton et al. (2009). However, the Lattavaram-P4 kimberlite had an εNd_i value (+1.7) within the ranges of both the NKF and WKF, so the similarity in εHf_i values between the two samples of this intrusion, combined with their low C.I. values of ~1.3, suggest that the measured Hf and Nd isotope ratios are representative of the magmatic composition at the time of emplacement.

However, when comparing analyses of the same samples there is some disagreement between the perovskite data in this study and the bulk-rock data from Paton et al. (2009) (Fig. 5.7).

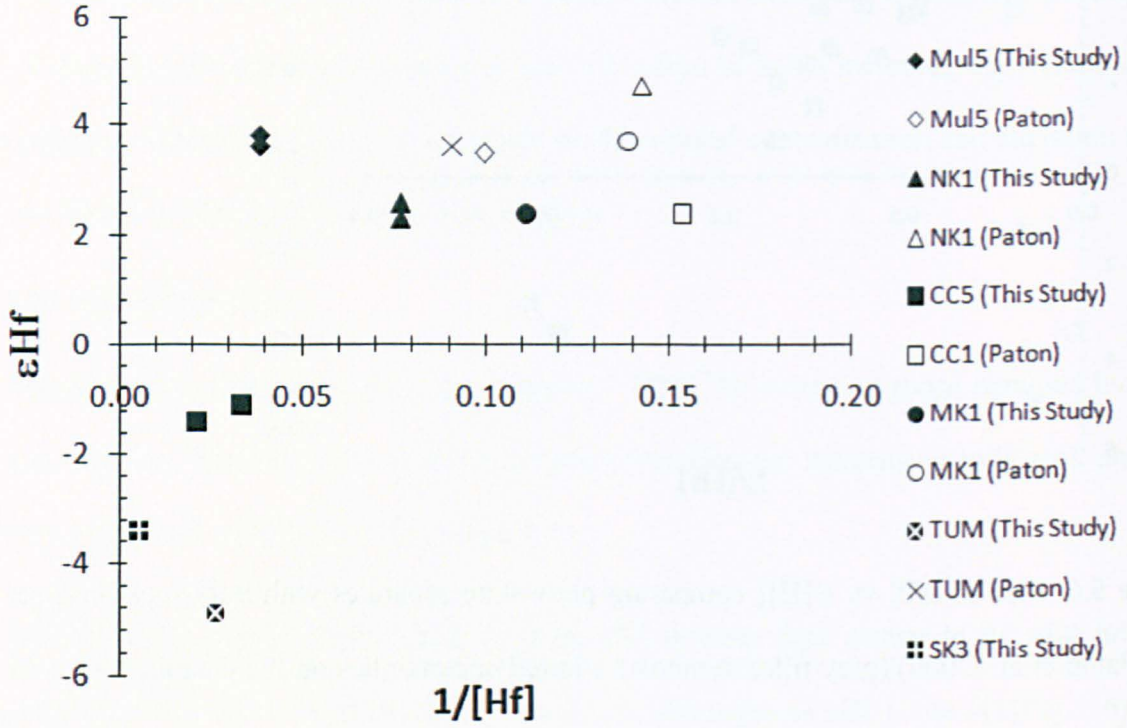

Figure 5.7. Plot of [1/Hf] against εHf_i for perovskite data from this study (solid symbols) and bulk-rock data from Paton et al. (2009) (open symbols). Samples CC5 and CC1 are from the same kimberlite cluster, but different pipes. Sample MK1 was deemed contaminated by Paton et al. (2009).

The Hf isotopic data for some of the samples are in agreement; most notably Mul5. However, two samples found to have negative εHf_i in this study (CC5 and TUM), are shown by Paton et al. (2009) bulk-rock data to have much higher positive εHf_i values.

The perovskite isotopic data are considered to more accurately represent the 'true source' of the kimberlite than bulk-rock data. It is possible that the bulk-rock Hf data are representative of several Hf-bearing phases common in Group I kimberlites, such as ilmenite, clinopyroxene, garnet and zircon. Nowell et al. (2004) performed Hf isotope analysis on

megacrysts from several kimberlites, including the Premier kimberlite located in South Africa, which like the EDC kimberlites is Group I and has a similar age (1180 Ma). They analysed garnet, ilmenite and clinopyroxene megacrysts, which had varying concentrations of Hf (Cpx 0.5305; Gt 2.4 ppm; Ilm 11.85 ppm). Cpx and ilmenite are present in varying modal proportions in the EDC kimberlites, but garnet has in most cases been altered and is no longer identifiable. These mineral phases would have contributed to the bulk-rock Hf isotopic signature and, unlike early-crystallizing perovskite, may not be representative of the true magmatic source. A simple mass balance calculation shows that the amount of Hf contained in the perovskite can not account for all the Hf measured in the bulk–rock samples (Table 5.4), with the exception of SK3 and possibly CC5. For these two samples, our estimates suggest that perovskite Hf dominates the bulk-rock Hf budget. However, for the other samples another Hf-bearing phase (or phases) must contribute to the bulk-rock Hf inventory to produce the elevated Hf bulk-rock concentrations.

One candidate mineral that could make up this Hf deficit in Mul5, NK1, MK1 and Tum is ilmenite, in which Hf is moderately compatible. Ilmenite is common in kimberlites and occurs in all these samples. The Ilmenite Index ($(FeO_t + TiO_2)/(2K_2O + MgO)$) provides a measure of ilmenite contamination in kimberlites (Taylor et al., 1994). The latter 4 samples all have Ilmenite Indices >0.52, implying contamination by additional ilmenite (Taylor et al., 1994), in contrast to SK3 and CC5, which have Ilmenite Indices of 0.36 and 0.41 respectively, as well as markedly lower bulk-rock TiO_2 contents. Rutile is a common phase in the EDC kimberlites, occurring as inclusions in olivine and could be another potential Hf host.

Table 5.4: Estimates of Hf contribution to bulk-rock from perovskite

Sample	Perovskite			Bulk-rock (estimated)		Bulk-rock (measured)	
	[Lu] (ppm)	[Hf] (ppm)	Lu/Hf	Pvs % (by vol)[1]	[Hf] (ppm)	[Hf] (ppm) This Study	[Hf] (ppm) Paton et al., 2009
Mul5	0.69	26	0.03	10	2.6	9.03	9.9
Mul5 (rpt)	0.69	26	0.03	10	2.6	9.03	9.9
NK1	0.59	13	0.05	15	1.95	5.32	7.0
NK1 (rpt)	0.59	13	0.05	15	1.95	5.32	7.0
CC5 45-90 μm	0.79	47	0.02	15	7.05	5.84	5.4 (CC1)
CC5 90-150 μm	0.51	30	0.02	15	4.5	5.84	6.2 (CC1)
MK1	0.51	9	0.06	10	0.9	6.20	7.3[2]
SK3	0.74	185	0.00	10	18.5	5.53	X
Tum	1.1	38	0.03	10	3.8	9.60	10.9

[1] estimated modal proportions; [2] MK1 considered contaminated by Paton et al. (2009)

5.6.2. Petrogenesis of the EDC kimberlites

A model where kimberlites form from the partial melting of metasomatically enriched sub-continental lithospheric mantle (SCLM) (Tainton and Mckenzie, 2004) is well supported for the EDC kimberlites (e.g. Chalapathi Rao et al., 2004; Becker and le Roex, 2006). This model proposes ~20 % melting within the garnet stability field, leaving residual SCLM depleted in incompatible trace elements but with relatively high abundances of HREEs. The depleted SCLM is then enriched by metasomatic melts derived from small-degree partial-melting of an asthenospheric source with residual garnet; such melts would have high LREE concentrations relative to HREEs. The enrichment would raise LREE abundances in the previously-depleted SCLM, while leaving HREE abundances relatively unchanged. The kimberlites would then be generated from this enriched source via 0.3-0.4 % melting within

the garnet stability field, further increasing LREEs in the melt and producing HREE abundances several times higher than chondritic values. We consider this model in the light of our isotopic data below.

Most mantle and crustal rocks lie on or near a linear, correlated array in Hf-Nd isotope space, known as the mantle or oceanic array (Fig. 5.8). Group I kimberlites, however, depart from this trend markedly, plotting at lower εHf_i values (Nowell et al., 1999), which implies that they tap a unique source characterised by a decoupling of the Lu-Hf and Sm-Nd systems (Nowell et al., 2004).

Perovskites analysed in this study also plot below the oceanic array, implying that a low εHf_i signature mantle source existed during the Proterozoic beneath India (Fig. 5.8). As previously discussed, perovskite data is thought to provide a closer approximation to the kimberlite source region than bulk-rock analysis, so the kimberlites' distinctive negative εHf_i signature likely originated deep in the sub-continental mantle, and may be indicative of a 'hidden mantle reservoir' not generally sampled by terrestrial rocks. Such a reservoir might account for the fact that mixtures of bulk crust and depleted mantle do not match most estimates of Bulk Silicate Earth composition from meteorite data (Blichert-Toft & Albarede, 1997).

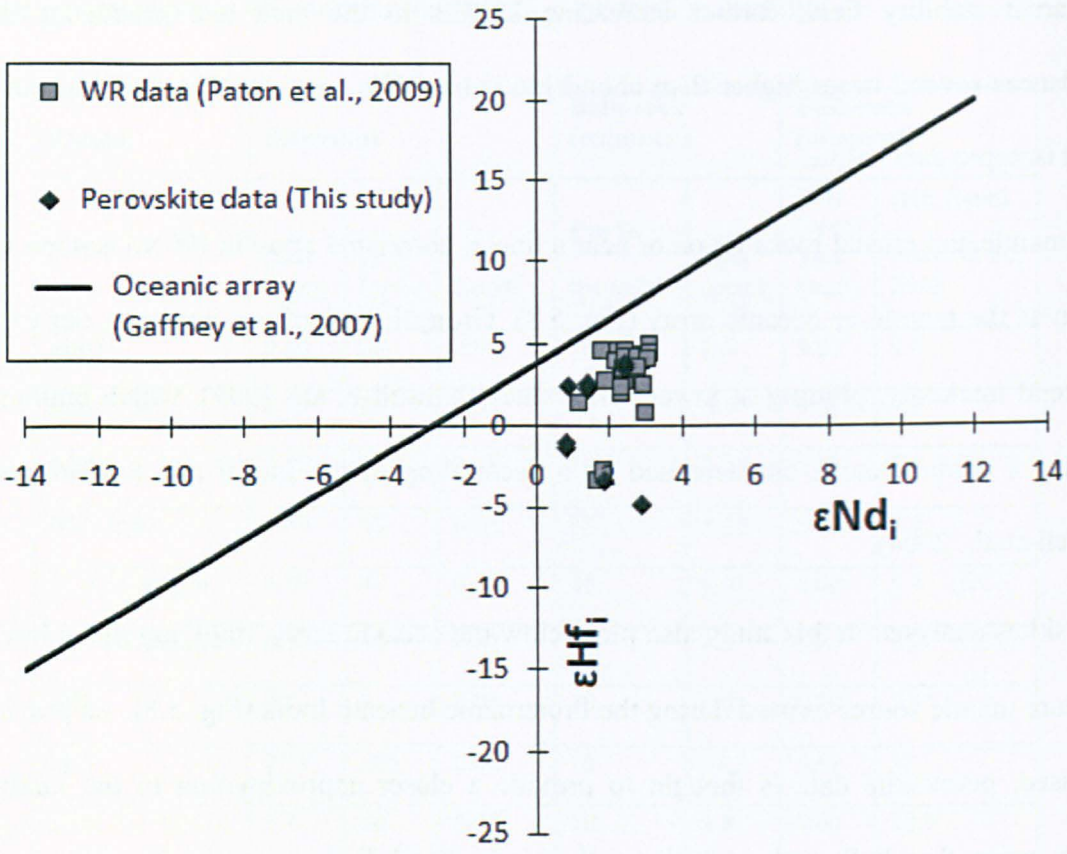

Figure 5.8. Plot of εHf_i against εNd_i for perovskites analysed in this study (black symbols) and bulk-rock analyses of Paton et al. (2009) (grey symbols). OIB array: $\varepsilon Hf = 1.33 * \varepsilon Nd + 3.19$ (Vervoort et al., 1999). Bulk-rock data used as proxy for εNd values for sample CC5, which lacks perovskite Nd data.

The existence of a hidden mantle reservoir that has remained chemically isolated from the convecting upper mantle for long periods of time (> 1 Ga) has been proposed as the source of the Hf-Nd isotopic signature in kimberlites (Bizzarro et al., 2002). There are several proposals for this hidden mantle reservoir, including the SCLM (Griffin et al., 2000; Janney et al., 2002). The SCLM would be suitably isolated and could have appropriate Lu/Hf ratios if subjected to ancient metasomatism, perhaps by asthenospheric melts. An alternative source proposed for the hidden mantle reservoir is ancient subducted crust. This can evolve to low Hf isotopic values relative to Nd isotopes given sufficient time (Bizzarro et al., 2002; Janney

et al., 2002; Nowell et al., 2004; Gaffney et al., 2007). It has also been suggested that oceanic crust might remain isolated from the convecting mantle (> 1 Ga) at the core-mantle boundary (Bizzarro et al., 2002), the transition zone (Ringwood et al., 1992), or as discrete pods within upwelling mantle (Janney et al., 2002).

It has been argued that heterogeneities in incompatible-element concentrations of the NKF and WKF require a heterogeneous source (Chalapathi Rao and Srivastava, 2009) such as the SCLM, which is highly variable over a length scale of kilometres (Hawkesworth et al., 1990). If the incompatible elements of kimberlites are determined by contributions from the SCLM, the Sr, Nd and Hf isotopic concentrations should also be controlled by this source (assuming contamination to be minimal), and therefore show variation. Hence, Paton et al. (2009) argued that SCLM material could not have made a significant contribution to the EDC kimberlites, because neither the bulk-rock incompatible-element chemistry, nor the Nd and Hf bulk-rock isotopic compositions, of NKF and WKF samples showed significant variation.

Our perovskite Nd isotopic data support the latter hypothesis (Paton et al., 2009), whereas our Hf isotopic data suggest at least some source heterogeneity to produce the two separate groups of kimberlites with positive and negative εHf_i values. Our contrasting Nd and Hf data imply decoupling of Nd and Hf in the source, while the two distinct Hf isotopic groups suggest a degree of heterogeneity in the source of the kimberlites in the EDC. The kimberlites are all found in such close proximity that lateral variations in the source are unlikely on this length scale. However, this does not preclude *vertical* heterogeneity in the source region(s).

We therefore propose a model of kimberlite generation with a vertically heterogeneous source that has undergone separate periods of enrichment and depletion (as outlined at the beginning of Section 5.6.3) before kimberlite melt generation and emplacement at ~1100 Ma (Chalapathi Rao et al., 1999; Kumar et al., 2007; Osborne et al., 2011).

One model that fits regional geological observations would be an asthenospheric melting event linked with the initial depletion in the mantle at ~ 2Ga. The timing of the depletion event is inferred from Hf isotopic data model ages (T_{DM}*) of the kimberlites that have negative εHf_i (2102-1891 Ma), which coincides with the time of recorded magmatism in the Cuddapah basin (Anand et al., 2003). If ~15% partial melting occurred during this event (Anand et al., 2003), all garnet could be consumed but some clinopyroxene retained in the source to account for the measured Nd isotopic composition. This would result in low Lu/Hf in the depleted mantle residue that would evolve to yield low εHf_i values. This depleted asthenosphere could eventually become part of the SCLM.

The next stage of our model is enrichment of the residual SCLM before 1.5 Ga. The timing of the enrichment event is inferred from Hf isotopic data model ages (T_{DM}*) from kimberlites with positive εHf_i (1705-1618 Ma) and lamproite recorded in the EDC around 1500 Ma that requires previously enriched SCLM for their generation (Osborne et al., 2011). The low Lu/Hf of the depleted SCLM source would ensure that Lu/Hf values were almost wholly determined by the characteristics of the enriching agent – most likely percolating asthenospheric melts. Hence enrichment would likely result in higher Lu/Hf values, evolving to higher εHf_i.

The fact that some kimberlites retained negative εHf_i values implies that their source was much less affected by the 1.5 Ga enrichment event in terms of Hf, or that it was enriched by melts of identically low Lu/Hf composition. The εNd_i values of both positive and negative εHf_i samples show a similar range of values, and were therefore probably determined mainly by the initial depletion event. It is interesting to note, however, that the T_{DM} (Nd) ages of the perovskites cluster quite tightly around 1.5 Ga, suggesting some sort of genetic link with the enrichment event.

The best evidence for vertical heterogeneity in the SCLM beneath southern India is shown by the Mul5 and Tum kimberlite data. The Tum kimberlite is located just to the west of the Muligiripalle kimberlite and has been shown to have the same emplacement age (~1100 Ma; Osborne et al., 2011). However, Mul5 shows positive εHf_i (3.6-3.8) whilst the Tum kimberlite shows negative εHf_i (-4.9). The contrast in εHf_i between these two kimberlites, despite their indistinguishable ages and close proximity, may be explained by a vertically heterogeneous source.

Figure 5.9 shows that the kimberlites with lower $^{176}Hf/^{177}Hf$ (negative εHf_i) also have higher La/Yb ratio (100-160) and those with higher $^{176}Hf/^{177}Hf$ (positive εHf_i) have lower La/Yb ratio (60-100). Two possible explanations for this correlation are explored below:

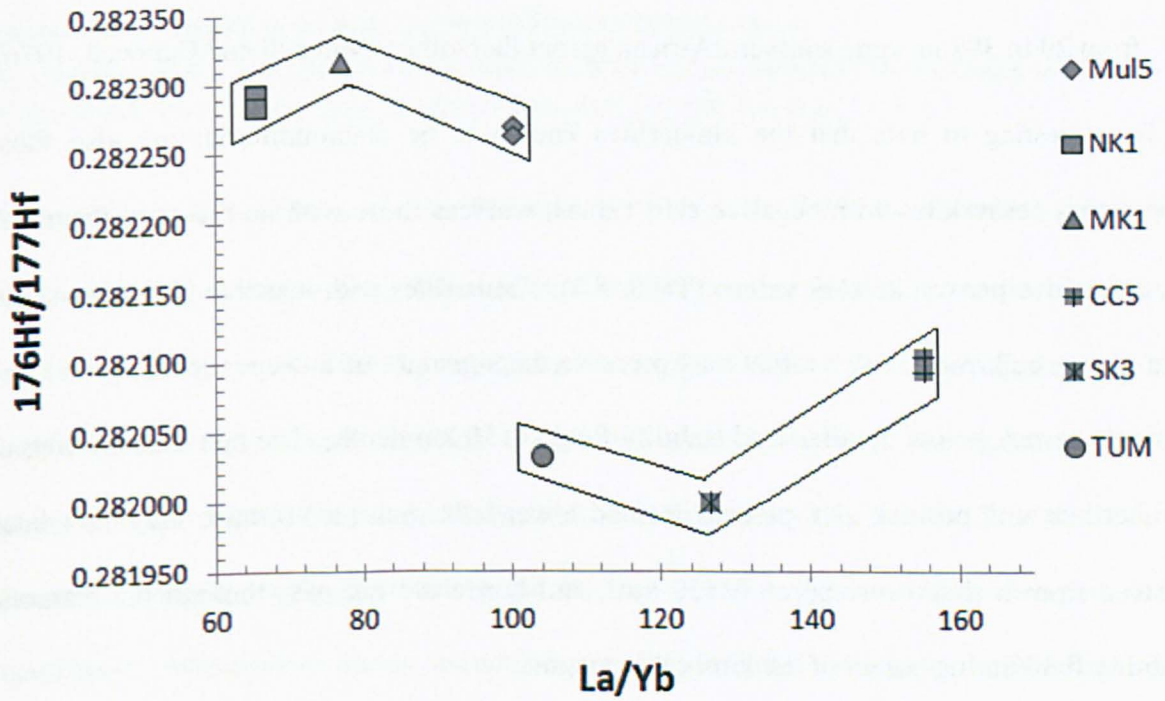

Figure 5.9. A plot of La/Yb against $^{176}Hf/^{177}Hf$. Hf data from perovskite separates. La/Yb ratios are from bulk-rock analyses.

1. Degree of partial melting. Melts with higher La/Yb ratios result from lower amounts of partial melting in the source in the presence of garnet (as Yb is preferentially retained in residual garnet, leading to La-enriched melt). An increase in the degree of partial melting progressively lowers the La/Yb ratio in the melt. It could therefore be inferred that the group of kimberlites with lower $^{176}Hf/^{177}Hf$ (and higher La/Yb) are derived from lower degrees of partial melting compared to the group with higher $^{176}Hf/^{177}Hf$.

2. Depth of melting. A higher La/Yb ratio could also reflect similar degrees of partial melting at greater depths, with more residual garnet in the mantle source.

3. Variation in the kimberlite source mineralogy. The minerals present in the mantle source of the kimberlites could occur in different proportions and also show heterogeneity. For example the La/Yb ratio of clinopyroxene has been shown to vary from 29 to 398 in some southern African garnet lherzolites (Mitchell and Carswell, 1976),

It is interesting to note that the kimberlites known to be diamondiferous are also those containing perovskites with negative εHf_i values, whereas those with no recorded diamonds yield positive perovskite εHf_i values (Table 5.5). Kimberlites with negative εHf_i perovskites and higher bulk-rock La/Yb ratios may preserve the signature of a deeper source with more residual garnet, below the diamond stability field (~150 km depth). The non-diamondiferous kimberlites with positive εHf_i perovskites and lower bulk-rock La/Yb ratios may have been derived from a shallower source (<150 km), and hence did not pass through the diamond stability field during ascent of the kimberlite magma.

Table 5.5: Hf and Nd isotopic data for diamondiferous and non-diamondiferous kimberlites.

NKF					WKF					RKF				
	εHf	εNd	TDM* Hf	TDM Hf		εHf	εNd	TDM* Hf	TDM Hf		εHf	εNd	TDM* Hf	TDM Hf
NK1	2.6	1.39	1687	1587	**CC5 45-90**	**-1.4**	**x**	**1909**	**1694**	**SK3**	**-3.4**	**1.83**	**2021**	**1744**
	2.3	1.39	1705	1602	**CC5 90-150**	**-1.1**	**x**	**1891**	**1681**					
MK1	2.4	0.86	1696	1617	**Tumm**	**-4.9**	**2.85**	**2102**	**1875**					
					Mul5[a]	3.8	2.39	1618	1496					
						3.6	2.39	1632	1506					

T_{DM}*: 2-stage Hf model ages were derived using a method derived from the Nd model age of Liew & Hoffman (1988), using an average crustal $^{176}Lu/^{177}Hf$ ratio of 0.012 (average passive margin mud, Vervoort et al., 1999). TDM is a single-stage Hf model age.

Diamondiferous kimberlites are bold, non-diamondiferous kimberlites are not.

The NKF is considered non-diamondiferous, while the WKF is diamondiferous. [a]Mul5 although in the WKF is not diamondiferous and is very poor in indicator minerals (Chalapathi Rao et al., 2004).

One puzzle is the positive bulk-rock εHf_i values (Paton et al., 2009) of kimberlites containing perovskites with negative εHf_i. This implies relatively early perovskite crystallization from a negative εHf_i melt, followed by modification of the Hf (but not Nd) signature of the remaining melt (and hence the bulk rock). One explanation that also accounts for the estimated bulk-rock Hf deficits in Mul5, NK1, MK1 and Tum (Section 5.6.2) is that Ti-rich material containing moderately radiogenic Hf was added to these samples after perovskite crystallized. Assimilation during ascent of cumulate material similar to the MARID suite (Dawson and Smith, 1977) could provide this ingredient (e.g. Choukroun et al., 2005), since Hf is compatible in Ti-bearing phases such as ilmenite and rutile commonly found in MARID xenoliths. The Hf budget of CC5 and SK3 seems to have been dominated by perovskite (Table 5.4), implying that no significant Hf-bearing material was added to these samples

during ascent. We cannot confirm this relationship, because no bulk-rock Hf data exist for SK3 or CC5 (only pipe CC1 was analysed by Paton et al. (2009)).

A vertically-heterogeneous source (Model 2) is supported by a recent study by Chalapathi Rao et al. (2011), which shows low fO_2 of the NKF magma, indistinguishable from that of diamondiferous kimberlites world-wide, indicating that redox conditions were favourable for diamond preservation. However, the NKF is known to be non-diamondiferous and it is therefore thought that magmatic emplacement could have played a major role in their low diamond potential (i.e. generation at depths above diamond stability). Thus, our model for the EDC kimberlitic magmatism is not only consistent with the geochemical and isotopic dataset but also able to account for other petrological observations.

5.7. Summary

- This paper presents the first Hf isotopic data on Indian kimberlitic perovskite. Two distinct Hf isotopic groups suggest a degree of heterogeneity in the source of the kimberlites in the EDC. The kimberlites are all found in close proximity for lateral variations in the source to be likely, but this does not preclude vertical heterogeneity in the source region(s).

- Perovskite is thought to provide a closer approximation to the kimberlite source region than bulk-rock analysis. Therefore, the close correspondence of bulk-rock with perovskite Nd isotopic values shows that the EDC kimberlites bulk-rock composition is not significantly affected by crustal contamination and alteration.

    - It is important to note that we are not suggesting that bulk-rock analyses of kimberlites can now be routinely used with the assumption that crustal contamination and alteration will have had no effect on bulk-rock composition. This may not be the case for other samples and in this instance, the coincidence

may be due to the great care that was taken to ensure minimal crustal contamination and alteration when collecting and processing samples.

- We propose a model of kimberlite generation with a vertically heterogeneous source that has undergone separate periods of enrichment and depletion before kimberlite melt generation and emplacement at ~1100 Ma.

- An initial asthenospheric melting event is linked with the initial depletion at ~ 2 Ga, coinciding with the time of recorded magmatism in the Cuddapah basin. This would result in low Lu/Hf in the depleted mantle residue that would evolve to yield low εHf_i values. This depleted asthenosphere could eventually become part of the SCLM.

- The next stage of the model is enrichment of the residual SCLM at ~1.5 Ga. The low Lu/Hf of the depleted SCLM source would ensure that Lu/Hf values were almost wholly determined by the characteristics of the enriching agent – most likely percolating asthenospheric melts. Hence enrichment would likely result in higher Lu/Hf values, evolving to higher εHf_i.

- The fact that some kimberlites retained negative εHf_i values implies that these kimberlites were largely unaffected by the enrichment event or were enriched by melts of identically low Lu/Hf composition.

- The variation in the presence of diamonds between the two εHf_i groups support the hypothesis that the group of kimberlites with lower $^{176}Hf/^{177}Hf$ are derived from a source located at deeper levels compared to the group with higher $^{176}Hf/^{177}Hf$. However, different amounts of partial melting cannot be ruled out and it could be that both depth and amount of partial melting vary between the two groups.

Chapter 6: Conclusions

6.1. Contamination: implications for sample processing

Kimberlites contain a diverse assemblage of entrained mantle and crustal fragments, and are usually subject to extensive post-emplacement alteration (Berg and Allsopp, 1972; Mitchell, 1986; Dawson, 1980). Hence, there is considerable uncertainty regarding whether measured bulk-rock analyses have been affected by processes such as contamination and alteration, or instead preserve a true record of kimberlite magma variability (Paton et al., 2007).

Magmatic perovskite is thought to provide a closer approximation to the kimberlite source region than bulk-rock analysis, but it has been shown that in some cases, it may also have been affected by contamination (Malarkey et al., 2010). However, direct analyses of isotopes in magmatic perovskite should bypass at least some of the effects of contamination and alteration, provided the perovskite equilibrated with the primary kimberlite melt at an early stage before contamination or alteration.

The close correspondence of isotopic values of both bulk-rock and perovskite in this study suggest that for the selected EDC kimberlite samples, crustal contamination and alteration have not significantly affected bulk-rock analyses and represent a closer approximation to the true isotopic signature of the source region of the melts that contributed to the kimberlites. However, it should be noted that in this study great care was taken to ensure that only the freshest bulk-rock samples were collected, and the samples were further filtered to exclude the minority that showed contamination signatures in their geochemistry. Such precautions are essential if bulk-rock analyses are to record the primary features of kimberlite geochemistry faithfully.

6.2. Kimberlites

6.2.1. Classification

Classification of the kimberlites in the EDC was not one of the main aims of this study. However, data from this study confirm that the EDC kimberlites are potassic and silica-undersaturated with peralkaline and perpotassic indices similar to those of archetypal kimberlites described by Mitchell (1995).

This study did not find any significant differences among kimberlites from the WKF, NKF or RKF in terms of their major- and trace-element compositions. However, the chondrite-normalised REE patterns of the WKF samples are slightly steeper than that of the NKF and RKF samples (Chapter 3; Figure 3.15). These data imply a slightly greater influence of residual garnet in the melt source regions of the WKF samples and suggest that their parental melts were derived from a deeper source compared to those for NKF and RKF samples.

The geochemical data obtained in this study further confirm that the EDC kimberlites predominantly lie within, or in a few cases just outside, the fields for South African Group I kimberlites on plots of Mg# against TiO_2 (Chapter 3; figure 3.5) and K_2O against TiO_2 (Chapter 3; figure 3.6), that have previously been used to distinguish Group I kimberlites from other ultramafic rocks (e.g. Chalapathi Rao and Srivastava, 2009; Taylor et al., 1994).

Care has to be taken, however, when employing elements susceptible to the effects of post-emplacement alteration such as K_2O, CaO and Al_2O_3 that Haggerty and Birkett (2004) used to suggest that the EDC kimberlites had similarities to olivine lamproites. Co-variations in the abundances of immobile elements such as Nb and Zr (Chapter 3; Fig 3.10) provide more reliable information, and, their behaviour in the case of EDC kimberlites is comparable to that of the archetypal Group I kimberlites of southern Africa. Such geochemical

characteristics reinforce previous suggestions that the EDC kimberlites should be considered as Group I kimberlites.

6.2.2. Ages of EDC kimberlites

This study presents new age data obtained by applying the Ar-Ar dating technique to phlogopite separates from two kimberlites located in the WKF. According to these Ar-Ar data, the Muligiripalle Pipe has a weighted mean age of 1113 ± 3 Ma and the Tummatapalle Pipe has a weighted mean age of 1105 ± 12 Ma. These ages support the growing evidence that all kimberlites in the EDC were emplaced contemporaneously at ~ 1100 Ma. Taken together with the near-contemporaneous Majhgawan kimberlite field of northern India (1070-1080 Ma; Kumar et al., 1993), they form part of a large group of kimberlite bodies emplaced in the India craton at ~ 1100 Ma, which in turn appears to be part of a global association of kimberlite and related rocks all formed during this short time period (Kumar et al., 2007).

6.2.3. Petrogenesis

The bulk-rock Nd isotopic data plotted on an Nd evolution diagram (Chapter 3; Figure 3.21) suggest a model for petrogenesis of the EDC kimberlites where the kimberlite magmas were derived ~ 1 Ga ago from an initially depleted mantle source that had been enriched at around 1.9–2 Ga. A "missing reservoir" (e.g. Bizzarro et al., 2002) may also have contributed to the source of the EDC kimberlites. The Nb/Ta and La/Nb ratios of the EDC kimberlites (Chapter 3; Fig. 3.23) scatter widely between primitive mantle composition and that of a proposed "missing reservoir" suggested by Agashev et al. (2010) to account for superchondritic Nb/Ta ratios in kimberlites.

This study proposes that the kimberlites in the EDC originated from a mantle source that was chemically and isotopically heterogeneous in the vertical dimension, and has undergone

separate periods of enrichment and depletion events before kimberlite melt generation and emplacement at ~ 1100 Ma (Chalapathi Rao et al., 1999; Kumar et al., 2007; Osborne et al., 2011).

The perovskite isotopic data show contrasting Nd and Hf signatures, which imply decoupling of Nd and Hf in the source. There are two distinct Hf isotopic groups, suggesting heterogeneity in the source of the melts parental to kimberlites in the EDC. The kimberlites are all found in too close proximity for lateral variations in the source to be likely, but this does not preclude vertical heterogeneity in the source.

A model is proposed where an asthenospheric melting event is linked with the initial depletion prior to ~ 2 Ga, coinciding with the time of recorded magmatism in the Cuddapah basin. This would result in low Lu/Hf in the depleted mantle residue that would evolve to yield low εHf_i values. This depleted asthenosphere could eventually become part of the SCLM. The next stage of the model is enrichment of the residual SCLM at ~ 1.5 Ga. The low Lu/Hf of the depleted SCLM source would ensure that Lu/Hf values were almost wholly determined by the characteristics of the enriching agent. Hence, enrichment would likely result in higher Lu/Hf values, evolving to higher εHf_i. The fact that some kimberlites retained negative εHf_i values implies that their contributing source regions were largely unaffected by the enrichment event or were enriched by melts of identically low Lu/Hf composition.

The variation in the presence of diamonds between the two εHf_i groups support the hypothesis that the group of kimberlites with lower $^{176}Hf/^{177}Hf$ are derived from a source located at deeper levels compared to the group with higher $^{176}Hf/^{177}Hf$. However, different amounts of partial melting cannot be ruled out and it could be that both depth and amount of partial melting vary between the two groups.

6.2.4. Kimberlite Melt Generation

This study has provided new ages that strongly support the emplacement of the EDC kimberlites during the most prolific known period of Precambrian ultramafic magmatism at around 1100 Ma, suggested to represent a global 'mantle event', when mantle conditions must have been favourable for kimberlite and lamproite emplacement (Skinner et al., 1985).

Kimberlites can be associated with mantle plumes (Gibson et al. 1995), however it is thought unlikely that a mantle plume is involved in the initiation of the southern Indian kimberlites (Chalapathi Rao et al., 2004) . Kimberlites are also often associated with periods of continental rifting and formation of ocean basins (Kumar et al., 2007); Chalapathi Rao et al. (2004) contended that the initiation of the EDC kimberlites was the result of extension of the lithosphere during the Mid-Proterozoic. Therefore the initiation of the EDC kimberlite magmatism may be linked to the formation of Rodinia approximately 1100 Ma ago when intracontinental rifting occurred, resulting in the formation of several Large Igneous Provinces; e.g., 1109-1086 Ma in Laurentia (Ernst and Buchan, 2001) and 1112-1102 Ma in the Kalahari Craton (Hanson et al., 2004).

6.3. Lamproites

6.3.1. Classification

A rock should be ultrapotassic and peralkaline if it is to be classified in the lamproite clan (Mitchell and Bergman, 1991). All the lamproites in the EDC can be considered ultrapotassic; however, they all have peralkaline and perpotassic indices < 1, indicating they are neither peralkaline nor perpotassic. Chalapathi Rao et al. (2010) attribute these low values to the effects of low degree hydrothermal alteration and the resulting carbonation and

silicification of the EDC lamproites. The EDC lamproites do contain enriched TiO_2 concentrations that are characteristic of a lamproite (Mitchell and Bergman, 1991).

A typical lamproite has high Ba (> 2000 ppm), Zr (> 500 ppm) and Sr (> 1000 ppm) concentrations (Mitchell and Bergman, 1991). The Sr abundance of the lamproites in the EDC is variable, with lamproites showing either typical or lower than expected abundances. The lamproites also show a wide range of Ba abundances but all appear lower than expected for a typical lamproite. However, it has been reported that relative to other types of lamproite, olivine lamproites can have significantly lower Ba and Sr contents (Reddy et al., 2003). The Zr abundances for the EDC lamproites are generally similar to those of a typical lamproite.

The Krishna lamproites display the well known phenomenon of heteromorphism (e.g. Rock, 1991) wherein a bulk-magma of a similar composition can give rise to rock types of varied modal mineralogy and diverse petrographic aspects. The varying modal proportions of different mineral phases (diopside, phlogopite and olivine) have been used to further classify the EDC lamproites. The lamproites located in the KLF have been classified as diopside lamproites (Ramannapeta, Vedadri South, Tirumalgiri), phlogopite lamproites (Pochampalle, Jayanthipuram) or olivine lamproites (Nallabandlagudem, Vedadri North) (Chalapathi Rao et al., 2010). It is thought that the EDC lamproites display heteromorphism, where a bulk-magma of similar composition can give rise to rock types of varied modal mineralogy and diverse petrographic aspects (Chalapathi Rao et al., 2010). The Chelima lamproite has been variously classified as a minette, lamprophyre, carbonatite-kimberlite and lamproite (Bergman, 1987; Scott-Smith, 1989), however, its current accepted classification is as a lamproite (Chalapathi Rao et al., 2004). The data from this study support the classifications of Chalapathi Rao et al. (2010) and suggest that the Reddikunta and Ramapuram lamproites

show mineralogy similar to those classified as diopside-lamproites, while the Chelima lamproite is most similar to those classified as phlogopite-lamproites.

6.3.2. Ages of EDC lamproites

There are few ages for the Indian lamproites, especially for those from the EDC, and those that are published are considered unreliable because of alteration effects in the kimberlites and lamproites. An age of 1224 ± 14 Ma was determined for the KLF, based on Rb-Sr age data from the Ramannapeta lamproite (Kumar et al., 2001). The Chelima lamproite has been previously dated using K-Ar, Ar-Ar and Rb-Sr methods, which suggest it was emplaced ~ 1350-1420 Ma ago (Chalapathi Rao et al., 1996, 1999; Kumar et al., 2001).

The Ar-Ar age data obtained in this study from phlogopite mica from the Pochampalle lamproite show that the youngest parts of the phlogopite grains are at their margins and are all within error of 1500 Ma. The internal parts of the mineral grains are significantly older and in the region of ca. 1550–1650 Ma. Whether the older core regions of the minerals reflect excess argon or retention of radiogenic argon under mantle lower crust conditions is difficult to discern, but this issue does not affect the minimum emplacement age calculated for the Pochampalle lamproite. It is the ages recorded by the rims of the minerals that are of importance since these are considered to represent the timing of eruption. Therefore, the Pochampalle lamproite preserves old ages in internal parts of the grain whilst the rims record an eruption age of ca.1500 Ma.

6.3.3. Petrogenesis

The complex geochemistry of lamproites, like kimberlites, suggests a mantle source region that experienced both depletion and enrichment. The mantle source from which the EDC lamproites were derived is not tightly constrained by the isotope evolution curves as

discussed in Chapter 4 (Fig. 4.8). Their enriched geochemistry indicates that they did not originate directly from a depleted mantle source, but clearly they have a different source to that of the kimberlites.

It is also apparent that the isotopic composition of Pochampalle and Chelima lamproites evolved differently compared to the other Krishna lamproites. The Ar-Ar age determinations (Chapter 4) suggest that the Pochampalle lamproite was emplaced ~ 1500 Ma ago, roughly 300 Ma before the rest of the Krishna lamproites. It would seem that the Pochampalle magma was also derived from an isotopically distinct mantle source with a lower $^{143}Nd/^{144}Nd$ ratio. Trace-element geochemistry implies that it may have been derived by relatively smaller degrees of partial melting from within the garnet stability-field compared to the rest of the KLF. The Nd-isotopic signature and the bulk-rock REE pattern of the Pochampalle lamproite appear to be consistent with a hypothesis that a heterogeneous mantle source was sampled by the Krishna lamproites during the Proterozoic.

The Pochampalle, Chelima and KLF lamproites could originate from a separate source altogether or alternatively could all be from the same source, e.g. ancient depleted mantle enriched prior to lamproite generation, but with the Pochampalle and Chelima lamproites derived at an earlier time. On Figure 6.1, the enriched mantle line (EM^*_x) has been revised to show enrichment of the source at an earlier time (EM^*_y), which then intersects the Pochampalle lamproite at its emplacement age ~1500 Ma followed by the Chelima lamproite and the KLF lamproites around their emplacement age of ~1225 Ma. These relationships are consistent with a very early (~ 3 Ga) enrichment event preserved in part of the SCLM, that evolved to generate lamproites at different times (1.5-1.4 Ga and then 1.2 Ga).

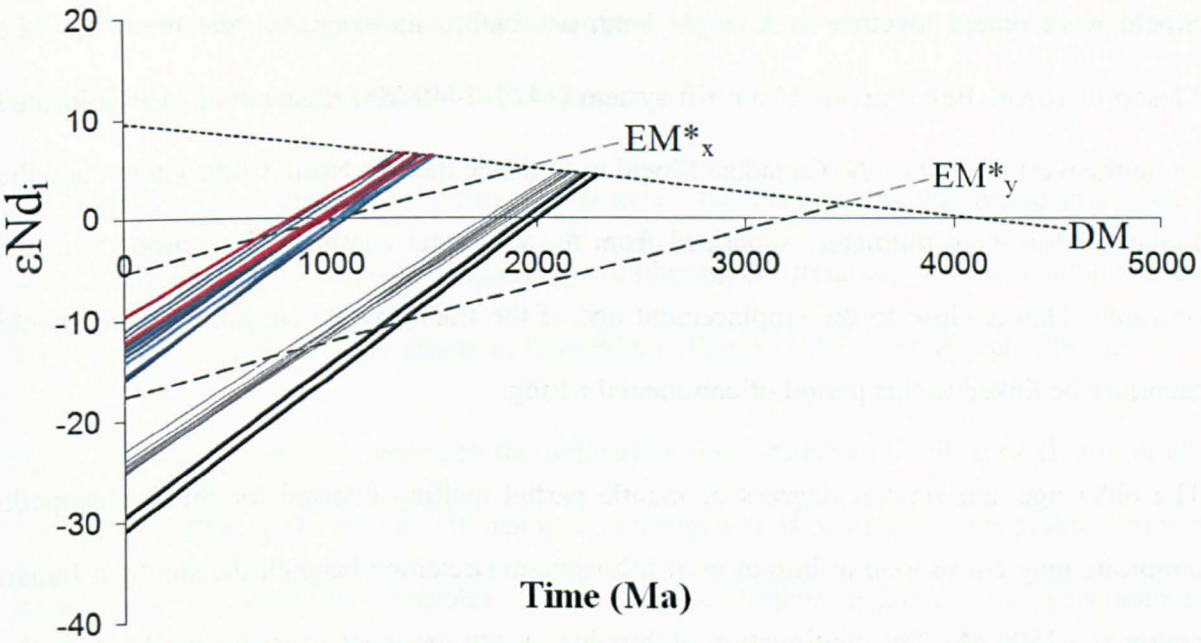

Figure 6.1. Plot of εNd_i against time for the EDC kimberlites (coloured lines) and lamproites (black lines). The single bold dashed line represents the potential Nd evolution of enriched mantle (EM^*_x) beneath India, modelled using the εNd of a xenolith from the Lattavaram kimberlite in the EDC (Karmalkar et al. 2009), and assuming a representative value of $^{147}Sm/^{144}Nd$ (0.5116) for EM (EMI; Hart et al., 1992). The EM^*_y line is plotted to show a proposed earlier enrichment event for the EDC lamproites. The depleted mantle (DM) trend (dotted line) is based on data from Workman and Hart (2005).

More definite conclusions are difficult to draw from Nd evolution modelling of the lamproites due to the isotopic heterogeneity of the sub-continental lithospheric mantle, even on relatively small length scales.

6.3.4. Lamproite melt generation

Insights into the possible tectonic setting for emplacement of the Pochampalle lamproite could come from recent work by Hou et al. (2008). Citing a giant radiating dyke swarm and LIPs at ~ 1.85 Ga, they propose that the North China Craton, Indian Craton and Canadian

Shield were united together in a single landmass before its extension and break-up. The Mesoproterozoic Belt–Purcell–Uinta rift system (1470–1440 Ma) (Sears et al., 1998) located along the west margin of the Canadian Shield is evidence that the North China Craton and the Indian Craton were ultimately separated from the Laurentia continent from around 1.5 Ga onwards. This is close to the emplacement age of the Pochampalle lamproite, which could therefore be linked to this period of continental rifting.

The older age and smaller degrees of mantle partial melting inferred for the Pochampalle lamproite may correspond to initiation of lithospheric stretching beneath the southern Indian craton at ~ 1500 Ma. The continuation of thinning, or pre-existence of such a weakness in the lithosphere, may have been exploited by later emplacement of the Krishna lamproites, by which time the mantle source region had acquired modified isotopic signatures through melt percolation from the asthenospheric mantle.

6.4. Future Work

The age of emplacement for the kimberlites from the EDC is now well resolved at ~ 1100 Ma. However, further age data for the lamproites in the EDC would be extremely useful for constraining the ages of ultrapotassic, ultramafic magmatic events in this region. Currently, the dated lamproites (Chelima, Ramannapeta and Pochampalle) have provided a large range of ages (1224-1500 Ma), and although these may represent accurate, genuinely different emplacement ages, there are some outstanding questions about the reliability of age dating techniques used and the lack of supporting data.

There is difficulty in dating the EDC lamproites due to alteration of mineral phases that are commonly used for current dating techniques (e.g. phlogopite). The majority of lamproites contain abundant titanite, which may be amenable to U/Pb dating. An investigation into the

feasibility of using titanite for dating techniques would be worthwhile and if successful would provide essential age data for the region.

The U-Pb dating of kimberlitic perovskite is also recommended as this phase is a robust mineral, thought not to be greatly affected by weathering or alteration processes and has been shown to be amenable to U-Pb dating of kimberlites (Kinny, 1997; Anand et al., 2008).

In light of the discrepancies between the perovskite (this study) and bulk-rock (Paton et al., 2009) Hf isotopic data, further Hf isotopic investigation is warranted. Perovskite from a larger suite of kimberlite samples could provide further evidence for geochemical heterogeneity in their mantle source regions. Hf isotopic measurements of perovskites from known diamondiferous kimberlites from worldwide collections may be able to confirm any link(s) between negative εHf signatures and the diamond-bearing potential of a kimberlite body.

Chapter 7: References

Agashev, A.M., Pokhilenko, N.P., McDonald, J.A., Takazawa, E., Vavilov, M.A., Sobolev, N.V., Watanabe, T., 2001. A unique kimberlite-carbonatite primary association in the Snap Lake dyke system, Slave craton: evidence from geochemical and isotopic studies. The Slave-Kaapvaal Workshop, Program with Abstract, 42–44.

Agashev, A.M., Pokhilenko, N.P., Cherepanova, Y.V., Golovin, A.V., 2010. Geochemical evolution of rocks at the base of the lithospheric mantle: Evidence from study of xenoliths of deformed peridotites from kimberlite of the Udachnaya pipe. Doklady Earth Sciences 432 (2), 746-749. doi: 10.1134/S1028334X10060073.

Akal, C., 2008. K-richterite-olivine-phlogopite-diopside-sanidine lamproites from the Afyon volcanic province, Turkey. Geological Magazine 145, 570–585.

Alibert, C., Albarede, F., 1988. Relationships between mineralogical, chemical and isotope properties of some North American kimberlites. Journal of Geophysical Research 93, 7643-7691.

Allsopp, H.L., Bristow, J.W., Smith, C.B., Brown, R., Gleadow, A.J.W., Kramers, J.D., Garvie, O.G., 1989. A summary of radiometric dating methods applicable to kimberlites and related rocks. Geological Society of Australia Special Publication 14, 343-357.

Anand, M., Gibson, S.A., Subbarao, K.V., Kelley, S.P., Dickin, A.P., 2003. Early Proterozoic melt generation processes beneath the intra-cratonic Cuddapah Basin, Southern India. Journal of Petrology 44, 2139–2171.

Anand, M., Terada, K., Osborne, I., Chalapathi Rao, N.V., Dongre, A., 2008. SHRIMP U-Pb dating of Perovskites from southern Indian kimberlites. 9th International Kimberlite Conference Extended Abstract No. 9IKC-A-00222.

Anders, E., Grevesse, N., 1989. Abundances of the elements: Meteoritic and solar. Geochimica et Cosmochimica Acta 53, 197-214.

Arndt, A.T., 2003. Komatiites, kimberlites, and boninites. Journal of Geophysical Research 108 (B6), 2293. doi:10.1029/2002Jb002157.

Arndt, N.T., Guitreau, M., Boullier, A.M., Le Roex, A., Tommasi, A., Cordier, P., Sobolev, A., 2010. Olivine, and the origin of kimberlite. Journal of Petrology 51 (3), 573-602.

Atkinson, W.J., Hughes, F.E., Smith, C.B., 1984. A review of kimberlitic rocks of western Australia. In: J Kornprobst (Ed.), Kimberlites and related rocks, 1, 195-224.

Babu, T.M., 1998. Diamonds in India. Geological Society of India, Bangalore. Economic Geology Series Publication, 332.

Basson, I.J., Viola, G., 2003. Structural overview of selected Group II kimberlite dyke arrays in South Africa. South African Journal of Geology 106, 375–394.

Batumike, J.M., O'Reilly, S.Y., Griffin, W.L., Belousova, E.A., 2007. U–Pb and Hf-isotope analyses of zircon from the Kundelungu kimberlites, D.R. Congo: implications for crustal evolution. Precambrian Research 156, 195–225.

Beard, A.D., Downes, H., Hegner, E., Sablukov, S.M., Vetrin, V.R., Balogh, K., 1998. Mineralogy and geochemistry of Devonian ultramafic minor intrusions of the southern Kola peninsula, Russia: implications for the petrogenesis of kimberlites and melilitites. Contributions to Mineralology and Petrology 130, 288-303. doi:10.1007/s004100050366

Beard, A.D., Downes, H., Mason, P.R.D., Vetrin, V.R., 2007. Depletion and enrichment processes in the lithospheric mantle beneath the Kola peninsula (Russia): evidence from spinel lherzolite and wehrilite xenoliths. Lithos 94, 1-24. doi:10.1016/j.lithos.2006.02.002

Becker, M., le Roex, A.P., 2006. Geochemistry of South African on- and off-craton, group I and group II kimberlites: petrogenesis and source region evolution. Journal of Petrology 47 (4), 673.

Bell, K., Blenkinsop, J., 1987. Archean depleted mantle: Evidence from Nd and Sr initial isotopic ratios of carbonatites. Geochimica et Cosmochimica Acta 51 (2), 291-298.

Berg, G.W., Allsopp, H.L., 1972. Low $^{87}Sr/^{86}Sr$ ratios in fresh South African kimberlites: Earth and Planetary Science Letters 16 (1), 27–30.

Bergman, S.C., 1987. Lamproites and other K-rich igneous rocks: review of their occurrence, mineralogy and geochemistry. In: Fitton, J. G. & Upton, B. G. J. (eds) Alkaline Igneous Rocks. Geological Society, London, Special Publications 30, 103-190.

Birkett, T.C., McCandless, T.E., Hood, C.T., 2003. Petrology of the Renard igneous bodies: host rock for diamonds in the northern Otish mountains region, Quebec, Proceedings of the 8th International Kimberlite Conference, Victoria, B.C., 57.

Bizzarro, M., Simonetti, A., Stevenson, R.K., David, J., 2002. Hf isotope evidence for a hidden mantle reservoir. Geology 30 (9), 771.

Blichert-Toft, J., Albarede, F., 1997. The Lu–Hf isotope geochemistry of chondrites and the evolution of the mantle–crust system. Earth and Planetary Science Letters 148 (1), 243–258.

Bogatikov, O.A., Kononova, V.A., Nosova, A.A., Kondrashov, I.A., 2007. Kimberlites and lamproites of East European Platform: petrology and geochemistry. Petrology 15, 315–334.

Brod, J.A., Gaspar, J.C., De Araujo, D.P., Gibson, S.A., Thompson, R.N., Junqueira-Brod, T.C., 2001. Phlogopite and tetra-ferriphlogopite from Brazilian carbonatite complexes: Petrogenetic constraints and implications for mineral-chemistry systematic. Journal of Asian Earth Sciences 19 (3), 65-296.

Canil, D., Bellis, A.J., 2007. Ferric Iron in $CaTiO_3$ Perovskite as an Oxygen Barometer for Kimberlite Magmas II: Applications. Journal of Petrology 48 (2), 231-252.

Carlson, J.A., Marsh, S.W., 1989. Discovery of the kimberlite dikes, Colorado. In: J. Ross, Editor, Proceedings of the Fourth International Kimberlite Conference, vol. 2, Kimberlites and Related Rocks: their mantle/crustal setting, diamonds and diamond exploration, Geological Society of Australia Special Publication 14, Blackwell Scientific Publications, Oxford,1169–1178.

Carlson, R.W., Irving, A.J., 1998. Depletion and enrichment history of sub-continental lithospheric mantle: an Os, Sr, Nd and Pb isotopic study of ultramafic xenoliths from the northwestern Wyoming Craton. Earth and Planetary Science Letters 126, 457–472. doi:10.1016/0012-821X(94)90124-4.

Caro, G., Kopylova, M.G., Creaser, R.A., 2004. The hypabyssal 5034 kimberlite of the gacho Kue cluster, Southeastern Slave craton, Northwest Territories, Canada: a granite contaminated Group-I kimberlite. Canadian Mineralogy 42, 183–207. doi:10.2113/gscanmin.42.1.183.

Chakrabarti, R., Basu, A.R., Paul, D.K., 2007. Nd-Hf-Sr-Pb isotopes and trace element geochemistry of Proterozoic lamproites from southern India: Subducted komatiite in the source. Chemical Geology 236, 291–302.

Chalapathi Rao, N.V., Miller, J.A., Pyle, D.M., Madhavan, V., 1996. New Proterozoic K–Ar ages for some kimberlites and lamproites from the Cuddapah Basin and Dharwar Craton, South India: evidence for non-contemporaneous emplacement. Precambrian Research 79, 363–369.

Chalapathi Rao, N.V., Miller, J.A., Gibson, S.A., Pyle, D.M., Madhavan, V., 1999. Precise 40Ar/39Ar age determinations of the Kotakonda kimberlite and the Chelima lamproite, India: implication to the timing of mafic dyke swarm emplacement in the Eastern Dharwar Craton. Journal of the Geological Society of India 53, 425–432.

Chalapathi Rao, N.V., Gibson, S.A., Pyle, D.M., Dickin, A.P., 2004. Petrogenesis of Proterozoic Lamproites and Kimberlites from the Cuddapah Basin and Dharwar Craton. Southern India: Journal of Petrology 45, 907–948.

Chalapathi Rao, N.V., Gibson, S.A., Pyle, D.M., Dickin, A.P., Day, J., 2005. Petrogenesis of Proterozoic lamproites and kimberlites from the Cuddapah Basin and Dharwar craton, southern India: a reply. Journal of Petrology 46, 1081–1084. doi:10.1093/petrology/egi041

Chalapathi Rao, N.V., 2007. Chelima dykes, Cuddapah basin, southern India: a review of the age, petrology, geochemistry and petrogenesis of world's oldest lamproites. Journal of the Geological Society of India 69, 523-538.

Chalapathi Rao, N.V., 2008. Precambrian alkaline potassic-ultrapotassic, maficultramafic magmatism in peninsular India. Journal of the Geolological Society of India 72, 57-84.

Chalapathi Rao, N.V., Srivastava, R.K., 2009. Petrology and geochemistry of diamondiferous Mesoproterozoic kimberlites from Wajrakarur kimberlite field, Eastern Dharwar craton, southern India: genesis and constraints on mantle source regions. Contributions to Mineralogy and Petrology 157, 245-265.

Chalapathi Rao, N.V., Anand, M., Dongre, A., Osborne, I., 2009b. Carbonate xenoliths hosted by the Mesoproterozoic Siddanpalli Kimberlite Cluster (Eastern Dharwar craton): implications for the geodynamic evolution of southern India and its diamond and uranium metallogenesis. International Journal of Earth Science. doi: 10.1007/s00531-00009-00484-00537.

Chalapathi Rao, N.V., Kamde, G., Kale, H.S., Dongre, A., 2010. Petrogenesis of the Mesoproterozoic Lamproites from the Krishna Valley, Eastern Dharwar craton, Southern India. Precambrian Research 177, 103-130.

Chalapathi Rao, N.V., Paton, C., Lehmann, B., 2011. Origin and diamond prospectivity of Mesoproterozoic kimberlites from the Narayanpet field, Eastern Dharwar Craton, southern India: insights from groundmass mineralogy, bulk-chemistry and perovskite oxybarometry. Geological Journal, Published online in Wiley Online Library (wileyonlinelibrary.com). doi: 10.1002/gj.1309.

Chalapathi Rao, N.V., Kamde, G., Kale, H.S., Dongre, A., 2011b. Diamond prospectivity of Mesoproterozoic lamproites from the Krishna valley, eastern Dharwar craton, southern India: Insights from whole-rock geochemistry. Geochemical Journal 45 (1), 79-85.

Choukroun, M., O'Reilly, S. Y., Griffin, W. L., Pearson, N. J. & Dawson, J. B., 2005. Hf isotopes of MARID (mica-amphibole-rutile-ilmenite-diopside) rutile trace metasomatic processes in the lithospheric mantle. Geology, 33(1), 45-48.

Chu, N.C., Taylor, R.N., Chavagnac, V., Nesbitt, R.W., Boella, R.M., Milton, J.A., German, C.R., Bayon, G., Burton, K., 2002. Hf isotope ratio analysis using multi-collector inductively coupled plasma mass spectrometry: an evaluation of isobaric interference corrections. Journal of Analytical Atomic Spectrometry 17, 1567–1574.

Clement, C.R., 1982. A comparative geological study of some major kimberlite pipes in northern Cape and Orange Free State, Ph.D. thesis, University of Cape Town.

Coe, N., le Roex, A., Gurney, J., Pearson, D.G., Nowell, G., 2008. Petrogenesis of Swartruggens and Star Group II kimberlite dyke swarms, South Africa: constraints from whole rock geochemistry. Contributions to Mineralogy and Petrology. doi:10.1007/s00410-008-0305-1

Cohen, A.S., O'Nions, R.K., Siegenthaler, R., Griffin, W.L., 1988. Chronology of the pressure-temperature history recorded by a granulite terrain. Contributions to Mineralogy and Petrology 98, 303–311.

Condie, K.C., 2003. Supercontinents, superplumes and continental growth: the Neoproterozoic record, Geological Society, London, Special Publications 206, 1-21.

Dalton, J.A., Presnell, D.C., 1998. The continuum of primary carbonatite–kimberlitic melt compositions in equilibrium lherzolite: data from the system CaO–MgO–Al2O3–SiO2–CaO at 6 GPa. Journal of Petrology 39, 1953–1964. doi:10.1093/petrology/39.11.1953

Dawson, J.B., Smith, J.V., 1977. The MARID (mica-amphibole-rutile-ilmenite-diopside) suite of xenoliths in kimberlite. Geochimica et Cosmochimica Acta 41 (2), 309-310.

Dawson, J.B., 1980. Kimberlites and their xenoliths. New York, Spinger-Verlag. p.252.

Davies, G.R., Stolz, A.J., Mahotkin, I.L., Nowell, G.M., Pearson, D.G., 2006. Trace element and Sr–Pb–Nd–Hf isotope evidence for ancient, fluid-dominated enrichment of the source of Aldan Shield lamproites. Journal of Petrology 47, 1119–1146.

Dalziel, I.W.D., Mosher, S., Gahagan, L.M., 2000. Laurentia-Kalahari collision and the assembly of Rodinia. The Journal of Geology 108, 499–513.

Dawson, J. B. (1994). Quaternary kimberlitic volcanism on the Tanzania craton. Contributions to Mineralogy and Petrology 116, 473-485.

DePaolo, D.J., Linn, A.M., Schubert, G., 1991. The continental crustal age distribution: Methods of determining mantle separation ages from Sm-Nd isotopic data and application to the Southwestern U.S. Journal of Geophysical Research 96 2071-2088.

Digonnet, S., Goulet, N., Bourne, J., Stevenson, R., Archibald, D., 2000. Petrology of the Abloviak aillikite dykes, New Québec: evidence for a Cambrian diamondiferous alkaline province in northeastern North America. Canadian Journal Earth Sciences 37, 517–533.

Doig, R., 1970. An alkaline province linking Europe and North America. Canadian Journal of Earth Science 7, 22–28.

Dongre, A., Chalapathi Rao, N.V., Kamde, G., 2008. Limestone xenolith in Siddanpalli kimberlite, Gadwal granite-greenstone terrain, Eastern Dharwar craton, Southern India: Remnant of Proterozoic Platformal cover sequence of Bhima/Kurnool age? Journal of Geology 116, 184–191.

Edgar, A.D., Charbonneau, H.E., 1993. Melting experiments on a SiO2-poor CaO-rich aphanitic kimberlite from 5-10 GPa and their bearing on the source of kimberlite magmas. American Mineralogist 78, 132-142.

Eggler, D.H., (1989). Kimberlites: how do they form? Geological Society of Australia Special Publication 14, 489-504.

Edwards, D., Rock, N.M.S., Taylor, W.R., Griffin, B.J., Ramsay, R.R., 1992. Mineralogy and petrology of the Aries diamondiferous kimberlite pipe, Central Kimberley block, Western Australia. Journal of Petrology 33, 1157–1191.

Ernst, R.E., Buchan, K.L., 2001. Large mafic magmatic events through time and links to mantle-plume heads. In: Ernst, R.E., Buchan, K.L. (Eds.), Mantle Plumes: Their Identification Through Time. Geological Survey of America Special Paper 352, 483–575.

Fareeduddin, 2008. Kimberlite pipes of Wajrakarur kimberlite field. In: Brochure on training course on an introduction to the petrology of diamond bearing rocks and modern methods in the exploration for, and evaluation of, primary diamond deposits. Geological Society of India 1-27.

Foley, S.F., Venturelli, G., Green, D.H., Toscani, L., 1987. The ultra-potassic rocks: characteristics, classification and constraints for petrogenetic models. Earth-Science Reviews 24, 81-134.

Foley, S.F., 1992. Vein-plus-wall-rock melting mechanisms in the lithosphere and the origin of potassic alkaline magmas. Lithos 28, 435-438. doi:10.1016/0024-4937(92)90018-T

Fraser, K.J., Hawkesworth, C.J., Erlank, A.J., Mitchell, R.H., Scott-Smith Sr., B.H., 1985. Nd and Pb isotope and minor element geochemistry of lamproites and kimberlites. Earth and Planetary Science Letters 76, 57-70.

Gaffney, A., Blichert-Toft, J., Nelson, B.K., Bizzarro, M., Rosing, M., Albarede, F., 2007. Constraints on source-forming processes of West Greenland kimberlites inferred from Hf–Nd isotope systematic, Geochimica et Cosmochimica Acta 71 (11), 2820-2836.

Gibson, S.A., Thompson, R.N., Leonardos, O.H., Dicken, A.P., Mitchell, J.G., 1995. The Late Cretaceous impact of the Trindade mantle plume: evidence from large-volume, mafic, potassic magmatism in SE Brazil. Journal of Petrology 36, 189-229.

Gibson, S.A., Thompson, R.N., Dickin, A.P., Leonardos, O.H., 1996. High Ti- and low-Ti mafic potassic magmas: key to plume-lithosphere interactions and continental flood basalt genesis. Earth and Planetary Science Letters 141, 325-341.

Gopalan, K., Kumar, A., 2008. Phlogopite K–Ca dating of Narayanpet kimberlites, south India: implications to the discordance between their Rb–Sr and Ar–Ar ages. Precambrian Research 167, 377–382.

Govindaraju, K., 1994. Compilation of working values and sample description for 383 geostandards. Geostandards and Geoanalytical Research 18 (S1), 1-158.

Grasty, R.L., Leelanandam, C., 1965. Isotopic ages of basic charnockite and khondalite from Kondapalle, Andhra Pradesh, India. Mineralogical Magazine 35, 529-535.

Gregoire, M., Bell, D. R. & Le Roex, A. P. (2003). Garnet lherzolites from the Kaapvaal craton (South Africa): trace element evidence for a metasomatic history. Journal of Petrology 44, 629–657.

Gregoire, M., Rabinowicz, M., Janse, A.J.A., 2006. Mantle mush compaction: a key to understand the mechanisms of concentration of kimberlite melts and initiation of swarms of kimberlite dykes. Journal of Petrology47 (3), 631-646.

Griffin, W.L., Pearson, N.J., Belousova, E., Jackson, S.E., van Achterbergh, E., O'Reilly, S.Y., Shee, S.R., 2000. The Hf isotope composition of cratonic mantle - LAM-MC-ICPMS analysis of zircon megacrysts in kimberlites, Geochimica et Cosmochimica Acta 64 (1), 133–147.

Gudffinsson, G.H., Presnell, D.C., 2005. Continuous gradations among primary kimberlitic, carbonatitic, melilititic and komatiitic melts in equilibrium with garnet lherzolite at 3–8 GPa. Journal of Petrology 46(8), 1645–1659. doi:10.1093/petrology/egi029

Günther, D., Heinrich, C.A., 1999. Enhanced sensitivity in laser ablation-ICP mass spectrometry using helium-argon mixtures as aerosol carrier, Journal of Analytical Atomic Spectrometry 14, 1363-1368.

Gupta, M.L., Sundar, A., Sharma, S.R., 1991. Heat flow and heat generation in the Archaean Dharwar Cratons and implications for the southern Indian shield geotherm and lithospheric thickness. Tectonophysics 194, 107-122.

Gurney, J.J., 1989. Diamonds. Geological Society of Australia, Special Publication 14 (2), 935–965.

Gurney, J.J., Moore, R.O., Otter, M.L., Kirkley, M.B., Hops, J.J., McCandless, T.E., 1991. Southern African kimberlites and their xenoliths. In: Kampunju, A. B. & Lubala, R. T. (eds) Magmatism in Extensional Tectonic Settings: the Phanerozoic African Plate. New York: John Wiley, 495-536.

Fairbairn, P.E., Robertson, R.H.S., 1966. Stages in the tropical weathering of kimberlite. Clay Mineralogy 6, 351-370.

Haggerty, S.E., 1982. Kimberlites in Western Liberia: an overview of the geological setting in a plate tectonic framework. Journal of Geophysical Research 87, 811-826.

Haggerty, S.E., 1994. Super kimberlites: a geodynamic window to the earth's core. Earth and Planetary Science Letters 122, 57–69. doi:10.1016/0012-821X(94)90051-5

Haggerty, S.E., 1999. Diamond formation and kimberlite clan magmatism. Geochemical Society, Special Publication 6, 105–123.

Haggerty, S.E., Birckett, T., 2004. Geological setting and chemistry of kimberlite clan rocks in the Dharwar craton, India. Lithos 76, 535–554. doi:10.1016/j.lithos.2004.03.055

Hanson, R.E., Crowley, J.L., Bowring, S.A., Ramezani, J., Gose, W.A., Dalziel, I.W.D., Pancake, J.A., Seidel, E.K., Blenkinson, T.G., Mukwakwami, J., 2004. Coeval large-scale magmatism in the Kalahari and Laurentian cratons during Rodinia assembly. Science 304, 1126–1129.

Harris, M., Le Roex, A.P., 2004. Geochemistry of the Uintiesberg kimberlite, South Africa: petrogenesis of an offcraton, group I kimberlite. Lithos 74, 149–165. doi:10.1016/ j.lithos.2004.02.001.

Hart, S.R., Hauri, E.H., Oschmann, L.A., Whitehead, J.A., 1992. Mantle plumes and entrainment- isotopic evidence. Science 256, 517–520.

Hathorne, E.C., 2004. The trace element and lithium isotope composition of planktonic foraminifera. PhD, The Open University.

Hathorne, E.C., James, R.H., Savage, P., Alard, O., 2008. Physical and chemical characteristics of particles produced by laser ablation of biogenic calcium carbonate. Journal of Analytical Atomic Spectrometry 23, 240-243.

Hamilton, M.A., Sobolev, N.V., Stern, R.A., and Pearson, D.G, 2003. SHRIMP U-Pb dating of a perovskite inclusion in diamond: evidence for a syneruption age for diamond formation, Sytykanskaya kimberlite pipe, Yakutia region, Siberia, Eighth International Kimberlite Conference, Victoria, British Columbia.

Hawkesworth, C.J., Erlank, A.J., Kempton, P.D.,Waters, F.G.,1990. Mantle metasomatism: isotope and trace element trends in xenoliths from Kimberley, South Africa, Chemical Geology 85, 19–34.

Heaman, L.M., 1989. The nature of the subcontinental mantle from Sr-Nd-Pb isotopic studies on kimberlitic perovskite, Earth and Planetary Science Letters 92, 323-334.

Heaman, L.M., Machado, N., 1992. Timing and origin of Midcontinent Rift alkaline magmatism North America: evidence from the Coldwell Complex. Contributions to Mineralalogy and Petrology 110, 289–303.

Heaman, L.M., 1997. Global mafic magmatism at 2.45 Ga: Remnants of an ancient large igneous province?. Geology 25, 299–302.

Heaman, L.M., Kjarsgaard, B.A., Creaser, R.A., 2003. The timing of kimberlite magmatism in North America: implications for global kimberlite genesis and diamond exploration. Lithos 71, 153–184.

Heaman, L.M., Kjarsgaard, B.A., Creaser, R.A., 2004. The temporal evolution of North American kimberlites. Lithos 76, 377–397. doi:10.1016/j.lithos.2004.03.047

Hou, G., Santosh, M., Qian, X., Lister, G.S., Li, J., 2008. Configuration of the Late Paleoproterozoic supercontinent Columbia: insights from radiating mafic dyke swarms. Gondwana Research 14, 395–409.

Janney, P.E., le Roex, A.P., Carlson, R.W., Viljoen, K.S., 2002. A chemical and multi-isotope study of the Western Cape olivine melilitite province, South Africa: implications for the sources of kimberlites and the origin of the HIMU signature in Africa. Journal of Petrology 43 (12), 2339–2370.

Janse, A.J.A., Sheahan, P.A., 1995. Catalogue of worldwide diamond and kimberlite occurrences: a selective and annotative approach. Journal of Geochemical Exploration 53, 73-111.

Jaques, A.L., Lewis, J.D., Smith, C.B., Gregory, G.P., Ferguson, J., Chappell, B.W., McCulloch, M.T., 1984. The diamond bearing ultrapotassic (lamproite) rocks of the west Kimberley region. In: J. Kornprobst (Ed.), Kimberlites and related rocks, 1, 225-244.

Jaques, A.L., Lewis, J.D., Smith, C.B., 1986. The kimberlites and lamproites of Western Australia. Geological Survey of W. Australia Bulletin 132, 268.

Kaila, K.L., Roychowdhury, K., Reddy, P.R., Krishna, V.G., Harinarain, Subbotin, S.I., Sollogub, V.B., Chekunov, A.V., Kharetchko, G.E., Lazarenko, M.A., Illchenko, T.V., 1979. Crustal structure along the Kavali-Udipi profile in the Indian peninsular shield from deep seismic soundings. Journal of the Geological Society of India 20, 307-333.

Kamenetsky,V.S., Kamenetsky, M.B., Sobolev, A.V., Golovin, A.V., Demouchy, S., Faure, K., Sharygin, V.V., Kuzmin, D.V., 2008. Olivine in the Udachnaya-East Kimberlite (Yakutia, Russia): Types, Compositions and Origins. Journal of Petrology 49 (4), 823-839.

Kamenetsky,V. S., Kamenetsky, M. B., Sobolev, A.V., Golovin, A.V., Sharygin,V.V., Pokhilenko, N. P., Sobolev, N.V., 2009. Can pyroxenes be liquidus minerals in the kimberlite magma?, Lithos 112, supplement 1, 213-222.

Karmalkar, N.R., Duraiswami, R.A., Sarma, P.K., Chauhan, S.P., Jonnalagadda, M.K., 2007. Peeping into the Interior of the Western Continental Margin of India: A Xenolith based perspective, IAGR Memoir 10, 143-155.

Kaminsky, F.V., Sablukov, S.M., Sablukova, L.I., and Shchukin, V.S., 2000. Petrology of kimberlites from the newly discovered Whitefish Lake field in Ontario. GeoCanada 2000, Abstract #1203.

Karmalkar, N.R., Duraiswami, R.A., Chelapathi Rao, N.V., Paul, D.K., 2009. Mantle-derived mafic-ultramafic xenoliths and the nature of Indian sub-continental lithosphere. Journal of the Geological Society of India 73, 657–679.

Kelley, S.P., Wartho, J.A., 2000. Rapid kimberlite ascent and the significance of Ar–Ar ages in xenolith phlogopites. Science 289.

Keshav, S., Corgne, A., Gudfinnsson, G.H., Bizimis, M., McDonough' W.F., Fei, Y., 2005. Kimberlite petrogenesis: Insights from clinopyroxene-melt partitioning experiments at 6 GPa in the CaO-MgO-Al_2O_3-SiO_2-CO_2 system. Geochimica et Cosmochimica Acta 69 (11), 2829-2845.

Kinny, P.D., Griffin, B.J., Heaman, L.M., Brakhfogel, F.F., and Spetsius, Z.V., 1997. SHRIMP U-Pb ages of perovskite from Yakution kimberlites, Russian Geology and Geophysics 38, 97-105.

Kjarsgaard, B.A., 2003. Volcanology of kimberlite: Diamonds Short Course Notes, Cordilleran Round-Up, Vancouver, British Columbia 29–30, 20.

Kostrovitsky, S. I., 1976. Physical conditions, hydraulics and kinematics of emplacement of kimberlite pipes 1–95, Nauka, Novosibirsk.

Kramers, J.D., Smith, C.B., 1983. A feasibility study of U-Pb and Pb-Pb dating of kimberlites using groundmass mineral fractions and whole rock samples. Chemical Geology 1, 23-38.

Kumar, A., Kumari, P., Dayal, A.M., Murthy, D.S.N., Gopalan, K., 1993. Rb–Sr ages of Proterozoic kimberlites of India: evidence for contemporaneous emplacement. Precambrian Research 62, 227–237.

Kumar, A., Gopalan, K., Rao, K.R.P., Nayak, S.S., 2001. Rb–Sr Age of kimberlites and lamproites from Eastern Dharwar Craton, South India. Journal of the Geological Society of India 58, 135–141.

Kumar, A., Gopalan, K., 2005. Comments on: 'Petrogenesis of Proterozoic Lamproites and Kimberlites from the Cuddapah Basin and Dharwar Craton, Southern India'. Journal of Petrology 46, 1077–1079.

Kumar, A., Heaman, L.M., Manikyamba, C., 2007. Mesoproterozoic kimberlites in south India: A possible link to ~1.1 Ga global magmatism. Precambrian Research 154, 192–204.

Langworth, A.P., Black, L.P., 1978. The Mordor complex, a highly differentiated potassic intrusion with kimberlitic affinities in central Australia. Contributions to Mineralogy and Petrology 67, 51–62.

Lapin, A.V., Tolstov, A.V., Vasilenko, V.B., 2007. Petrogeochemical characteristics of the kimberlites from the Middle Markha region with application to the problem of the geochemical heterogeneity of kimberlites. Geochemistry International 45 (12), 1197-1209.

Larsen, L.M., Rex, D.C., 1992. A review of the 2500Ma span of alkaline-ultramafic-potassic and carbonatitic magmatism in West Greenland. Lithos 28, 367-402.

Lehmann, B., Burgess, R., Frei, D., Belyatsky, B., Mainkar, D., Chalapathi Rao, N.V., Heaman, L.M., 2010. Diamondiferous kimberlites in central India synchronous with Deccan flood basalts. Earth and Planetary Science Letters 290, 142–149.

Le Roex, A.P., Bell, D.R., Davis, P., 2003. Petrogenesis of group I kimberlites from Kimberley, South Africa: evidence from bulk-rock geochemistry. Journal of Petrology 44 (12), 2261–2286.

Letendre, J.P.L., Heureux, M.L., Mowicki, T.E., Creaser, R., 2003. The Wemindji kimberlites: exploration and geology, Proceedings of the 8th International Kimberlite Conference, Victoria, B.C., 71.

Li, Z.X., Bogdanova, S.V., Collins, A.S., Davidson, A., De Waele, B., Ernst, R.E., Fitzsimons, I.C.W., Fuck R.A., Gladkochub, D.P., Jacobs, J., Karlstrom, K.E., Lul, S., Natapov, L.M., Pease, V., Pisarevsky, S.A., Thrane, K., Vernikovsky, V., 2008. Assembly, configuration, and break-up history of Rodinia: A synthesis. Precambrian Research 160, 179-210.

Liew, T.C., Hoffmann, A.W., 1988. Precambrian crustal components, plutonic associations, plate environment of the Hercynian Fold Belt of central Europe: Indications from a Nd and Sr isotopic study. Contributions to Mineralogy and. Petrology 88, 129–138.

Lorenz, V., Zimanowski, B., Buttner, R., Kurszlaukis, S., 1999. Formation of kimberlite diatremes by explosive interaction of kimberlite magma with groundwater: field and experimental aspects. In Proc. VII International Kimberlite Conference, eds Gurney, J. J., Gurney, J. L., Pascoe, M. D. and Richardson, S. H., Red Roof Design, Cape Town, 2, 522–528.

Ludwig, K.R., 2003. ISOPLOT 3.00: A Geochronological Toolkit for Microsoft Excel Berkeley Geochronology Center, Berkeley, CA. Mitchell, R.H., 1986. Kimberlites: Mineralogy, Geochemistry, and Petrology. Plenum Press, New York, 442.

Luttinen, A.V., Zhang, X., Foland, K.A., 2002. 159 Ma Kjakebeinet lamproites (Dronning Maud Land, Antarctica) and their implications for Gondwana breakup processes. Geology Magazine 39, 525–539.

Lynn, M., 2005. The discovery of kimberlites in the Gulburga and Raichur districts of Karnataka. In: Proceedings of the group discussion on kimberlites and related rocks of India. Geological Society, Bangalore, India, 48–49.

Mahadevan, T.M., 1995. Deep Continental Structure of India: a Review. Geological Society of India Memoir 28, 562.

Malarkey, J., Pearson, D.G., Kjarsgaard, B.A., Davidson, J.P., Nowell, G.M., Ottley, C.J., Stammer, J., 2010. From source to crust: Tracing magmatic evolution in a kimberlite and a melilitite using microsample geochemistry. Earth and Planetary Science Letters 299, 80-90.

Masun, K.M., Doyle, B.J., Ball, S.A., Walker, S., 2003. The geology and mineralogy of the Anuri kimberlite, Nunavut, Canada, Proceedings of the 8th International Kimberlite, Victoria, B.C., 70.

McDonough, W.F., Sun, S.S., 1995. The composition of the Earth. Chemical Geology 120, 223-253.

McGetchin, T.R., Nikhanj, Y.S., Chodos, A.A., 1973. Carbonatite-kimberlite relations in the Cane Valley diatreme, San Juan County, Utah. Journal of Geophysical Research 78, 1854–1869.

McKenzie, D., 1989. Some remarks on the movement of small melt fractions in the mantle. Earth and Planetary Science Letters 95, 53–72. doi:10.1016/0012-821X(89)90167-2.

Mertanen, S., Pesonen, L.J., Huhma, H., 1996. Palaeomagnetism and Sm–Nd ages of the Neoproterozoic diabase dykes in Laanila and Kautokeino, northern Fennoscandia. In: Brewer, T.S. (Ed.), Precambrian Crustal Evolution in the North Atlantic Region, Geological Society (London) special publication, 112, 331–358.

Mirnejad, H., Bell, K., 2006. Origin and source evolution of the Leucite Hills lamproites: evidence from Sr-Nd-Pb-O isotopic compositions. Journal of Petrology 47, 2463–2489.

Mitchell, R.H., 1970. Kimberlite and Related Rocks- A Critical Reappraisal. The Journal of Geology 78 (6), 686-704.

Mitchell, R.H., 1972. Composition of perovskite in kimberlite, American Mineralogist 57, 1748-1753.

Mitchell, R.H., Carswell, D.A., 1976. Lanthanium, samarium and ytterbium abundances in some southern African garnet lherzolites. Earth and Planetary Science Letters 31(1), 175-178.

Mitchell, R.H., 1985. A review of the mineralogy of lamproites. Transactions of the Geological Society of South Africa 88, 411-437.

Mitchell, R.H., 1986. Kimberlites: Mineralogy, Geochemistry, and Petrology. New York, Plenum Press, pp. 442.

Mitchell, R.H., Bergman, S.C., 1991. Petrology of Lamproites. New York: Plenum Press, pp. 447.

Mitchell, R.H., 1994. The lamprophyre facies. Mineralogy and Petrology 51 (2-4), 137-146.

Mitchell, R.H., 1995. Kimberlites: orangeites and related rocks. New York: Plenum Press, pp. 406.

Mitchell, R.H., 2004. Experimental studies at 5–12 GPa of the Ondermatjie hypabyssal kimberlite. Lithos 76, 551–564.

Mitchell, R.H., 2006. Potassic magmas derived from metasomatised lithospheric mantle: nomenclature and relevance to exploration for diamond-bearing rocks. Journal of the Geological Society of India 67, 317–327.

Mitchell, R.H., 2008. Petrology of hypabyssal kimberlites: relevance to primary magma compositions. Journal of Volcanic Geothermal Research. doi:10.1016/j.jvolgeores.2007.12.024.

Moorhead, J., Beaumier, M., Girard, R., Heaman, L.M., 2003. Distribution, structural controls and ages of kimberlite fields in the Superior Province of Québec, Proceedings of the 8th International Kimberlite, Victoria, B.C., 128.

Munker, C., Weyer, S., Scherer, E., Mezger, K., 2001. Geochemistry Geophysics Geosystems 2, Paper number GC000183, ISSN: 1525-2027.

Murthy, D.S.N., Dayal, A.M., Natarajan, R., 1994. Mineralogy and geochemistry of Chigicherla kimberlite and its xenoliths, Anantapur district, South India. Journal of the Geological Society of India 43, 329-341.

Murphy, D.T., Collerson, K.D., Kamber, B.S., 2002. Lamproites from Gaussberg, Antarctica: possible transition zone melts of Archaean subducted sediments. Journal of Petrology 43, 981–1001.

Nagaraja Rao, B.K., Rajurkar, S.T., Ramalingaswamy, G., Ravindra Babu, B., 1987. Stratigraphy, structure and evolution of the Cuddapah Basin. Geological Society of India Memoir 6, 33–86.

Naqvi, S.M., Rogers, J.J.W., 1987. Precambrian Geology of India. Oxford Monographs on Geology and Geophysics 6, 223.

Nayak, S.S., Kudari, S.A.D., 1999. Discovery of diamond-bearing kimberlites in Kalyandurg area, Anantapur district, Andhra Pradesh. Current Science 76, 1077-1079.

Nayak, S.S., Rao, K.R.P., Kudari, S.A.K., Ravi, S. 2001. Geology and tectonic setting of kimberlites and lamproites of southern India. Geological Survey of India Special Publication 58, 603-613.

Nelson, D.R., Chivas, A.R., Chappell, B.W., McCulloch, M.T., 1988. Geochemical and isotopic systematics in carbonatites and implications for the evolution of ocean-island sources. Geochimica et Cosmochimica Acta 52, 1–17.

Nelson, D.R., 1992. Isotopic characteristics of potassic rocks- evidence for the involvement of subducted sediments in the magma. Lithos 28, 403–420.

Nixon, P.H., Thirlwall, M.F., Buckley, F., Davies, C.J., 1984. Spanish and Western Australian lamproites: aspects of whole rock geochemistry. In: Kornprobst, J. (Ed), Kimberlites I: Kimberlites and Related Rocks. Proceedings of the Third International Kimberlite Conference, Elsevier, 1, 255–284.

Nixon, P.H., 1987. Mantle Xenoliths. New York: John Wiley and Sons Inc, pp. 904.

Nixon, P.H., Davies, G.R., Rex, D.C., Gray, A., 1992. Venezuela kimberlites. Journal of Volcanology and Geothermal Research 50, 101–115.

Nixon, P.H., 1995. Morphology and nature of primary diamondiferous occurrences. Journal of Geochemical Exploration 53, 41–71.

Nowell, G. M., Pearson, D. G., Kempton, P. D., Noble, S. R., Smith, C.B., 1999. Origins of kimberlites: a Hf isotope perspective. In: Gurney, J. J., Gurney, J. L., Pascoe, M. D. & Richardson, S. H. (eds): Proceedings 7th International Kimberlite Conference, Cape Town. Goodwood, S. Africa: National Book Printer, 616–624.

Nowell, G.M., Pearson, D.G., Bell, D.R., Carlson, R.W., Smith, C.B., Kempton, P.D., Noble, S.R., 2004. Hf isotope systematics of kimberlites and their megacrysts: new constraints on their source regions. Journal of Petrology 45 (8), 1583–1612.

Osborne, I., Sherlock, S., Anand, M., Argles, T.W., 2011. New Ar–Ar ages of southern Indian kimberlites and a lamproite and their geochemical evolution. Precambrian Research 189, 91-103. doi:10.1016/j.precamres.2011.05.004.

Patel, S.C., Ravi, S., Rao, C.R.M., Rama Rao, G., Nayak, S.S., 2008. Mineralogy and Geochemistry of Wajrakarur Kimberlites. Southern India. 9th International Kimberlite Conference Extended Abstract No. 9IKC-A-00040.

Paton, C., Hergt, J.M., Phillips, D., Woodhead, J.D., Shee, S.R., 2007. New insights into the genesis of Indian kimberlites from the Dharwar Craton via in situ Sr isotope analysis of groundmass perovskite. Geology 35, 1011-1014.

Paton, C., Hergt, J.M., Woodhead, J.D., Phillips, D., Shee, S.R., 2009. Identifying the asthenospheric component of kimberlite magmas from the Dharwar Craton, India. Lithos 112, 296–310.

Paul, D.K., Ray Barman, T., 1988. Isotopic and geochemical evolution of granulites of the Eastern Ghats belt. Workshop on 'Proterozoic Rocks of India' IGCP-217. Calcutta: Geological Society of India (unpaginated).

Paul, K.K., Nayak, S.S., Pant, N.C., 2006. Indian Kimberlites and Related Rocks: Petrology and Geochemistry. Journal of the Geological Society of India 67, 328-355.

Paul, D.K., Crocket, J.H., Reddy, T.A.K., Pant, N.C., 2007. Petrology and geochemistry including Plantinum Group Element abundances of the Mesoproterozoic ultramafic (lamproite) rocks of Krishna District, southern India: implications for source rock characteristics and petrogenesis. Journal of the Geological Society of India 69, 577-596.

Pearson, D.G., Carlso, R.W., Shirey, S.B., Boyd, F.R., Nixon, P.H., 1995. Stabilisation of Archean lithospheric mantle: a Re-Os isotope study of peridotite xenoliths from the Kaapvaal craton. Earth and Planetary Science Letters 134, 341-357.

Pearson, D.G., Kelley, S.P., Pokhilenko, N.P., Boyd, F.R., 1997. Laser $^{40}Ar/^{39}Ar$ analyses of phlogopites from Southern African and Siberian kimberlites and their xenoliths: Constraints on eruption ages, melt degassing and mangle volatile compositions. Russian Journal of Geology and Geophysics 38, 106-117.

Pearson, D.G., Canil, D., Shirey, S.B., 2003. Mantle samples included in volcanic rocks: Xenoliths and diamonds: Treatise on Geochemistry, Elsevier, 2, 171-275.

Phillips, D., Onstott, T.C., 1988. Argon isotopic zoning in mantle phlogopite. Geology 16, 542–546.

Phillips, D., 1991. Argon isotope and halogen chemistry of phlogopite from South African kimberlites: a combined step-heating, laser probe, electron micro-probe and TEM study. Chemical Geology (Isotope Geoscience Section) 87, 71–98.

Phillips, D., Kiviets, G.B., Barton, E.S., Smith, C.B., Viljoen, K.S., Fourie, L.F., 1999. 40Ar/39Ar dating of kimberlites and related rocks: problems and solutions. 7th International Kimberlite Conference (Cape Town) 2, 677–688.

Pidgeon, R.T., Smith, C.B., Fanning, C.M., 1989. Kimberlite and lamproite emplacement ages in Western Australia. Geological Society of Australia Special Publication 14, 369-381.

Piper, J.D.A., 1981. Palaeomagnetic study of the (Late Precambrian) West Greenland kimberlite-lamprophyre suite: definition of the Hadrynian Track. Physics of the Earth and Planetary Interiors 27 (3), 164-186.

Prelevic, D., Foley, S.F., Romer, R., Conticelli, S., 2008. Mediterranean Tertiary lamproites derived from multiple source components in postcollisional geodynamics. Geochimica et Cosmochimica Acta 72 (8), 2125-2156.

Price, S.E., Russell, J.K., Kopylova, M.G., 2000. Primitive magma from the Jericho Pipe, N.W.T., Canada: constraints on primary kimberlite melt chemistry. Journal of Petrology 41, 789–808. doi:10.1093/petrology/41.6.789.

Radhakrishna, T., Piper, J.D.A., (eds), 1999. The Indian Subcontinent and Gondwana: a Palaeomagnetic and Rock Magnetic Perspective. Geological Society of India Memoir 44, 270.

Ramsey, M.H., Potts, P.J., Webb, P.C., Watkins, P., Watson, J.S., Coles, B.J., 1995. An objective assessment of analytical method precision: comparison of ICP-AES and XRF for the analysis of silicate rocks. Chemical Geology 124 (1-2), 1-19.

Rao, K.R.P., Rao, K.S.B., Satyanarayana, S.V., 1991. Assessment of diamond resources in kimberlites of Venkatampalle-Lattavaram areas, Anantapur district, Andhra Pradesh. Records of the Geological Survey of India 124, 33-39.

Rao, P.V., Puffer, J.H., 1996. Geochemistry, petrogenesis and tectonic setting of Proterozoic mafic dyke swarms, Eastern Dharwar Craton, India. Journal of the Geological Society of India 47, 165-174.

Rau, T.K., Srinivas Chowdary, V., Reddy, N.S., Ravi, S., Sridhar, M., Bhaskar Rao, K.S., Sinha, K.K., 2005. Excursion guide to Wajrakarur Kimberlite Field, In: Group discussion on kimberlites and related rocks of India, 22 to 26 November 2005, Bangalore, India, pp 13.

Reddy, T.A.K., 1987. Kimberlite and lamproitic rocks of Wajrakarur area, Andhra Pradesh. Journal of the Geological Society of India 30, 1-12.

Reddy, T.A.K., Sridhar, M., Ravi, S., Chakravarthi, V., Neelakantam, S., 2003. Petrography and geochemistry of the Krishna lamproite field, Andhra Pradesh. Journal of the Geological Society of India 61, 131–146.

Renne, P.R., Swisher, C.C., Deino, A.L., Karner, D.B., Owens, T.L., DePaolo, D.J., 1998. Intercalibration of standards, absolute ages and uncertainties in $^{40}Ar/^{39}Ar$ dating. Chemical Geology 145, 117–152.

Ringwood, A.E., Kesson, S.E., Hibberson, W., Ware, N., 1992. Origin of kimberlites and related magmas, Earth and Planetary Science Letters, 113 (4), 521–538.

Rock, N.M.S., 1991. Lamprophyres. Blackie and Sons Ltd., Glasgow, pp. 285.

Roeder, P.L., Schulze, D.J., Crystallization of groundmass spinel in Kimberlite. Journal of Petrology 49 (8), 1473-1495. doi: 10.1093/petrology/egn034

Sano, Y., Oyama, T., Terada, K., Hidaka, H., 1999. Ion microprobe U–Pb dating of apatite. Chemical Geolology 153, 249–258.

Satyanarayana, S.V., 2002. Diamond Provinces of India: an overview. In: Proceedings of the International Conference on Diamond & Gemstones organized by South Asian Association of Economic Geologists (SAAEG) at Raipur, Chattisgarh, India, 9-15 February, Extended Abstracts, 44-45.

Scott, B.H., 1981. Kimberlite and lamproite dykes from Holsteinsborg, West Greenland. Meddelelser om Grønland, Geoscience 3, 13-24.

Scott-Smith, B.H., Skinner, E.M.W., 1984. A new look at Prairie Creek, Arkansas. In: J. Kornprobst (Ed.), Kimberlites and related rocks, 1, 255-284.

Scott-Smith, B.H., 1989. Lamproites and kimberlites in India. Neues Jahrbuch fur Mineralogie, Abhandlungen 86, 193-225.

Scott-Smith, B.H., 1992. Kimberlites and lamproites. Exploration Mining Geology 1, 371-381.

Sears, J.W., Chamberlain, K.R., Buckley, S.N., 1998. Structural and U–Pb geochronologic evidence for 1.47 Ga rifting event in the Belt basin, western Montana. Canadian Journal of Earth Sciences 35, 467–475.

Shee, S.R., Bristow, J.W., Bell, D.R., Smith, C.B., Allsopp, A.L., Shee, P.B., 1989. The petrology of kimberlites, related rocks and associated mantle xenoliths from the Kuruman province, South Africa. Geological Society of Australia Special Publication 14, 60-82.

Sherlock, S.C., Jones, K.A., Kelley, S.P., 2002. Fingerprinting polyorogenic detritus using the 40Ar/39Ar UV laserprobe. Geology 30, 515–518.

Skinner, E.M.W., Smith, C.B., Bristow, J.B., Scott Smith, B.H., Dawson, J.B., 1985. Proterozoic kimberlites and lamproites and a preliminary age for the Argyle lamproite pipe, Western Australia. Geological Society of South Africa 88, 335–340.

Skinner, E.M.W., 1989. Contrasting Group I and Group II kimberlite petrology: towards a genetic model for kimberlites. In: Ross, J. (ed.) Kimberlites and Related Rocks, Vol. 1, Proceedings of the 4th International Kimberlite Conference. Perth: Geological Society of Australia, 528–544.

Skinner, E.M.W., Marsh, J.S., 2004. Distinct kimberlite pipe classes with contrasting eruption processes. In: Mitchell, et al. (Eds.), 8th International Kimberlite Conference. Sel. Papers (1), 183–200.

Smith, C.B., Allsopp, H.L., Garvie, O.G., Kramers, J.D., Jackson, P.F.S., and Clement, C.R., 1989. Note on the U-Pb perovskite method for dating kimberlites: Examples from the Wesselton and De Beers mines, South Africa, and Somerset Island, Canada. Chemical Geology (Isotope Geoscience Section), 79.

Smith, C.B., Gurney, J.J., Skinner, E.M.W., Clement, C.R., Ebrahim, N., 1985. Geochemical character of the southern African kimberlites: a new approach based on isotopic constraints. Transcripts of the Geological Society of S Africa 88, 267–280.

Sparks, R.S.J., Baker, L., Brown, R.J., Field, M., Schumacher, J., Stripp, G., Walters, A., 2006. Dynamical constraints on kimberlite volcanism. Journal of Volcanology and Geothermal Research 155, 18-48.

Sparks, R.S.J., Brown, R.J., Field, M., Gilbertson, M., 2007. Kimberlite ascent and eruption. Nature 450, E21.

Sreeramachandra Rao, K., 1988. Geological setting of the kimberlite dykes in the Zangamarajupalle Lead Zinc prospect, Cuddapah district, Andhra Pradesh. Records of the Geological Survey of India 116 (3-8), 146-155.

Sridhar Choudhury, V., Rau, T.K., Bhaskara Rao, K.S., Sridhar, M., Sinha, K.K., 2007. Taimmasamudram kimberlite cluster, Wajrakarur kimberlite field, Anantpur district, Andhra Pradesh. Journal of the Geological Society of India 69, 597-610.

Steiger, R.H., Jager, E., 1977. Subcommision on geochronology: Convention on the use of decay constants in geo- and cosmochronology. Earth and Planetary Science Letters, 359–362.

Sumino, H., Kaneoka, I., Matsufuji, K., Sobolov, A., 2006. Deep mantle origin of and kimberlite magmas revealed by neon isotopes. Geophysics Research Letters 33, L16318. doi:10.1029/2006GL027144

Tainton, K.M., McKenzie, D., 1994. The generation of kimberlites, lamproites and their source rocks, Journal of Petrology 35, 787-817.

Tappe, S., Foley, S.F., Jenner, G.A., Ryan, B., Besserer, D., Kjarsgaard, B.A., 2003. Ultramafic lamprophyre dyke swarm, Torngat Mountains, Québec and Labrador: mineralogy and geochemistry, Proceedings of the 8th International Kimberlite Conference, Victoria, B.C., 56.

Tappe, S., Jenner, G.A., Foley, S.F., Heaman, L., Besserer, D., Kjarsgaard, B.A., Ryan, B., 2004. Torngat ultramafic lamprophyres and their relation to the North Atlantic Alkaline Province. Lithos 76, 491–518.

Taylor, W.R., Tompkins, L.A., Haggerty, S.E., 1994. Comparative geochemistry of West African kimberlites: evidence for a micaceous kimberlite end member of sub-lithospheric origin. Geochimica et Cosmochimica Acta 58, 4017–4037.

Tiepolo, M., Oberti, R., Vannucci, R., 2002. Trace element incorporation in titanite: constraints from experimentally determined solid/liquid partition coefficients. Chemical Geology 191, 105–119.

Thompson, M., Potts, P.J., Kane, J.S., Webb, P.C., Watson, J.S., 2000. GeoPT4. An international proficiency test for analytical geochemistry laboratories- report on round 4 (March 1999). Geostandards Newsletter 24, E1-E37.

Torsvik, T.H., Carter, L.M., Ashwal, L.D., Bhushan, S.K., Pandit, M.K., Jamtveit, B., 2001. Rodinia refined or obscured: palaeomagnetism of the Malani igneous suite (NW India). Precambrian Research 108 (3-4), 319-333.

Van Achterbergh, E., Ryan, C.G., Jackson, S.E., Griffin, W.L ., 2001. Data reducing software for LA-ICP-MS. Mineralogical Association of Canada, Short Course Series 29, 239–243.

Vervoort, J.D., Patchett, P.J., Blichert-Tof, J., Albarede, F., 1999. Relationships between Lu–Hf and Sm–Nd isotopic systems in the global sedimentary system. Earth and Planetary Science Letters 168 (1), 79–99.

Vladykin, N.V., 2009. Potassium alkaline lamproite-carbonatite complexes: petrology, genesis, and ore reserves. Russian Geology and Geophysics 50, 1119-1128.

Wagner, P. A., 1914. The Diamond Fields of Southern Africa. The Transvaal Leader, Johannesburg.

Watson, R.D., 1967. Kimberlites of eastern North America. In: P.J. Wyllie, Editor, Ultramafic and Related Rocks, Wiley, New York, 312–323.

Watson, J.S., 1998. Fast, Simple Method of Powder Pellet Preparation for X-Ray Fluorescence Analysis. X-Ray Spectrometry 25, 173-174.

Wilson, L., Head, J.W., 2007. An integrated model of kimberlite ascent and eruption. Nature 447, 53-57.

Wingate, M.T.D., Pirajno, F., Morris, P.A., 2004. Warakurna large igneous province: a new Mesoproterozoic large igneous province in west central Australia. Geology 32, 105–108.

Wolfe, J. A., 1980. Fluidization versus phreatomagmatic explosions in breccia pipes. Economic Geology 75, 1105–1111.

Woolley, A.R., Bergman, S.C., Edgar, A.D., Le Bas, M.J., Mitchell, R.H., Rock, N.M.S., Scott-Smith, B.H., 1996. Classification of lamprophyres, lamproites, kimberlites and the kalsilitic, melilitic and leucitic rocks. Canadian Mineralogist 34, 175-186.

Workman, R.K., Hart, S.R., 2005. Major and trace element composition of the depleted MORB mantle (DMM). Earth and Planetary Science Letters 231, 53–72.

Wyatt, B.A., Mitchell, M., Shee, S.R., Griffin W.I., Tomlinson, N.,White, B., 2003. The Brockman Creek Kimberlite, East Pilbara, Australia. Extended Abstracts, 8th International Kimberlite Conference, Victoria, BC, Canada.

Wyllie, P. J., 1980. The origin of kimberlite. Journal of Geophysical Research 85, 6902–6910.

Zhang, C., Yang, D., Wang, H., Dong, Y., Ye, H., 2010. Neoproterozoic Mafic Dykes and Basalts in the Southern Margin of Tarim, Northwest China: Age, Geochemistry and Geodynamic Implications. Acta Geologica Sinica (English Edition) 84 (3).

Zhao, G., Sun, M., Wilde, S.A., Sanzhong, L., 2004. A Paleo-Mesoproterozoic supercontinent: assembly, growth and breakup. Earth-Science Reviews 67 (1–2), 91-123.

http://webmineral.com/data/Perovskite.shtml

http://www.indianrealtynews.com/indian-states/andhra-pradesh

Appendices

Appendix A1: Methodology

A.1.1. Sample Preparation

1-2 kg of visibly unaltered kimberlite and lamproite were cut on a rock saw to remove any weathered portions and then reduced to small fragments in a jaw-crusher. These fragments were then crushed to powder in an agate ring mill to produce the powders used in all bulk-rock geochemical analysis.

A.1.2. Bulk-Rock Analyses

A.1.2.1. XRF

Major and trace element analysis was *determined using XRF (*X-ray fluorescence) at the Open University (Data tables in section A.2.7).

Major Element Analyses

A total of 36 samples were analysed for major elements (SiO_2, TiO_2, Al_2O_3, Fe_2O_3, MnO, MgO, CaO, Na_2O, K_20, P_2O_5) and loss on ignition (LOI). Major element concentrations were determined at the Open University by x-ray fluorescence (XRF) spectrometry on fused glass discs made from pre-ignited rock powders fused with dried lithium metaborate/teraborate flux in a ratio of 1:5 by weight. The percentage LOI of volatile components (CO_2, H_2O etc.) was determined by calculating percentage weight loss after ignition at 1000°C for approximately 1 hour.

An ARL 8420+ dual goniometer wavelength dispersive XRF spectrometer was used to conduct the analysis. XRF analysis was undertaken. Element intensity data were corrected for background and significant peak overlap interferences. Normalisation to two standards (WS-E and OU-3) was used to correct for instrumental drift. Ramsey et al. (1995) provide further information and conditions of element determination. External reproducibility is better than ± 2 % (2 s.d.)

Table A1: Normalisation data for the WS-E standard

wt. %	WS-E	WS-E	WS-E	WS-E	Average	2 s.d.	% Error	Recommended
SiO2	51.19	51.24	51.22	51.18	51.21	0.06	0.11	51.10
TiO2	2.433	2.403	2.441	2.432	2.43	0.03	1.36	2.43
Al2O3	13.85	13.87	13.86	13.86	13.86	0.02	0.13	13.78
Fe2O3	13.17	13.15	13.16	13.20	13.17	0.04	0.30	13.15
MnO	0.164	0.166	0.164	0.166	0.16	0.00	1.23	0.17
MgO	5.68	5.62	5.62	5.64	5.64	0.05	0.92	5.55
CaO	9.07	9.07	9.07	9.07	9.07	0.00	0.05	8.95
Na2O	2.44	2.44	2.44	2.42	2.43	0.02	0.89	2.47
K2O	0.99	0.99	0.99	0.98	0.99	0.01	1.18	1.00
P2O5	0.306	0.302	0.303	0.299	0.30	0.01	1.87	0.30
LOI	0.85	0.85	0.85	0.85	0.85	–	–	0.85
Total	100.13	100.12	100.10	100.09	100.11	–	–	99.75

Recommended values are taken from Govindaraju et al. (1994) and Thompson et al. (2000).
For more information on this technique see Ramsey et al. (1995).

Trace Element Analysis

Trace element abundances (Rb, Sr, Y, Zr, Nb, Ba, Pb, Th, U, Sc, V, Cr, Co, Ni, Cu Zn, Ga, Mo, As, S,) were determined at The Open University via XRF spectrometry carried out on powder pellets. The pellets were made from 9-10g of powdered sample mixed with 0.7-0.9 P.V.P (polyvinylpyrrolidone-methycellulose) binding solution, as detailed by Watson (1998). The mixture was then compressed (~0.79 x 10^6 kPa) and dried (100°C) overnight.

An ARL 8420+ dual goniometer wavelength dispersive XRF spectrometer was used to conduct the analysis. To monitor instrumental drift and precision the standards BHVO-1, QLO-1, DNC-1 and W-2 were used. Pb, U, Mo, and As are below detection limits, however the rest of the data show long term reproducibility better than ± 10 % (2 s.d.), with the exception of Th and Sc.

Table A2: XRF data for the BHVO-1 standard

Sample pos.	Approx. Det.Lt.	BHVO-1 1	BHVO-1 26	BHVO-1 1	BHVO-1 25	Average	2 s.d.	% 2 s.d.
Rb	**2**	9	10	10	9	9.6	0.8	8.8
Sr	**2**	399	403	402	404	401.9	4.0	1.0
Y	**2.0**	28.2	28.2	28.4	28.0	28.2	0.3	1.2
Zr	**2**	175	177	176	177	176.2	1.6	0.9
Nb	**1.5**	18.0	18.5	18.8	17.7	18.3	1.0	5.4
Ba	**12**	134	140	135	138	137.0	5.7	4.2
Pb	**5**	5	b.d.l.	b.d.l.	b.d.l.	5.0	–	–
Th	**4**	4	4	b.d.l.	b.d.l.	4.0	1.3	32.2
U	**3**	b.d.l.	b.d.l.	b.d.l.	b.d.l.	–	–	–
Sc	**5**	34	34	30	33	32.6	4.2	12.8
V	**5**	315	311	311	318	313.8	6.5	2.1
Cr	**4**	290	290	295	288	290.7	5.5	1.9
Co	**2**	40	42	42	41	41.0	2.4	5.9
Ni	**3**	121	119	124	125	122.0	6.1	5.0
Cu	**3**	137	138	140	140	138.9	3.4	2.5
Zn	**3**	106	108	108	109	107.9	3.0	2.7
Ga	**3**	21	22	21	22	21.7	1.1	4.9
Mo	**2**	b.d.l.	b.d.l.	b.d.l.	b.d.l.	–	–	–
As	**5**	b.d.l.	b.d.l.	b.d.l.	b.d.l.	–	–	–
S	**50**	186	186	185	180	184.0	5.7	3.1

For more information on this technique see Ramsey et al. (1995).

A.1.2.2. ICP-MS and ICP-AES

A total of 36 whole rock powders were analysed for bulk-rock major, trace and REE data (data tables are in section A.2.6). A combination of Inductively-Coupled Plasma Atomic Emission Spectroscopy (ICP-AES) and Inductively Coupled Plasma Mass-Spectrometry (ICP-MS) was used at the Natural History Museum (NHM) in London.

Reference materials were selected based on their similarities to the samples to be analysed and included BCR-1 (major and trace) and GA (trace and REE).

ICP-AES with Lithium Metaborate Flux

Major and some minor elements (Al, Ca, Fe, K, Mg, Mn, Na, P, Si, Ti, Ba, Cr, Ni, Sr, Y, Zr), were analysed using Inductively-Coupled Plasma Atomic Emission Spectroscopy (ICP-AES). 100 mg of powdered sample was fused with 300 mg $LiBO_2$ (lithium metaborate) flux, and then dissolved in

dilute HNO_3. The concentrations of selected major- and trace-elements were then determined on a Varian Vista Pro ICP-AES detector at the Natural History Museum, London. These solutions were not spiked. Reference materials were selected based on their similarities to the samples to be analysed and included BCR-1 (major and trace) and GA (trace and REE).

ICP-AES and ICP-MS with $HF/HClO_4$

$HF/HClO_4$ (hydrofluoric acid/perchloric acid) digestion was used for the other minor, trace and rare earth elements analysed. 500 mg of powdered sample underwent a total digestion in $HF/HClO_4$. The resulting solution was evaporated to dryness, and the residue was then dissolved in dilute nitric acid.

The concentrations of trace elements were then determined on a Varian Vista ICP-AES detector and Varian Vista ICP-MS detector as required, at the Natural History Museum, London. Solutions for ICP-MS were diluted a further 10 times and were spiked with 1 ppb In and 1 ppb Rh as internal standards prior to analysis. ICP-AES solutions were not spiked.

To monitor instrumental drift and precision the standard BCR-1 (data tables are in section A.2.6) was used. Major, trace and REE element analysis were found to be better than ± 20 % (2 s.d.) to that of the certified values, with the exception of Ni, Cr, Sn and Be which were found to be better than ± 30 % (2 s.d.) to that of the certified values and Bi, Cd, and Ta which showed slightly greater deviation to that of certified values.

A.1.2.3. XRF v ICP

XRF and ICP data can be plotted to assess reliability. The graphs show a strong positive with elements plotted showing R^2 values greater than 0.95. This provides strong support to the reliability of the data.

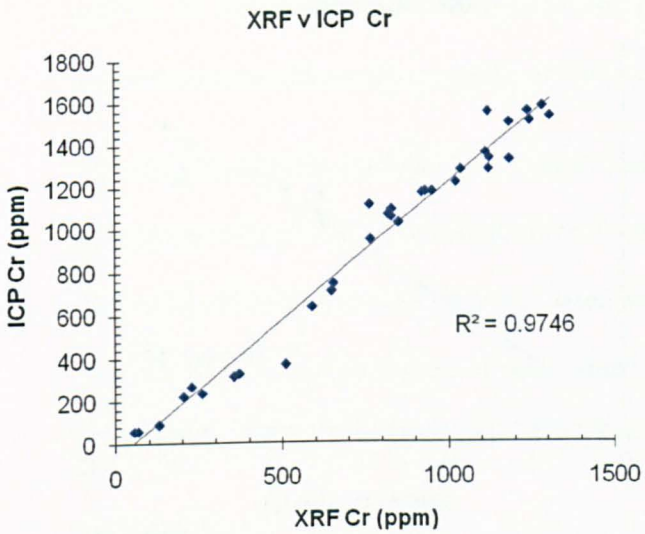
XRF v ICP Cr
ICP Cr (ppm)
XRF Cr (ppm)
R² = 0.9746
0
200
400
600
800
1000
1200
1400
1600
1800
0
500
1000
1500

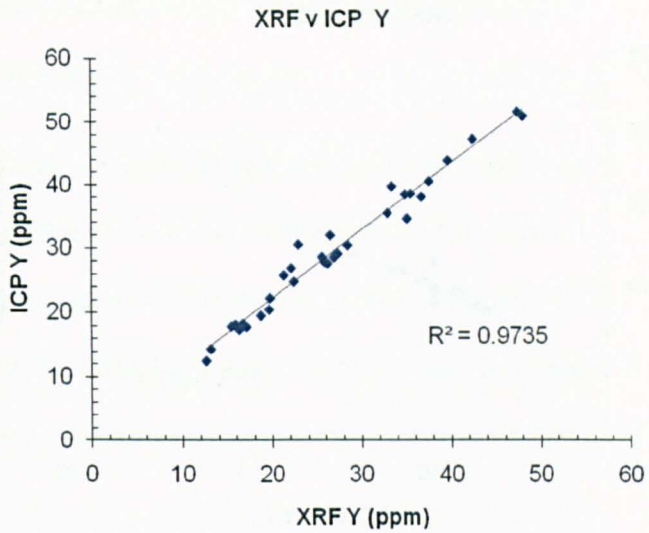
XRF v ICP Y
ICP Y (ppm)
XRF Y (ppm)
R² = 0.9735
0
10
20
30
40
50
60
0
10
20
30
40
50
60

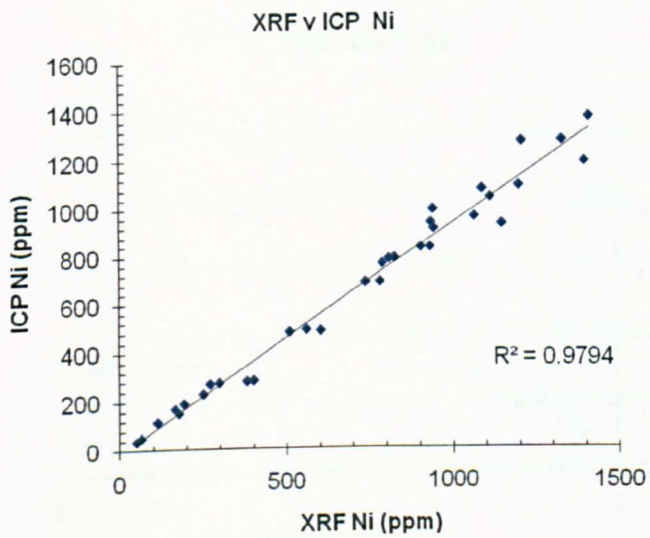
XRF v ICP Ni
ICP Ni (ppm)
XRF Ni (ppm)
R² = 0.9794
0
200
400
600
800
1000
1200
1400
1600
0
500
1000
1500

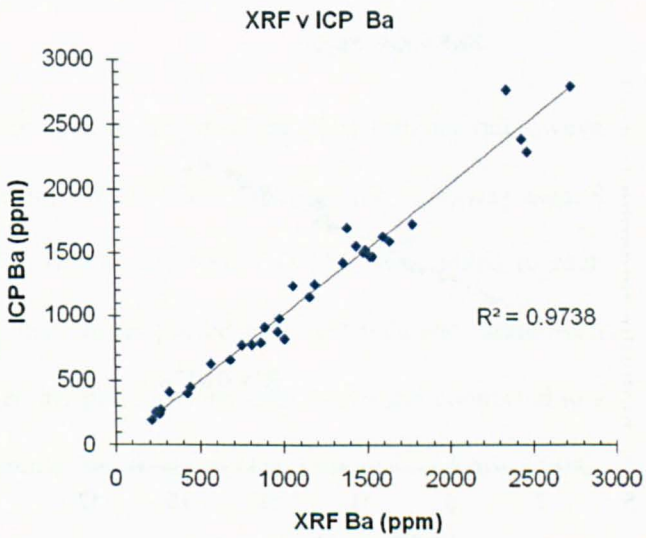
XRF v ICP Ba
ICP Ba (ppm)
XRF Ba (ppm)
R² = 0.9738
0
500
1000
1500
2000
2500
3000
0
500
1000
1500
2000
2500
3000

a)

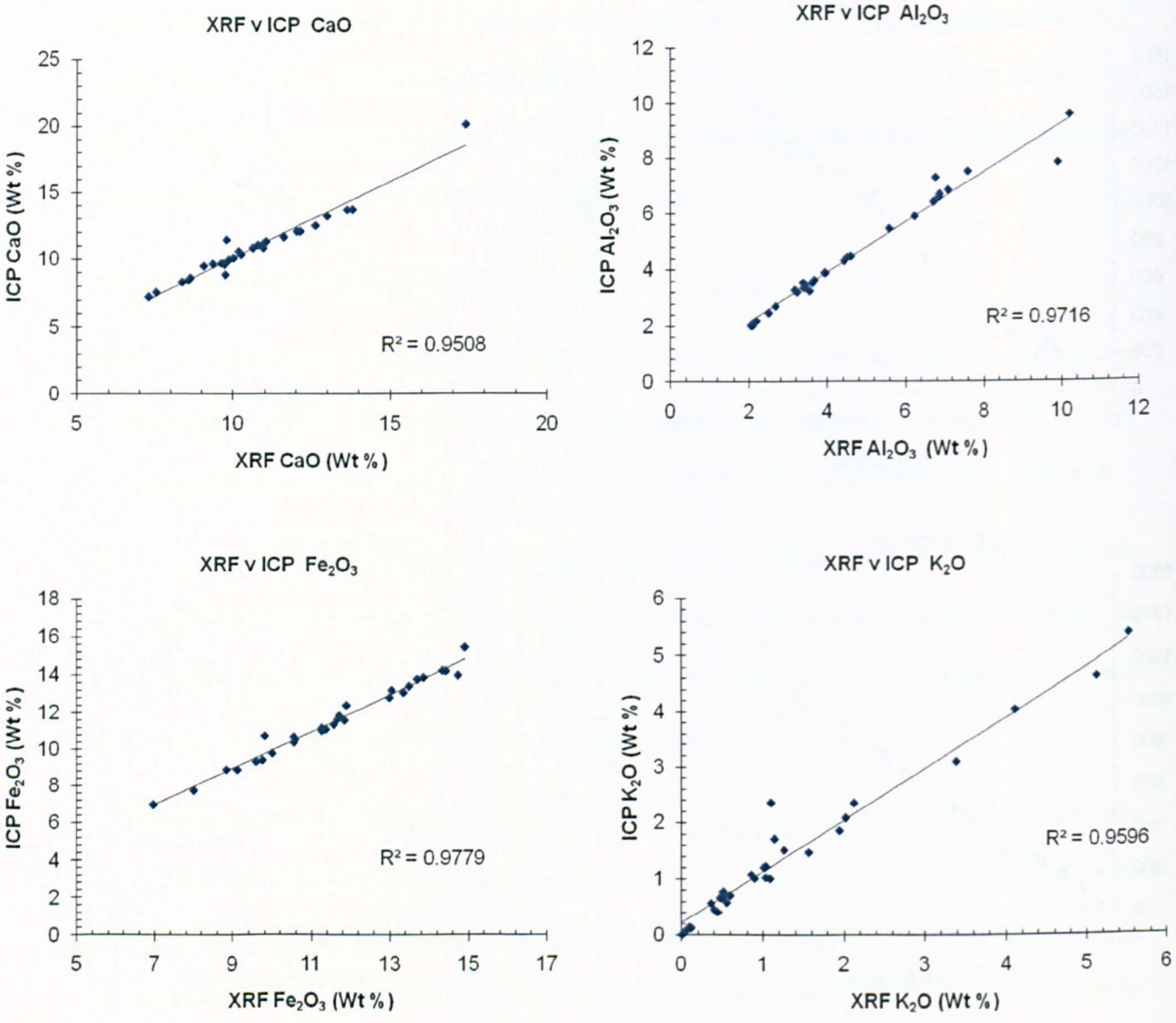

b)

Figure A1: Graphs of XRF data plotted against ICP-AES data for a) trace elements and b) major elements.

A.1.2.4. Bulk-Rock Nd Isotopic Analyses

Sample Preparation

1-2 kg of visibly unaltered kimberlite and lamproite were cut on a rock saw to remove any weathered portions and then reduced to small fragments in a jaw-crusher. These fragments were then crushed to

powder in an agate ring mill to produce the powders used in the Nd isotopic analysis. In all, 23 kimberlite/lamproite samples underwent Nd isotope analysis.

The samples were then weighed and spiked. 50mg of each powdered sample was used. The spike used was SmNd Low ($^{150}Nd/^{144}Nd$ solution) for samples and SmNd Low Dil (Diluted $^{150}Nd/^{144}Nd$ solution) for blanks. The amount to be used was based on Nd concentration in each sample obtained from ICP-MS bulk-rock data. The amount of spike added varied from 200µl to 1400µl. Once the spike had been added to the powdered sample 250µl HNO_3 was added to each sample. (Data table is in section A.2.5).

Dissolution

Microwave Dissolution

The first stage of the analysis was dissolution of the spiked powdered samples. Initially microwave dissolution using a CEM MARS 5^{TM} Digestion System with HP-500 Plus high-pressure, was used. 8 microwave vessels were cleaned with 4ml 'Aristat' HNO_3 and 3mls QD 6M HCL added to each vessel. The vessels were then sealed and pressure membranes placed into vent nuts and thermowell added. The vessels were then loaded onto a carousel and placed in the microwave and connected to a thermometer and pressure sensor. A 'clean' programme was then run (15min ramp to 150psi, 200°C, then 15min holding).

There were seven samples (CC1, Mul5, KK6, POCG, CHEL, RED, MK1) and one blank that underwent microwave digestion. 4ml TD HF and 4ml TD HNO_3 were added to each sample, which were then each decanted to one of the cleaned microwave vessels. These were then sealed, placed in carousel with pressure and temperature sensors attached and placed in safety jackets. The samples were then run on a programme, with the following conditions:

Target pressure = 150 psi; target temperature = 210°C

15 min ramp to target pressure, the 30 min hold

30min cooling prior to removal from microwave (<30°C)

During the digestion process two samples vented (MK1 and RED) due to the pressure, making them unusable, these were therefore discarded. The other samples (CC1, Mul5, KK6, POCG and CHEL) were put on a hotplate (~140°C) and dried down. Once dried, 500µl HNO_3 was added to the samples and they were then placed in an ultrasonic bath for ~10min and dried down, this was then repeated twice. 8ml QD 6M HCl was then added to the samples and they were left in this form until ready to start using columns.

It was found that although this method of dissolution was quicker than most other dissolution techniques, depending on the number of lost samples due to venting actually it could actually make it less efficient. Therefore, for the rest of the samples and the 2 that vented (MK1 and RED) a more conventional method of dissolution was used.

Total Dissolution

The weighed and spiked samples and two blanks were first digested. The samples were placed in conical vials to which 3ml HF and 250µl HNO_3 were added. These were then sealed and placed on a hotplate (~150°C) for 3 days.

The solutions looked clear after 3 days and were subsequently dried down. They were then added to 500µl HNO_3, placed in an ultrasonic bath for ~10min and then dried down. This was repeated twice. 8ml QD 6M HCl was then added to the samples and they were left in this form until ready to start using columns.

Column Separation

Nd and Sm were separated from the dissolved samples by standard ion-exchange techniques (Cohen et al., 1988), using cation columns to collect the REE fraction, which was then passed through HDEHP columns to collect Nd and Sm fractions.

650µl of each digested sample was dried down. 500µl 6m QD HCl was then added and placed in an ultrasonic bath for 10min and dried down. 1M HCl was then added and placed in ultrasonic bath for 10min. The samples were then placed in a centrifuge to remove any residues before loading.

The cation columns were first cleaned. They were drained. Then 8ml 6m QD HCl followed by 1ml MQ H_2O was passed through them. They were then equilibrated by passing through 0.6ml 1M HCl.

The samples were then added to the cation columns and three times 100µl 2.5M HCl was passed through them to wash sample through. 5ml 2.5M HCl was then passed through the column. Then 2.5ml 6M QD HCl was passed through and collected, which should contain the REE. The REE vials were then dried down on hotplate (~150°C).

50µl 0.33M HCl was added to the dried REE beakers collected from the cation columns. The DEP columns were cleaned. They were drained, and then 2ml QD 6M HCl was passed through. They were then equilibrated by passing through 0.5ml 0.33M HCl twice. The 50µl of sample was then added to the column and three times 100µl 0.33M HCl was added to wash sample through. Then 3.5ml 0.33M HCL was passed through.4ml 0.33M HCl was then added and collected containing Nd. The Nd collected was then dried down on hotplate (~150°C). 1.5ml 0.66M HCl was then added to the columns. Then 2ml 0.66M HCl was added and collected containing Sm. The Sm collected was then dried down on a hotplate (~150°C).

Analysis

The Nd fractions that were evaporated to dryness from each of the samples had 1ul 2M HCl added and were then loaded with 0.6µl 0.01M H_3PO_4 onto the centre of an outgassed Re filament. The La Jolla Nd standard was also analysed with each batch of samples (5 standards with first batch; 3 standards with second batch). 150ng La Jolla was loaded onto each outgassed filament.

Nd isotopic ratios were measured statically on the Triton thermal ionization mass spectrometer at the Open University. Reproducibility of the La Jolla Nd standard over the analysis period was 0.511849 ± 0.000002147 (8 ppm, 2SD).

The Sm fractions that were evaporated to dryness from each of the samples were then loaded with 1ul 0.01M H_3PO_4 onto the centre of an outgassed Ta single filament. The SmE standard was also analysed with each batch of samples (3 standards with first batch; 2 standards second batch). 300ng SmE standard was loaded onto each outgassed filament.

Sm isotopic ratios were measured statically on the Triton thermal ionization mass spectrometer at the Open University. However, there was no trace of Sm on the filaments from the samples. However, the standards ran well. We tested for loading and machine problems; however, after performing a column calibration and testing acid strengths, it appeared that the columns had broken down to a point where no Sm was coming off. Therefore, no Sm measurements were made.

A.1.3. Ar-Ar dating technique

Age data for three samples are presented here, including two kimberlites (Muligiripalle Pipe 5 and Tummatapalle pipe 13) from the WKF and one lamproite (Pochampalle) from the KLF (data tables are in section A.2.4). The Pochampalle lamproite is a NW-SE trending body located 2.5 km west of the Pochampalle village. Petrographic analysis of thin sections identified samples with the most suitable phlogopite grains for dating. The samples with freshest phlogopite were selected, with several samples discounted on the basis of high calcite content and alteration of phlogopite to chlorite. Once selected, microprobe analysis of phlogopite within each selected sample was used to determine the mineral chemistry.

Small blocks of each of the selected samples were then sawn, avoiding any crustal xenoliths, and crushed in a jaw crusher. The fragments were then sieved into fractions from which the phlogopite could be carefully picked (predominantly 300μm-500μm in length). The picked phlogopite grains were then washed in acetone using an ultrasonic bath to remove any adhering material. The visibly fresh grains with fewest inclusions were then selected using a binocular microscope. These grains were then packaged in aluminium foil and sent for sample irradiation at McMaster University in Ontario, Canada. Irradiation flux was monitored using the GA1550 biotite standard with an age of

98.79 ± 0.54 Ma (Renne et al., 1998). Sample J values were calculated by linear interpolation between two bracketing standards and are included in Table 3; a standard was included between every 8-10 samples in the irradiation tube. Blanks were measured either side of each measurement and used to correct each unknown, and ^{37}Ar decay and neutron-induced interference reactions using the correction factors $(^{39}Ar/^{37}Ar)_{Ca}$ = 0.00065±0.000033. $(^{36}Ar/^{37}Ar)_{Ca}$ = 0.000264±0.000013 and $(^{40}Ar/^{39}Ar)_{K}$ = 0.0085, and the mass discrimination value used was 283. The decay constant of Steiger & Jäger (1977) was used.

Samples were loaded into an ultra-high-vacuum laser port and placed under a heat lamp for 8 hours to reduce atmospheric blank levels. Samples were analysed by total fusion of single grains using Nd-YAG 1064 nm infrared laser, or Nd-YAG 213 nm UV laserprobe, both coupled to a MAP 215-50 mass spectrometer. Gases were gettered for 5 minutes using two SAES getters one at 450°C and one at room temperature, and a liquid nitrogen cold trap, before inlet to the mass spectrometer. Peaks between ^{35}Ar and ^{41}Ar were scanned 10 times and amounts extrapolated back to the inlet time. Each analysis was background corrected using blank measurements bracketing every 1-2 samples.

The infrared-laser single-grain-fusion technique was applied to Muligiripalle Pipe 5 (Mul) and Tummatapalle pipe 13 (Tum) and Pochampalle (POCg) samples. Here individual mineral grains were fused to yield a single age, and the final age is a weighted mean average, error and MSWD as calculated using Isoplot 3a (Ludwig, 2003) and reported at 2σ level. The UV intragrain laserprobe technique was applied to POC and POCg samples, in which mineral grains were large enough to enable several measurements within each grain in order to test for heterogeneity (Figure 4.) (e.g., Kelley & Wartho, 2000; Sherlock et al., 2002). Each age determination was derived from a rastered laser pit measuring 75μm x 75μm, with a 10 μm diameter beam and reported at 2σ level. In addition, grain margins were analysed using trenches parallel to the grain margins with a beam size of 10μm.

A.1.4. Nd and Hf isotopic analyses of perovskite

1-2 kg of visibly unaltered kimberlite samples were cut using a rock saw to remove any weathered portions and then reduced to small fragments in a jaw-crusher. The samples were then washed and sieved into separate size fractions: >300 μm, 150-300 μm, 90-150 μm, 63-90 μm and 45-63 μm. Samples were then assessed using a binocular microscope for perovskite abundance and sizes. It was clear that in all samples the majority of perovskite grains were concentrated in the 45-90 μm size fraction, with the exception of CC5 which contained perovskite grains up to 400 μm in size. The samples with the highest perovskite abundances were selected for isotopic analysis and were MUL5, NK1, SK3, MK1, Tum and CC5 (two size fractions were analysed separately for CC5: 45-90 μm and 90-150 μm). (Data tables are in section A.2.8).

In the first step, a simple bar magnet was passed over the samples to remove the most magnetic phases (e.g. ilmenite and spinel). Dense liquid separation was then carried out on the remaining fraction. Perovskite density is ~ 4 g/cm^3 (http://webmineral.com/data/Perovskite.shtml). Initially Na heteropolytungstate (Fastflow™) was used, with a density of 2.9 g/cm^3. This removed much of the less dense material, particularly the silicates, leaving a separate 10-50 % (by volume) perovskite. To improve the percentage of perovskite these samples were then passed through a higher density liquid (methylene iodide: density 3.3 g/cm^3), which removed additional less dense minerals. Further magnetic separation was carried out on the samples using a Frantz magnetic separator. After this step, the samples (0.001-0.026 g) contained ~ 75-80 % by volume perovskite. The final step involved removal of any visible impurities by handpicking, leaving perovskite separates with an estimated purity of 95 % by volume.

For isotopic analysis, perovskite samples were dissolved in HF-HNO_3 and spiked with mixed ^{176}Lu-^{180}Hf and ^{149}Sm-^{150}Nd isotopic tracers, dried down and then subsequently converted to chloride by dissolution in 3M HCl. Hafnium was separated using the method of Münker et al. (2001), modified in order to elute more Zr from the sample prior to Hf collection. Lu was separated from the HREE cut from the Hf separation, and was further purified using LN-SPEC ion exchange columns. The

LREE/matrix cut from the Hf separation was subsequently passed through Eichrom AG50 resin in order to concentrate LREE, and finally Sm and Nd were separated using LN-SPEC ion exchange columns.

Hafnium was analysed on a Thermo Scientific Neptune Plus mass spectrometer. Correction for Lu interference on mass 176 was negligible. Minor Yb interference on mass 176 was carried out using $^{173}Yb/^{176}Yb$ values empirically determined using doped JMC475 solutions. 54 analyses of the JMC475 standard solution gave a value of 0.282160 ± 0.000014 (46ppm, 2-sigma) across the time of analysis. Seven analyses of the BCR-2 rock standard gave a value of 0.282867 ± 0.000010 (32ppm, 2-sigma) at the time of analysis, with a hafnium concentration of 4.92 ± 0.04 ppm. Lu concentration was also measured on a Thermo Scientific Neptune Plus mass spectrometer. Lu samples were doped with sufficient natural Yb to allow mass bias correction. Correction of the ^{176}Lu peak for ^{176}Yb was carried out using the natural $^{176}Yb/^{173}Yb$ of 0.79622 (Chu et al. 2002), corrected for exponential mass bias using the measured $^{172}Yb/^{173}Yb$ ratio relative to the natural ratio of 1.35274 (Chu et al., 2002). Correction of the ^{176}Lu peak for ^{176}Hf used the measured $^{176}Hf/^{177}Hf$ for each sample, corrected using the measured Yb mass bias.

Nd was loaded on Re-Re double filament assemblies and analysed on a Thermo Scientific Triton mass spectrometer using a multidynamic algorithm. Three analyses of the La Jolla standard run with the Nd samples gave 0.511854 ± 0.000016 (2-sigma).

A.1.5. LA-ICP-MS measurements protocol

Laser-ablation ICP-MS analysis was performed on polished thin sections at the Open University on the Agilent 7500s ICP-MS coupled with a New Wave 213Nd:YAG deep (213 nm) laser system (data tables are in section A.2.9).

Table A3: LA-ICP-MS operating conditions

SCAN PARAMETERS	Detection modes	Dwell time	Integration time	
	Dual[1]	10-100 ms	10 ms	
LASER	**Laser**	**Type**	**Wavelength**	**Repetition rate**
	UP-213 (New Wave)	Nd:YAG frequency quintupled	213 nm	10 Hz
SPOTS	**Ablation duration**	**Spot size**	**Energy**	
	60 s	80 μm	0.8 mJ	

[1] Analogue and pulse detector are cross-calibrated prior to each session

Samples were ablated in a pure He atmosphere, and the analyte was carried in the He and then mixed with Argon via a "y" connector before entering the plasma. The use of He gives a 2-3 fold increase in sensitivity and significantly reduces background intensity (e.g. Günther and Heinrich, 1999). Data were acquired across the mass range from ^{7}Li to ^{208}Pb. The total time for each analysis was 240s. During the first 120s the gas blank was measured, during which the laser beam was blocked by a shutter. The shutter was then removed, the sample ablated for 60s and the transient signals from the analyte were acquired for a further 60s. A further 60s wash out period was carried out between analyses. Data reduction was carried using the GLITTER software (Van Achterbergh et al., 2001).

A glass standard (NIST 612) was used to provide external calibration. The standard was analysed twice at the start of each run and then after every 8 or 9 samples. The standard was also analysed twice at the end of each run. The trace element measurements of the standard were all found to be within ± 30 % (2 s.d.), Mn was higher at ± 40 % (2 s.d.). Detection limits are usually between 1 and 10 ppb range (Hathorne et al., 2004).

Appendix A2: Data Tables

A.2.1. Sample list and location of southern Indian kimberlites and lamproites

Table A4: Sample list and location WKF kimberlites.

Locality	Pipe	Date Collected	Latitute	Longitude
WKF Kimberlites				
Lattavaram	Pipe 3	09/02/2008	14.92454	77.28905
Lattavaram	Pipe 4	09/02/2008	14.92422	77.29696
Muligiripalle	Pipe 5	09/02/2008	14.84874	77.32106
Tummatapalle	Pipe 13	09/02/2008	14.84155	77.30209
Kalyandang Cluster				
Mukkalkunta	KL2	10/02/2008	14.57118	77.03261
Pillalpalli	KL1	10/02/2008	14.57828	77.01374
Nagiredypalle	KL3	10/02/2008	14.56546	76.96423
Chigicherla	CC2	10/02/2008	14.52676	77.69822
Chigicherla	CC1	10/02/2008	14.52687	77.67996
Chigicherla	CC5	10/02/2008	14.51881	77.63594
Chigicherla	CC4	10/02/2008	14.51471	77.62132
Wajrakarpur	Pipe 1	11/02/2008	15.03417	77.38821
Wajrakarpur	Pipe 2	11/02/2008	15.02487	77.40813
Wajrakarpur	Pipe 2N	11/02/2008	15.02363	77.40608
Chintalampalle	Pipe 12	11/02/2008	15.04663	77.46460
Timasamudram	TK4	11/02/2008	14.52484	77.29910
Timasamudram	TKO	11/02/2008	14.52639	77.29290
Timasamudram	TK3	11/02/2008		

Table A5: Sample list and location NKF kimberlites.

Locality	Pipe	Date Collected	Latitude	Longitude
NKF Kimberlites				
Narayapet	NK1	16/02/2008	16.77163	77.49593
Narayapet	NK2	16/02/2008	16.77202	77.50189
Kotakonda	KK6	16/02/2008	16.72683	77.59045
Kotakonda	KK1	16/02/2008	16.77437	77.68055
Maddur	MK1	16/02/2008	16.82409	77.64051
Maddur	MK5	16/02/2008	16.84052	77.59486

Table A6: Sample list and location RKF kimberlites.

Locality	Pipe	Date Collected	Latitude	Longitude
RKF Kimberlites				
Siddanpalle	SK1	15/02/2008	16.19089	77.55430
Siddanpalle	SK2	15/02/2008	16.18727	77.55560
Siddanpalle	SK3	15/02/2008	16.17817	77.55683

Table A7: Sample list and location EDC lamproites.

Locality	Pipe	Date Collected	Latitude	Longitude
Lamproites				
Chelima	CHE	12/02/2008	15.43054	78.70277
Ramannapeta	RAM	13/02/2008	16.72128	80.15411
Pochampalle	POC	13/02/2008	16.83379	80.16061
Pochampalle	POC (g)	13/02/2008	16.83559	80.15938
Vedadri North	VED	13/02/2008	16.82005	80.15853
Vedadri South	VED S	13/02/2008	16.81266	80.15570
Jayantapur	JAY	13/02/2008	16° 51' 38'	080° 7' 35"
Tirumalgiri	T1	14/02/2008	16.92366	80.13657
Nallabandlagudem	NAL	14/02/2008	16.95667	80.03778
Reddikunta	RED	14/02/2008	16.94476	80.04073
Ramapuram	RPM	14/02/2008	16.94943	80.04639

A.2.2. Compilation of world-wide kimberlite and lamproite ages

Table A8: Age compilation of the oldest reported ultrapotassic and alkaline magmatism

Name, location	**Rock-type**	**Age** (Ma)	**Dating method**	**Reference**
Bobi, Ivory Coast	Lamproite	1430	Rb-Sr	Nixon et al. (1992)
Venezuela	Kimberlite	1732 ± 82	Rb-Sr	Nixon et al. (1992)
West Greenland	Kimberlite	1743 ± 70	K-Ar	Larsen & Rex (1992)
Kuruman Province, South Africa	Kimberlite	1700 ± 1600	Rb-Sr	Shee et al. (1989)
Chelima, India	Lamproite	1354 ± 7	Rb-Sr	Kumar et al. (2001)
Kotakonda, India	Kimberlite	1401 ± 8	Ar-Ar	Chalapathi Rao et al. (1999)
Brockman Creek, Pilbara Craton, Australia	Kimberlite	1867 ± 8	Ar-Ar	Wyatt et al. (2003)

Table A9: Age compilation for Mesoproterozoic ultrapotassic and alkaline magmatism (adapted from Kumar et al., 2007).

Name, location	**Rock-type**	**Age** (Ma)	**Dating method**	**Reference**
AFRICA				
Premier	Kimberlite	1202 ± 72	U-Pb	Kramers & Smith (1983)
National	Kimberlite	1180 ± 30	Rb-Sr	Allsopp et al. (1989)
Liberia	Kimberlite	1072	Rb-Sr	Haggerty (1982)
Gaudini	Carbonatite	1190 ± 80	Sm-Nd	Nelson et al. (1988)
Gaudini	Carbonatite	1100 ± 300	Pb-Pb	Nelson et al. (1988)
Umkondo event	Mafic	1112 - 1102	U-Pb	Hanson et al. (2004)
Camucuo event	Mafic	1119 ± 27	Rb-Sr	*in* Ernst & Buchan (2001)
AUSTRALIA				
Argyle	Lamproite	1177 ± 47	Rb-Sr	Pidgeon et al. (1989)
Argyle	Lamproite	1126 ± 9	Rb-Sr	Skinner et al. (1985)

Mordor	Kimberlite	1128 ± 20	Rb-Sr	Langworth & Black (1985)
Mordor	Kimberlite	1118 ± 17	Rb-Sr	Langworth & Black (1985)
Giles event	Mafic	1079 - 1070	U-Pb	Wingate et al. (2004)
Lakeview events	Mafic	1130	U-Pb	*in* Ernst & Buchan (2001)
Fraser event	Mafic	1212 ± 10	U-Pb	*in* Ernst & Buchan (2001)
INDIA				
Majhgawan	Kimberlite	1067 ± 31	Rb-Sr	Kumar et al. (1993)
Mudalbid	Kimberlite	1099 ± 12	Rb-Sr	Kumar et al. (2001)
Kotakonda	Kimberlite	1085 ± 14	Rb-Sr	Kumar et al. (2001)
Wajrajarur Pipe 1	Kimberlite	1091 ± 20	Rb-Sr	Kumar et al. (1993)
Wajrajarur Pipe 2	Kimberlite	1092 ± 15	Rb-Sr	Kumar et al. (1993)
Wajrajarur Pipe 5	Kimberlite	1093 ± 20	Rb-Sr	Kumar et al. (1993)
Wajrajarur Pipe 7	Kimberlite	1091 ± 15	Rb-Sr	Kumar et al. (1993)

Name, location	**Rock-type**	**Age** (Ma)	**Dating method**	**Reference**
N. AMERICA				
Ontario Whitefish Lake	Kimberlite	1035 ± 13	Rb-Sr	Kaminsky et al. (2000)
Ontario Kyle Lake 1	Kimberlite	1023 ± 20	Rb-Sr	Heaman et al. (2004)
Ontario Kyle Lake 5	Kimberlite	1076.2 ± 3.8	U-Pb	Heaman et al. (2004)
Pele Mountain	UML	1172.3 ± 4.6	U-Pb	Heaman et al. (2004)
Bachelor Lake	Kimberlite	1104 ± 17	Rb-Sr	Alibert & Albarede (1988)
Coldwell	Alkaline gabbro	1108 ± 1	U-Pb	Heaman & Machado (1992)
Big Beaver House	Carbonatite	1060	Rb-Sr	Bell & Blenkinsop (1987)
Firesand River	Carbonatite	1060	Rb-Sr	Bell & Blenkinsop (1987)
Sea Brook Lake	Carbonatite	1100	Rb-Sr	Bell & Blenkinsop (1987)
Schryburt Lake	Carbonatite	1140	Rb-Sr	Bell & Blenkinsop (1987)

Prairie Lake	Ijolite	1156 ± 45	U-Pb	Sano et al. (1999)
SW USA province	Mafic	1090 – 1083	U-Pb	*in* Ernst & Buchan (2001)
Keweenawan	Mafic	1109 – 1083	U-Pb	*in* Ernst & Buchan (2001)
Abitibi event	Mafic	1141 ± 1	U-Pb	*in* Ernst & Buchan (2001)
Late Garder	Mafic	1185-1119	Rb-Sr/ Sm-Nd	*in* Ernst & Buchan (2001)
Pecos event	Mafic	1163 ± 4	U-Pb	*in* Ernst & Buchan (2001)
Wak-Tsh-Alg	Mafic	1170	Rb-Sr	Kaminsky et al. (2000)
Ontario Whitefish Lake 121	Kimberlite	1035 ± 13	Rb-Sr phlogopite	Kaminsky et al. (2000)
Ontario Kyle Lake 5	Kimberlite	1076.2 ± 3.8	U-Pb perovskite	Heaman et al. (2004)
Ontario Kyle Lake 1	Kimberlite	1123 ± 20	Rb-Sr phlogopite	Heaman et al. (2004)
Ontario Wawa Pele Mountain	Kimberlite	1072.3 ± 4.6	U-Pb perovskite	Heaman et al. (2004)
Le Tac Bachelor Lake	Kimberlite	1100	K-Ar phlogopite	Watson (1967)
EUROPE				
Kautokeino, Norway	Mafic	1066 ± 34	Sm-Nd	Mertanen et al. (1996)

Table A10: Age compilation for kimberlite magmatism ~ 800 Ma.

Name, location	**Rock-type**	**Age** (Ma)	**Dating method**	**Reference**
North, East and Central Kimberly province, Australia	Kimberlites and lamproites	~800	Sm-Nd	Edwards et al. (1992)
East European Platform (Kepino + other occurrences)	High-Ti Kimberlites	800	Sm-Nd	Bogatikov et al. (2007)
Weasua, Man Craton, Liberia	Kimberlites	800	Ar-Ar and Rb-Sr	In: Skinner et al. (2004)

Table A11: Age compilation for Neoproterozoic/early Cambrian kimberlite magmatism (adapted from Heaman et al., 2004).

Name, location	Rock-type	Age (Ma)	Dating method	Reference
CANADA				
Nunavut, Northern Slave, Anuri	Kimberlite	613 ± 6	Rb-Sr phlogopite	Masun et al. (2003)
Slave, Kennady Lake	Kimberlite	542.2 ± 2.6	Rb-Sr phlogopite	Heaman et al. (1997, 2003)
Slave, Snap Lake Dyke	Kimberlite	535 ± 11	Rb-Sr phlogopite	Agashev et al. (2001)
Slave, Snap Lake Dyke	Kimberlite	522.9 ± 6.9	Rb-Sr phlogopite	Heaman et al. (2004)
Torngat	Kimberlite	550 ± 15	Ar-Ar phlogopite	Digonnet et al. (2000)
Otish Mtns Lac Beaver	Kimberlite	550.9 ± 3.5	U-Pb perovskite	Moorhead et al. (2003)
Torngat K35	Kimberlite	584.0 ± 3.6	U-Pb perovskite	Tappe et al. (2003)
Otish Mtns Lac Beaver	Kimberlite	550.9 ± 3.5	U-Pb perovskite	Tappe et al. (2003)
Wemindji	Kimberlite	629 ± 29	Rb-Sr phlogopite	Birkett et al. (2003)
USA				
CO State Line Georges Creek	Kimberlite	600	Rb-Sr phlogopite	Carlson and Marsh (1989)
CO State Line Georges Creek	Kimberlite	614.5 ± 2.1	U-Pb perovskite	Heaman et al. (2003)
GREENLAND				
Nagssugtoqidian Mobile Belt	Kimberlites	580-570	K-Ar, Rb-Sr	Piper (1981)

A.2.3. Diamondiferous nature of the southern Indian kimberlites and lamproites

Table A12: Diamondiferous nature of the WKF kimberlites.

Locality	Pipe	Diamondiferous or Non-Diamondiferous	Reference
WKF			
Lattavaram	Pipe 3	Diamondiferous. Rich in indicator minerals.	Chalapathi Rao et al., 2004.
Lattavaram	Pipe 4	Diamondiferous	Chalapathi Rao et al., 2004.
Muligiripalle	Pipe 5	Non diamondiferous. Very poor in indicator minerals.	Chalapathi Rao et al., 2004
Tummatapalle	Pipe 13	Diamondiferous	Rao et al., 2005
Kalyandang Cluster			
Mukkalkunta	KL2	Diamondiferous	Paul et al., 2006
Pillalpalli	KL1	Diamondiferous	Paul et al., 2006
Nagiredypalle	KL3	No reported diamonds	Nayak and Kudari, 1999
Chigicherla	CC2	Diamondiferous	Paul et al., 2006
Chigicherla	CC1	Diamondiferous	Paul et al., 2006
Chigicherla	CC5	Diamondiferous	Chalapathi Rao and Srivastava, 2009
Chigicherla	CC4	Diamondiferous	Fareeduddin, 2008
Wajrakarpur	Pipe 1	Diamondiferous. Rich in indicator minerals.	Chalapathi Rao et al., 2004.
Wajrakarpur	Pipe 2	No reported diamonds. Indicator minerals are rare.	Chalapathi Rao et al., 2004.
Wajrakarpur	Pipe 2N	Untested	-
Chintalampalle	Pipe 12	Non Diamondiferous	Paul et al. 2006
Timasamudram	TK4	Diamondiferous	Sridhar et al., 2007
Timasamudram	TKO	Diamondiferous	Sridhar et al., 2007
Timasamudram	TK3	Diamondiferous	Sridhar et al., 2007

Table A13: Diamondiferous nature of the NKF kimberlites.

Locality	Pipe	Diamondiferous or Non-Diamondiferous	Reference
NKF			
Narayapet	NK1	No reported diamonds	Chalapathi Rao et al., 2004
Narayapet	NK2	No reported diamonds	Chalapathi Rao et al., 2004
Kotakonda	KK6	No reported diamonds	Chalapathi Rao et al., 2004
Kotakonda	KK1	No reported diamonds	Chalapathi Rao et al., 2004
Maddur	MK1	No reported diamonds	Chalapathi Rao et al., 2004
Maddur	MK5	No reported diamonds	Chalapathi Rao et al., 2004

Table A14: Diamondiferous nature of the RKF kimberlites.

Locality	Pipe	Diamondiferous or Non-Diamondiferous	Reference
RKF			
Siddanpalle	SK1	No reported diamonds. Proposed to be diamondiferous	Lynn, 2005. Chalapathi Rao et al., 2009
Siddanpalle	SK2	No reported diamonds. Proposed to be diamondiferous	Lynn, 2005. Chalapathi Rao et al., 2009
Siddanpalle	SK3	No reported diamonds. Proposed to be diamondiferous	Lynn, 2005. Chalapathi Rao et al., 2009

Table A15: Diamondiferous nature of the EDC lamproites.

Locality	Pipe	Diamondiferous or Non-Diamondiferous	Reference
KLF			
Rammanapeta	RAM	No reported diamonds	Chalapathi Rao et al., 2010
Pochampalle	POC	No reported diamonds	Chalapathi Rao et al., 2010
Pochampalle	POC (g)	No reported diamonds	Chalapathi Rao et al., 2010
Vedadri North	VED	No reported diamonds	Chalapathi Rao et al., 2010
Vedadri South	VED S	No reported diamonds	Chalapathi Rao et al., 2010
Jayantapur	JAY	No reported diamonds	Chalapathi Rao et al., 2010
Tirumalgiri	T1	No reported diamonds	Chalapathi Rao et al., 2010
Nallabandlagudem	NAL	No reported diamonds	Chalapathi Rao et al., 2010
Reddikunta	RED	No reported diamonds	Chalapathi Rao et al., 2010
Ramapuram	RAM	No reported diamonds	Chalapathi Rao et al., 2010
CLF			
Chelima	CHE	Chelima has been extensively mined for diamonds since antiquity. Not tested for diamond by modern exploration techniques.	Chalapathi Rao et al., 2010

A.2.4. Ar-Ar Geochronology Data Tables

Table A16: H1 Standard Data

Run No	Type	40Ar	+/-	39Ar	+/-	38Ar	+/-	37Ar	+/-	36Ar	+/-	35Ar	+/-	41Ar	+/-
09A51389	McM51 stds H1	1.59788	0.00028	0.06396	0.00004	0.00272	0.00001	0.03536	0.00008	0.00009	0	0.00068	0.00018	0.00007	0.00023
09A51390	McM51 stds H1	1.60838	0.00045	0.06447	0.00006	0.00237	0.00001	0.03759	0.00006	0.00014	0	0.00092	0.00012	0.00003	0.00019
09A51392	McM51 stds H1	2.20571	0.00028	0.08886	0.00004	0.00305	0.00001	0.04767	0.00005	0.00012	0	0.00076	0.00014	0.00016	0.00009
09A51393	McM51 stds H1	1.89211	0.00029	0.07695	0.00008	0.00248	0.00001	0.04147	0.00005	0.00014	0.00001	0.00048	0.00012	0.00004	0.00012
09A51395	McM51 stds H1	3.23742	0.0012	0.1314	0.00007	0.00465	0.00001	0.07194	0.00006	0.00019	0	0.00064	0.00013	0.00007	0.00008
09A51396	McM51 stds H1	1.4361	0.00017	0.05719	0.00004	0.0019	0.00001	0.03249	0.00002	0.00012	0	0.00058	0.00013	0.00016	0.0001
09A51398	McM51 stds H1	2.68364	0.00073	0.10979	0.00004	0.00329	0.00001	0.0583	0.00005	0.0001	0.00001	0.00063	0.00016	0.0001	0.00006
09A51399	McM51 stds H1	1.83073	0.00036	0.07387	0.00005	0.00217	0.00001	0.0471	0.00004	0.0001	0	0.00068	0.0002	0.00012	0.0001
09A51401	McM51 stds H1	0.56043	0.00037	0.02248	0.00004	0.00079	0.00001	0.03194	0.00005	0.00008	0	0.00064	0.00014	0.00009	0.00012
09A51402	McM51 stds H1	2.15536	0.00015	0.08616	0.00008	0.00293	0.00001	0.04702	0.00001	0.0001	0	0.00071	0.00015	0.0001	0.00008
09A51404	McM51 stds H1	1.50367	0.0004	0.06087	0.00003	0.00216	0.00001	0.03427	0.00005	0.0001	0	0.00074	0.0002	0.00007	0.00012
09A51405	McM51 stds H1	2.15176	0.00038	0.08679	0.00002	0.00317	0.00001	0.0488	0.00003	0.00012	0	0.00067	0.00018	0.0001	0.00006

Table A17: H2 Standard Data

Run No	Type	40Ar	+/-	39Ar	+/-	38Ar	+/-	37Ar	+/-	36Ar	+/-	35Ar	+/-	41Ar	+/-
09A51369	McM51 stds H2	0.91732	0.00045	0.03687	0.00001	0.00134	0.00001	0.02274	0.00005	0.00007	0	0.00076	0.00022	0.00007	0.0002
09A51370	McM51 stds H2	0.59033	0.0002	0.02381	0.00002	0.00069	0.00001	0.01292	0.00003	0.00001	0.00001	0.00071	0.00014	-0.00001	0.00019
09A51372	McM51 stds H2	0.50719	0.00019	0.02052	0.00001	0.00083	0.00001	0.01255	0.00002	0.00002	0	0.00057	0.0002	0.0001	0.00018
09A51373	McM51 stds H2	1.63282	0.00016	0.06713	0.00005	0.00236	0.00001	0.03807	0.00005	0.00011	0	0.00072	0.00014	0.00012	0.00013
09A51375	McM51 stds H2	1.74796	0.00063	0.07088	0.00004	0.00289	0.00001	0.04156	0.00006	0.00006	0	0.00063	0.00019	0.00006	0.00011
09A51376	McM51 stds H2	3.59365	0.00103	0.14705	0.00008	0.00581	0.00001	0.084	0.00011	0.00017	0	0.00065	0.00014	0.00021	0.00015
09A51378	McM51 stds H2	1.70936	0.00041	0.06951	0.00005	0.00318	0.00001	0.04058	0.00002	0.00009	0	0.00072	0.00015	0	0.00012
09A51379	McM51 stds H2	1.94506	0.00038	0.07948	0.00005	0.00292	0.00001	0.04241	0.00004	0.00009	0	0.00076	0.00018	0.00011	0.00011
09A51381	McM51 stds H2	1.72875	0.00023	0.07091	0.00004	0.0029	0.00001	0.04065	0.00005	0.00007	0	0.00073	0.00019	0.00013	0.00012
09A51382	McM51 stds H2	2.27527	0.00102	0.09265	0.00004	0.00372	0.00001	0.05251	0.00008	0.00015	0	0.00082	0.00017	0.00005	0.00013
09A51384	McM51 stds H2	2.19607	0.00019	0.08979	0.00003	0.00381	0.00001	0.05149	0.00003	0.00013	0	0.00067	0.00011	0.00007	0.00016
09A51385	McM51 stds H2	2.19828	0.00102	0.0903	0.00008	0.0034	0.00001	0.04164	0.00005	0.00021	0.00001	0.00073	0.0002	0.00012	0.0001

Table A18: G2 Standard Data

Run No	Type	40Ar	+/-	39Ar	+/-	38Ar	+/-	37Ar	+/-	36Ar	+/-	35Ar	+/-	41Ar	+/-
10A53645	G2	0.90967	0.00021	0.1951	0.00008	0.0031	0.00001	0.00007	0	0.00044	0	0.00028	0.00005	0.00086	0.00014
10A53646	G2	1.12239	0.00024	0.24022	0.00009	0.00354	0.00001	0.00009	0	0.00047	0	0.00023	0.00006	0.00089	0.00013
10A53648	G2	1.43741	0.00062	0.30989	0.00012	0.00443	0.00004	0.00009	0	0.00053	0	0.00019	0.00006	0.00095	0.00017
10A53649	G2	1.62155	0.00032	0.36025	0.00004	0.00541	0.00002	0.00007	0	0.00043	0	0.00023	0.00006	0.00104	0.00009
10A53651	G2	0.56074	0.00019	0.12027	0.00005	0.00204	0.00002	0.00007	0	0.00042	0.00001	0.00026	0.00008	0.00102	0.00014
10A53652	G2	0.84498	0.00033	0.18176	0.0001	0.00306	0.00004	0.00016	0	0.00045	0	0.00025	0.00008	0.00103	0.00022
10A53654	G2	0.10975	0.00005	0.02241	0.00003	0.00039	0	0.00006	0	0.00026	0	0.00027	0.00005	0.00101	0.00019
10A53655	G2	1.67125	0.00042	0.34323	0.00007	0.00466	0.00003	0.00008	0	0.00081	0	0.0002	0.00006	0.00104	0.00007
10A53657	G2	0.63622	0.00015	0.13782	0.00006	0.00207	0.00001	0.00007	0	0.0004	0.00001	0.00029	0.00007	0.00106	0.00021
10A53658	G2	2.24294	0.00077	0.49649	0.00014	0.00764	0.00005	0.00019	0	0.00055	0	0.00024	0.00005	0.00106	0.0001
10A53660	G2	1.91862	0.00045	0.42623	0.00013	0.00585	0.00011	0.00011	0	0.00048	0	0.00028	0.00007	0.00114	0.00011
10A53661	G2	0.4301	0.00023	0.09198	0.00003	0.00148	0.00001	0.00007	0	0.00041	0	0.00033	0.00008	0.0011	0.00017

Table A19: G3 Standard Data

Run No	Type	40Ar	+/-	39Ar	+/-	38Ar	+/-	37Ar	+/-	36Ar	+/-	35Ar	+/-	41Ar	+/-
10A53663	G3	0.3193	0.00017	0.06611	0.00002	0.00115	0.00001	0.00006	0	0.0004	0	0.0003	0.00008	0.00111	0.00016
10A53664	G3	0.37998	0.00015	0.07695	0.00002	0.00103	0.00001	0.00005	0	0.0004	0	0.00027	0.00009	0.00112	0.0001
10A53668	G3	0.32518	0.00004	0.06885	0.00002	0.00107	0.00001	0.00005	0	0.00031	0	0.0002	0.00005	0.00098	0.00017
10A53669	G3	1.42275	0.00031	0.31247	0.00004	0.00418	0.00004	0.00006	0	0.00043	0	0.00021	0.00006	0.00092	0.00012
10A53671	G3	0.99388	0.00008	0.2178	0.00011	0.00281	0.00002	0.00005	0	0.00037	0	0.00025	0.00005	0.001	0.00014
10A53672	G3	1.83108	0.00029	0.39139	0.00016	0.00521	0.00003	0.00006	0	0.00065	0	0.00027	0.00007	0.00103	0.00013
10A53674	G3	0.5858	0.00016	0.1313	0.00008	0.00195	0.00001	0.00007	0	0.00032	0	0.00027	0.00006	0.00099	0.00012
10A53675	G3	1.57275	0.00056	0.34544	0.00014	0.00512	0.00003	0.0001	0	0.00054	0.00001	0.00022	0.00006	0.00108	0.00015
10A53677	G3	0.50864	0.00011	0.10716	0.00003	0.00182	0.00001	0.00008	0	0.00043	0	0.00027	0.00003	0.00102	0.00017
10A53678	G3	0.45497	0.00015	0.09901	0.00005	0.00175	0.00001	0.00007	0	0.0004	0	0.0003	0.00005	0.00108	0.00015
10A53680	G3	0.56088	0.00011	0.1216	0.00002	0.00202	0.00001	0.00009	0	0.00042	0	0.00028	0.0001	0.00103	0.00018
10A53681	G3	0.55235	0.00013	0.11962	0.00004	0.00162	0.00002	0.00008	0	0.00035	0	0.00025	0.00005	0.00102	0.00015

Table A20: G4 Standard Data

Run No	Type	40Ar	+/-	39Ar	+/-	38Ar	+/-	37Ar	+/-	36Ar	+/-	35Ar	+/-	41Ar	+/-
10A53683	G4	2.81745	0.00197	0.63325	0.00031	0.00867	0.00007	0.00031	0	0.00055	0.00001	0.00021	0.00006	0.00115	0.00013
10A53684	G4	1.45657	0.00106	0.32014	0.00012	0.00427	0.00001	0.00008	0	0.00054	0	0.00024	0.00008	0.0011	0.00017
10A53686	G4	1.19611	0.00023	0.25329	0.00009	0.00393	0.00001	0.00022	0	0.00063	0	0.00028	0.00009	0.00114	0.00013
10A53687	G4	1.33194	0.00035	0.29961	0.00011	0.00472	0.00001	0.00022	0	0.00045	0	0.00028	0.00007	0.00117	0.00014
10A53691	G4	1.5722	0.00086	0.3442	0.00041	0.00402	0.00002	0.00009	0	0.00046	0	0.0002	0.00005	0.00092	0.00012
10A53692	G4	4.8162	0.00071	1.06546	0.00021	0.01453	0.00006	0.00069	0	0.001	0	0.00016	0.00008	0.00108	0.00013
10A53694	G4	2.31092	0.00057	0.49958	0.00027	0.007	0.00014	0.00013	0	0.00079	0	0.00025	0.00008	0.00111	0.00015
10A53695	G4	0.68139	0.00011	0.15263	0.00012	0.0022	0.00002	0.00008	0	0.00031	0	0.00024	0.00006	0.00098	0.00018
10A53697	G4	1.06122	0.00019	0.23705	0.00009	0.0038	0.00002	0.00019	0	0.00038	0	0.00029	0.00006	0.00106	0.00018
10A53698	G4	2.49709	0.00045	0.55501	0.00022	0.00763	0.00003	0.00018	0	0.00055	0	0.00025	0.00006	0.00108	0.00007
10A53700	G4	3.84355	0.00096	0.87152	0.0008	0.0127	0.00019	0.00131	0	0.00056	0	0.00024	0.00005	0.00107	0.00012
10A53701	G4	1.5442	0.00066	0.33573	0.00011	0.00493	0.00003	0.00008	0	0.00057	0	0.00029	0.00006	0.00112	0.00015

Table A21: Muligiripalle (Mul5) Ar-Ar geochronology Data

Type	Comment	40Ar	+/-	39Ar	+/-	38Ar	+/-	37Ar	+/-	36Ar	+/-	35Ar	+/-	41Ar	+/-
MUL	1a	0.34466	0.00006	0.01335	0.00002	0.00024	0	0.00039	0	0.00003	0	0.00025	0.0002	0.00014	0.00019
MUL	2a	1.27556	0.0001	0.04964	0.00003	0.00065	0.00001	0.00152	0.00001	0.00005	0	0.00015	0.00017	0.00006	0.00014
MUL	3a	0.77479	0.00015	0.03017	0.00002	0.00035	0	0.00048	0	0.00001	0	0.0002	0.00017	-0.00006	0.00015
MUL	4a	1.84973	0.00016	0.07222	0.00002	0.00089	0	0.00092	0	0.00003	0	0.00015	0.0001	-0.00003	0.00008
MUL	5a	0.11606	0.00002	0.00449	0	0.00005	0	0.00016	0	0	0	0.00013	0.00014	0	0.00012
MUL	6a	1.68486	0.00026	0.06557	0.00001	0.00087	0.00001	0.0034	0.00001	0.00005	0	0.00016	0.00012	0.00005	0.00013
MUL	1	0.20721	0.00005	0.00808	0.00001	0.00009	0	0.00008	0	0.00001	0	0.00011	0.00008	0	0.00008
MUL	2	0.43468	0.00006	0.01713	0.00002	0.0002	0	0.00047	0	0.00002	0	0.00018	0.00009	0.00007	0.00008
MUL	3	0.1593	0.00005	0.00622	0.00001	0.00009	0	0.00027	0	0.00002	0	0.00013	0.00006	0.00003	0.00008
MUL	4	0.61588	0.00009	0.02401	0.00002	0.00033	0	0.00043	0	0.00004	0	0.00018	0.00009	0.00002	0.00005
MUL	5	0.78103	0.00012	0.03133	0.00002	0.00041	0	0.00093	0	0.00003	0	0.00023	0.00009	0.00006	0.00006
MUL	6	0.36625	0.00005	0.01431	0.00002	0.00018	0	0.00013	0	0.00001	0	0.00017	0.0001	0.00001	0.00003
MUL	7	1.55318	0.00019	0.06103	0.00005	0.00076	0	0.00144	0.00001	0.00003	0	0.00021	0.00012	0.00001	0.00008
MUL	8	1.62636	0.00021	0.063	0.00003	0.0008	0	0.00087	0	0.00003	0	0.0002	0.00013	0.00006	0.00009
MUL	9	0.76121	0.00004	0.02963	0.00002	0.00037	0	0.00105	0.00001	0.00002	0	0.00013	0.00012	0.00002	0.0001
MUL	10	0.64905	0.00017	0.0254	0.00001	0.00033	0	0.00056	0	0.00003	0	0.00025	0.00011	-0.00001	0.0001
MUL	11	0.68234	0.00017	0.02672	0.00002	0.00033	0	0.00072	0	0.00003	0	0.00024	0.0001	0.00004	0.00009
MUL	12	0.67314	0.00013	0.02617	0.00001	0.00032	0	0.00069	0	0.00003	0	0.00014	0.00009	0.00002	0.00013
MUL	13	0.00107	0.00001	0.00002	0	0.00002	0	0.0001	0	0.00003	0	0.00015	0.00012	0	0.00011
MUL	1	0.13848	0.00036	0.00402	0.00002	0.00008	0	0.00009	0	0.00032	0	0.00031	0.00008	0.00163	0.00019
MUL	2	0.03055	0.00006	0.00067	0.00001	0.00005	0	0.00021	0	0.00031	0	0.00033	0.00007	0.00163	0.00013
MUL	3	0.12417	0.00013	0.00406	0.00002	0.00008	0	0.00008	0	0.00033	0	0.00026	0.00008	0.00152	0.00018
MUL	4	0.09343	0.00009	0.00373	0.00001	0.00007	0	0.00007	0	0.00026	0	0.00022	0.00005	0.00173	0.00014
MUL	5	0.0094	0.00001	0.00004	0	0.00003	0	0.00005	0	0.00028	0	0.00026	0.00005	0.00163	0.00016
MUL	6	0.02763	0.00003	0.00035	0	0.00004	0	0.00031	0	0.00027	0	0.00027	0.00006	0.00157	0.00014
MUL	7	0.02229	0.00003	0.00012	0	0.00003	0	0.00032	0	0.00029	0	0.00026	0.00006	0.00154	0.00018
MUL	8	0.01526	0.00002	0.0002	0	0.00003	0	0.00026	0	0.00028	0	0.00028	0.00007	0.00142	0.00015
MUL	1	0.01575	0.00003	0.00022	0	0.00005	0	0.0001	0	0.00026	0	0.00032	0.00007	0.00088	0.0001

Table A22: Tummatapalle (Tumm) Ar-Ar geochronology Data

Type	Comment	40Ar	+/-	39Ar	+/-	38Ar	+/-	37Ar	+/-	36Ar	+/-	35Ar	+/-	41Ar	+/-
Tumm	1	0.1634	0.00004	0.00618	0.00001	0.00007	0	0.00024	0	0.00002	0	0.0002	0.00024	-0.00004	0.00012
Tumm	2	0.17985	0.00006	0.00694	0.00001	0.00011	0.00001	0.00056	0	0.00003	0	0.00016	0.00015	0.00011	0.00018
Tumm	3	0.255	0.00044	0.00988	0.00003	0.00014	0.00001	0.00045	0.00001	0.00004	0	0.00027	0.00019	0.00007	0.00016
Tumm	4	0.26313	0.00016	0.01003	0.00001	0.00014	0	0.00044	0	0.00005	0	0.0002	0.00015	0.00008	0.00016
Tumm	5	0.2881	0.00028	0.01103	0.00002	0.00012	0	0.00039	0	0.00005	0	0.00021	0.00014	0.00009	0.00016
Tumm	6	0.3162	0.00016	0.01201	0.00001	0.00018	0	0.00049	0	0.00007	0	0.00028	0.00017	0.00016	0.00015
Tumm	7	0.2716	0.00003	0.01041	0.00001	0.00019	0.00001	0.00022	0.00001	0.00005	0.00001	0.00023	0.00016	0.0001	0.00018
Tumm	8	0.31044	0.00011	0.01207	0.00001	0.00017	0	0.0003	0	0.00004	0	0.00009	0.00018	0.00013	0.00017
Tumm	9	0.35834	0.00027	0.01375	0.00001	0.0002	0	0.00024	0	0.00004	0	0.00009	0.00016	-0.00007	0.00011
Tumm	10	0.1641	0.00004	0.00628	0.00001	0.00006	0	0.00012	0.00001	0.00004	0	0.00019	0.0002	0.00008	0.00008
Tumm	11	0.04904	0.00003	0.00178	0.00001	0.00003	0	0.00018	0	0.00004	0	0.00028	0.0001	0	0.00016
Tumm	12	0.04653	0.00001	0.00171	0	0.00005	0	0.00012	0	0.00005	0	0.00025	0.00013	-0.00002	0.00012
Tumm	13	0.00246	0.00001	0.00002	0	0.00003	0	0.00021	0	0.00007	0	0.00023	0.00016	0.00003	0.0001
Tumm	14	0.1116	0.00005	0.00407	0.00001	0.00006	0	0.00064	0	0.0001	0	0.00028	0.00012	0.00006	0.00009
Tumm	1	0.00797	0.00002	0.00004	0	0.00004	0	0.00006	0	0.00034	0	0.0003	0.00007	0.00157	0.00014
Tumm	2	0.0078	0.00002	0.00004	0	0.00003	0	0.00007	0	0.00034	0	0.00029	0.00006	0.00158	0.00019
Tumm	1	0.00792	0.00001	0.00007	0	0.00004	0	0.00032	0	0.00027	0	0.00033	0.00009	0.00096	0.00018

Table A23: Pochampalle (POC) Ar-Ar geochronology Data

Type	Comment	40Ar	+/-	39Ar	+/-	38Ar	+/-	37Ar	+/-	36Ar	+/-	35Ar	+/-	41Ar	+/-
POC	1a	0.07306	0.00003	0.00167	0.00001	0.00004	0	0.00005	0	0.00003	0	0.00013	0.00018	0.00002	0.00021
POC	2a	0.05753	0.00002	0.00138	0	0.00002	0	0.00007	0	0	0	0.00021	0.00017	-0.00006	0.00016
POC	3a	0.07513	0.00005	0.00178	0	0.00003	0	0.0001	0.00001	0.00001	0	0.00022	0.00016	0.00002	0.0002
POC	4a	0.07251	0.00004	0.00165	0	0.00002	0	0.00008	0	0.00001	0	0.00018	0.00018	-0.00011	0.00012
POC	L5a	0.07832	0.00002	0.00191	0.00001	0.00004	0	0.0001	0	0.00002	0	0.0002	0.00017	-0.00002	0.0001
POC	L6a	0.08238	0.00002	0.00185	0.00001	0	0	0.00007	0.00001	0.00001	0	0.00008	0.00016	-0.00011	0.00013
POC	x1	0.04794	0.00003	0.00109	0	0.00005	0	0.00011	0	0.00006	0	0.0002	0.00022	0.00007	0.00018
POC	x2	0.04101	0.00002	0.001	0.00001	0.00001	0	0.00011	0	0.00003	0	0.0002	0.00014	-0.00006	0.00015
POC	x3	0.03291	0.00002	0.00074	0.00001	0.00002	0	0.00017	0.00001	0.00005	0	0.00022	0.00019	-0.00003	0.00016
POC	1x	0.26453	0.00003	0.00631	0.00001	0.0001	0	0.00011	0	0.00004	0	0.00015	0.00013	0.00009	0.00011
POC	2x	0.62794	0.00008	0.01471	0.00001	0.00021	0	0.00009	0	0.00002	0	0.0002	0.00013	0.00004	0.00014
POC	3x	0.48523	0.00005	0.01134	0.00001	0.00018	0.00001	0.00009	0	0.00001	0	0.00021	0.00015	-0.00006	0.00017
POC	4x	0.80441	0.00013	0.01879	0.00002	0.00029	0.00001	0.00012	0.00001	0.00004	0.00001	0.00018	0.00023	-0.00001	0.00017
POC	5x	0.75712	0.00032	0.01743	0.00002	0.00024	0	0.0001	0	0.00003	0	0.00021	0.00017	0	0.00015
POC	6x	2.16764	0.00007	0.06054	0.00002	0.00085	0	0.00177	0.00001	0.0001	0	0.0002	0.00017	0.00009	0.00017
POC	1	0.03373	0.00002	0.00083	0	0.00003	0	0.00012	0	0.00005	0	0.00021	0.00021	0.00016	0.00021
POC	2	0.02131	0.00001	0.00044	0	0	0	0.00003	0	0	0	0.0002	0.00022	0.00005	0.00015
POC	3	0.13236	0.00006	0.00309	0	0.00006	0	0.0001	0	0.00003	0	0.00017	0.00016	-0.00001	0.00016
POC	4	0.13529	0.00003	0.00316	0	0.00005	0	0.00009	0	0.00001	0	0.00002	0.00015	-0.00006	0.00015
POC	5	0.09025	0.00004	0.00204	0	0.00003	0	0.0001	0	0.00004	0	0.00025	0.00017	0.00012	0.00018
POC	6	0.10327	0.00006	0.00241	0.00001	0.00002	0	0.00006	0	0.00001	0	0.00009	0.00013	-0.00004	0.00016
POC	7	0.08827	0.00004	0.00207	0	0.00002	0	0.00009	0	0.00001	0	0.00013	0.00018	0.00006	0.00018
POC	8	0.10538	0.00003	0.00244	0.00001	0.00003	0	0.00008	0	0.00002	0	0.00018	0.00014	0	0.00017
POC	9	0.11393	0.00005	0.00266	0.00001	0.00005	0	0.00008	0	0.00001	0	0.00012	0.0002	0.00004	0.00012
POC	10	0.12066	0.00003	0.00283	0.00001	0.00004	0.00001	0.00007	0.00001	0.00002	0.00001	0.00024	0.00015	-0.00002	0.00012
POC	L11	0.09441	0.00002	0.00235	0	0.00004	0	0.00007	0	0.00003	0	0.0002	0.00019	0.00004	0.00017
POC	L12	0.10129	0.00003	0.00244	0	0.00004	0.00001	0.00015	0.00001	0.00002	0	0.00026	0.00019	0.00002	0.0002
POC	L13	0.15338	0.00013	0.00362	0.00001	0.00004	0	0.00007	0	0.00001	0	0.00023	0.00015	-0.00002	0.00017

Type	Comment	40Ar	+/-	39Ar	+/-	38Ar	+/-	37Ar	+/-	36Ar	+/-	35Ar	+/-	41Ar	+/-
POC	L14	0.07313	0.00011	0.00177	0.00001	0.00004	0	0.00009	0	0.00001	0	0.00016	0.00012	0.00002	0.00016
POC	L15	0.11797	0.00003	0.00278	0.00001	0.00006	0	0.00011	0	0.00003	0	0.00025	0.00016	0	0.00013
POC	L16	0.10681	0.00005	0.00251	0.00001	0.00005	0	0.00012	0	0.00003	0	0.00021	0.00014	0.00011	0.0001
POC	1	0.00699	0.00002	0.00012	0	0.00006	0	0.00024	0	0.00037	0.00001	0.00035	0.00008	0.00145	0.00015
POC	2	0.01946	0.00005	0.00026	0	0.00004	0	0.00009	0	0.00026	0	0.00025	0.00006	0.00151	0.00023
POC	3	0.24428	0.00003	0.00257	0.00001	0.00005	0	0.00007	0	0.00028	0	0.00028	0.00006	0.00152	0.00017
POC	4	0.21762	0.00005	0.0018	0	0.00005	0	0.00004	0	0.00025	0	0.00026	0.00004	0.00158	0.0002
POC	5	0.33518	0.00011	0.00232	0.00001	0.00003	0	0.00006	0	0.00023	0	0.00025	0.00007	0.00162	0.00017
POC	6	0.26246	0.00007	0.00202	0.00001	0.00005	0	0.00005	0	0.00027	0	0.0003	0.00007	0.0017	0.00017

Table A24: Pochampalle (POCg) Ar-Ar geochronology Data

Type	Comment	40Ar	+/-	39Ar	+/-	38Ar	+/-	37Ar	+/-	36Ar	+/-	35Ar	+/-	41Ar	+/-
POCg	1a	0.00056	0	0	0	0	0	0.00005	0	0.00001	0	0.00021	0.00014	0.00005	0.00019
POCg	2a	0.00054	0	0	0.00001	-0.00001	0	0.00003	0	0	0	0.00026	0.0001	-0.00001	0.00021
POCg	3a	0.00053	0	-0.00004	0.00001	-0.00004	0	0.00004	0	-0.00002	0	0.00014	0.00015	0.00001	0.0002
POCg	4a	0.11725	0.00005	0.00281	0	0.00008	0	0.00013	0	0.00004	0	0.00015	0.00015	0.00009	0.00014
POCg	5a	0.18155	0.00006	0.00428	0.00001	0.00006	0	0.00013	0	0.00003	0	0.00012	0.00013	-0.00012	0.00017
POCg	6a	0.20528	0.00006	0.00478	0.00001	0.00008	0	0.00008	0	0.00006	0	0.00021	0.00017	0	0.00016
POCg	7a	0.19693	0.00005	0.00458	0.00001	0.00008	0	0.00012	0	0.00004	0	0.00022	0.00019	0.00002	0.00013
POCg	8a	0.2191	0.00003	0.00513	0.00001	0.00007	0.00001	0.00014	0.00001	0.00002	0.00001	0.00016	0.00013	0.00002	0.00015
POCg	9a	0.18226	0.00006	0.00422	0.00001	0.00007	0	0.00008	0.00001	0.00001	0	0.00011	0.00014	-0.00003	0.00015
POCg	10a	0.20529	0.00006	0.0048	0.00001	0.00008	0	0.00011	0	0.00002	0	0.00021	0.00015	0.0001	0.00011
POCg	11a	0.13291	0.00005	0.00321	0.00001	0.00005	0	0.0001	0	0.00001	0	0.00016	0.00006	0.00003	0.00017
POCg	L12a	0.05426	0.00002	0.00128	0	0.00003	0	0.00006	0	0.00001	0	0.00017	0.00011	0.00003	0.00009
POCg	L13a	0.05639	0.00003	0.00135	0	0.00004	0.00001	0.00009	0	0.00002	0	0.0001	0.00011	-0.00001	0.00012
POCg	L14a	0.0908	0.00004	0.00215	0	0.00006	0	0.00009	0	0.00003	0	0.00022	0.00013	-0.00003	0.00012
POCg	L15a	0.07966	0.00003	0.00183	0	-0.00002	0	0.00008	0	-0.00001	0	0.00017	0.00012	-0.00001	0.00012
POCg	1a	0.00056	0	0	0	0	0	0.00005	0	0.00001	0	0.00021	0.00014	0.00005	0.00019
POCg	2a	0.00054	0	0	0.00001	-0.00001	0	0.00003	0	0	0	0.00026	0.0001	-0.00001	0.00021
POCg	3a	0.00053	0	-0.00004	0.00001	-0.00004	0	0.00004	0	-0.00002	0	0.00014	0.00015	0.00001	0.0002
POCg	4a	0.11725	0.00005	0.00281	0	0.00008	0	0.00013	0	0.00004	0	0.00015	0.00015	0.00009	0.00014
POCg	5a	0.18155	0.00006	0.00428	0.00001	0.00006	0	0.00013	0	0.00003	0	0.00012	0.00013	-0.00012	0.00017
POCg	6a	0.20528	0.00006	0.00478	0.00001	0.00008	0	0.00008	0	0.00006	0	0.00021	0.00017	0	0.00016
POCg	7a	0.19693	0.00005	0.00458	0.00001	0.00008	0	0.00012	0	0.00004	0	0.00022	0.00019	0.00002	0.00013
POCg	8a	0.2191	0.00003	0.00513	0.00001	0.00007	0.00001	0.00014	0.00001	0.00002	0.00001	0.00016	0.00013	0.00002	0.00015
POCg	9a	0.18226	0.00006	0.00422	0.00001	0.00007	0	0.00008	0.00001	0.00001	0	0.00011	0.00014	-0.00003	0.00015
POCg	10a	0.20529	0.00006	0.0048	0.00001	0.00008	0	0.00011	0	0.00002	0	0.00021	0.00015	0.0001	0.00011
POCg	11a	0.13291	0.00005	0.00321	0.00001	0.00005	0	0.0001	0	0.00001	0	0.00016	0.00006	0.00003	0.00017
POCg	L12a	0.05426	0.00002	0.00128	0	0.00003	0	0.00006	0	0.00001	0	0.00017	0.00011	0.00003	0.00009
POCg	L13a	0.05639	0.00003	0.00135	0	0.00004	0.00001	0.00009	0	0.00002	0	0.0001	0.00011	-0.00001	0.00012

Type	Comment	40Ar	+/-	39Ar	+/-	38Ar	+/-	37Ar	+/-	36Ar	+/-	35Ar	+/-	41Ar	+/-
POCg	L14a	0.0908	0.00004	0.00215	0	0.00006	0	0.00009	0	0.00003	0	0.00022	0.00013	-0.00003	0.00012
POCg	L15a	0.07966	0.00003	0.00183	0	-0.00002	0	0.00008	0	-0.00001	0	0.00017	0.00012	-0.00001	0.00012
POCg	1b	0.04921	0.00005	0.00111	0	-0.00001	0	0.00008	0	0.00002	0	0.0002	0.00018	-0.00003	0.00014
POCg	2b	0.07462	0.00003	0.00178	0.00001	0.00004	0	0.00007	0	0.00002	0	0.00021	0.00016	0.00001	0.00012
POCg	3b	0.06613	0.00003	0.00155	0.00001	0.00004	0	0.00009	0.00001	0.00002	0	0.00017	0.00014	0.00011	0.00019
POCg	4b	0.05517	0.00001	0.00132	0.00001	0.00001	0.00001	0.00008	0.00001	0	0.00001	0.00006	0.00013	0.00001	0.00017
POCg	5b	0.07601	0.00002	0.00175	0	0.00004	0	0.0001	0	0.00005	0	0.00019	0.00016	0.00003	0.00013
POCg	6b	0.07314	0.00002	0.00171	0	0.00002	0	0.00006	0	0.00001	0	0.00016	0.00017	-0.00005	0.00013
POCg	7b	0.09601	0.00027	0.00224	0.00002	0.00003	0	0.00006	0	0.00002	0	0.00019	0.00019	0.00003	0.00019
POCg	L8b	0.02514	0.00002	0.00061	0	0.00001	0.00001	0.00006	0	0.00003	0	0.00017	0.00019	0	0.00013
POCg	L9b	0.03082	0.00002	0.00071	0	0.00002	0	0.00007	0	0.00003	0	0.00027	0.00019	0.00009	0.00015
POCg	L10b	0.05732	0.00005	0.00132	0	0.00001	0	0.00007	0	0.00003	0	0.0002	0.00014	-0.00009	0.00012
POC g	1	0.07551	0.00004	0.00173	0.00001	-0.00002	0	0.00017	0	0.00004	0	0.00014	0.00014	0.00005	0.00017
POC g	2	0.22893	0.00002	0.00543	0.00001	0.00011	0	0.00027	0	0.00006	0	0.00024	0.00021	0.00004	0.00019
POC g	3	0.29888	0.00009	0.00701	0	0.00012	0	0.00015	0	0.00005	0	0.00017	0.00016	0	0.00017
POC g	4	0.27955	0.00005	0.0066	0.00001	0.00009	0	0.00023	0	0.00003	0	0.00014	0.00016	0	0.0001
POC g	5	0.22997	0.00003	0.00546	0.00001	0.00006	0	0.00009	0	0.00002	0	0.00024	0.00015	0.00008	0.00017
POC g	6	0.26667	0.00004	0.00626	0.00001	0.00008	0	0.00029	0	0.00003	0	0.00023	0.00008	0.00002	0.00013
POC g	7	0.26925	0.00011	0.00622	0.00001	0.00007	0	0.00024	0	0.00002	0	0.00017	0.00013	0	0.00013
POC g	8	0.27804	0.00004	0.00655	0.00001	0.0001	0	0.00024	0	0.00003	0	0.00016	0.00011	0.00008	0.00009
POC g	9	0.28098	0.00004	0.00664	0.00001	0.00011	0.00001	0.0002	0.00001	0.00004	0	0.00019	0.00013	0.00009	0.00013
POC g	10	0.15577	0.00003	0.00364	0.00001	0.00003	0	0.00005	0	0.00003	0	0.00018	0.00016	-0.00002	0.00015
POC g	11	0.24	0.00005	0.00568	0.00001	0.00007	0	0.00013	0	0.00004	0	0.00013	0.00008	0.00005	0.00013
POC g	12	0.09875	0.00003	0.00235	0	0.00004	0	0.00009	0	0.00005	0	0.00023	0.00013	0.00008	0.00014
POC g	13	0.10872	0.00003	0.00254	0.00001	0.00001	0	0.00004	0	-0.00001	0	0.00019	0.00011	-0.00005	0.00016
POC g	14	0.01827	0.00002	0.00063	0	-0.00004	0	0.00012	0.00001	-0.00001	0	0.00013	0.00012	-0.00002	0.00016
POC g	15	0.09593	0.00006	0.00231	0.00001	0.00005	0	0.00011	0	0.00002	0	0.00029	0.00014	0	0.00016
POC g	16	0.10645	0.00006	0.0025	0.00001	0.00004	0	0.00008	0	0.00001	0	0.00015	0.00013	0.00004	0.00022
POC g	1	0.07551	0.00004	0.00173	0.00001	-0.00002	0	0.00017	0	0.00004	0	0.00014	0.00014	0.00005	0.00017

Type	Comment	40Ar	+/-	39Ar	+/-	38Ar	+/-	37Ar	+/-	36Ar	+/-	35Ar	+/-	41Ar	+/-
POC g	2	0.22893	0.00002	0.00543	0.00001	0.00011	0	0.00027	0	0.00006	0	0.00024	0.00021	0.00004	0.00019
POC g	3	0.29888	0.00009	0.00701	0	0.00012	0	0.00015	0	0.00005	0	0.00017	0.00016	0	0.00017
POC g	4	0.27955	0.00005	0.0066	0.00001	0.00009	0	0.00023	0	0.00003	0	0.00014	0.00016	0	0.0001
POC g	5	0.22997	0.00003	0.00546	0.00001	0.00006	0	0.00009	0	0.00002	0	0.00024	0.00015	0.00008	0.00017
POC g	6	0.26667	0.00004	0.00626	0.00001	0.00008	0	0.00029	0	0.00003	0	0.00023	0.00008	0.00002	0.00013
POC g	7	0.26925	0.00011	0.00622	0.00001	0.00007	0	0.00024	0	0.00002	0	0.00017	0.00013	0	0.00013
POC g	8	0.27804	0.00004	0.00655	0.00001	0.0001	0	0.00024	0	0.00003	0	0.00016	0.00011	0.00008	0.00009
POC g	9	0.28098	0.00004	0.00664	0.00001	0.00011	0.00001	0.0002	0.00001	0.00004	0	0.00019	0.00013	0.00009	0.00013
POC g	10	0.15577	0.00003	0.00364	0.00001	0.00003	0	0.00005	0	0.00003	0	0.00018	0.00016	-0.00002	0.00015
POC g	11	0.24	0.00005	0.00568	0.00001	0.00007	0	0.00013	0	0.00004	0	0.00013	0.00008	0.00005	0.00013
POC g	12	0.09875	0.00003	0.00235	0	0.00004	0	0.00009	0	0.00005	0	0.00023	0.00013	0.00008	0.00014
POC g	13	0.10872	0.00003	0.00254	0.00001	0.00001	0	0.00004	0	-0.00001	0	0.00019	0.00011	-0.00005	0.00016
POC g	14	0.01827	0.00002	0.00063	0	-0.00004	0	0.00012	0.00001	-0.00001	0	0.00013	0.00012	-0.00002	0.00016
POC g	15	0.09593	0.00006	0.00231	0.00001	0.00005	0	0.00011	0	0.00002	0	0.00029	0.00014	0	0.00016
POC g	16	0.10645	0.00006	0.0025	0.00001	0.00004	0	0.00008	0	0.00001	0	0.00015	0.00013	0.00004	0.00022

A.2.5. Bulk-rock Nd Isotopic Data

Table A25: Bulk-rock Nd Isotopic Data

	Age (Ma)	Sm (ppm)	Nd (ppm	$^{147}Sm/^{144}Nd$	Error +/-	$^{143}Nd/^{144}Nd(m)$	Error +/-	ε(Nd)t
WKF								
CHIN 12	1100	18.7	129	0.0873	0.00006	**0.511944**	0.000004	**1.9**
MUL 5	1100	13.7	88.3	0.0934	0.00020	**0.512072**	0.000141	**3.5**
KL3	1100	12.9	83.7	0.0928	0.00007	**0.511979**	0.000003	**1.8**
Waj 2	1100	12.9	84.8	0.0916	0.00007	**0.511970**	0.000002	**1.8**
Lat 3	1100	8.11	58.7	0.0832	0.00006	**0.511839**	0.000003	**0.4**
Tumm	1100	14.5	92.7	0.0942	0.00019	**0.512046**	0.000101	**2.9**
CC1	1100	10.2	68.2	0.0900	0.00047	**0.511909**	0.000228	**0.8**
NKF								
NK2	1100	11.7	73.9	0.0953	0.00006	**0.512015**	0.000003	**2.1**
MK1	1100	8.83	53.4	0.0995	0.00009	**0.512016**	0.000003	**1.6**
KK6	1100	8.32	48.2	0.1039	0.00029	**0.512144**	0.000147	**3.4**
RKF								
SK3	1100	19.3	124	0.0937	0.00005	**0.512001**	0.000002	**2.1**
KLF								
POCg	1550	34.3	280	0.0737	0.00003	**0.511059**	0.000003	**-6.4**
JAY	1225	21.3	142	0.0903	0.00006	**0.511459**	0.000002	**-6.3**
Rampu	1225	17.6	119	0.0890	0.00005	**0.511358**	0.000003	**-8.1**
VEDN	1225	17.2	119	0.0870	0.00005	**0.511364**	0.000003	**-7.7**
Rampet	1225	14.2	101	0.0846	0.00007	**0.511348**	0.000002	**-7.6**
T1	1225	16.4	110	0.0898	0.00006	**0.511413**	0.000003	**-7.1**
RED	1225	20.5	144	0.0857	0.00006	**0.511379**	0.000004	**-7.2**
NAL	1225	17.4	116	0.0903	0.00021	**0.511391**	0.000132	**-7.7**
CBL								
Chelima	1350	39.8	319	0.0751	0.00018	**0.511129**	0.000130	**-8.4**

La Jolla	1	2	3	4	5	6
$^{143}Nd/^{144}Nd$	0.511848	0.511852	0.511849	0.511850	0.511850	0.511846

A.2.6. Bulk-rock ICP-MS and ICP-AES Data

Table A26: Bulk-Rock ICP-MS and ICP-AES Major-Element Data

	T1	LAT 3	POCG	KL2	SK2	RED	WAJ2N	WAJ1	MUL5	RAMMAN	CC1	CC2	CC4	CC5	KK6
Majors %	L16212	L16213	L16214	L16215	L16216	L16217	L16218	L16219	L16220	L16221	L16222	L16223	L16224	L16225	L16226
Al_2O_3	5.48	3.29	9.60	2.74	1.80	6.59	4.58	5.15	3.92	7.30	3.55	3.63	2.71	2.18	4.45
CaO	9.71	9.67	8.34	33.3	46.5	9.71	13.0	20.4	10.6	11.5	9.52	8.50	11.3	13.3	12.1
Fe_2O_3 (t)	7.75	8.89	8.88	7.11	4.01	11.03	14.3	8.01	13.8	10.8	12.4	11.2	10.7	10.5	13.2
K_2O	1.03	1.72	5.38	0.026	0.010	4.63	0.036	0.040	2.35	2.36	0.671	1.52	0.073	0.566	0.457
MgO	5.92	34.7	8.18	7.86	5.93	8.32	26.0	20.3	27.7	12.0	35.9	31.2	34.8	30.3	29.8
MnO	0.089	0.144	0.129	0.131	0.034	0.133	0.247	0.199	0.204	0.124	0.183	0.163	0.187	0.193	0.195
Na_2O	0.036	0.093	1.03	0.386	0.029	0.957	0.015	0.136	0.341	0.318	0.287	0.278	0.027	0.026	0.110
P_2O_5	1.29	0.551	2.22	0.344	0.081	1.64	0.438	0.936	0.975	1.05	0.755	0.620	1.17	1.092	0.576
SiO2	58.6	35.1	49.1	18.6	9.71	48.8	33.5	43.6	36.0	47.8	40.1	40.4	31.6	28.1	39.1
TiO_2	4.72	1.52	2.93	1.33	0.186	5.18	3.42	1.42	5.22	3.49	2.56	2.39	2.23	2.47	3.12

Field numbers	VEDN	VEDS	CHEL	THUR13	MK5	JAY	POC	MK1	RAMAPU	LAT4	KL1	SK3	TK4	KL3	KK1
Majors %	L16227	L16228	L16229	L16230	L16231	L16232	L16233	L16234	L16235	L16236	L16237	L16238	L16239	L16240	L16241
Al_2O_3	7.52	5.91	2.48	3.37	3.43	6.70	7.84	4.33	6.85	3.64	3.52	2.02	1.11	3.21	3.25
CaO	11.7	12.5	20.2	10.1	12.1	11.1	10.9	13.7	9.96	7.25	36.6	10.4	25.1	11.2	8.88
Fe_2O_3 (t)	11.4	11.6	6.98	15.5	14.2	11.7	11.9	13.43	14.3	9.34	4.67	9.78	6.49	13.9	14.0
K_2O	1.87	0.408	0.773	2.10	0.121	1.48	3.09	0.579	4.03	0.667	0.846	0.001	0.082	1.21	1.08
MgO	12.4	11.1	19.1	26.8	28.1	11.4	7.97	24.9	6.27	34.9	7.55	33.3	17.4	29.3	31.8
MnO	0.103	0.215	0.202	0.211	0.214	0.140	0.118	0.188	0.096	0.142	0.264	0.140	0.090	0.202	0.206
Na_2O	0.260	0.136	0.013	0.232	0.018	0.312	0.069	0.219	0.197	0.267	0.339	0.012	0.014	0.077	0.021
P_2O_5	0.767	1.67	1.66	0.909	0.754	1.78	1.72	0.547	1.65	0.498	0.131	1.33	0.089	0.680	0.389
SiO2	46.2	46.7	25.9	30.8	34.5	48.5	48.4	36.9	49.7	38.6	20.8	32.8	29.8	30.2	35.3
TiO_2	3.66	5.17	4.78	5.32	4.78	5.25	5.52	4.62	4.96	1.34	1.32	2.16	1.01	4.81	4.28

Field numbers	NK1	NK2	WAJ2	NALLA	BALS	CHIN12	TK0	SK1	TK3	LOD	BCR-1	BCR-1
Majors %	L16242	L16243	L16244	L16245	L16246	L16247	L16248	L16249	L16250			
Al_2O_3	3.54	3.89	6.00	6.43	14.1	4.48	0.729	2.01	4.205	0.600	12.9	13.6
CaO	8.63	7.58	14.1	9.63	9.03	10.9	31.4	13.7	22.2	0.250	6.80	6.95
Fe_2O_3(t)	13.1	12.8	12.9	9.42	14.8	11.1	5.60	10.4	12.5	0.030	13.0	13.4
K_2O	1.01	1.23	2.02	1.01	1.65	0.709	<	0.137	0.052	0.001	1.79	1.69
MgO	32.3	31.1	24.6	11.1	3.83	28.9	14.0	31.4	11.4	0.030	3.47	3.48
MnO	0.202	0.185	0.220	0.076	0.258	0.174	0.193	0.148	0.132	0.005	0.177	0.180
Na_2O	0.055	0.105	1.06	0.248	0.994	0.178	0.100	0.015	0.186	0.005	3.09	3.27
P_2O_5	0.579	0.750	0.863	1.49	0.186	0.512	0.113	1.97	0.922	0.025	0.360	0.360
SiO2	35.9	38.6	37.8	48.8	43.0	37.6	45.0	28.0	33.7	0.700	53.0	54.1
TiO_2	5.41	2.80	2.45	4.84	1.71	2.17	1.07	3.27	4.35	0.040	2.15	2.24

Table A27: Bulk-Rock ICP-MS and ICP-AES Trace-Element Data

	T1	LAT 3	POCG	KL2	SK2	RED	WAJ2N	WAJ1	MUL5	RAMMAN	CC1	CC2	CC4	CC5	KK6
As	13.8	7.45	46.4	6.07	1.45	17.3	13.9	17.7	9.15	12.5	7.80	6.92	16.2	14.2	3.74
Ba	416	2389	1528	129	10080	983	796	1350	2292	1152	1559	781	2792	1426	1253
Be	2.93	1.86	8.87	1.27	0.704	8.88	3.28	4.09	3.46	4.80	2.29	2.32	3.95	3.71	1.83
Bi	7.32	5.32	41.9	1.44	2.81	6.39	1.50	1.54	1.78	4.04	3.57	3.77	2.57	1.50	0.506
Cd	1.37	0.069	0.081	0.059	0.115	0.164	0.092	0.032	0.085	0.130	0.099	0.078	0.068	0.062	0.064
Co	27.6	79.7	39.3	65.4	19.2	43.6	94.1	52.9	92.7	55.6	103.2	96.0	84.6	79.9	98.9
Cr	61.8	1504	373	1007	30.9	224	1112	600	1090	640.3	1535	1333	1583	1555	1280
Cs	0.452	2.19	2.44	0.154	0.676	1.70	0.634	1.19	7.95	0.655	2.80	3.14	0.624	1.33	6.86
Cu	5.14	77.8	77.8	39.1	15.7	25.8	97.5	56.5	127	45.6	82.1	71.5	55.4	82.9	89.1
Ga	20.8	7.06	20.2	7.75	2.94	24.1	11.4	7.80	12.8	18.9	8.27	10.1	8.57	7.48	11.3
Ge	1.48	0.672	1.89	0.620	0.462	2.14	1.10	0.774	1.10	1.39	1.01	0.964	0.775	0.681	1.09
Hf	12.5	3.21	23.76	7.46	3.26	16.1	5.37	3.47	9.03	10.8	4.62	4.81	8.19	5.84	5.35
Li	30.6	9.16	77.6	18.4	14.1	86.2	55.9	51.0	12.7	68.7	12.1	7.12	1.73	51.5	18.0
Mo	3.36	0.407	4.39	0.537	0.279	1.72	0.326	0.333	0.298	0.408	0.553	0.549	0.803	2.70	0.345
Nb	30.6	161	34.2	109	10.1	54.6	280	97.2	96.0	52.2	126	100	87.1	119	107
Ni	51.4	1077	231	688	73.8	169	491	366	784	284	1372	1190	1043	937	962
Pb	13.8	7.45	34.34	3.45	7.42	26.8	6.29	7.71	6.97	20.8	7.18	8.55	9.06	8.72	3.22
Rb	17.3	302	320	1.96	2.1	120.9	13.4	3.6	164	41.6	85.5	136	25.0	71.0	91.8
S	661	349	868	71	1882	628	466	151	247	620	514	241	704	1412	497
Sb	<	0.061	0.054	0.010	0.018	0.011	0.049	0.032	0.059	0.015	0.065	0.059	0.101	0.126	0.026
Sc	16.4	12.4	24.7	9.22	2.97	22.2	25.1	16.0	19.2	20.3	16.4	15.4	17.8	17.3	18.4
Sn	0.560	1.36	1.95	1.36	1.53	1.12	2.54	0.735	1.45	0.852	1.59	1.25	0.914	1.12	1.54
Sr	1174	991	676	514	2026	2144	325	640	1099	1009	499	934	1273	2044	944
Ta	1.16	8.76	1.53	6.43	0.483	1.71	14.1	3.36	2.54	1.89	6.00	3.84	2.10	4.84	6.71
Th	10.8	14.6	96.0	9.9	18.8	7.97	23.9	25.2	13.7	11.4	11.3	12.6	20.6	18.3	7.19
Tl	0.076	0.131	0.691	0.019	0.011	0.373	0.049	<	0.008	0.118	0.056	0.067	0.116	0.647	0.088
U	2.16	2.46	15.3	2.00	3.77	1.79	3.89	3.91	2.51	1.56	2.00	2.48	3.75	3.62	1.88
V	114	165	179	61.1	15.2	148	49.9	95.7	237	145	121	125	56.3	129	158
W	0.868	0.458	2.92	0.311	2.65	0.232	0.331	1.35	0.410	0.353	0.751	0.249	0.644	1.00	0.637
Y	34.7	14.4	51.0	10.7	25.6	38.6	28.8	23.4	30.6	30.5	17.9	17.5	27.9	24.9	18.2
Zn	312	69.3	144	55.8	24.5	179	120	79.3	120	143	100	98.6	82.0	105	106
Zr	815	150	424	382	121	1001	260	214	472	492	241	240	428	316	252

Field numbers	VEDN	VEDS	CHEL	THUR13	MK5	JAY	POC	MK1	RAMAPU	LAT4	KL1	SK3	TK4	KL3	KK1
As	13.2	12.5	70.4	10.1	10.8	13.7	25.0	5.2	14.3	4.19	6.49	12.9	13.7	7.94	10.5
Ba	916	272	778	1734	195	254	452	1704	633	881	413	664	163	1506	826
Be	4.15	4.31	4.99	3.24	2.01	6.42	8.61	1.93	7.73	1.65	1.62	2.64	1.59	2.77	1.31
Bi	4.61	4.21	6.35	1.52	1.35	5.59	5.44	1.99	11.3	3.86	3.14	5.93	10.3	3.71	4.67
Cd	0.094	0.112	0.134	0.095	0.089	0.052	0.086	0.067	0.139	0.075	0.125	0.034	0.378	0.094	0.153
Co	58.5	55.0	58.4	97.6	103	48.2	39.5	94.7	36.6	90.0	45.8	86.5	85.4	93.3	107.5
Cr	712	317	745	1172	1221	329.4	93.06	1055	270.1	1327	179	1361	1818	1066	1559
Cs	0.492	0.571	1.68	3.50	0.543	2.26	2.73	7.88	0.501	3.21	0.086	0.059	0.145	14.2	1.31
Cu	31.0	30.6	5.13	110	93.6	33.8	17.1	125	236	85.8	44.4	40.4	27.4	119	45.2
Ga	20.3	20.8	9.31	12.2	12.0	24.4	29.4	12.7	20.6	6.28	8.19	6.42	3.54	12.7	9.24
Ge	1.51	1.98	1.76	1.15	1.03	2.17	1.48	1.15	2.97	0.781	0.541	0.715	0.631	1.01	1.09
Hf	9.63	11.6	9.88	9.60	6.29	16.7	14.5	6.20	15.1	2.76	3.01	5.53	1.26	12.4	4.41
Li	46.1	42.2	51.1	17.6	6.28	77.9	66.0	62.3	37.7	11.6	74.3	30.5	78.8	152	17.2
Mo	1.82	0.250	0.259	0.750	0.255	0.213	1.84	1.15	0.467	0.229	0.502	0.313	0.075	0.197	1.95
Nb	99.6	52.0	47.0	127	159	23	76.1	112	103	109	21.9	39.1	76.8	170	171
Ni	281	276	482	787	931	271	116	688	152	1276	208	1272	1473	686	992
Pb	11.7	16.6	83.8	7.62	4.20	4.37	32.2	4.06	225	6.37	5.66	11.5	10.1	3.85	6.27
Rb	11.3	25.4	11.3	51.3	7.53	12.1	37.2	103	118	84.6	108.0	27.3	0.59	4.9	129
S	1127	1049	477	457	223	590	544	903	560	168	157	205	148	318	840
Sb	0.024	0.010	0.088	0.074	0.044	0.004	0.011	0.037	0.003	0.031	<	0.035	0.052	0.053	0.057
Sc	21.8	19.7	15.7	20.0	21.7	23.6	20.4	19.7	23.7	12.6	5.84	16.5	9.09	17.0	20.5
Sn	2.27	0.910	0.394	1.69	2.08	0.531	1.24	1.81	2.21	1.20	1.01	0.637	0.6	2.42	2.06
Sr	708	1253	494	1071	956	1177	1279	776	904	598	280	826	222	1058	381
Ta	4.19	2.40	2.26	4.96	9.87	0.642	2.33	7.18	3.77	6.01	1.32	0.507	6.41	10.4	11.8
Th	10.9	12.9	31.8	13.3	10.7	10.5	12.2	10.2	11.2	9.49	7.70	16.9	29.2	16.8	16.2
Tl	0.081	0.052	0.046	0.020	0.214	0.192	0.636	0.216	0.227	0.079	0.136	0.082	0.080	0.233	1.66
U	0.601	1.88	3.61	2.47	4.57	2.17	1.29	2.39	6.93	1.76	2.08	3.22	3.14	3.35	2.83
V	123	99.0	30.2	201	95.9	113	93.3	224	163	73.6	48.1	94.5	45.2	176	195
W	0.533	0.261	0.219	0.637	0.626	0.253	1.43	0.658	1.82	0.690	0.213	0.230	0.587	0.803	1.38
Y	40.6	35.6	38.6	27.7	19.6	43.9	47.3	18.3	51.6	12.6	30.9	29.2	15.6	20.5	27.0
Zn	161	152	373	127	92.9	150	226	112	108	80.9	51.7	79.0	51.5	121	127
Zr	460	579	519	432	300	499	952	288	917	141	150	307	45.5	559	192

Field numbers	NK1	NK2	WAJ2	NALLA	BALS	CHIN12	TK0	SK1	TK3	LOD
As	5.83	7.42	9.67	12.2	1.68	17.6	2.76	16.8	9.88	1.00
Ba	1597	1635	2764	405	244	1475	96.1	1240	850	5.00
Be	1.68	2.46	2.50	6.60	2.13	4.24	1.76	3.47	2.69	0.035
Bi	4.99	4.26	4.54	3.22	2.95	10.6	1.52	8.03	5.41	0.379
Cd	0.100	0.114	0.075	0.045	0.081	0.154	0.036	0.054	0.136	0.003
Co	99.9	102	83.9	44.5	57.2	83.7	17.2	80.3	69.8	0.002
Cr	1282	1514	948	238	63.4	1178	877	1028	796	30.0
Cs	10.9	16.5	1.18	0.244	0.601	6.76	0.105	0.490	0.685	0.001
Cu	205	188	167	76.9	235	222	4.27	159	551	3.00
Ga	10.0	10.3	12.0	22.5	20.6	10.3	1.76	8.12	11.7	0.006
Ge	1.06	1.07	0.921	2.07	1.93	0.982	1.04	0.610	0.901	0.005
Hf	5.32	5.45	4.13	17.3	2.52	7.72	3.52	3.78	7.44	0.001
Li	23.0	21.0	10.3	40.2	91.9	19.6	8.42	11.1	108	0.037
Mo	0.462	0.176	0.475	0.305	0.389	3.93	0.333	1.53	0.819	0.330
Nb	150	102	143	38.7	8.86	235	45.5	15.9	121	0.026
Ni	763	1091	486	190	37	832	154	912	681	20.0
Pb	6.01	8.33	6.34	2.27	5.50	15.6	5.25	18.8	11.3	0.019
Rb	100	115.1	133.5	38.0	21.0	118.0	11.4	96.7	0.80	0.007
S	420	317	575	536	580	580	27.7	139	156	7.00
Sb	0.009	0.014	0.009	0.012	0.005	0.137	0.039	0.007	0.056	0.006
Sc	18.8	18.7	20.0	20.1	42.9	19.6	56.5	18.6	18.9	5.00
Sn	1.77	1.49	1.39	1.03	1.41	2.15	0.866	0.181	2.29	0.020
Sr	592	371	813	953	116	1177	229	1879	1036	10.0
Ta	10.1	4.53	6.56	1.90	0.615	11.0	3.23	0.222	7.11	0.003
Th	11.5	12.9	19.2	8.83	2.34	26.5	3.29	19.7	14.2	0.008
Tl	0.194	0.179	0.058	0.124	0.351	0.159	0.099	0.502	0.114	0.003
U	2.72	2.51	3.00	1.86	0.316	4.87	0.746	3.83	2.67	0.007
V	345	313	277	298	961	274	182	635	1462	10.0
W	1.15	1.01	0.822	0.369	0.644	1.03	2.12	1.12	2.94	0.254
Y	18.0	22.3	25.8	38.2	32.0	28.6	3.9	39.8	27.0	3.00
Zn	111	114	110	87.1	141	105	36.4	85.6	108	2.00
Zr	230	260	198	965	136	378	113	339	381	35.0

BCR-1	BCR-1	GA	GA
2.40	0.65		
634	681		
		3.98	3.60
		10.5	-
		0.280	0.130
		5.40	5.00
15.0	16.0		
		6.20	6.00
15.3	19.0		
		17.0	16.0
		1.85	--
		2.12	4.00
		96.4	90
		1.07	0.500
		12.3	12.0
<	13.0		
		27.2	30.0
		183	175
457	410		
		0.14	0.2
32.8	32.6		
		2.80	2.70
322	330		
		1.92	1.30
		16.6	17.0
		0.797	0.008
		4.75	5.00
469	407		
		2.76	1.50
37.6	38.0		
113	80.0		
188	190		

Table A28: Bulk-Rock ICP-MS and ICP-AES REE Data

Field numbers	T1	LAT 3	POCG	KL2	SK2	RED	WAJ2N	WAJ1	MUL5	RAMMAN	CC1	CC2	CC4	CC5	KK6
La	134	98.9	378	71.6	16.2	182	170	176	116	142	91.2	92.2	174	153	58.4
Ce	271	169	751	129	32	349	296	302	222	270	172	178	330	284	112
Pr	30.8	17.1	82.8	13.8	4.07	39.8	30.6	30.1	24.3	29.0	18.8	19.3	35.6	30.6	12.6
Nd	110	58.7	280	48.8	16.8	144	107	102	88.3	101	68.2	70.0	128	109	48.2
Sm	16.4	8.11	34.3	6.89	3.86	20.5	16.1	14.4	13.7	14.2	10.2	10.4	18.3	15.8	8.32
Eu	4.46	2.26	6.85	1.74	2.23	5.95	4.31	4.23	3.76	4.20	2.80	2.76	4.98	4.20	2.46
Gd	13.7	6.57	25.3	5.58	3.79	15.6	13.4	11.8	11.1	11.9	8.16	8.33	14.4	12.6	7.21
Tb	1.54	0.681	2.39	0.569	0.611	1.56	1.41	1.20	1.20	1.29	0.872	0.880	1.46	1.29	0.823
Dy	6.65	2.84	9.12	2.31	3.64	6.38	5.87	4.83	5.13	5.62	3.61	3.64	5.76	5.21	3.69
Ho	1.02	0.446	1.44	0.355	0.722	1.03	0.906	0.737	0.797	0.909	0.556	0.556	0.851	0.773	0.584
Er	2.45	1.18	4.04	0.892	2.11	2.79	2.22	1.84	1.99	2.35	1.38	1.42	2.08	1.88	1.43
Tm	0.245	0.130	0.424	0.091	0.284	0.310	0.231	0.186	0.209	0.256	0.150	0.149	0.203	0.186	0.154
Yb	1.30	0.760	2.48	0.482	1.68	1.71	1.25	1.02	1.16	1.41	0.798	0.830	1.08	0.986	0.847
Lu	0.161	0.102	0.339	0.063	0.235	0.225	0.161	0.134	0.149	0.182	0.105	0.111	0.136	0.122	0.110

Field numbers	VEDN	VEDS	CHEL	THUR13	MK5	JAY	POC	MK1	RAMAPU	LAT4	KL1	SK3	TK4	KL3	KK1
La	159	151	440	119.6	102	157	229	67.9	142	70.2	76.2	148	155	109	128
Ce	311	325	841	230	193	321	425	132	289	125	98.6	295	291	209	250
Pr	34.4	38.0	90.2	25.2	21.0	37.7	45.5	14.3	32.4	12.7	12.9	33.2	30.8	22.7	27.4
Nd	119	140	319	92.7	77.3	142	162	53.4	119	44.6	47.0	124	104	83.7	103
Sm	17.2	20.5	39.8	14.5	11.7	21.3	22.0	8.83	17.6	6.52	7.39	19.3	12.4	12.9	16.5
Eu	3.90	5.55	9.49	4.0	3.12	5.50	6.02	2.54	4.56	1.80	1.83	5.09	2.56	3.53	4.50
Gd	14.0	16.2	27.2	12.0	9.47	16.7	18.1	7.5	14.7	5.59	7.02	15.5	9.32	10.5	13.5
Tb	1.58	1.68	2.50	1.29	1.00	1.80	1.90	0.839	1.57	0.587	0.780	1.62	0.829	1.10	1.46
Dy	7.03	6.94	8.85	5.5	4.13	7.84	8.00	3.74	7.02	2.54	3.61	6.47	2.94	4.47	6.11
Ho	1.16	1.06	1.27	0.85	0.622	1.24	1.26	0.586	1.23	0.414	0.635	0.950	0.446	0.666	0.915
Er	2.94	2.66	3.34	2.10	1.52	3.18	3.19	1.45	3.34	1.05	1.62	2.29	1.21	1.65	2.17
Tm	0.308	0.271	0.284	0.22	0.155	0.342	0.312	0.161	0.394	0.120	0.179	0.225	0.106	0.169	0.221
Yb	1.65	1.43	1.48	1.15	0.825	1.82	1.56	0.882	2.20	0.688	0.957	1.17	0.556	0.884	1.15
Lu	0.212	0.180	0.178	0.15	0.109	0.235	0.196	0.115	0.294	0.094	0.133	0.149	0.071	0.118	0.146

Field numbers	NK1	NK2	WAJ2	NALLA	BALS	CHIN12	TK0	SK1	TK3	LOD
La	98.6	98.5	133	142	11.9	201	40.0	196	124	0.003
Ce	187	184	234	282	27.3	357	70.2	382	238	0.004
Pr	20.2	20.0	23.8	31.5	3.34	36.6	7.35	42.5	26.4	0.003
Nd	73.6	73.9	84.8	116	14.6	129	24.5	161	97.5	0.005
Sm	11.4	11.7	12.9	17.4	3.69	18.7	3.09	24.9	15.2	0.008
Eu	3.21	3.34	3.70	4.39	1.34	4.99	1.34	6.54	3.95	0.005
Gd	9.40	9.94	10.9	14.2	4.42	15.3	2.39	19.8	12.2	0.003
Tb	0.991	1.07	1.15	1.50	0.713	1.57	0.224	2.03	1.31	0.003
Dy	4.14	4.64	4.93	6.50	4.46	6.29	0.847	8.25	5.48	0.005
Ho	0.623	0.716	0.771	1.06	0.887	0.932	0.131	1.23	0.851	0.000
Er	1.50	1.74	1.97	2.70	2.48	2.22	0.340	2.94	2.10	0.005
Tm	0.151	0.186	0.215	0.299	0.352	0.220	0.038	0.294	0.229	0.006
Yb	0.771	0.993	1.20	1.63	2.17	1.15	0.252	1.52	1.22	0.003
Lu	0.099	0.126	0.167	0.212	0.317	0.150	0.045	0.194	0.163	0.006

BCR-1	BCR-1	GA	GA
		40.0	40.0
		76.9	76.0
		8.15	8.30
		28.9	27.0
		5.18	5.00
		1.11	1.08
		4.64	3.80
		0.631	0.600
		3.48	3.30
		0.670	0.700
		1.95	1.90
		0.292	0.300
		1.85	2.00
		0.281	0.300

A.2.7. Bulk-rock XRF Data

Table A29: XRF Major-Element Data

Sample	LAT3	LAT4	MUL5	THU13	KL-2	KL1	KL3	CC2	CC1	CC5	CC4	CHIN12	TK4	TKO	TK3
Wt. %	8	10	26	21	25	14	8	16	13	4	5	23	19	20	10
SiO2	32.49	38.11	34.39	31.63	18.13	20.05	28.00	38.62	37.40	25.52	28.50	37.06	31.31	44.61	30.53
TiO2	1.528	1.360	4.640	4.805	1.377	1.342	4.212	2.422	2.469	2.473	2.269	2.264	1.143	1.074	4.113
Al2O3	3.15	3.64	3.92	3.38	2.86	3.61	3.21	3.65	3.36	2.17	2.66	4.59	1.19	0.71	4.13
Fe2O3	8.84	9.59	13.69	14.89	7.77	5.07	13.85	11.26	11.89	10.58	10.55	11.36	6.92	5.61	12.39
MnO	0.142	0.148	0.193	0.203	0.139	0.264	0.190	0.165	0.174	0.184	0.183	0.177	0.098	0.194	0.126
MgO	29.23	29.60	22.57	22.63	8.39	7.59	24.09	25.63	28.41	25.53	28.73	24.33	17.19	13.09	11.33
CaO	9.34	7.30	10.18	10.01	31.63	32.17	10.95	8.57	9.06	12.99	11.05	10.95	23.43	28.10	20.41
Na2O	0.05	0.34	0.33	0.27	0.80	0.46	0.09	0.34	0.38	0.07	0.06	0.24	0.07	0.16	0.24
K2O	1.14	0.48	2.12	2.02	0.02	0.43	1.01	1.26	0.50	0.36	0.05	0.59	0.06	0.01	0.04
P2O5	0.562	0.531	0.942	0.890	0.313	0.119	0.658	0.608	0.753	1.030	1.130	0.542	0.112	0.124	0.765
LOI	12.78	8.69	6.24	8.62	28.12	27.55	12.87	6.34	4.87	17.99	13.36	7.69	24.16	6.10	15.41
Total	99.26	99.80	99.23	99.34	99.55	98.66	99.14	98.85	99.27	98.90	98.54	99.79	105.68	99.77	99.48
Ppm															
Ba	3020	1104	2496	1971	237	676	1820	946	1706	1927	3494	1740	287	117	1068
Cr	1182	1087	880	907	753	161	788	1126	1205	1312	1282	878	1215	618	631
Ni	1009	1203	777	787	762	214	698	1069	1244	938	1028	823	1323	138	749
S%	0.05	0.02	0.03	0.06	0.00	0.00	0.03	0.02	0.08	0.17	0.16	0.07	0.00	0.00	0.00

Sample	CHE	RAME	POC	POC G	VEDN	VEDS	JAY	T1	NALLA	RED	RAMU
Wt. %	16	22	12	15	29	7	5	28	17	11	27
SiO2	23.63	50.84	49.43	49.60	45.04	45.90	46.68	57.81	50.78	50.31	48.51
TiO2	4.104	4.274	4.860	2.954	3.241	4.644	4.593	4.272	4.281	4.741	4.419
Al2O3	2.48	6.75	9.90	10.20	7.58	6.22	6.86	5.57	6.70	6.84	7.08
Fe2O3	6.96	9.81	11.71	9.12	11.57	11.84	11.66	8.00	9.74	11.26	14.33
MnO	0.187	0.079	0.115	0.132	0.104	0.202	0.137	0.087	0.078	0.133	0.096
MgO	16.67	9.97	7.17	7.48	11.45	10.29	10.24	5.33	9.90	7.72	5.61
CaO	17.39	9.79	10.62	8.37	11.60	12.62	10.78	9.61	9.73	9.70	9.86
Na2O	0.08	0.31	0.13	1.12	0.30	0.18	0.36	0.09	0.31	1.05	0.24
K2O	0.51	1.10	3.39	5.52	1.94	0.45	1.56	1.03	1.08	5.12	4.10
P2O5	1.242	1.204	1.514	2.201	0.745	1.410	1.562	1.099	1.213	1.554	1.377
LOI	25.06	4.49	3.91	3.40	5.96	5.87	5.36	6.66	5.64	2.90	3.55
Total	98.32	98.63	102.75	100.08	99.54	99.61	99.79	99.55	99.46	101.31	99.17
Ppm											
Ba	1155	471	509	1558	978	342	298	368	494	1025	631
Cr	570	209	82	347	532	289	291	49	197	181	195
Ni	564	202	101	223	380	299	282	66	206	164	152
S%	0.00	0.01	0.01	0.12	0.04	0.10	0.04	0.02	0.01	0.02	0.02

Sample	SK1	SK2	SK3	NK1	NK2	KK6	KK1	MK1	MK5
Wt. %	6	9	7	6	9	14	24	15	18
SiO2	25.81	52.08	30.28	34.16	36.52	37.52	37.59	36.20	32.06
TiO2	2.937	0.182	2.196	4.978	2.898	2.814	4.408	4.107	4.276
Al2O3	2.07	0.80	2.03	3.59	3.93	4.49	3.52	4.41	3.40
Fe2O3	10.55	1.85	10.00	13.35	12.98	13.04	14.72	13.49	14.42
MnO	0.147	0.017	0.138	0.196	0.181	0.189	0.210	0.183	0.208
MgO	25.51	2.73	27.95	27.10	25.34	23.97	29.96	20.75	23.76
CaO	13.63	19.54	10.25	8.62	7.54	12.14	9.75	13.80	12.03
Na2O	0.06	0.05	0.04	0.08	0.13	0.14	0.03	0.25	0.04
K2O	0.10	0.00	0.01	0.90	1.03	0.40	0.85	0.55	0.12
P2O5	1.694	0.041	1.202	0.621	0.760	0.603	0.549	0.531	0.744
LOI	16.56	33.73	16.36	7.24	7.62	4.65	8.96	4.86	9.12
Total	99.08	111.02	100.45	100.84	98.94	99.95	110.56	99.13	100.18
Ppm									
Ba	1501	6865	948	2003	1688	1424	1118	1724	278
Cr	846	8	1074	978	1193	951	985	801	950
Ni	888	33	1230	770	1026	898	857	697	926
S%	0.07	0.00	0.03	0.06	0.03	0.05	0.14	0.05	0.02

Table A30: XRF Loss on Ignition Data

	% Weight Loss
RED	2.8986
POC G	3.3992
RAMU	3.5482
POC	3.9141
RAME	4.4894
KK6	4.6488
MK1	4.8563
CC1	4.8742
WAJ2	5.0904
JAY	5.3557
WAJ1	5.4241
NALLA	5.6374
VED S	5.8730
VED N	5.9559
TKO	6.0964
MUL 5	6.2396
CC2	6.3396
T1	6.6595
KL-2	28.1240
SK2	33.7305

	% Weight Loss
NK1	7.2380
NK2	7.6244
CHIN 12	7.6910
THU13	8.6233
LAT 4	8.6917
KK1	8.9561
MK5	9.1212
WAJ 2N	11.4481
LAT 3	12.7791
KL3	12.8739
CC4	13.3644
TK3	15.4070
SK3	16.3626
SK1	16.5611
CC5	17.9872
TK4	24.1629
CHE	25.0562
KL1	27.5460

Table A31: XRF Trace-Element Data

X1801T	LAT3	LAT4	MUL5	Tum13	KL2	KL1	KL3	CC2	CC1	CC5	CC4	CHIN12B	WAJ1	WAJ2	WAJ2NEW
Sample pos.	14	24	18	16	9	5	9	17	15	5	16	17	7	13	23
Rb	217	99	182	180	2	26	153	161	80	67	23	92	3	173	13
Sr	944	592	1072	1064	533	285	1025	895	473	1651	1202	1170	638	823	316
Y	13.1	12.6	22.9	26.2	12.0	22.6	19.6	16.3	17.1	22.4	25.9	26.9	22.9	21.3	27.0
Zr	135	134	469	483	358	149	611	232	225	303	435	390	205	206	239
Nb	133.7	99.3	153.2	170.7	94.9	59.1	158.7	111.2	118.2	170.3	187.6	209.3	195.4	190.1	237.5
Ba	2438	968	2471	1783	155	485	1486	815	1444	1364	2738	1541	1467	2352	869
Pb	7	6	9	10	5	7	2	12	8	9	9	19	10	5	7
Th	17	10	17	15	9	10	19	16	15	21	24	33	30	21	31
U	3	2	3	3	4	2	2	3	2	4	4	7	4	3	2
Sc	16	16	20	21	23	16	22	17	16	21	16	18	16	21	27
V	135	90	275	267	54	70	133	163	143	179	79	85	106	130	38
Cr	1186	1187	831	921	796	222	821	1126	1309	1122	1287	953	554	766	764
Co	66	73	70	76	48	40	70	80	87	64	68	69	37	67	67
Ni	1089	1329	808	825	757	256	737	1397	1411	935	1113	932	444	603	560
Cu	52	76	138	136	41	53	91	82	83	108	68	70	62	79	84
Zn	55	61	76	79	42	48	64	67	76	68	58	75	66	79	78
Ga	6	5	11	11	7	9	12	10	8	6	7	9	7	9	12
Mo	0	0	0	0	0	0	0	0	0	0	0	0	0	0	0
As	1	0	2	1	5	1	0	0	1	5	5	1	5	5	0
S	215	48	147	303	94	110	172	111	273	1007	597	425	275	387	231
TiO2%	1.25	1.34	3.24	3.62	1.07	1.11	3.42	2.03	2.26	1.94	1.68	1.89	1.28	1.92	2.53
Fe2O3%	8.81	9.71	13.70	14.71	7.58	5.32	13.49	11.18	12.41	10.30	10.81	12.00	8.29	12.25	13.83

X1801T	TK4	TKO	TK3
Sample pos.	21	19	11
Rb	4	0	4
Sr	220	220	987
Y	14.9	4.8	26.1
Zr	45	112	386
Nb	109.1	43.8	141.9
Ba	174	84	688
Pb	11	8	13
Th	28	4	14
U	4	0	5
Sc	17	53	24
V	52	42	242
Cr	1341	674	655
Co	61	10	62
Ni	1446	153	929
Cu	29	8	124
Zn	36	31	77
Ga	4	2	14
Mo	0	0	0
As	4	2	1
S	72	38	107
TiO2%	0.91	0.64	2.73
Fe2O3%	6.48	4.86	13.60

X1801T	Approx.	SK1	SK2	SK3	NK1	NK2	KK6	KK1	MK1	MK5
Sample pos.	Det.Lt.	18	8	7	10	23	22	6	11	8
Rb	**2**	16	1	0	106	124	87	96	111	11
Sr	**2**	1522	1685	808	570	349	916	350	742	913
Y	**2.0**	33.4	24.2	27.3	15.4	19.7	15.9	22.1	16.7	18.7
Zr	**2**	355	109	294	226	255	248	180	297	293
Nb	**1.5**	169.9	11.7	136.8	132.4	118.2	93.6	142.2	110.3	136.6
Ba	**12**	1061	5995	685	1644	1606	1192	1008	1390	217
Pb	**5**	25	4	13	3	7	5	8	6	7
Th	**4**	21	21	20	10	14	11	17	13	13
U	**3**	3	2	3	3	4	2	4	2	5
Sc	**5**	24	20	19	22	18	17	23	20	24
V	**5**	150	28	104	227	167	183	146	237	113
Cr	**4**	851	20	1114	1123	1247	1040	1241	830	1025
Co	**2**	65	11	75	80	80	79	85	75	92
Ni	**3**	943	76	1208	788	1200	1066	941	781	1149
Cu	**3**	36	24	38	111	100	102	40	120	128
Zn	**3**	56	20	53	64	74	74	90	70	54
Ga	**3**	9	0	7	10	8	10	8	12	12
Mo	**2**	0	0	0	0	0	0	1	0	0
As	**5**	3	3	2	1	2	1	0	1	5
S	**50**	365	1289	209	179	151	244	505	213	178
TiO2%		2.10	0.11	2.02	3.51	2.23	2.17	2.76	3.14	3.06
Fe2O3%		10.34	3.81	9.90	14.16	13.36	13.49	13.58	14.03	14.31

X1801T	Approx.	CHELIMA	RAMPET	POC	POC(G)	VEDN	VEDS	JAY	T1	NALLA	REDD	RAMAPU
Sample pos.	Det.Lt.	19	13	6	20	22	21	14	12	20	24	12
Rb	**2**	48	40	143	244	23	10	35	17	19	116	82
Sr	**2**	482	1001	1270	672	696	1253	1114	1142	947	1797	906
Y	**2.0**	34.9	28.4	42.5	48.1	37.6	32.9	39.7	35.1	36.7	35.5	47.5
Zr	**2**	560	549	809	1403	487	658	936	779	868	963	802
Nb	**1.5**	216.3	109.4	130.0	115.0	93.8	139.8	118.9	108.4	116.2	109.4	123.5
Ba	**12**	754	1161	444	1498	892	269	241	323	428	979	567
Pb	**5**	98	25	46	42	14	23	7	16	3	35	285
Th	**4**	40	18	17	125	16	17	14	16	12	12	20
U	**3**	6	1	2	20	0	1	3	3	1	3	10
Sc	**5**	17	20	25	22	24	19	26	15	20	25	25
V	**5**	50	171	91	149	136	109	139	77	128	132	174
Cr	**4**	655	591	130	511	649	355	371	56	259	204	228
Co	**2**	43	38	25	24	42	35	32	18	33	28	21
Ni	**3**	509	400	113	250	380	298	270	65	193	166	177
Cu	**3**	13	51	26	48	36	41	42	9	28	29	233
Zn	**3**	313	115	193	115	128	123	122	251	64	142	79
Ga	**3**	9	19	30	17	19	19	23	19	22	23	22
Mo	**2**	-1	0	1	6	2	0	0	4	0	2	0
As	**5**	16	0	4	0	4	0	0	0	0	3	2
S	**50**	183	112	42	231	263	343	100	84	76	76	83
TiO2%		3.95	2.66	4.16	2.82	2.78	3.53	3.88	3.94	3.55	3.94	3.82
Fe2O3%		6.93	11.50	12.65	9.23	12.45	13.03	12.55	8.39	10.50	11.48	15.17

A.2.8. Perovskite Nd and Hf Isotopic Data

Table A32: Perovskite Nd Isotopic Data

Sample#	Wt (g)	Sm ppm	Nd ppm	$^{147}Sm/^{144}Nd$	$^{143}Nd/^{144}Nd$	± 2SE	TDM	TDM*	εNd(1100)
Mul5	0.031	235.015	1531.366	0.0928	0.512010	0.000004	1300.67	1468.79	2.39
NK1	0.017	174.358	1128.57	0.0934	0.511963	0.000006	1362.30	1552.43	1.39
CC5 45-90	0.01	x	3762.957	X	0.511922	0.000003	X	x	x
CC5 90-150	0.018	x	3958.102	x	0.511915	0.000002	X	x	X
MK1	0.0025	172.21	996.238	0.1045	0.512016	0.000005	1422.08	1595.64	0.86
SK3	0.0004	145.172	963.549	0.0911	0.511969	0.000014	1331.37	1515.80	1.83
Tumm	0.001	280.699	1909.462	0.0889	0.512005	0.000006	1268.36	1430.29	2.85

X: Not analysed for Sm

T_{DM}*: 2-stage model ages calculated using the method of Depaolo et al. (1991).

Table A33: Perovskite Hf Isotopic Data

Sample#	Wt (g)	Lu ppm	Hf ppm	Lu/Hf	$^{176}Lu/^{177}Hf$	$^{176}Hf/^{177}Hf$	±2SE	TDM	TDM*	εHf1100
Mul5	0.031	0.69	26.16	0.0265	0.0038	0.282270	0.000004	1496	1619	3.8
Mul5		0.69	26.16	0.0265	0.0038	0.282263	0.000005	1506	1633	3.6
NK1	0.017	0.59	12.67	0.0462	0.0066	0.282293	0.000006	1587	1687	2.6
NK1		0.59	12.67	0.0462	0.0066	0.282284	0.000005	1602	1705	2.3
CC5 45-90	0.01	0.79	47.21	0.0167	0.0024	0.282093	0.000005	1694	1910	-1.4
CC5 90-150	0.018	0.51	30.33	0.0168	0.0024	0.282103	0.000004	1681	1891	-1.1
MK1	0.0025	0.51	9.05	0.0559	0.0079	0.282317	0.000017	1617	1696	2.4
SK3	0.0004	0.74	184.52	0.0040	0.0006	0.281999	0.000026	1744	2021	-3.4
Tumm	0.001	1.10	37.52	0.0294	0.0042	0.282032	0.000008	1875	2103	-4.9

T_{DM}*: 2-stage Hf model ages were derived using a method derived from the Nd model age of Liew & Hoffman (1988), using an average crustal $^{176}Lu/^{177}Hf$ ratio of 0.012 (average passive margin mud, Vervoort et al., 1999).

A.2.9. Perovskite LA-ICP-MS Data

Table A34: Perovskite LA-ICP-MS Data (All values in ppm)

Sample CC1

Element	Standard	Standard	003SMPL	004SMPL	005SMPL	006SMPL	007SMPL	008SMPL	Standard	Standard
Li7	39.76	37.47	0.373	0.43	86	0.272	0.396	1.42	35.93	35.82
Mg24	79.36	77.12	1423.94	272.91	709335.8	645.34	375.64	21318.57	74.76	77.49
Mg26	77.15	76.53	1267.24	284.01	642611.2	681.96	312.22	19389.14	81.65	75.44
Si29	351980.5	331652.7	1767.42	449.55	220672	767.36	399.11	7239.89	327963.6	316357.2
Ca43	86499.37	84136.23	292826	291642	286309.2	289225.7	292600.6	293476.8	85347.72	85773.22
Ca44	85262.52	85262.52	285880.4	285880.4	285880.4	285880.4	285880.4	285880.4	85262.52	85262.52
Sc45	41.64	41.1	3.84	3.91	61.85	3.49	3.91	6.95	40.7	40.11
Ti47	41.58	38.66	349244.8	350091.9	206706.5	347751	346575.7	351700.4	43.59	43.84
V51	37.67	37.09	117.4	118.64	8275.36	116.09	110.48	214.37	38.63	35.69
Cr53	33.71	35.22	730.12	685.49	2178070	1180.78	797.68	16515	35.29	35.59
Mn55	35.84	34.83	133.2	121.65	51818.07	144.02	130.87	2572.12	36.85	34.74
Fe57	59.66	56.56	11485.45	10638.42	1889706	11691.8	10767.49	171269.3	67.98	41.86
Co59	33.22	32.82	0.66	0.5	2626.73	1.09	0.594	87.3	33.08	31.79
Ni60	37.19	36.27	1.95	2.37	8152.19	4.1	2.34	449.33	35.97	34.3
Cu63	44.68	43.43	4.06	1.42	1348.44	2.33	2.3	10.78	44.84	44.37
Zn66	39.6	44.99	12.1	5.45	8654.18	9.9	6.47	517.27	43.1	46.66
Ga69	33.11	31.85	2.48	2.09	238.68	2.07	2.16	9.63	32.74	31.68
Ge72	36.35	33.03	12.28	13.45	12.48	14.83	13.99	13.74	35.57	35.06
As75	39.34	35.6	10.12	11.5	<7.05	13.03	11.21	11.21	35.13	41.2
Rb85	32.14	31.41	0.273	<0.028	109.41	0.292	<0.034	2	31.9	31.07
Sr88	75.73	73.99	2615.87	2539.68	596.09	2424.9	2458.01	2635.9	71.85	73.2
Y89	42.99	40.34	164.26	175.48	9.33	160.93	168.39	162.44	38.15	39.33
Zr90	40.43	39.27	278.21	284.41	660.87	247.67	276.31	315.91	37.49	38.47
Nb93	43.23	42.05	3069.23	3058.02	57.78	2888.6	2842.55	2947.56	42.14	41.25

Element	Standard	Standard	003SMPL	004SMPL	005SMPL	006SMPL	007SMPL	008SMPL	Standard	Standard
Mo95	37.85	39.69	0.4	0.27	3.2	0.3	0.44	0.34	38.71	35.98
Cd111	28.96	27.94	<0.30	<0.20	<3.68	<0.21	0.19	0.44	28.03	28.13
In115	44.03	42.55	<0.020	<0.016	<0.24	<0.014	0.022	0.185	42.57	42.22
Sn118	38.37	37.92	3.75	3.07	22.27	3.16	3.27	5.82	38.53	36.87
Sb121	39.75	38.62	0.055	<0.046	<0.76	<0.039	0.069	0.09	37.38	37
Cs133	42.39	41.19	<0.018	0.024	2.45	0.035	<0.019	0.228	43.07	40.11
Ba137	40.94	39.91	142.37	23.62	836.24	27.31	25.17	232.09	35.99	38.6
La139	36.87	35.84	3816.71	3844.06	36.2	4134.95	3706.29	3700.97	35.34	34.23
Ce140	39.09	38.9	8850.13	8886.73	57.2	10327.65	9034.04	8615.2	37.69	36.62
Pr141	39.41	37.8	991.84	1023.2	7.02	1202.66	1029.32	984.71	37.42	37.89
Nd146	35.63	35.06	3515.21	3722.97	23.34	4296.23	3807.69	3606.64	35.69	34.62
Sm147	39.09	37.69	461.9	470.58	5.2	531.14	481.61	460.56	38.62	37.71
Eu153	37.4	35.36	113.25	113.17	1.32	122.87	113.9	106.42	34.91	35.3
Gd157	41.4	38.68	232.16	241.55	3.41	246.86	230.91	218.97	39.52	38.89
Tb159	39.8	38.64	21.19	21.3	0.31	21.99	21.48	20.64	36.74	37.18
Dy163	37.88	37.66	80.1	84.3	1.95	82.19	78.55	77.32	35.62	36.73
Ho165	40.78	39.66	9.82	10.25	0.17	9.35	9.96	9.12	38.92	38.96
Er166	41	39.84	16.38	16.8	0.71	15.74	15.78	14.82	38.37	38.81
Tm169	41.44	39.78	1.37	1.43	<0.070	1.257	1.335	1.22	38.01	39.58
Yb172	42.94	41.31	5.38	5.6	<0.45	5.47	5.04	5.22	39.59	41.32
Lu175	40.96	39.67	0.448	0.59	<0.090	0.509	0.435	0.4	38.05	38.95
Hf178	38.69	38.73	13.78	15.53	17.25	13.38	13.23	14.92	36.11	37.62
Ta181	42.42	41.44	341.04	368.02	2.79	385.1	352.96	340.71	40.14	41.02
W182	41.04	38.78	3.06	3.1	7.55	2.73	3.8	3.78	38.37	40.18
Pb208	35.38	35.87	73	76.46	24.98	103.07	86.63	75.24	35.01	34.73
Bi209	31.35	29.81	0.158	0.161	0.19	0.143	0.142	0.159	28.85	28.65
Th232	40.79	39.01	774.11	920.9	2.74	1104.47	944.49	772.78	37.5	38.98
U238	35.92	36.14	35.89	39.27	3.19	35.88	35.06	32.92	35.13	34.47

Element	011SMPL	012SMPL	013SMPL	014SMPL	015SMPL	Standard	Standard	Standard
Li7	5.94	0.429	1.74	4.47	2.11	30.94	38.41	38.45
Mg24	65336.09	643.63	3680.96	32487.88	28958.71	533430	77.47	78.66
Mg26	59416.79	584.18	3275.8	29088.34	25593.52	483693.1	78.47	76.08
Si29	70662.37	458.41	2865.51	35339.23	22395.42	583280.9	341953.8	345770.4
Ca43	292428.1	286688.2	293442.3	291774.1	291135.7	282132.2	83573.97	86694.96
Ca44	285880.4	285880.4	285880.4	285880.4	285880.4	285880.4	85262.51	85262.51
Sc45	20.32	3.83	5.46	6.2	6.29	185.48	41.86	41.08
Ti47	261012.1	348102.5	359263.7	334266.5	346020.1	86584.92	37.3	42.34
V51	586.89	111.45	88.28	228.87	114.69	1643.01	37.55	37.41
Cr53	128588.5	1518.78	216.34	1330.28	1009.27	312.92	32.44	36.45
Mn55	6904.39	130.61	217	584.3	260.84	12778.15	34.54	36.08
Fe57	454995	10629.75	10846.99	50427.64	17804.86	1614925	55.22	63.83
Co59	283.3	0.64	1.36	13.55	7.4	549.86	31.93	34.23
Ni60	1145.41	2.7	10.32	84.37	127.96	2356.06	34.92	38.66
Cu63	54.21	3.1	3.3	26.04	3.13	90.97	45.65	42.72
Zn66	2190	6.85	7.15	52	17.96	1378.37	41.28	42.73
Ga69	31.75	2.28	3.54	7.53	3.56	73.75	31.2	33.74
Ge72	7.58	20.4	27.77	14.57	14.46	18.33	32.96	35.96
As75	6.11	13.9	25.48	10.79	12.33	<5.66	37.06	36.91
Rb85	10.69	0.034	1.61	36.46	9.06	167.82	30.87	32.68
Sr88	2470.62	2531.3	2607.82	2734.18	2528.67	1621.93	74.67	74.95
Y89	116.68	150.95	270.62	158.85	153.49	39.13	41.21	41.96
Zr90	399.45	242.2	519.21	455.34	290.83	372.44	40.65	39.18
Nb93	1911.22	2761.53	3953.35	2846.24	2970.85	275.97	42.22	43.05
Mo95	1.18	<0.10	<0.108	0.28	0.2	5.53	39.94	38.18
Cd111	0.92	0.48	<0.29	0.45	<0.27	3.52	30.37	27.04
In115	0.189	<0.014	<0.024	0.046	0.041	1.03	43.43	43.1
Sn118	12.57	2.63	2.94	5.51	3.92	34.96	37.87	38.48
Sb121	1.8	<0.043	<0.059	0.123	<0.066	<0.62	38.66	39.65

Element	011SMPL	012SMPL	013SMPL	014SMPL	015SMPL	Standard	Standard	Standard
Cs133	0.204	<0.018	0.229	0.98	1.45	17.89	42.78	41.09
Ba137	1674.4	30.59	33.8	541.82	55.95	1909.91	41.37	39.53
La139	2300.71	4648.79	6874.7	3861.24	4016.41	235.82	36.15	36.62
Ce140	5236.56	12441.04	18341.43	9624.53	9936.65	421.51	39.22	38.94
Pr141	598.43	1415.42	2206.21	1115.38	1142.77	44.44	38.25	38.76
Nd146	2170.33	5110.6	8128.86	4071.49	4125.68	161.17	34.78	35.89
Sm147	274.06	582.55	989.69	490.23	500.38	29.45	38.54	38.19
Eu153	62.16	133.14	217.12	113.53	115.28	6.75	36.21	36.32
Gd157	138.03	253.6	448.76	226.08	229.56	17.78	39.83	39.95
Tb159	12.37	21.3	39.77	20.16	20.09	2.16	39.05	39.34
Dy163	49.48	78.73	146.58	76.63	77.78	9.22	38.11	37.47
Ho165	6.41	8.97	16.66	8.76	9.05	1.92	40.35	40.06
Er166	12.24	15.13	26.82	16.18	15.25	2.03	40.19	40.57
Tm169	1.04	1.27	2.17	1.28	1.24	0.38	40.6	40.39
Yb172	4.08	4.7	8.57	5.41	4.74	0.98	40.78	43.19
Lu175	0.288	0.445	0.778	0.333	0.413	0.36	40.16	40.34
Hf178	18.22	12.54	27.16	19.37	14.26	8.88	39.33	38.19
Ta181	206.91	427.6	696.42	341.33	367.17	17.87	41.38	42.33
W182	3.61	3.07	1.41	3.83	3.44	5.7	38.26	41.17
Pb208	140.19	137.65	287.02	87.24	90.42	13.74	35.32	35.96
Bi209	0.249	0.11	0.259	0.251	0.163	<0.13	29.94	30.97
Th232	497.74	1534.07	3065.32	986.09	979.17	23.2	39.56	39.94
U238	19.66	32.25	84.26	28.92	32.42	4.07	35.6	36.46

Sample KK6

Element	Standard	Standard	003SMPL	004SMPL	005SMPL	006SMPL	007SMPL	008SMPL	009SMPL	Standard	Standard
Li7	38.33	36.54	1.99	1.16	0.65	2.09	6.49	9.41	165.61	37.87	37.31
Mg24	77.47	77.58	6192.99	6045.93	3372.25	6130.26	92383.07	39549.79	1429923	75.61	79.06
Mg26	75.54	79.15	6401.94	6221.65	2461.59	6213.73	89601.25	38126.53	1433296	80.3	74.8
Si29	337435.2	334601.8	18187.12	1939.24	3558.67	12897.24	105307.8	56867.21	229127.9	332219.3	339414.1
Ca43	85157.55	85339.84	291781.6	284782.1	285792.9	287583.3	285547.1	288332.2	281768.4	85856.23	84783.39
Ca44	85262.53	85262.53	285880.4	285880.4	285880.4	285880.4	285880.4	285880.4	285880.4	85262.5	85262.5
Sc45	40.83	41.35	8.47	10.02	4.74	7.57	19.71	5.75	670.16	40.92	41.12
Ti47	40.04	41.7	319456.3	356718.9	341159.3	337381.4	339942.5	308786.5	2139686	43.9	38.77
V51	37.26	37.23	203.38	467.25	213.79	218.1	1638.8	211.76	51460.88	37.03	37.42
Cr53	34.45	35.09	173.55	13751.1	230.12	254.93	13448.24	167.66	4749504	34.84	34.62
Mn55	34.83	36.11	252.52	2883.44	181.05	253.05	6784.06	529.14	292324.7	35.58	35.17
Fe57	67.24	45.65	16516.32	137114.2	10591.33	14638.85	310070.5	45854.82	*******	55.1	59.06
Co59	32.92	32.62	2.3	38.8	14.39	2.19	181.46	35.01	6976.73	32.66	32.89
Ni60	36.37	35.79	6.72	221.76	40.91	6.84	795.45	91.51	29732.39	35.79	36.37
Cu63	45.1	43.23	18.11	8.56	613.82	15.71	76.98	301.33	1181.78	43.68	44.75
Zn66	41.95	44.38	26.17	487.39	9.54	19.43	1143.83	96.6	69493.96	43.39	42.55
Ga69	32.53	32.07	6	8.36	2.31	7.22	21.37	10.92	1304.42	31.88	32.68
Ge72	33.84	35.86	7.95	12.34	10.21	9.31	10.2	7.56	29.17	33.69	35.39
As75	37.96	36.68	6.49	8.37	6.87	10.49	8.17	8.24	<44.27	36.58	38.04
Rb85	32.01	31.18	9.52	0.54	6.57	7.4	49.51	48.86	339.72	31.64	31.67
Sr88	73.63	74.52	1461.25	1315.38	1487.37	1458.68	1534.23	1678.57	3020.34	73.96	74.02
Y89	40.43	40.58	157.62	145.12	165.93	182.22	175.97	170.51	102.32	41.05	40.1
Zr90	39.36	38.98	352.69	242.28	319.14	319.84	441.16	401.24	3175.75	39.2	39.2
Nb93	42.44	42.03	2284.55	1983.64	2305.2	2321.29	1951.88	2201.47	1321.77	42.64	42
Mo95	39.48	37.05	0.34	0.3	0.72	0.89	0.69	0.62	9.05	37.73	38.94
Cd111	27.93	29.1	<0.30	<0.35	0.33	0.28	<0.63	0.45	<21.82	26.22	30.5
In115	42.5	43.49	0.023	0.059	0.042	0.059	0.168	0.055	5.05	42.87	42.92
Sn118	38.03	37.77	3.26	4.28	3.24	3.25	9.71	3.49	214.4	39.07	37.1

Element	Standard	Standard	003SMPL	004SMPL	005SMPL	006SMPL	007SMPL	008SMPL	009SMPL	Standard	Standard
Sb121	38.16	38.9	0.094	<0.093	<0.080	<0.076	<0.15	<0.078	<5.11	37.52	39.21
Cs133	41.68	41.57	0.388	0.065	0.292	0.305	6	5.66	19.87	41.88	41.45
Ba137	38.62	40.25	515.13	21.41	77.89	880.41	279.62	619.69	1938.97	38.37	39.97
La139	35.61	35.96	1775.91	2215.6	1887.56	1993.51	1772.04	1672.54	1132.03	35.86	35.68
Ce140	38.08	38.75	4412.1	6153.96	4923.11	5063.59	4579.86	4066.96	3042.76	37.8	38.78
Pr141	37.73	38.82	501.99	729.68	556.23	582.54	551.48	469.46	366.66	38.42	37.99
Nd146	35.1	35.46	1878.01	2768	2093.01	2196.88	2150.75	1794.96	1463.68	34.81	35.58
Sm147	38.17	38.36	291.32	382.77	325.01	329.85	308.92	275.68	208.83	38.15	38.32
Eu153	35.64	36.13	76.07	94.85	82.62	85.64	77.98	71.55	50.56	35.8	35.87
Gd157	38.79	40.69	169.87	205.12	177.81	190.83	177.58	158.79	114.7	40	39.2
Tb159	38	38.84	16.25	18.95	17.98	18.24	17.11	16.6	14.08	38.99	37.88
Dy163	36.58	38.13	70.32	74.42	73.16	78.78	72.15	69.59	36.87	37.08	37.26
Ho165	39.09	40.63	8.75	8.71	9.67	10.01	9.63	9.17	4.71	39.83	39.6
Er166	39.55	40.01	14.92	15	17.81	18.15	17.64	16.82	10.68	39.63	39.82
Tm169	39.13	40.97	1.41	1.18	1.55	1.64	1.59	1.57	<0.69	40.04	39.7
Yb172	40.63	42.5	6.36	5	7.29	6.93	7.54	6.27	<1.91	42.44	40.64
Lu175	38.89	40.66	0.503	0.428	0.546	0.602	0.642	0.534	1.07	39.63	39.54
Hf178	37.38	39.04	17.01	12.19	14.35	14.68	14.05	15.07	95.56	38.35	37.79
Ta181	40.49	42.73	259.63	349.09	279.55	295.54	270.04	240.48	205.74	41.52	41.23
W182	39.27	39.92	4.94	2.41	6.05	6.18	5.93	6.56	3.29	39.37	39.66
Pb208	34.63	36.41	37.12	69.23	46.69	49.64	62.68	36.39	54.53	35.51	35.17
Bi209	29.17	30.78	0.049	0.068	0.048	0.083	0.064	0.062	0.89	29.78	29.79
Th232	38.38	40.38	364.27	777.76	454.41	500.79	584.44	362.29	389.41	39.75	38.74
U238	34.85	36.62	35.67	33.68	38.78	39.28	37.03	34.38	17.66	35.8	35.34

Sample MK1

Element	Standard	Standard	003SMPL	004SMPL	005SMPL	006SMPL	007SMPL	008SMPL	009SMPL
Li7	38.75	36.31	4.35	3.72	1.78	8.47	1.452	0.338	0.671
Mg24	78.56	76.28	2154.19	1246.31	729.45	4758.3	804.97	427.09	876.31
Mg26	75.68	79.57	1942.28	1107.03	641.3	4373.46	737.02	371.19	778.49
Si29	337760.4	334072.1	3939.39	1062.09	915.75	3405.25	1159.71	1275.65	1460.81
Ca43	84645.3	85959.38	291254.5	291005.2	290460.6	290970.8	289520.2	286167.2	287966
Ca44	85262.39	85262.39	285880.4	285880.4	285880.4	285880.4	285880.4	285880.4	285880.4
Sc45	40.78	41.35	3.94	4.08	3.51	7.09	3.92	3.46	3.38
Ti47	42.86	39.03	349335.7	356711.9	351165.3	366597.8	354919.9	348179.1	351710.3
V51	36.95	37.57	222.29	332.11	224.07	504.18	229.61	213.93	228.25
Cr53	34.43	35.08	577.52	1888.09	615.45	5998.1	570.06	509.21	632.41
Mn55	35.67	35.1	257.59	954.7	237.94	2181.45	232.93	207.51	239.77
Fe57	53.69	59.4	9621.53	41258.49	7276.46	111271.3	7355.25	6954.02	7623.75
Co59	32.36	33.26	1.355	11.2	1.102	43.21	0.958	0.715	1.367
Ni60	35.67	36.57	1.46	51.55	1.51	172.99	1.32	0.73	2.16
Cu63	43.24	45.34	4.96	4.66	4.28	16.17	3.67	3.03	5.15
Zn66	42.43	43.63	13.82	155.38	9.63	386.79	9.45	10.87	9.05
Ga69	32.32	32.27	2.6	3.39	1.83	8.45	1.64	1.43	1.854
Ge72	34.76	34.51	10.65	9.62	10.91	12.77	9.63	8.39	10.9
As75	37.03	37.69	8.83	6.57	10.02	9.77	8.82	6.76	8.79
Rb85	31.82	31.43	5.31	0.043	0.183	0.529	0.26	0.043	1.538
Sr88	74.32	73.7	1219.03	1217.27	1191.68	1193.09	1204.06	1201.85	1181.91
Y89	40.34	40.72	148.84	141.99	137.05	146.56	148.91	136.81	138.93
Zr90	39.01	39.4	169.51	157.6	140.53	215.13	157.05	149.35	139.01
Nb93	42.26	42.28	1768.58	1854.35	1799.12	1812.97	1807.81	1853.14	1808.2
Mo95	38.9	37.68	0.212	0.48	0.428	0.54	0.62	0.37	0.44
Cd111	27.89	28.83	0.133	0.25	<0.139	0.35	0.23	0.21	<0.150
In115	42.34	43.61	0.0194	0.035	<0.0120	0.092	<0.014	0.017	0.0256
Sn118	37.87	38.06	2.79	2.87	2	3.86	2.49	2.14	2.01

Element	Standard	Standard	003SMPL	004SMPL	005SMPL	006SMPL	007SMPL	008SMPL	009SMPL
Sb121	38.58	38.29	0.041	0.085	<0.035	0.066	<0.035	<0.028	0.061
Cs133	41.33	41.99	0.122	<0.0106	0.022	0.016	0.023	0.013	0.0313
Ba137	40.57	38.02	65.38	17.82	17.43	62.06	40.9	12.13	29.77
La139	35.64	35.91	2020.6	1855.77	2020.78	2129.18	1952.13	1820.35	2010.39
Ce140	38.11	38.62	5590.24	5285.47	6001.21	6425.52	5361.75	4968.6	5998.26
Pr141	38.19	38.23	664.25	597.94	704.28	781.94	637.01	557.75	711.6
Nd146	34.73	35.84	2459.02	2166.98	2578.33	2854.67	2330.06	1972.48	2579.42
Sm147	38.36	38.13	353.33	319.38	367.61	404.06	343.14	290.6	364.7
Eu153	35.45	36.31	89.8	84.78	93.75	100.13	88.5	80.13	93.03
Gd157	40.26	38.94	190.14	172.98	183.12	200.36	182.25	157.45	183.91
Tb159	38.24	38.55	18.43	16.56	17.76	18.95	18.01	16.04	17.55
Dy163	37.6	36.84	73.31	65.98	69.63	75.05	71	65.23	69.1
Ho165	39.81	39.69	9.01	8.58	8.72	9.4	9.02	8.05	8.73
Er166	39.77	39.73	15	14.8	14.51	15.39	15.1	14.35	14.63
Tm169	39.82	40.01	1.338	1.251	1.214	1.27	1.268	1.311	1.223
Yb172	41.4	41.53	5.23	5.06	5.06	5.24	5.87	5.18	4.96
Lu175	39.26	40.07	0.529	0.486	0.401	0.449	0.473	0.508	0.429
Hf178	37.93	38.27	7.28	7.05	5.57	7.51	6.88	6.41	5.95
Ta181	40.9	42.05	306.84	294.67	311.71	342.76	292.58	270.48	322.78
W182	39.42	39.69	2.49	2.78	2.58	2.86	2.87	2.7	2.76
Pb208	34.75	36.12	63.92	50.27	77.65	88.95	57.47	33.85	82.87
Bi209	29.41	30.34	0.094	0.099	0.134	0.094	0.1	0.087	0.122
Th232	38.53	40.08	599.55	479.99	653.48	863.86	541.96	331.82	708.11
U238	34.97	36.35	43.71	44.89	45.88	51.3	44.76	43.29	48.17

Sample Mul5

Element	Standard	Standard	003SMPL	004SMPL	005SMPL	006SMPL	007SMPL	008SMPL	Standard	Standard
Li7	39.42	33.04	0.061	1.09	1.31	1.01	1.65	1.08	33.31	33.76
Mg24	76.7	81.26	1167.62	598.77	645.78	559.84	853.24	633.78	82.01	76.84
Mg26	424.77	<****	<****	<****	<****	8919.29	4856.02	2307.89	209.61	178.08
Si29	354805.1	327116.5	1112.86	613.51	573.75	312.18	550.69	566.76	322374	325652
Ca43	85925.11	82502.26	278209.9	280466.8	295669.3	284929	286082.9	286151	83948.73	84383.87
Ca44	85262.52	85262.52	285880.4	285880.4	285880.4	285880.4	285880.4	285880.4	85262.52	85262.52
Sc45	40.8	42.21	4.42	5.23	4.75	4.67	4.31	4.17	41.78	41.46
Ti47	39.83	48.64	367591	377599.6	378327	372193.6	374380.9	364719.4	41.89	44.53
V51	36.33	43.15	142.73	144.19	141.26	139.15	151.08	135.36	39.22	39.68
Cr53	30.36	56	39.07	21.38	53.39	23.43	299.02	23.32	39.77	36.85
Mn55	23.56	66.6	284.09	383.39	348.26	311.24	367.96	293.47	44.34	43.04
Fe57	54.92	64.58	9685.28	9346.06	8911.7	9228.4	9818.35	9298.19	65.18	79.53
Co59	32.2	36.39	0.75	1.24	0.97	0.88	1.44	1.04	34.49	33.37
Ni60	35.21	42.31	3.6	2.06	1.5	1.87	4.83	1.65	38.29	37.38
Cu63	43.64	49.73	1.72	3.27	3.08	3.25	3.6	2.52	43.86	43.28
Zn66	41.61	52.9	6.08	6.56	6.8	6.17	7.72	5.18	50.88	44.18
Ga69	31.79	35.51	1.96	3.01	2.88	2.3	2.51	2.15	33.27	32.79
Ge72	34.09	39.04	4.3	21.03	19.04	17	24.34	19.03	34.96	35.03
As75	36.99	41.45	4.3	18.23	14.64	14.11	22.24	13.64	40.04	34
Rb85	30.71	38.97	0.514	0.038	0.075	0.078	0.185	0.144	33.86	33.36
Sr88	72.17	88.11	3126.22	2548.23	2625.58	2519.92	2403.53	2540.59	77.05	77.74
Y89	39.23	50.97	240.08	295.02	279.96	247.19	304.15	247.11	43.85	43.52
Zr90	37.98	49.03	628.79	390.43	395.6	364.08	339.04	363.93	42.05	41.62
Nb93	40.96	53.34	3074.73	2943.87	3031.21	2781.4	3080.83	2584.51	45.44	44.76
Mo95	37.17	47.11	0.69	0.46	0.23	0.66	0.42	0.33	42.34	39.7
Cd111	27.38	35.1	0.34	<0.31	<0.33	0.39	0.54	<0.35	35.22	28.94
In115	41.35	58.33	0.029	0.061	0.031	0.043	0.054	<0.022	47.7	46.39
Sn118	36.64	52.2	4.58	3.05	3.86	3.18	3.16	2.9	41.46	41.29

Element	Standard	Standard	003SMPL	004SMPL	005SMPL	006SMPL	007SMPL	008SMPL	Standard	Standard
Sb121	36.9	53.99	<0.063	<0.076	<0.062	<0.060	<0.065	<0.077	44.35	41.79
Cs133	39.99	59.02	0.109	<0.022	<0.027	0.048	0.044	<0.028	47.05	46.91
Ba137	37.64	58.04	48.31	34.77	33.24	32.87	31.1	39.97	44.88	43.66
La139	34.35	51.06	2733.67	5688.85	5689.98	4882.62	5880.09	5042.57	40.72	39.54
Ce140	36.83	54.94	4729.99	14878.54	14614.75	12547.42	16538.85	12994.99	43.33	42.7
Pr141	36.69	54.82	474.37	1761.02	1715.39	1456.26	2013.38	1548.17	43.24	42.52
Nd146	33.75	52.33	1724.76	6883.06	6490.66	5475.07	7766.53	5829.08	42.05	38.55
Sm147	36.65	57.65	299.82	936.45	876.27	744.11	1050.37	771.25	43.14	42.51
Eu153	34.36	52.85	87.09	217.38	206.57	176.89	234.44	178.59	41.5	39.67
Gd157	37.98	58.56	225.39	488.98	461.21	386.9	507.39	395.43	45.8	43.6
Tb159	36.79	58.56	24.44	45.54	42.17	36.07	46.83	35.96	44.4	43.32
Dy163	35.68	55.55	112.28	179.49	165.86	137.25	179.23	138.09	43.55	40.66
Ho165	38.06	62.13	15.06	21.66	20.06	17.46	21.15	16.51	45.69	45.91
Er166	38.05	62	27.2	35.33	34.28	28.33	35.18	25.86	45.75	44.38
Tm169	38.22	62.57	2.58	2.85	2.67	2.52	2.64	2.08	46.07	45.41
Yb172	39.61	64.88	10.56	11.26	10.49	9.23	10.81	8.37	47.98	47.75
Lu175	37.93	63.49	1.05	1.12	1.03	0.84	1.03	0.78	46.8	45.22
Hf178	36.41	60.75	40.35	24.72	23.97	20.49	18.37	19.95	44.87	42.86
Ta181	39.64	66.75	241.01	604.92	564.6	500.12	633.2	478.97	48.11	47.47
W182	37.94	60.23	4.96	4.04	3.69	4	3.8	3.57	43.6	43.6
Pb208	33.77	58.1	12.19	187.93	155.89	128.1	286.52	154.48	42.7	40.4
Bi209	28.6	47.42	0.264	0.259	0.337	0.2	0.316	0.285	34.05	32.12
Th232	37.51	64.87	79.34	2098.11	1682.81	1435.75	3037.7	1774.04	46.87	44.41
U238	34.04	59.26	55.87	97.6	97.66	75.24	123.83	67.42	42	40.77

Element	011SMPL	012SMPL	013SMPL	014SMPL	015SMPL	016SMPL	Standard	Standard
Li7	1.02	0.9	0.99	1.02	1.03	0.27	39.91	40.16
Mg24	730.67	971.52	1098.93	1730.71	1621.99	1773.51	76.62	76.59
Mg26	1160.33	1377.11	1302.41	1826.61	1543.82	1546.36	64.02	54.54
Si29	229.09	1068.87	770.83	1513.84	1136.38	1529.51	343527.6	342203.1
Ca43	286417.2	290647.1	293850.2	295132.1	295678.4	292405.2	85477.26	86379.45
Ca44	285880.4	285880.4	285880.4	285880.4	285880.4	285880.4	85262.52	85262.51
Sc45	4.93	4.27	4.57	4.82	4.41	5.34	40.86	40.6
Ti47	359344.7	350094.2	357232.6	357348.5	352612.2	344403	40.13	38.98
V51	142.63	130.35	135.37	125.65	131.52	120.87	35.96	36.14
Cr53	275.61	18.53	17.17	13.75	13.59	44.72	34.84	31.21
Mn55	272.94	228.45	244.72	214.49	202.75	178.57	32.5	31.14
Fe57	8182.45	8796.72	9120.79	8703.12	9039.2	8103.14	58.71	39.64
Co59	1.15	0.89	0.95	1.14	0.94	1.02	32.29	32.05
Ni60	2.48	1.93	2.8	1.78	3.2	1.5	36.03	34.31
Cu63	3.77	2.98	3.56	2.75	2.36	7.76	43.18	45.81
Zn66	7.46	6.97	9.96	6.09	6.66	6.3	41.81	40.54
Ga69	2.01	1.98	1.74	2.44	2.54	1.59	32.04	31.66
Ge72	17.5	15.52	15.51	12.62	18.03	6.13	34.28	34.37
As75	17.32	12.14	13.18	10.83	13.72	5.06	37.6	38.18
Rb85	0.063	0.127	0.075	0.212	0.126	0.159	30.65	30.43
Sr88	2349.76	2356.42	2347.53	2357.76	2153.58	2464.63	72.28	71.68
Y89	265.27	216.81	224.53	238.43	197.74	223.51	38.82	38.87
Zr90	327.68	323.05	333.97	376.77	307.13	454.83	38.08	37.38
Nb93	2778.14	2345.49	2595.08	2688.12	2046.65	2836.09	40.84	40.54
Mo95	0.2	0.41	0.52	0.47	0.43	0.22	36.43	37.38
Cd111	0.44	<0.32	<0.23	0.67	<0.33	<0.34	29.38	25.12
In115	0.046	<0.022	0.029	<0.022	<0.022	0.086	41.44	40.2
Sn118	3.13	2.52	3.39	2.9	2.71	3.09	36.55	35.7
Sb121	<0.090	<0.062	<0.063	<0.071	<0.060	0.059	37.5	35.13

Element	011SMPL	012SMPL	013SMPL	014SMPL	015SMPL	016SMPL	Standard	Standard
Cs133	<0.027	0.046	<0.020	0.082	0.024	<0.021	39.6	38.5
Ba137	25.2	36.54	32.17	31.41	30.18	30.94	36.5	37.19
La139	4871.13	4126.19	3971.96	3653.99	3845.92	2546.91	33.56	33.72
Ce140	12969.56	10598.81	10523.38	8621.3	10447.06	4584.51	36.02	36.05
Pr141	1534.26	1204.82	1186.6	1000.55	1249.57	478.15	36.17	35.67
Nd146	5664.78	4505.04	4333.17	3642.38	4597.05	1637.34	32.43	33.52
Sm147	785.41	612.96	603.67	535.4	617.76	278.06	36.09	35.82
Eu153	185.92	146.79	150.79	130.28	136.95	80.01	34.25	32.97
Gd157	389.22	302.8	308.93	288.02	283.97	179.2	37.27	36.84
Tb159	36.9	28.53	29.21	27.92	26.46	19.74	35.64	35.93
Dy163	144.68	111.75	112.71	114.16	99.76	86.56	34.79	35
Ho165	17.16	13.36	13.76	14.15	11.68	11.79	36.52	37.32
Er166	27.44	22.51	23.01	23.31	19.22	19.94	37.42	36.77
Tm169	2.35	1.79	1.87	1.98	1.64	1.93	36.87	37.39
Yb172	9.45	7.56	7.86	7.8	6.9	7.71	38.68	38.32
Lu175	0.69	0.64	0.58	0.68	0.56	0.69	36.76	36.68
Hf178	15.69	16.38	16.47	18.19	16.18	21.72	36.27	34.53
Ta181	452.88	373.19	380.89	366.08	380.39	193.78	38.61	38.26
W182	3.18	2.96	3.38	2.82	2.18	2.92	38.05	36.57
Pb208	133.52	98.9	97.24	65.56	121.08	8.47	34.25	31.29
Bi209	0.178	0.199	0.228	0.175	0.124	0.174	28.71	27.6
Th232	1509.03	1021.23	995.43	708.75	1372.18	48.19	36.61	36.04
U238	95.99	58.73	66.41	57.94	39.89	45.98	33	32.87

Sample CC5

Element	Standard	Standard	003SMPL	004SMPL	005SMPL	006SMPL	007SMPL	008SMPL	Standard	Standard
Li7	37.47	39.91	0.125	0.543	0.47	0.585	0.665	0.859	36.52	35.73
Mg24	76.02	85.21	719.6	5317.63	532.72	2287.82	3134.43	7782.76	78.84	78.3
Mg26	<17.46	245.62	1688	12024.23	934.29	3897.21	4969.82	11962.81	110.92	102.39
Si29	348120.2	331782.1	621.76	2418.38	477.16	1362.89	1844.77	2213.5	330833	322045.5
Ca43	85438.39	85306.64	287093.9	292192.2	286550	280581.6	280861.3	287268.6	84853.9	84112.32
Ca44	85262.39	85262.39	285880.4	285880.4	285880.4	285880.4	285880.4	285880.4	85262.4	85262.4
Sc45	40.96	40.72	5.4	5.97	4.62	5.75	6.08	4.71	42.52	40.55
Ti47	40.12	44.51	365707	388699.6	356280.6	366351.9	371120	430589.6	41.5	42.03
V51	36.45	40.55	93.48	100.51	91.71	92.8	97.06	223.35	38.38	38.66
Cr53	32.98	38.24	161.08	282.8	263.81	162.25	278.88	129.34	36.65	39.61
Mn55	28.18	53.4	305.92	732.29	287.56	930.37	1364.05	1338.22	41.49	39.23
Fe57	55.7	59.64	10715.16	11948.2	9857.21	17322.34	20890.59	15422.06	53.92	61.55
Co59	32.12	36.76	0.8	0.609	0.74	0.61	0.82	2.59	33.48	32.63
Ni60	35.69	37.95	3.06	3.35	2.92	3.05	7.56	28.55	35.98	36.93
Cu63	43.77	46.07	2.91	3.65	4.28	3.96	23.36	5.23	45.55	43.55
Zn66	42	46.83	6.91	7.02	8.47	8.2	7.57	23.99	46.87	42.73
Ga69	31.51	35.58	5.4	5.54	5.06	5.06	4.88	105.11	34.19	33.06
Ge72	33.83	39.35	41.02	37.32	32.02	37.98	35.77	21.25	35.93	34.55
As75	36.53	40.29	34.31	28.69	25.41	32.38	26.73	19.04	40.92	38
Rb85	30.63	36.4	0.041	<0.023	0.035	<0.028	0.108	3.22	34.11	32.7
Sr88	71.6	86.71	3111.18	3162.27	3068.5	2914.41	2891.04	5142.78	79.23	76.77
Y89	39.1	47.78	349.38	381.12	289.19	340.24	323.86	412.37	43.8	42.26
Zr90	37.99	45.42	663.66	834.31	557.04	715.76	664.34	846.53	41.43	40.52
Nb93	40.83	49.47	5052.84	4483.98	4172.01	4950.83	4597.65	8353.3	45.98	43.56
Mo95	36.8	47.61	0.28	1.4	0.2	0.35	0.33	1.6	40.14	41.08
Cd111	27.24	36.73	0.49	0.65	0.42	0.43	0.39	<0.25	28.63	30.64
In115	41.07	55.17	0.033	0.021	0.041	<0.020	0.027	0.032	47.13	45.57
Sn118	36.3	50.07	3.41	3.97	4.55	3.37	4.21	5.14	41.36	40.06

Element	Standard	Standard	003SMPL	004SMPL	005SMPL	006SMPL	007SMPL	008SMPL	Standard	Standard
Sb121	36.62	51.4	<0.064	<0.054	0.055	0.114	0.056	0.107	43.04	40.92
Cs133	39.61	56.71	<0.028	0.022	<0.021	0.038	<0.023	0.146	47.66	44.41
Ba137	37.03	58.42	34.66	89.59	31.36	85.63	105.44	18642.26	45.46	44.48
La139	34.05	48.48	10038.29	9866.63	8318.88	9277.13	8672.94	6564.66	39.86	38.72
Ce140	36.39	53.51	27333.72	25617.74	22811.01	26172.9	22761.51	15245.56	44.02	42.02
Pr141	36.3	53.34	3250.37	3047.9	2626.31	3090.13	2702.89	1751.66	43.13	41.84
Nd146	33.51	49.17	12123.94	11281.21	9387.46	11313.59	9823.37	6359.56	39.24	38.06
Sm147	36.21	54.51	1540.13	1426	1168.11	1409.23	1244.5	867.48	44.96	41.06
Eu153	33.79	54.3	340.92	323.29	272.41	319.95	275.15	215.96	42.79	40.6
Gd157	37.45	56.44	711.37	690.98	554.58	652.51	578.94	481.52	46.01	45.01
Tb159	36.29	56.79	63.19	62.03	48.55	57.21	52.99	48.56	45.64	42.86
Dy163	35.12	55.61	233.59	232.85	182.67	211.99	191.14	200.88	43.81	42.33
Ho165	37.54	59.42	27.79	27.37	21.17	25.35	22.19	25.88	47.13	45.12
Er166	37.58	58.71	44.58	44.16	35.45	38.69	38.75	46.62	46.77	43.85
Tm169	37.75	59.77	3.33	3.53	2.68	3.11	3	4.03	46.76	44.52
Yb172	39.07	62.58	13.81	14.62	11.06	12.3	11.07	17.73	49.11	47.83
Lu175	37.47	60.41	1.07	1.33	0.86	1.12	0.98	1.35	46.46	44.89
Hf178	35.91	58.68	46.31	43.08	37.63	43.82	40.86	33.67	45.51	43.43
Ta181	39.18	62.47	1227.33	920.91	804.8	1047.26	883.14	683.76	48.73	46.25
W182	37.3	61.91	4.02	8.87	2.31	5.06	5.8	19.29	47.68	43.03
Pb208	33.35	55.71	473.45	336.61	304.01	395.86	312.88	235.5	42.22	40.27
Bi209	28.2	45.21	0.36	0.353	0.303	0.291	0.317	0.332	34.58	33.68
Th232	37.04	60.91	5725.12	3834.39	3322.59	4634.52	3708.67	1999.25	46.43	44.39
U238	33.61	56.24	146.28	133.51	110.97	117.83	108.64	165.59	42.45	40.36

Element	011SMPL	012SMPL	013SMPL	014SMPL	015SMPL	016SMPL	Standard	Standard
Li7	0.313	0.138	0.536	0.245	0.203	0.293	37.97	38.72
Mg24	1058.91	544.7	604.31	575.42	759.67	400.46	77.27	75.87
Mg26	1229.88	584.78	622.32	560.22	686.06	351.63	70.16	62.94
Si29	678.22	504.92	501.44	372.6	725.15	619.31	343627.2	339140.4
Ca43	288341.6	288074.3	284524	283565.8	279159.3	286391.9	85741.15	85767.38
Ca44	285880.4	285880.4	285880.4	285880.4	285880.4	285880.4	85262.4	85262.4
Sc45	6.16	6	5.08	6.27	5.21	4.24	41.56	40.04
Ti47	358592.7	358774.8	361539.4	356177.1	357645.5	351869.7	39.09	41.56
V51	82.87	89.59	88.79	87.55	87.7	108.29	36.9	35.95
Cr53	149.52	60.02	211.35	240.87	216.64	426.12	30.99	35.6
Mn55	378.35	241.62	429.47	211.74	380.69	227.9	33.21	32.4
Fe57	12945.45	10812.49	12408.18	10941.83	13312	9172.83	59.75	52.22
Co59	0.509	0.7	0.71	0.61	0.64	0.66	32.83	32.2
Ni60	1.87	2.5	2.05	3.27	2.39	2.99	37.77	34.2
Cu63	2.26	3.42	3.69	3.77	2.87	3.24	44.32	43.59
Zn66	7.38	5.84	7.76	7.14	4.86	5.7	42.24	41.62
Ga69	4.43	4.94	5.08	5.53	4.37	3.79	31.76	31.21
Ge72	25.92	32.59	31.44	45.52	29.78	27.42	33.64	34.71
As75	20.08	26.43	25.16	37.67	23.41	25.19	36.6	35.64
Rb85	0.037	0.057	0.09	<0.028	<0.026	0.127	31.27	29.84
Sr88	2807.75	2728.59	2685.05	2921.9	2624.88	2624.55	71.67	71.33
Y89	333.4	314.44	283.16	310.73	266.2	298.9	40.06	37.98
Zr90	944.56	588.94	518.4	1246.68	519.93	695.02	38.47	37.55
Nb93	5574.53	4683.66	4038.72	5083.23	3602.91	5590.46	41.66	39.86
Mo95	0.17	0.138	0.105	0.11	0.095	0.2	38.47	35.45
Cd111	<0.20	<0.21	0.24	0.34	0.46	<0.15	28.03	26.85
In115	<0.018	0.042	0.026	0.024	<0.015	0.039	41.45	40.25
Sn118	4.09	4.07	3.12	2.65	2.77	3.34	37.4	35.24
Sb121	<0.046	<0.050	<0.042	0.074	<0.038	<0.038	36.97	35.68

Element	011SMPL	012SMPL	013SMPL	014SMPL	015SMPL	016SMPL	Standard	Standard
Cs133	<0.018	0.031	0.021	0.044	<0.017	0.018	40.09	38.14
Ba137	35.57	30.86	36.31	24.46	67.59	16.74	38.42	34.41
La139	7315.52	7754.52	6999.87	9043.97	6802.72	6662.81	34.06	33.31
Ce140	16902.01	20467.76	18111.22	25321.24	18074.97	16874.53	36.15	35.31
Pr141	1900.04	2419.82	2137.18	3049.47	2057.77	1945.48	36.35	35.12
Nd146	6764.25	8931.95	7927	11504.1	7631.5	7081.57	32.65	33.69
Sm147	934.51	1129.6	991.4	1389.17	952.31	910.81	36.49	34.78
Eu153	224.56	247	218.26	286.18	201.36	208.61	33.53	32.17
Gd157	496.86	524.41	447.63	591.39	422.47	432.26	36.39	36.52
Tb159	47.25	46.24	39.39	50	37.3	40.06	35.77	34.81
Dy163	181.59	174.25	146.1	180.17	137.26	151.48	34.59	33.71
Ho165	21.68	20	17.11	20.57	16.39	18.49	37.03	35.86
Er166	35.11	32.46	28.28	32.42	25.95	29.69	37.12	36.22
Tm169	2.77	2.66	2.22	2.38	2.01	2.45	37.07	36.46
Yb172	11.84	9.63	9.11	8.76	8.16	9.96	38.48	37.24
Lu175	0.94	0.87	0.74	0.78	0.68	0.91	37.09	35.64
Hf178	52.12	33.15	27.65	69.46	24.97	35.23	34.71	34.73
Ta181	597.94	898.42	673.09	1089.18	603.11	574.66	38.52	37.67
W182	2.7	2.52	2.38	1.05	2.39	1.58	37.56	35.29
Pb208	87.38	374	245.21	616.44	220.52	203.6	32.33	32.25
Bi209	0.262	0.19	0.29	0.36	0.248	0.4	27.77	27.18
Th232	819.52	3954.19	2668.11	7195.49	2506.81	2215.69	36.03	35.82
U238	104.33	95.5	88.04	110.77	72.28	110.8	32.59	32.38

Element	Standard	Standard	003SMPL	004SMPL	005SMPL	006SMPL	007SMPL	008SMPL	Standard	Standard
Li7	50.56	40.38	0.88	0.156	0.78	0.74	3.24	4.28	48.21	37.29
Mg24	88.77	81.19	7271.75	556.96	7293.8	9456.57	19545.37	21085.51	92.52	76.2
Mg26	93.03	74.91	7346.25	505.78	7199.62	9244.82	19927.69	20349.66	94.08	84.11
Si29	367177.5	335712.1	2924.65	661.72	2281.29	1669.41	3813.52	12269.75	363270.1	326213.7
Ca43	86065.84	86040.38	292063.6	284925.4	276304.7	284481.1	278358.5	284932.8	87189.91	87050.5
Ca44	85262.39	85262.51	285880.4	285880.4	285880.4	285880.4	285880.4	285880.4	85262.51	85262.51
Sc45	37.06	41.4	10.85	5.58	5.18	7.77	34.23	26.13	37.97	43.08
Ti47	41.6	43.51	442085.3	350548.1	360917.5	536664.8	453094.8	389608.9	42.52	40.94
V51	45.79	37.05	125.49	88.73	93.99	162.16	274.03	231.45	49	36.2
Cr53	45.18	36.35	697.82	98.16	224.87	793.82	5258.95	2420.65	47.03	33.14
Mn55	39.01	35.66	4606.48	231.36	1097.79	5653.67	7193.96	2866.4	39.53	34.88
Fe57	60.2	55.07	81137.64	9654.36	12700.16	32910.46	244834.9	169255.5	56.88	74.29
Co59	35.46	33	2.65	0.75	1.7	4.61	31.87	17.46	42.62	32.76
Ni60	45.92	35.93	35.41	2.91	5.91	23.24	501.43	602.4	41.02	35.16
Cu63	53.36	43.91	4.67	3.67	10.49	5.52	8.25	235.88	56.05	42.51
Zn66	62.59	41.19	119.37	7.39	12.03	22.54	610.43	265.86	74.25	43.36
Ga69	35.63	32.35	6.27	4.5	6.33	11.42	24.83	8.38	37.46	30.91
Ge72	38.83	34.05	34.85	33.7	38.19	45.01	34.42	29.77	41.82	35.51
As75	50.44	38.36	28.65	25.92	30	35.38	30	26.07	40.48	35.11
Rb85	37.91	31.73	0.105	<0.034	<0.046	0.675	0.104	<0.042	38.09	31.08
Sr88	79.18	76.11	2764.97	2603.04	2743.3	2200.73	2941.9	2757.53	78.28	76.03
Y89	38.23	40.87	346.6	322.41	408.07	451.25	349.53	301.12	38.07	44.07
Zr90	38.35	38.92	879.46	739.66	958.83	1018.17	1116.11	958.5	36.93	42.18
Nb93	44.14	42.78	6181.33	5549.55	4650.66	7981.35	5307.06	4339.52	42.83	43.31
Mo95	46.97	38.88	1.26	0.124	1.06	1.2	5.6	1.01	42.67	38.17
Cd111	39.92	28.29	0.62	<0.25	<0.29	<0.27	0.48	<0.32	41.72	26.94
In115	47.08	43.28	0.098	<0.022	<0.029	0.064	0.114	0.207	47.49	42.12
Sn118	44.29	38.29	7.17	3.58	2.82	6.96	7.63	6.02	45.73	38.2
Sb121	45.32	39.91	0.169	0.056	0.113	0.257	0.86	0.8	47.12	38.96

Element	Standard	Standard	003SMPL	004SMPL	005SMPL	006SMPL	007SMPL	008SMPL	Standard	Standard
Cs133	51.67	43.1	0.037	<0.024	<0.030	0.046	<0.044	<0.031	52.26	41.77
Ba137	41.13	37.71	246.61	27.59	107.86	454.08	326.69	265.35	38.86	39.88
La139	35.31	36.13	8042.19	7788.6	8967.69	10654.54	8221.04	7034.3	35.21	37.17
Ce140	42.67	38.91	21347.36	20808.7	23871.61	29166.85	22097.22	17478.26	41.84	39
Pr141	40.05	39.56	2519.24	2483.44	2821.05	3376.36	2613.78	2042.21	38.4	39.61
Nd146	34.72	36.33	9024.06	8833.69	9857.02	12180.14	9467.96	7252.07	31.76	37.57
Sm147	38.46	39.24	1153.67	1135.94	1243.78	1559.17	1214.41	944.9	34.24	42.33
Eu153	37.04	36.76	259.79	252.74	277.95	340.03	266.23	212.44	35.22	37.21
Gd157	37.79	39.98	546.87	527.03	596.07	716.69	569.96	450.9	37.63	42.89
Tb159	38.69	39.4	49.92	48	51.89	64.2	49.63	42.44	37.02	42
Dy163	37.14	38.07	186.63	176.8	195.46	238.77	193.15	155.21	36.3	40.06
Ho165	38.11	39.45	21.54	21.08	23.54	28.9	21.95	19.11	37.61	43.55
Er166	36.84	39.86	36.02	33.21	38.13	45.23	34.61	30.73	36.03	42.86
Tm169	37.4	40.62	2.97	2.75	2.96	3.74	2.72	2.34	38.34	43.75
Yb172	41.25	42.05	10.69	10.97	11.84	14.83	11.32	10.83	38.88	45.3
Lu175	38.87	40.57	0.845	0.864	0.965	1.36	1.09	0.847	37.15	44.33
Hf178	37.25	38.85	42.47	41.5	29.94	52.16	40.7	38.14	35.92	42.62
Ta181	41.24	42.03	902.56	959.65	774.72	1094.34	850.25	656.61	39.73	44.08
W182	49.28	41.19	15.13	2.41	8.43	18.48	10.96	6.05	48.94	39.88
Pb208	44.22	36.37	247.84	323.08	327.39	480.37	307.01	198.38	47.89	35.27
Bi209	37.59	31.01	0.382	0.291	0.279	0.687	0.29	0.34	36.54	29.73
Th232	39.23	40.55	2843.71	3696.77	3721.59	4787.27	3936.24	2229.88	38.47	42.79
U238	45.1	37.62	135.93	118.22	128.18	180.03	113.81	95.08	43.92	35.82

Element	011SMPL	012SMPL	013SMPL	014SMPL	015SMPL	016SMPL	Standard	Standard
Li7	0.132	0.172	0.531	0.31	0.465	0.166	36.11	36.51
Mg24	517.05	603.04	2033.72	2187.12	524.77	553.27	75.8	76.1
Mg26	490.23	563.23	1918.46	2105.75	464.58	577.95	74.72	75.33
Si29	573.55	609.04	782.11	1064.2	560.85	647.05	329877.2	324511.2
Ca43	286258.2	289049.4	295635.8	287915.8	286601.3	288323.4	83851.65	84823.3
Ca44	285880.4	285880.4	285880.4	285880.4	285880.4	285880.4	85262.51	85262.51
Sc45	5.03	6.11	5.14	5.08	4.91	4.94	41.36	39.6
Ti47	348154.8	366929.1	353944	355846.5	358644.2	351305.3	38.88	41.3
V51	89.63	90.71	93.21	141.5	90.13	87.67	37.14	37.36
Cr53	203.29	123.73	324.41	702.45	197.7	163.68	34.39	34.06
Mn55	199.7	216.28	319.16	434.68	261.39	208.99	35.32	35.05
Fe57	8453.36	9270.03	10560.56	14021.08	9281.73	9147.21	47.67	55.5
Co59	0.78	0.77	0.62	1.34	0.53	0.82	32.71	31.86
Ni60	2.72	2.45	17.59	13.52	2.37	2.1	36.34	36.09
Cu63	2.86	2.66	3.55	4.13	2.54	2.46	44.48	44.36
Zn66	6.39	4.28	7.12	9.69	6.55	5.34	43.18	42.4
Ga69	3.9	4.28	5.05	4.21	3.48	4.45	32.33	32.86
Ge72	31.82	32.26	33.32	29.96	32.28	30.83	33.67	34.84
As75	27.33	28.96	25.57	24.61	26.72	27.86	37.37	37.94
Rb85	<0.025	<0.039	0.088	0.08	0.084	<0.029	31.5	31.48
Sr88	2600.74	2600.25	2649.85	2578.14	2633.44	2732.51	72.14	72.84
Y89	266.13	310.75	269.81	350.73	276.17	254.05	39.88	39.21
Zr90	470.8	609.3	510.6	1254.24	528.44	433.32	39.02	38.05
Nb93	3582.78	4309.56	4228.97	7714.07	3656.35	3354.66	41.77	41.66
Mo95	0.091	0.52	0.2	0.59	<0.070	0.13	37.81	38.03
Cd111	0.23	<0.33	<0.22	<0.18	0.35	0.22	28.42	28.43
In115	0.028	0.05	<0.021	0.058	<0.017	0.033	43.33	42.27
Sn118	2.16	2.82	2.74	4.95	3.26	2.75	37.75	36.83
Sb121	<0.042	0.081	0.066	<0.045	0.145	0.08	36.99	37.99

Element	011SMPL	012SMPL	013SMPL	014SMPL	015SMPL	016SMPL	Standard	Standard
Cs133	<0.019	0.04	<0.023	<0.017	<0.020	<0.023	40.9	40.44
Ba137	22.04	37.54	51.59	43.56	26.24	29.85	39.69	39.73
La139	6868.83	7614.47	6863.5	6877.38	6679.99	6789.1	35.24	35.24
Ce140	18580.95	19544.38	18863.12	17704.15	17300.27	18374.8	37.6	37.94
Pr141	2233.39	2347.36	2235.37	2168.7	2082.24	2160.5	37.14	37.57
Nd146	7970.52	8648.88	8076.69	7546.6	7546.9	7688.59	33.69	35.55
Sm147	997.58	1105.33	1025.49	990.88	949.1	966.99	36.59	37.88
Eu153	214.22	232.59	217.03	225.48	204.46	204.17	34.97	35.42
Gd157	446.83	514.15	442.23	482.8	432.53	431.99	38.58	38.82
Tb159	38.75	46.17	39.9	44.94	37.84	37.18	36.99	37.42
Dy163	146.14	165.02	141.88	169.29	140.37	135.83	36.09	36.34
Ho165	16.88	19.9	16.71	21.12	17.48	15.64	38.68	39.31
Er166	25.96	31.22	26.65	34.75	27.09	24.72	38.87	39.41
Tm169	2.12	2.34	2.19	3.07	2.08	1.94	38.98	38.45
Yb172	7.34	9.74	9.35	11.66	8.71	7.17	39.64	41.39
Lu175	0.628	0.833	0.639	1.12	0.767	0.654	38.45	38.14
Hf178	25.47	32.43	25.21	63.12	26.4	22.2	36.32	37.45
Ta181	670.8	797.39	714.78	663.42	595.92	576.24	40.66	40.45
W182	1.4	3.63	3.9	3.7	2.5	1.8	38.78	38.22
Pb208	264.73	248.89	269.63	199.01	193.75	190.41	34.64	34.66
Bi209	0.232	0.2	0.234	0.503	0.259	0.164	29.17	29.27
Th232	3031.49	3272.21	3333.74	2393.22	2449.44	2403.18	37.8	38.04
U238	81.7	92.12	90.81	150.54	77.8	65.4	34.21	35.04